

Chemical Rocket Propulsion

Guest Editors: David Greatrix, Ivett Leyva, Dario Pastrone,
Valsalayam Sanal Kumar, and Michael Smart





Chemical Rocket Propulsion

International Journal of Aerospace Engineering

Chemical Rocket Propulsion

Guest Editors: David Greatrix, Ivett Leyva, Dario Pastrone,
Valsalayam Sanal Kumar, and Michael Smart



Copyright © 2012 Hindawi Publishing Corporation. All rights reserved.

This is a special issue published in "International Journal of Aerospace Engineering." All articles are open access articles distributed under the Creative Commons Attribution License, which permits unrestricted use, distribution, and reproduction in any medium, provided the original work is properly cited.

Editorial Board

Noor Afzal, India
Brij N. Agrawal, USA
Saad A. Ahmed, UAE
C. B. Allen, UK
N. Ananthkrishnan, India
Hikmat Asadov, Azerbaijan
Nicolas Avdelidis, Greece
Hyochoong Bang, Korea
Wen Bao, China
Ronald M. Barrett, USA
D. Bhattacharyya, New Zealand
I. D. Boyd, USA
Keh-Chin Chang, Taiwan
Christopher J. Damaren, Canada
Roger L. Davis, USA
Gang Ding, China
Dany Dionne, Canada
Boris Epstein, Israel
Jinghong Fan, China
Jiancheng Fang, China
Ikkoh Funaki, Japan
Mohamed Gad-el-Hak, USA
R. Ganguli, India
M. R. Hajj, USA
Tasawar Hayat, Pakistan
Kathleen C. Howell, USA

Hui Hu, USA
Qinglei Hu, China
Mikhail S. Ivanov, Russia
Ratneshwar Jha, USA
Jacob I. Kleiman, Canada
John B. Kosmatka, USA
Hamid M. Lankarani, USA
Yunhua Li, China
T. T. Lim, Singapore
Rick Lind, USA
W. W. Liou, USA
Richard W. Longman, USA
Enrico C. Lorenzini, Italy
T. J. Lu, UK
Siao Chung Luo, Singapore
Joseph Majdalani, USA
Pier Marzocca, USA
Josep Masdemont, Spain
Philippe Masson, USA
Franco A. Mastroddi, Italy
James J. McGuirk, UK
Giovanni Mengali, Italy
Achille Messac, USA
Koorosh Mirfakhraie, USA
Hong Nie, China
Christian O. Paschereit, Germany

Chris L. Pettit, USA
Mark Price, UK
N. Qin, UK
Markus Raffel, Germany
Srinivasan Raghunathan, UK
Mahmut Reyhanoglu, USA
Corin Segal, USA
Kenneth M. Sobel, USA
K. Sudhakar, India
Martin Tajmar, Germany
Paolo Tortora, Italy
Jean-Yves Trépanier, Canada
Srinivas R. Vadali, USA
Linda L. Vahala, USA
Mehdi Vahdati, UK
George Vukovich, Canada
Shaoping Wang, China
Paul Williams, The Netherlands
R. K. Yedavalli, USA
Youngbin Yoon, Korea
Huang Yuan, Germany
Gecheng Zha, USA
Youmin Zhang, Canada
Xiaolin Zhong, USA
Mei Zhuang, USA

Contents

Chemical Rocket Propulsion, David Greatrix, Ivett Leyva, Dario Pastrone, Valsalayam Sanal Kumar, and Michael Smart

Volume 2012, Article ID 715706, 2 pages

Recent Experimental Efforts on High-Pressure Supercritical Injection for Liquid Rockets and Their Implications, Bruce Chehroudi

Volume 2012, Article ID 121802, 31 pages

Solid Rocket Motor Design Using Hybrid Optimization, Kevin Albarado, Roy Hartfield, Wade Hurston, and Rhonald Jenkins

Volume 2012, Article ID 987402, 9 pages

Testing and Modeling Fuel Regression Rate in a Miniature Hybrid Burner, Luciano Fanton, Christian Paravan, and Luigi T. De Luca

Volume 2012, Article ID 673838, 15 pages

Feasibility Study and Demonstration of an Aluminum and Ice Solid Propellant, Timothee L. Pourpoint, Tyler D. Wood, Mark A. Pfeil, John Tsohas, and Steven F. Son

Volume 2012, Article ID 874076, 11 pages

Approaches to Low Fuel Regression Rate in Hybrid Rocket Engines, Dario Pastrone

Volume 2012, Article ID 649753, 12 pages

Burning Characteristics of Ammonium-Nitrate-Based Composite Propellants with a Hydroxyl-Terminated Polybutadiene/Polytetrahydrofuran Blend Binder, Makoto Kohga, Tomoki Naya, and Kayoko Okamoto

Volume 2012, Article ID 378483, 9 pages

Multisized Inert Particle Loading for Solid Rocket Axial Combustion Instability Suppression,

David R. Greatrix

Volume 2012, Article ID 173129, 13 pages

Boron Particle Ignition in Secondary Chamber of Ducted Rocket, J. X. Hu, Z. X. Xia, W. H. Zhang, Z. B. Fang, D. Q. Wang, and L. Y. Huang

Volume 2012, Article ID 160620, 9 pages

Editorial

Chemical Rocket Propulsion

**David Greatrix,¹ Ivett Leyva,² Dario Pastrone,³
Valsalayam Sanal Kumar,⁴ and Michael Smart⁵**

¹ Department of Aerospace Engineering, Ryerson University, Toronto, ON, Canada M5B 2K3

² Aerophysics Branch, Air Force Research Laboratory, Edwards AFB, CA 93524, USA

³ Dipartimento di Ingegneria Meccanica e Aerospaziale, Politecnico di Torino, 10129 Torino, Italy

⁴ Department of Aeronautical Engineering, Kumaraguru College of Technology, Coimbatore, Tamil Nadu 641006, India

⁵ School of Mechanical and Mining Engineering, The University of Queensland, Brisbane, QLD 4072, Australia

Correspondence should be addressed to David Greatrix, greatrix@ryerson.ca

Received 31 October 2012; Accepted 31 October 2012

Copyright © 2012 David Greatrix et al. This is an open access article distributed under the Creative Commons Attribution License, which permits unrestricted use, distribution, and reproduction in any medium, provided the original work is properly cited.

We are pleased to present to you this special issue on chemical rocket propulsion. It is hoped that experts and nonexperts alike will enjoy the discussion of a number of international research efforts that are taking place across the breadth of this diverse field, as conveyed by the authors of the papers appearing herein. The submitted papers certainly reveal the wide number of disciplines (chemistry, fluid dynamics, structures, etc.) that currently play important roles towards ultimately producing effective chemical rocket systems.

Recently, an important milestone has been reached in the history of chemical rocket propulsion, with the retirement of the Space Shuttle. The end of one era brings the dawn of a new era in space transportation, with the anticipation that, with time, new and better flight vehicles will come on the scene and flourish in their respective applications. Almost surely, those new vehicles will still be propelled in large part by chemical rocket systems, systems that have been updated and improved over those of the previous generation through the efforts of today's researchers and engineers.

Liquid-propellant rocket engines continue as the preeminent chemical rocket propulsion system, from millinewton spacecraft thrusters to meganewton first-stage engines for space launch vehicles. Although it is commonly perceived that liquid rocket engines are a mature technology, there are still many active research areas. For example, replacing highly toxic and expensive-to-handle propellants used in hypergolic systems with greener, less toxic propellants is a current challenge. As the thrust demands go up, achieving longer life for monopropellant systems especially remains an objective. For missions beyond Earth's orbit, proven reflight capability

for upper stage engines, and long-term storage for cryogenics, will become some of the engineering issues researchers will face. Liquid propulsion will remain a critical component in launch systems in the foreseeable future. In conjunction, the interest in making these systems more reliable, more durable, and less expensive to develop and acquire for a number of diverse flight mission applications will continue, and the engineering challenges associated with these objectives will have to be met.

Solid-propellant rocket motors maintain their importance in meeting the propulsion needs for a number of flight applications, big and small. While solid rockets have had, for a long time now, the reputation as being the cost-effective, ready-to-go option, research continues on improving all aspects of their performance, including their safety and friendliness to the surrounding environment. For example, ammonium dinitramide (ADN) appears to be making inroads as a potential greener replacement for ammonium perchlorate (AP) as an effective oxidizer for a number of solid propellants. There is some interest in going to higher chamber pressures to increase thrust-related performance; at higher pressures, one may encounter the need to more actively inhibit the appearance of combustion instability symptoms during a given motor's operation.

Manned suborbital flights powered by hybrid rocket engines have recently become reality, mainly due to reasons related to low cost and safety. Potential applications of hybrid rockets range from microgravity platforms to launchers and landing vehicles, but researchers must face some challenges, in part due to the peculiar combustion process of hybrid

propellants. Different concepts are being studied as a means to increase grain regression rate, from innovative fuels (e.g., paraffin-based solid fuels or solid methane) to innovative engine architectures (e.g., advanced vortex-hybrid or cascaded multistage impinging-jet designs). Other important issues, which must be dealt with, are mixture ratio shifting, combustion efficiency, and combustion instability.

Air-breathing rocket engines continue to be a practical propulsion system candidate for some smaller, longer-range, and high-speed missile applications. Challenges remain moving up in scale and scope, for military and civil applications such as single-stage-to-orbit flight vehicles. International computational and experimental research efforts continue in this regard.

Within the aerospace propulsion community, one commonly hears that every significant advance in aerospace transportation has been made possible by a significant advance in propulsion technology. One also hears that, as engineers and scientists, when we are fortunate enough to make significant progress in our time, we do so with the realization that we stand on the shoulders of giants. The giants, of course, are those who paved the way before us, with their insight, perseverance, and skill. This is certainly true of the field of chemical rocket propulsion. With this in mind, one can say, with some confidence, that despite, the inevitable challenges to come, the future of chemical rocket propulsion is bright.

*David Greatrix
Ivett Leyva
Dario Pastrone
Valsalayam Sanal Kumar
Michael Smart*

Review Article

Recent Experimental Efforts on High-Pressure Supercritical Injection for Liquid Rockets and Their Implications

Bruce Chehroudi

Advanced Technology Consultants, Laguna Niguel, CA 92677, USA

Correspondence should be addressed to Bruce Chehroudi, chehroudi@aol.com

Received 6 March 2012; Revised 3 June 2012; Accepted 11 June 2012

Academic Editor: David Greatrix

Copyright © 2012 Bruce Chehroudi. This is an open access article distributed under the Creative Commons Attribution License, which permits unrestricted use, distribution, and reproduction in any medium, provided the original work is properly cited.

Pressure and temperature of the liquid rocket thrust chambers into which propellants are injected have been in an ascending trajectory to gain higher specific impulse. It is quite possible then that the thermodynamic condition into which liquid propellants are injected reaches or surpasses the critical point of one or more of the injected fluids. For example, in cryogenic hydrogen/oxygen liquid rocket engines, such as Space Shuttle Main Engine (SSME) or Vulcain (Ariane 5), the injected liquid oxygen finds itself in a supercritical condition. Very little detailed information was available on the behavior of liquid jets under such a harsh environment nearly two decades ago. The author had the opportunity to be intimately involved in the evolutionary understanding of injection processes at the Air Force Research Laboratory (AFRL), spanning sub- to supercritical conditions during this period. The information included here attempts to present a coherent summary of experimental achievements pertinent to liquid rockets, focusing only on the injection of nonreacting cryogenic liquids into a high-pressure environment surpassing the critical point of at least one of the propellants. Moreover, some implications of the results acquired under such an environment are offered in the context of the liquid rocket combustion instability problem.

1. Introduction

In designs of chemical rocket engines, liquid fuel and oxidizer are often injected as round jets into a hot and elevated-pressure environment of the thrust chamber. The coaxial and impinging jets injectors are two of the well-established designs in liquid rocket engines (LREs). On the other hand, higher specific impulse is a major motivation for operating rocket thrust chambers at progressively higher pressures. Conditions therefore exist in which the injected liquid finds itself near or even above the thermodynamic critical point. Examples are Space Shuttle Main Engine and Vulcain (Ariane 5) with liquid H_2 /liquid O_2 .

In such cases, major changes occur in some important and key properties of a substance as it approaches the thermodynamic critical point. For example, under thermodynamic equilibrium, the distinction between the liquid and gas phases disappears at and above the critical point and hence it is referred to as a “fluid.” Also, large changes in density occur near the critical point. The constant-pressure specific heat becomes very large and surface tension vanishes

at and beyond the critical point. As the ambient pressure into which a liquid jet is injected increases, the importance of the solubility of ambient gases into the injected liquid phase increases and one should consider multicomponent phase equilibrium information. For mixtures, determination of the critical conditions, called the “critical mixing temperature or pressure”, is a complex process; see Bruno and Ely [1] and Lazar and Faeth [2]. For example, when a pure liquid hydrocarbon fuel drop is introduced into a nitrogen gas, a thin layer on its surface is a mixture of dissolved nitrogen and the fuel which spreads spatially in time; see Umemura [3].

Understanding the behavior of jets under supercritical conditions therefore is critical to design and modeling of the liquid rockets, in particular, cryogenic liquid rockets. For this reason, systematic research programs, both experimental and computations, have been initiated in the past 20 years to understand behaviors of jets under transcritical and supercritical conditions both with and without externally forced (acoustic) excitations. The reason the external excitation is considered stems from the combined experimental/theoretical work suggesting that interaction between

acoustic resonance modes of the chamber and the jets could play an important role in combustion instability. The basic premise here is that when an important dynamic feature, such as the injected jet's dark-core or breakup zone, of an injector design becomes sufficiently sensitive to thermofluid parameters of its environment, it is highly likely that this could strengthen the feedback link thought to be critical in the amplification process and hence push the system into an unstable operating regime.

The purpose of this paper is to present an overview of important experimental achievements, characterizing and understanding nonreacting steady liquid jets injected into supercritical conditions, and offer some implications of these results and potential linkages to production engines. It is not the intention of this work to provide a comprehensive review of the subject, rather to present important findings reported in recent decades.

The coverage of the injectors' experimental data in this paper is divided into three parts: single liquid jets, coaxial jets, and impinging jets. However, the treatment for the impinging jets is comparatively shorter due to limited data available extending to supercritical conditions. Two sections are considered for each part. One focuses on jets injected into an environment devoid of any externally imposed acoustic excitations and the other considers the impact of such excitations on jet characteristics. Most cases reviewed here pertain to cryogenic liquid jets with the environment, into which the jets are injected, existing at thermodynamic supercritical temperatures. This is similar to those experienced in cryogenic liquid rocket engines.

2. Single Jet without External Excitation

In this section, relevant experimental work conducted on a single steady round jet injected into an environment lacking any externally imposed acoustic disturbances is considered. The purpose here is to examine the behavior of such jets under high pressures, specifically supercritical conditions. In the selection of candidate cases, the test matrix is chosen to cover supercritical conditions. However, it is preferred that the matrix spans a broader range encompassing both sub- and supercritical conditions because it generally provides a more comprehensive picture of differences and similarities between the two conditions.

Historically, research on supercritical injection of relevance to liquid rockets started with a published work of Newman and Brzustowski [4]. They used a steady CO_2 jet injected into a chamber of pure N_2 and also into mixtures of $\text{CO}_2 + \text{N}_2$ at both sub- and supercritical pressures and temperatures. Obviously, if the chamber is at a supercritical pressure, the injected jet pressure is higher and must also be at a supercritical pressure. They showed that when the chamber pressure approached just above the critical pressure of the CO_2 , injection of CO_2 into mixtures of $\text{CO}_2 + \text{N}_2$ (varying initial CO_2 concentration to change mixture density) widened the visual appearance of the jet. This was explained to be due to changes in chamber-to-injectant density ratio. At a higher chamber supercritical pressure, injection of CO_2 into a pure nitrogen gas, but varying

temperature (from sub- to supercritical), caused shortening of both the jet visible length and width with chamber temperature.

Newman and Brzustowski [4] also investigated and explained effects of increased chamber temperature on jet appearance. They found that such effects were due to progressive reduction in ambient gas density, hence lowering surface tension to zero at critical temperature, and to increase in liquid CO_2 evaporation. In other experiments, CO_2 was injected into a mixture of $\text{CO}_2 + \text{N}_2$ with fixed but large initial CO_2 mass fraction in order to reduce jet evaporation. The chamber temperature was fixed at a supercritical value, but its pressure was varied from sub- to supercritical pressures. They hypothesized and conjectured that at supercritical chamber temperatures and pressures the jet may be considered as a variable-density single-phase turbulent submerged gas jet. Finally, assuming self-preserving flow, negligible gravity, zero latent heat of vaporization, ideal gas behavior, and thermal equilibrium between gas and drops, they develop a model for predicting the profile of the outer extent of a supercritical steady jet and its centerline mean axial velocity. Comparison of this model with experiment was very poor near the injector exit area where most important and complex processes take place. Hence, the proposed hypothesis was not backed by this effort and the matter remained unresolved.

After the aforementioned initial study, two organizations (DLR in Germany and AFRL in USA) dominated the field by pursuing systematic research programs to understand jet breakup and dynamics under high chamber pressures at, and specifically exceeding, the critical condition of the injectant. The majority of the experimental works presented here is thus coming from these two organizations plus other satellite universities they collaborated and/or supported. Each organization has constructed a unique facility from which most of the results for nonreacting jets were acquired and presented here. For more details on their facility designs readers are referred to their publications, many of which are listed in the references.

Researchers at DLR began working with the most simplest and fundamental of all cases, that is, the injection of a single nonreacting round jet into a quiescent environment. At AFRL, although initially droplet studies were planned and conducted, a transition to jets at high Reynolds numbers of practical interest was initiated by the author of this paper and his team members; for example, see Chehroudi et al. [5]. The injection of jets were studied at various chamber pressures ranging from subcritical to supercritical (mostly at supercritical temperatures), which included chamber pressures representative of those experienced in typical cryogenic liquid rocket engine (LRE). For safety reasons, and for the H_2/LOX liquid rockets, it was preferred to simulate liquid oxygen with liquid nitrogen. Early studies have shown that at a nonreacting condition the injection behaviors of these two fluids were similar. To avoid complications introduced by mixture effects, however, many of these studies involved injection of cryogenic liquid nitrogen (LN_2) into room temperature gaseous nitrogen (GN_2). Critical pressure and temperature of nitrogen are 3.39 MPa and 126.2 K,

respectively. Injections into other ambient gases were also investigated.

The objective of this section of the paper is to present key findings and discuss representative results. In some cases, key conclusions confirmed independently by both organizations (DLR and AFRL) are highlighted when appropriate and if they add to the reader's understanding. Before delving into details of the results, it worth indicating that Mayer et al. [6] were the first to take active steps towards a large-scale facility investigating both single and coaxial cryogenic jets under cold and fired conditions. They used LN₂ jets at 105 K injected into a GN₂ environment at 300 K, but at varying ambient pressures ranging from sub- to supercritical conditions. They reported drastic changes in the jet structure near and above the critical pressure. The jet behaved similar to the classical atomization of liquid fuels, with ligaments and drops, below the critical pressure. Mayer et al. [6] attributed this behavior to a continual decline of surface tension until it vanished at and beyond the critical point.

2.1. Visualization of the Jet Interface. Figure 1 presents results published in a work led by Chehroudi which shows representative images of cryogenic LN₂ jets injected into gaseous nitrogen at 300 K (supercritical in temperature); see Chehroudi et al. [5]. The initial temperature of the jets was measured in a separate experiment and under identical flow conditions with a very small thermocouple. Depending on the flow condition, the measured initial injection temperature varied from 99 K to 110 K, that is, injected at a subcritical value. Pressures in Figure 1 are reported as reduced pressures (P_r), defined to be the chamber pressure divided by the critical pressure of the injected nitrogen. In frames 1 to 4 (of Figure 1), where the chamber pressure is subcritical, the jets have a classical liquid spray appearance. Figure 2 shows magnified images of the three injection cases under sub-, near-, and super-critical chamber pressures. This software magnification is performed to more clearly show the shear layer structure near the injector exit area. As shown in Figure 1, and consistent with the classical liquid jet breakup regimes described by Reitz and Bracco [7], surface instabilities grow downstream from the injector, and very fine ligaments and drops are ejected from the jet (see also the left image in Figure 2). This behavior corresponds to the second wind-induced liquid jet break-up regime described by Reitz and Bracco [7].

Major structural and interfacial changes occur at about $P_r = 1.03$ as shown in frame 5 of Figure 1. Above this chamber pressure, drops are no longer detected, and as characterized by Chehroudi et al. [5], regular "finger-like" entities are observed at the interface. Rather than breaking up into droplets, the interface appears to dissolve at different distances from the dense and dark core. These structures are illustrated at $P_r = 1.22$ in the middle frame of Figure 2. Such a change in morphology of the mixing layer is evidently due to combined effects of the reduction in the surface tension, as the critical pressure is exceeded, and disappearance of the enthalpy of vaporization because of this transition to supercritical pressures.

As the chamber pressure is further increased, the length and thickness of the dense (and dark) core decrease, and the jet begins to appear similar to a turbulent gaseous jet injected into a gaseous environment. This is illustrated in frames 7 and higher in Figure 1. Any further droplet production, and consequently any additional classical liquid atomization, is completely suppressed. These observations were confirmed by Mayer et al. [6, 8], Chehroudi et al. [5], and Roy and Segal [9]. As mentioned earlier, similar results were also found when injecting liquid oxygen instead of the liquid nitrogen.

It is important to indicate that because of the very large density variations between the jet core and the chamber, Chehroudi et al. [5] investigated whether the evolution of the jet within the region of their measurement was affected by the buoyancy forces. Therefore, they calculated the Froude number values under each test condition. As an example, Chehroudi et al. [5, 10] showed that the Froude number ranged from 42,000 to 110,000. To make sense of these values, they looked at the Chen and Rodi [11] results. Chen and Rodi [11] suggested that the flow is momentum dominated when a defined length scale x_b is less than 0.53, while Papanicolaou and List [12] suggested $x_b < 1$. The length scale is given by $x_b = Fr^{-1/2}(\rho/\rho_\infty)^{-1/4}(x/d)$, where x is the axial distance, d is the initial jet diameter, and ρ and ρ_∞ are the jet and ambient densities, respectively. The Froude number is defined as $Fr \equiv \rho U^2/gd|\rho_\infty - \rho|$ where U is the velocity difference and g is the gravitational acceleration. Considering a more conservative estimate by Chen and Rodi [11], the jet used by Chehroudi et al. [5, 10] is momentum dominated for distances less than 30 to 40 mm from the injector exit plane. Pictures presented in Figures 1 and 2 cover up to about 5.5 mm (axial distance/diameter ratio of 21.6) from the injector, and hence buoyancy effects can be ignored in favor of inertial forces.

2.2. Length Scale Investigation. Injection of a single LN₂ jet into gaseous N₂ (at 298 K) has been investigated by Branam and Mayer [13] at ambient pressures of 4 MPa and 6 MPa, corresponding to reduced pressures of 1.17 and 1.76, respectively. The initial injection temperature of the nitrogen was near the critical point. They provided a measure of the length scales by analyzing shadowgraph images and called it as the "visible length scale." More details on their image analysis can be found in Branam and Mayer [13].

Figure 3 shows a typical result of the geometrically averaged length scale (average of radial and axial length scales) measured at the x/D of 10 as a function of the radial position. Results from the $k-\epsilon$ computational method are also shown. This suggests that the measured visible length scale is comparable in magnitude to the Taylor length scale determined by the computational method.

The ratio of the axial to the radial length scales indicates whether the visible structures are spherical or more ellipsoidal in shape. Both length scales are shown in Figure 4 for an injection temperature of 123 K, that is, injection of N₂ at a high density. In the near-injector region, the axial length scales are much larger than the radial ones. Further downstream, however, the visible structures become more

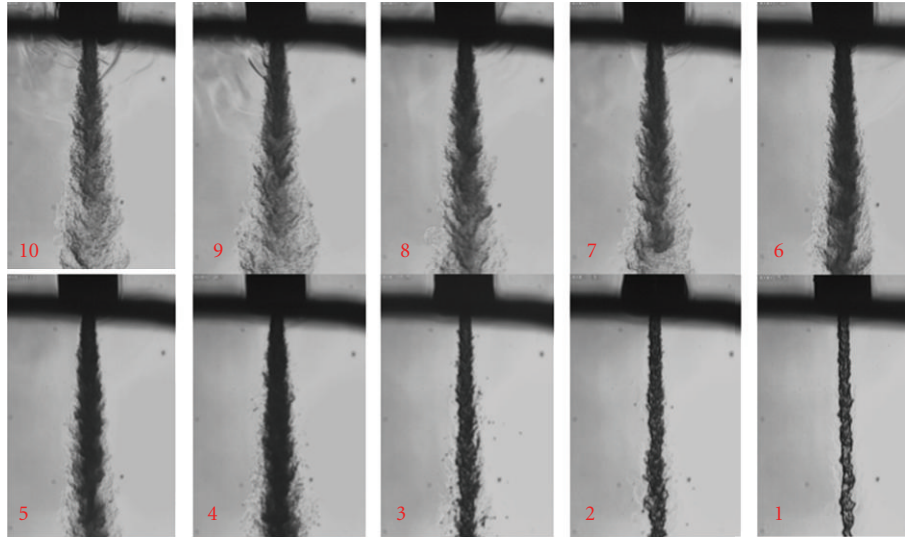


FIGURE 1: Back-illuminated images of a single nitrogen jet injected into nitrogen at a fixed supercritical temperature of 300 K but varying sub- to supercritical pressures (For N_2 : $P_{critical} = 3.39$ MPa; $T_c = 126.2$ K). From lower right to upper left: $P_{ch}/P_{critical}$ (frame no.) = 0.23 (1), 0.43 (2), 0.62 (3), 0.83 (4), 1.03 (5), 1.22 (6), 1.62 (7), 2.44 (8), 2.74 (9). Reynolds' number (Re) was from 25,000 to 75,000. Injection' velocity: 10–15 m/s. Froude' number: 40,000 to 110,000. Injectant temperature: 99 to 120 K. Chehroudi et al. [5].

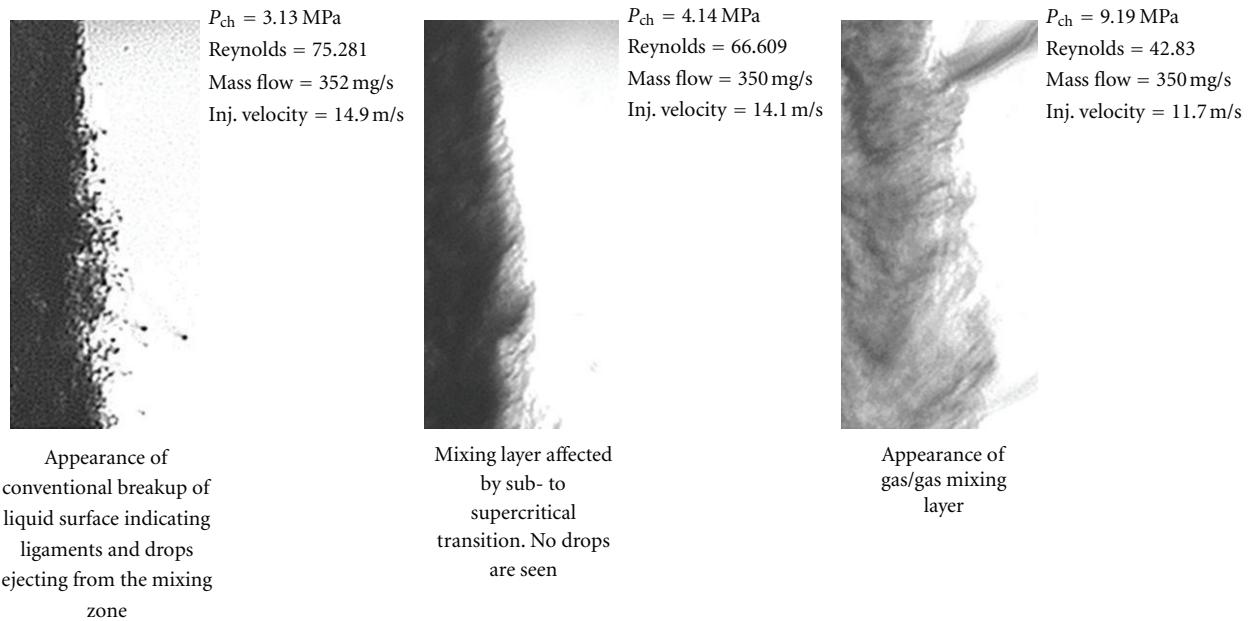


FIGURE 2: Software magnified images of the jets in Figure 1 at their outer boundaries showing transition to the gas-jet-like appearance starting at just below the critical pressure of the injectant. Images are at fixed supercritical chamber temperature of 300 K. Chehroudi et al. [5].

circular in shape. At a higher injection temperature (132 K), the asymmetry between the radial and axial length scales is not as pronounced as that seen under the lower temperature condition (123 K).

2.3. *Jet Spreading Angle or Growth Rate.* Measurements and estimations of the growth rate of a jet have been a subject of intense research for years because it provides a primary measure of mixing and development of the jet itself. Chehroudi's group was the first to extract quantitative

measurements of this physical parameter using the images taken from a cryogenic N_2 jet injected into GN_2 under both subcritical and supercritical pressures; see Chehroudi et al. [5]. These measurements led to important conclusions regarding the character of the growth rate and the behavior of the jet near the injector and under such conditions, specifically at supercritical chamber pressures.

The spreading angle or growth rate was measured from a field of view within 5.5 mm of the injector exit plane (distance-to-diameter ratio of up to 21.6) and was inertially

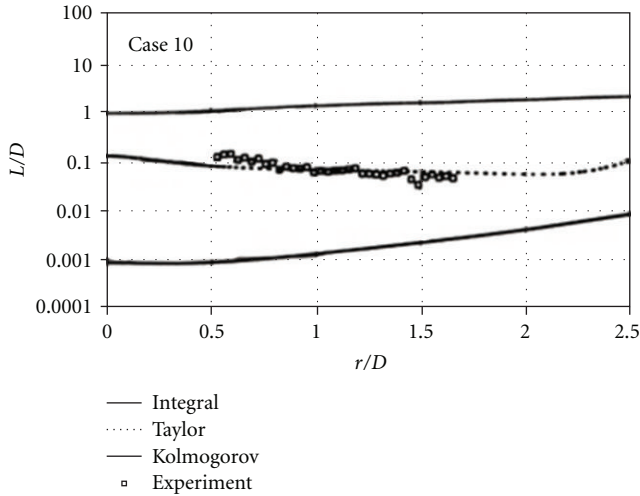


FIGURE 3: Comparison between calculated and experimental length scales for a single jet of LN₂ injected into GN₂ at $x/d = 10$, chamber pressure of 6 MPa, 1.9 m/s, injected temperature of $T = 132$ K. Branam and Mayer [13].

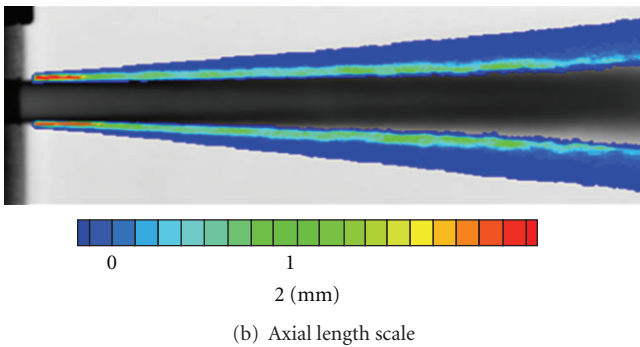
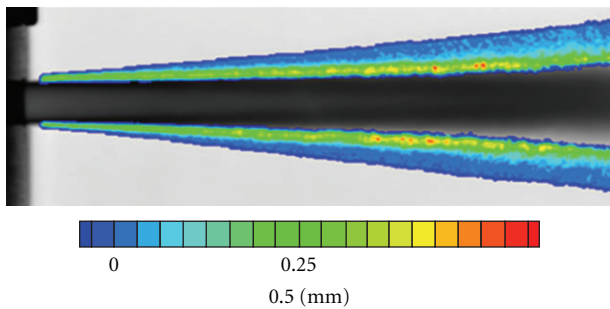


FIGURE 4: Experimental length scales for LN₂ into GN₂, chamber pressure of 4 MPa, LN₂ injected temperature of 123 K. Branam and Mayer [13].

dominated as discussed earlier. Chehroudi et al. [5] indicated that their data were also taken from the corresponding and appropriate initial region of the jet to ensure existence of a classical mixing layer. The initial jet spreading angle, or its growth rate, was then measured for all acquired images, and results along with those of others are presented in Figure 5. Of importance in this figure is the justification for the selection of the data sets and the nature of their

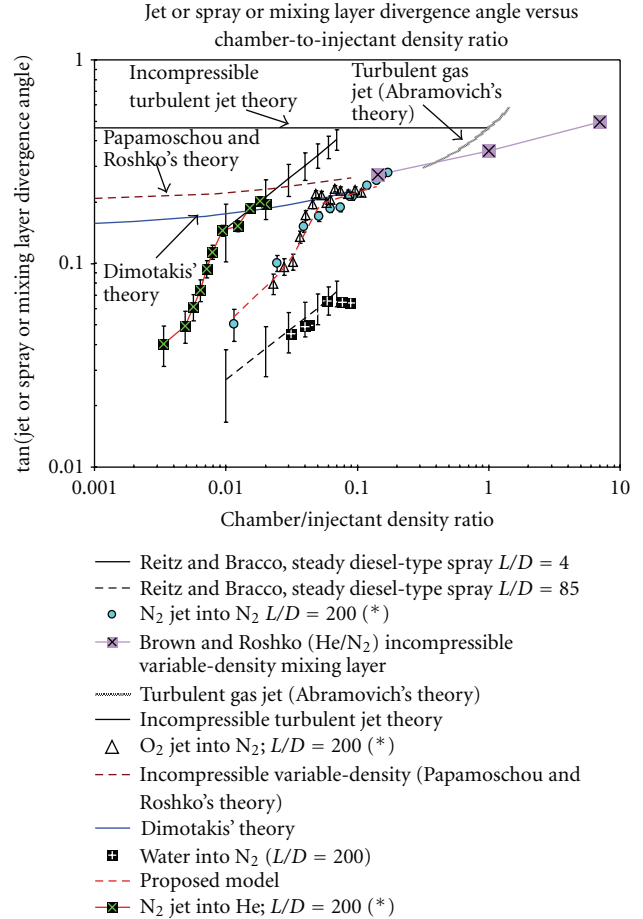


FIGURE 5: Spreading or growth rate of single jets as a tangent of the visual spreading angle versus the chamber-to-injectant density ratio. Data taken by Chehroudi are indicated by an asterisk (*) in the legend. Chehroudi et al. [5].

measurements by other researchers. They are elaborated at sufficient detail in earlier papers. In order to gain a deeper appreciation of these selections, the reader is referred to Chehroudi et al. [10]. Therefore, they are only mentioned here in brief.

Because the jets investigated by Chehroudi et al. [5] exhibited both liquid-spray-like and gas-jet-like (two-phase and single-phase, resp.) appearances, depending on pressure (see Figure 1), appropriate comparisons with both liquid sprays (injected into a gas) and gas jets (injected into a gas) were justified and hence these results are presented in Figure 5. The simplest is the prediction of the linear growth or constant spreading angle for the turbulent incompressible submerged jet using the mixing length concept. Following Abramovich [14], a semiempirical equation was used which attempts to incorporate the effects of density variations by an introduction of a characteristic velocity (see Chehroudi et al. [10] for more details).

Brown and Roshko [15] measured spreading angles for a subsonic, two-dimensional, incompressible, turbulent mixing layer in which helium and nitrogen were used. Brown [16] (for a temporally growing mixing layer) and Papamoschou and Roshko [17] proposed a theoretical equation for incompressible variable-density gaseous mixing layers. Finally, Dimotakis [18] used the observation that, in general, the entrainment into the mixing layer from each stream was not the same and, in a system moving with a convection velocity, offered a geometrical argument to derive an equation for two-dimensional incompressible variable-density mixing layers. Chehroudi et al. [5] included predictions from these models as shown in Figure 5. Results by Richards and Pitts [19] for variable-density jets are also included.

Because both liquid-spray-like and gas-jet-like visual behaviors were observed, the growth rate for the liquid sprays produced from single-hole nozzles, typical of the ones used in diesel engines, was also incorporated in this figure. Figure 5 covers a density ratio of four orders of magnitude and is regarded as a unique and new plot in its own right. To some extent, and for comparable cases, disagreements between some results in this figure can be attributed to differences in the definition of the mixing layer thicknesses and the adopted measurement methods. For detailed discussion of this figure, see Chehroudi et al. [5, 10].

The important point which was stressed by Chehroudi et al. [10] is that for a range of density ratios in which images exhibit gas-jet-like appearance, the experimental data agrees well with the proposed theoretical equation by Dimotakis [18] and closely follows the trend of the Brown/Papamoschou and Roshko equation as shown in Figure 5. This can be taken as an important quantitative evidence that at supercritical pressures, the injected jets visually behave like a gas. Chehroudi's work appears to be the first time such a rigorous and quantitative evidence had been developed. The fractal dimension results discussed later provide additional evidence in support of this behavior.

Chehroudi et al. [20] also used the Raman scattering studies to measure density distributions. Initially, the growth rate measurements by them, using results acquired during the Raman scattering work, did not provide the same jet thickness values as those determined by the shadowgraphy approach. Apparently, as discussed by Brown and Roshko [15], different thickness definitions exist, and one can explore their relationship. Similar attempts in the context of supercritical jets showed that within the distances investigated, twice the full-width half-maximum (FWHM) of the Raman intensity radial profiles was equivalent to the thickness values measured through shadowgraphy. Realization of this relationship was very critical to consolidate the results from two different methodologies (Raman versus shadowgraphy). Figure 6 shows the growth rate measured using the Raman data in contrast to those determined through shadowgraph images.

These results were subsequently confirmed and extended by Oswald and Micci [21] through a similar measurement technique. For example, they showed that when twice the FWHM of the Raman radial intensity profiles is used for

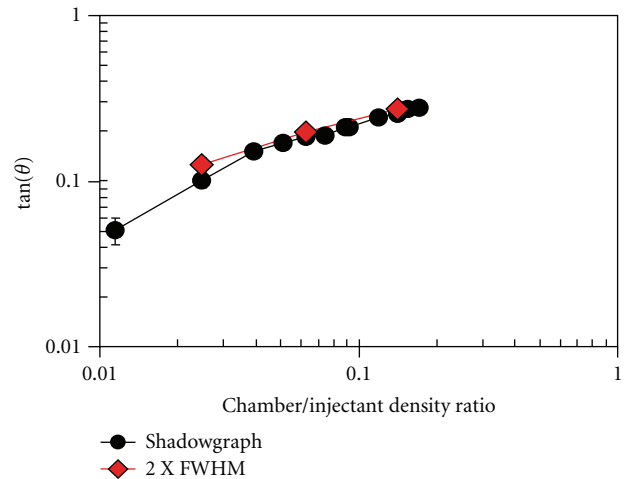


FIGURE 6: Comparison of the tangent of the spreading angle for a single jet of LN₂ injected into GN₂ measured using shadowgraph and Raman's techniques at twice the FWHM values. Chehroudi et al. [20].

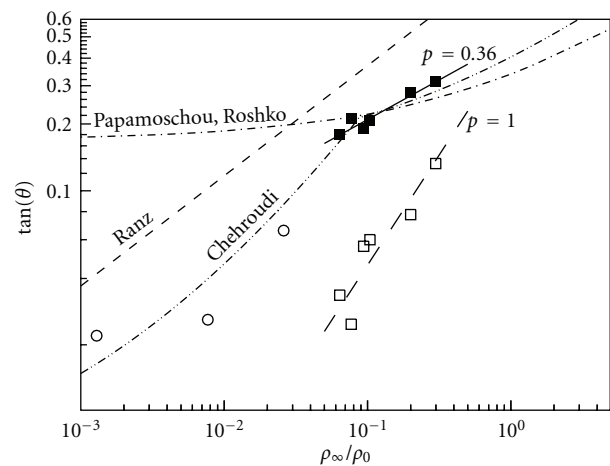


FIGURE 7: Comparison of the tangent of the spreading angle by Raman's techniques using twice the FWHM values (DLR data). Solid squares are for data from x/D of 15 to 32 whereas hollow squares are from x/D of 0.5 to 14. Chehroudi's model is also shown as dash-dot-dot curve. Single jet LN₂ into GN₂ with injector $L/D = 11.6$. Data from Oswald and Micci [21]. Open circles are data points from Reitz and Bracco [7].

x/D values within 15 and 32, a good agreement exists between their results and those by Chehroudi's group (see the case designated as " $p = 0.36$ " in Figure 7, where " p " is the exponent of the curve fitted through the data). However, the twice FWHM criterion did not fully agree with shadowgraphs for $x/D < 15$ in the study conducted by Oswald and Micci [21] (see the case identified as " $p = 1.0$ " in Figure 7).

Note that Oswald and Micci [21] measured a larger range of axial distances and found that the criterion was not universal at extended ranges. There are several reasons why different trends might be observed at different distances.

It has to do with the fact that shadowgraphy and Raman scattering approaches measure different physical properties. The Raman signal is taken to be proportional to density whereas shadowgraphy is sensitive to the gradients of the density distribution. Thus a unique relationship between the results measured by the two methods may only be valid for a limited region and/or perhaps specific configurations. Recall that the data discussed above were obtained from injectors with different L/D ratios. Another potential cause, and hence discrepancies, is errors in attempting to perform Raman's measurements close to the injector inlet where density variations and thus index of refraction variations can be very large.

2.4. Fractal Dimension of the Interface. Fractals are intimately connected to the concept of self-similarity; see Mandelbrot [22]. The fractal dimension of any curve is between 1 and 2. The more wrinkled and space-filling a curve is, the larger the values of its fractal dimension. Natural curves, such as the outline of a cauliflower, are self-similar only to that within a narrow range of scales. The objective of the analysis here was to measure the fractal dimension of the interface of jets injected into the chamber in order to see if any pattern was uncovered.

The fractal dimension of jets at various pressures ranging from subcritical to supercritical was calculated and compared to results by other researchers. Reference results were taken from Sreenivasan and Meneveau [23] who measured the fractal dimensions of a variety of turbulent gaseous jets, mixing layers, and boundary layers. These results indicated a fractal dimension between 1.33 and 1.38. In addition, the fractal dimensions of a turbulent water jet (Dimotakis et al. [18]) and of a liquid jet in the second wind-induced atomization regime (Taylor and Hoyt [24]) were computed from high-resolution scanned images.

The fractal dimensions from the above reference cases are shown as horizontal lines in Figure 8. Overlaid on top of these lines are discrete points indicating the fractal dimension of LN_2 jets injected into GN_2 at various chamber pressures. One sees that at supercritical chamber pressures, the fractal dimension approaches a value similar to gaseous turbulent jets and mixing layers. As the chamber pressure is decreased, the fractal dimension also decreases. Below a reduced pressure of 0.8, the fractal dimension rapidly declines to a value approximately equal to that of liquid sprays in the second wind-induced liquid jet break-up regime.

A detailed discussion of the above results is also found in Chehroudi et al. [25, 26]. The key conclusion reached by Chehroudi's group is that the results from fractal analysis complement and extend the imaging data they acquired for the initial jet growth rate. At supercritical pressures, jets have a fractal dimension similar to turbulent gas jets, and at subcritical pressures, cryogenic jets have a fractal dimension similar to liquid sprays. The transition occurs at about the same chamber pressure as that when the transition in visual appearance and growth rate data discussed in Figure 5 takes place. Such distinctly different behaviors for jets under sub- and supercritical conditions were first demonstrated by

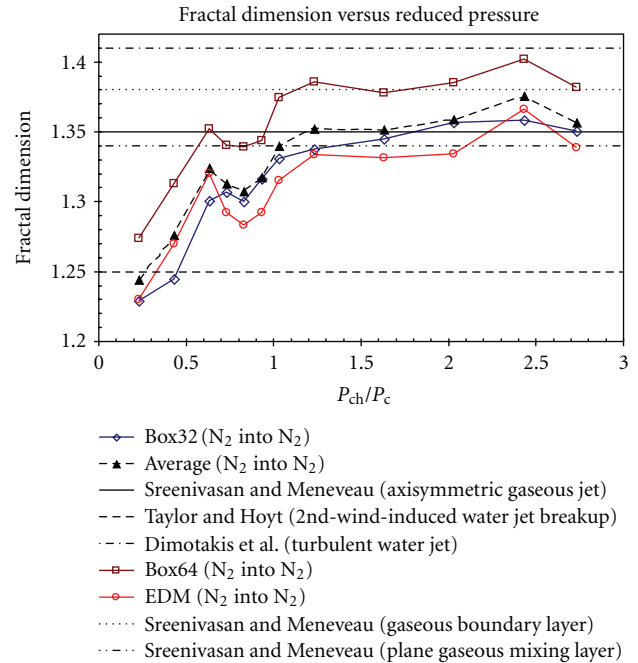


FIGURE 8: Fractal dimensions of the boundaries of various single jets as a function of reduced chamber pressure (chamber pressure divided by the critical pressure of the jet material). Discrete points are data from Chehroudi et al. [25, 26]. Box 32, Box 64, and EDM are different methods of calculating the fractal dimension, giving an impression of the extent of variability; for details, see Chehroudi et al. [25, 26].

Chehroudi's group in a quantitative manner using fractal analysis.

2.5. Measurement of the Dark-Core Length. Before presenting their results under supercritical conditions, Chehroudi et al. [25, 26] discussed some measurements from (gaseous and liquid) jets at subcritical conditions to set the stage and provide a contrast to their data. It is therefore useful to summarize what they recalled in their work.

According to Abramovich [14], the length of the "potential core" in isothermal uniform-density axisymmetric and two-dimensional jets is estimated to be about 6 to 10 injector diameters; whereas for nonisothermal cold jets injected into hot environments, it can reach up to about 25 injector diameters depending on jet temperature.

Also, according to Chehroudi et al. [27] the "intact core" length of the liquid sprays similar to the ones used in diesel engines is given by the equation $Cd_j(\rho_l/\rho_g)^{1/2}$ where ρ_l and ρ_g are liquid injectant and chamber gas densities, respectively, d_j is an effective jet exit diameter, and C is a constant between 3.3 and 11. This reflects an intact core length between 33 and 110 injector diameters for the chamber-to-injectant density ratio of 0.01 and between 16.5 and 55 diameters for the chamber-to-injectant density ratio of 0.04. These results are presented in Figures 9(a) and 9(b) for better comparison with what is measured for LN_2 injection into both sub- and supercritical GN_2 environment.

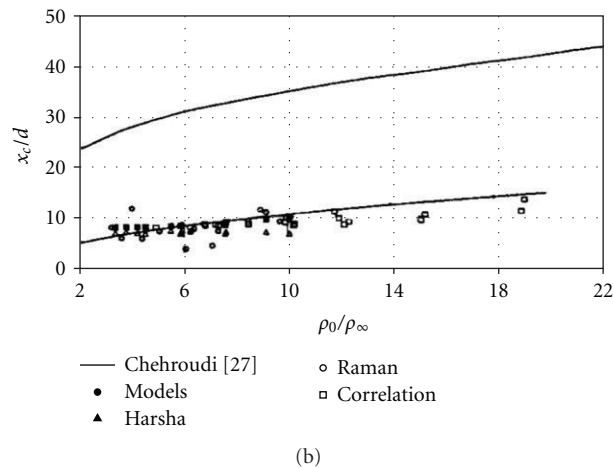
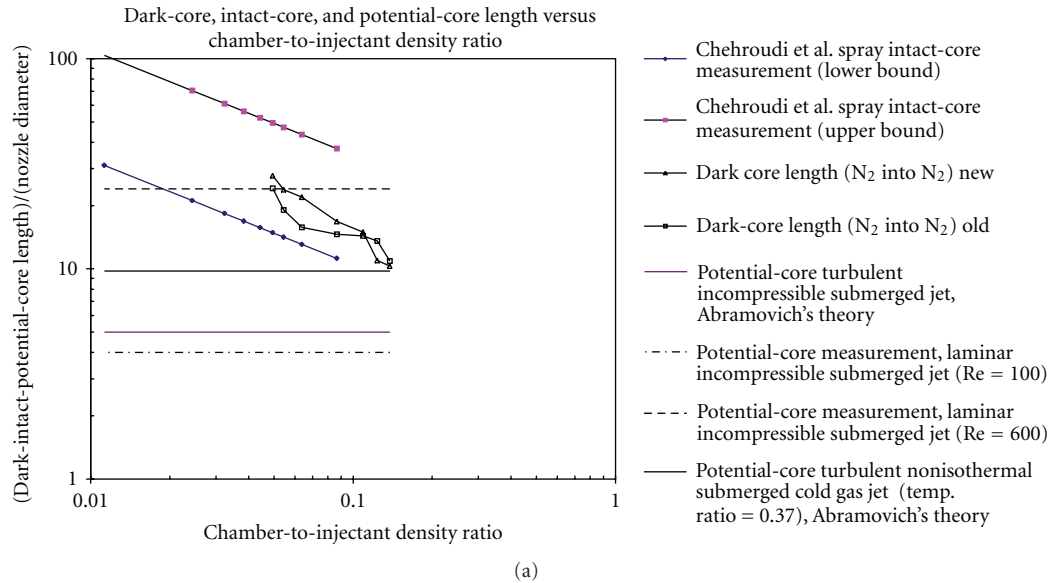


FIGURE 9: Ratio of either the dark-core, intact-core, or potential-core length, depending on the case, divided by the density ratio for single jets. (a): Chehroudi et al. [10], determined by analysis of shadowgraphs, for an injector $L/D = 200$. (b): Branam and Mayer [13], determined via Raman data, injector $L/D = 40$. Models: determined by computer simulation. Correlation: a correlation using a set of Raman's data by Branam and Mayer [13].

Considering that the classical two-stream mixing layer should start from the injector exit and extends to approximately the end of the potential core (or intact core) of the jet, Chehroudi et al. [5, 10] assumed that the jet “dark-core” region seen in their images played a similar role as the intact core or potential core. Figure 9(a) shows the dark-, intact-, or potential-core lengths normalized by the injector hole diameter plotted versus density ratio. By referring to Figure 9(a), Chehroudi et al. [5, 10] indicated that the growth rate data taken by them, which is presented earlier in Figure 1, was indeed from the corresponding and appropriate initial region to ensure existence of a classical mixing layer. They emphasized that it is only then when a valid comparison can be made (as they did) between their results and the two-stream mixing layers available in the

literature. Finally, they found that the core length fluctuation levels at supercritical condition were several times lower than those observed at subcritical chamber pressures.

Complementary results by the Branam and Mayer [13] are also shown in Figure 9(b). These results were determined through a log-log plot of the centerline intensity measured by the Raman scattering to distinguish different flow regions. Note that the horizontal axis for Figures 9(a) and 9(b) are inverse of each other. The Branam and Mayer [13] data are at or below the lower bound of the Chehroudi et al. [27] model (i.e., solid curves in Figure 9(b)) which was proposed based on the liquid spray data in various atomization regimes. For chamber-to-injectant density ratios of less than 0.1 in Figure 9(a) (or injectant-to-chamber ratio of greater than 10 in Figure 9(b)), it appears that the Chehroudi et al. [25, 26]

experimental data shown in Figure 9(a) is larger by about a factor of 1.5 to 2 compared to the “correlation” given by Branam and Mayer [13] in Figure 9(b).

Considering that the raw data used by the two groups are from two different injectors and measurement methodologies, the agreement is considered adequate. However, further investigations are warranted.

2.6. Density and Temperature Fields. The main purpose of the Raman scattering measurements was to provide quantitative information and to enable mapping of the jet density field. Temperatures, for example, were calculated assuming application of a suitable equation of state. Radial density profiles were reported by Oswald and Schik [28] in a normalized fashion. In this section, the centerline density and/or temperature profiles as functions of the axial distance from the injector exit plane and their self-similarity assessment are discussed.

The test conditions were chosen in order to assess the influence of the thermodynamic state of the injected cryogenic N_2 on the jet disintegration process. For example, above the critical pressure, the specific heat is finite but exhibits a maximum at a particular temperature. At this same point, the thermal diffusivity exhibits a minimum value. Three test cases were therefore investigated as shown in Figure 10(a). In test case A, the initial injection temperature is both above the critical temperature and above the temperature where the specific heat assumes a maximum value, whereas for test cases B and C the initial injection temperatures are both below the critical value and the temperature where the specific heat is at a maximum value.

Figures 10(b) and 10(c) show normalized centerline axial profiles of the density and temperature acquired by Oswald and Schik [28] at a chamber pressure of 4 MPa (near the critical pressure of nitrogen). Note that the density decay behavior becomes slower as the initial injection temperature is decreased. The temperature profile, however, stays flat for up to a normalized distance (x/D) of about 25 to 30. They indicated that the development of the centerline temperature reflects the thermophysical properties of the nitrogen, being specific to the region where the specific heat reaches a maximum. For initial injection temperatures below the temperature where the specific heat reaches a maximum value, as the jet heats up, the fluid has to pass through a state with a maximum specific heat. The fluid temperature can then reach a value where a large amount of heat can be stored without any noticeable increase in temperature. It appears that the maximum specific heat line in a supercritical fluid results in a behavior similar to a liquid at its boiling point. That is, heat transfer to the nitrogen does not increase its temperature but simply expands the fluid (i.e., increases its specific volume). It is also for this reason that the dashed curves in Figure 10(a) are referred to as “pseudo boiling lines.” Note that the density of the fluid varies strongly with temperature in this zone. At 6 MPa ($P_r = 1.76$, data not shown), the maximum of the specific heat is much less pronounced and the effects of the pseudo-boiling line is not as distinct as those seen under chamber pressure of 4 MPa. As shown by Oswald and Schik [28], however, far

downstream, it was observed that the temperature of the disintegrating and mixing supercritical fluid jet approached a value representative of a fully mixed jet but at a slower pace than that for the jet density.

The self-similarity of the density field has also been investigated by Chehroudi et al. [20] and the results are presented in Figure 11. According to Wygnanski and Fiedler [29], a fully self-preserved velocity field of a turbulent air jet should be observed at an x/D of greater than 40 when the Reynolds number is near 100,000. So et al. [30] reported self-preservation for x/D values larger than about 20 in a binary gas jet at Reynolds’ number (Re) of about 4300. Although it appears that some inconsistencies exist for this criterion, one can see that for the near-critical and supercritical pressures, the density radial profiles approach the similarity model curve shown in Figure 11. The disagreement increases at subcritical pressures where the model is least applicable. It is worth indicating that results from a modeling and computational simulation by Zong et al. [31] also agrees well with Chehroudi’s Raman scattering measurements.

Chehroudi et al. [20] using their Raman scattering data determined the FWHM of the radial density profiles at each axial distance from the injector, and the results, along with data by other investigators, are shown in Figure 12. More information on their experimental conditions is given in Table 1. Note that except for Chehroudi et al. [5, 25] and Oswald et al. [32], all others performed injection of gaseous fluids into an ambient gas at subcritical pressures (based on the injectant critical pressure). Also, the FWHM was determined using the mass fraction profiles in both So et al. [30] and Richards and Pitts [19]. However, reported FWHM values by So et al. [30] using both density and mass fraction profiles were comparable. Chehroudi et al. [20] data in Figure 12 shows an increasingly larger spreading rate as chamber pressure is raised. The data at the supercritical condition ($P_r = 2.03$) approaches that of Richards and Pitts [19] acquired at a density ratio of 1.56 even though this ratio is substantially smaller than Chehroudi et al. [20] data. Results at larger distances were not available for their jet to enable a more comprehensive comparison between the cases.

Richards and Pitts [19] concluded that if care is exercised to ensure that the flow is free of buoyancy and coflow effects, the spreading rate in variable-density jets was independent of the initial density ratio, velocity profile, and turbulence level and conformed with the constant-density results of others. In addition, they proposed a slope in the range between 0.212 and 0.220 for the linear jet growth rate equation; see Figure 12. However, a linear least-square fit to Chehroudi et al. [20] data at $P_r = 2.03$ gives a slope of 0.102, almost half of that by Richards and Pitts [19]. One possible explanation for this difference is that Chehroudi’s data covers a range much closer to the injector exit plane than that by Richards and Pitts [19], leading to a lowered growth rate value. A tendency towards higher growth rates can be seen if only the farthest two data points are considered in Chehroudi’s data. However, a solid conclusion cannot be drawn based on these two points. It is also possible that at some high enough injectant-to-chamber density ratio, the spread rate universality indicated by Richards and Pitts breaks down and

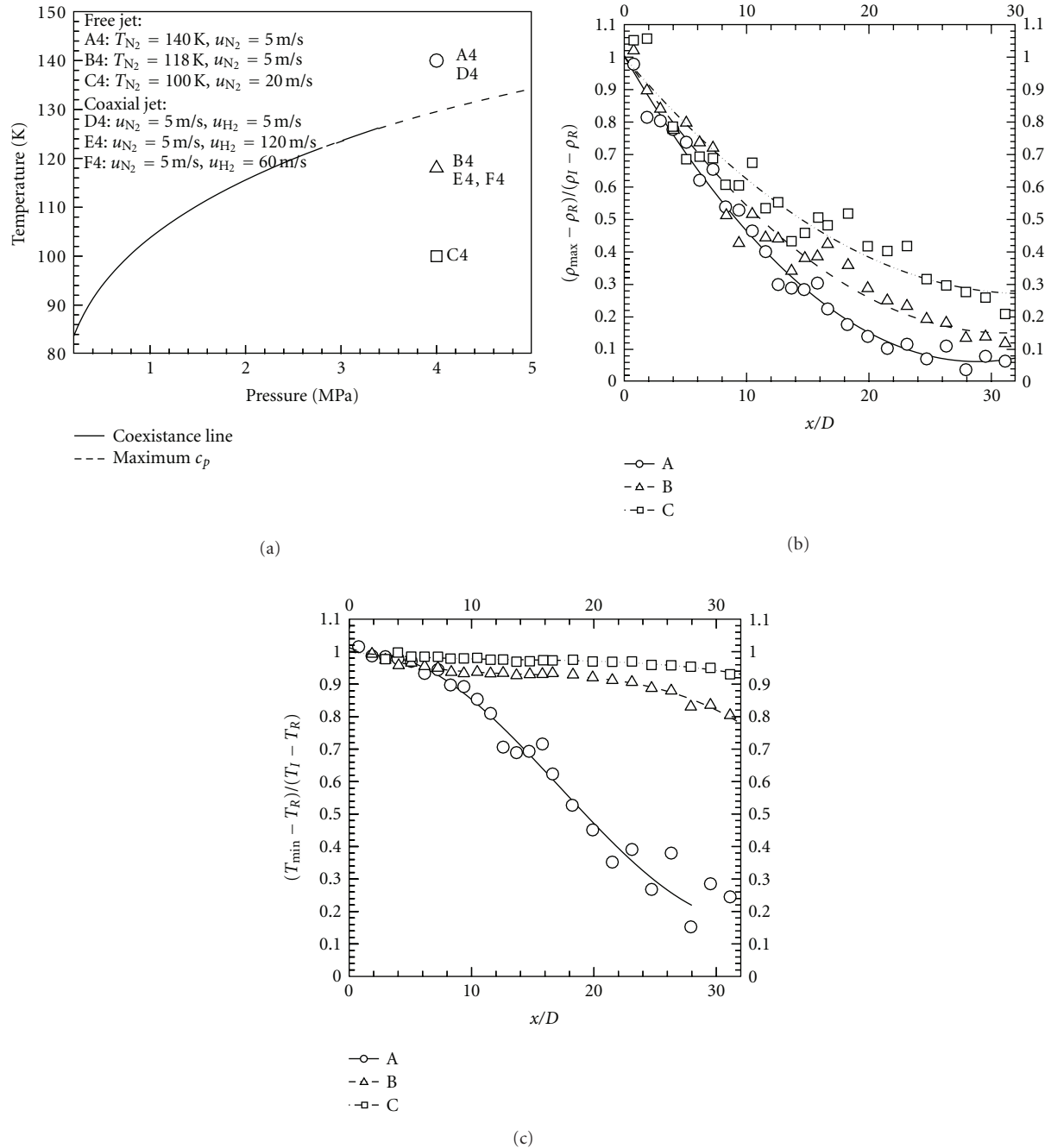


FIGURE 10: Normalized centerline density (b) and temperature (c) axial profiles of LN₂ injected into GN₂ at three different injection temperatures and a chamber pressure of 4 MPa (i.e., near critical pressure). The plot (a) shows the thermodynamic conditions under which test cases A, B, and C are conducted. The dashed line is the pseudoboiling line. Note, A4, B4, and C4 symbols represent A, B, and C cases, respectively. Oswald and Schik [28].

one observes a somewhat retarded growth rate for variable-density turbulent jets. Some evidence in support of this position was given by Chehroudi et al. [20].

2.7. Phenomenological Model of the Jet Growth Rate. Using the experimental data collected on the growth of a cryogenic jet, a phenomenological model for the growth rate was

proposed by Chehroudi et al. [5, 10] for the first time in the literature. Complete details on the development of this equation are to be found in these references. However, the physical reasoning motivating the proposed model equation is outlined below.

It was noticed by Chehroudi that previous expressions for the growth rate of liquid sprays and of turbulent jets have

TABLE 1: Some information extracted from works by other investigators reported here. T_{inj} and T_{ch} are injection and chamber temperatures. P_{ch} is chamber pressure. L/D is the injector hole-to-diameter ratio, x/D is the normalized distance from injector exit within which measurements were made. Chehroudi et al. [20].

	(Fluid inj./cham.)	T_{inj} K	P_{ch} MPa	T_{ch} K	Reduced pressure P_r	Inj./chamb. density ratio	Diameter			Raynolds' number Re	Profile used to measure FWHM
							D mm	L/D	x/D		
Oswald et al.	N ₂ /N ₂	118	4	298	1.17	3.34	1.9	11.5	8.42	1.2E + 05	Density
Oswald et al.	N ₂ /N ₂	140	4	298	1.17	12.5	1.9	11.5	1.05	1.3E + 05	Density
Chehroudi et al.	N ₂ /N ₂	95	6.9	295	2.03	7.1	0.505	100	4.8 to 24.4	3.5E + 04	Density
Chehroudi et al.	N ₂ /N ₂	110	1.5	295	0.43	40.6	0.505	100	4.8 to 24.5	1.2E + 04	Density
So et al.	(He + Air)/Air	275	0.1	275	0.08	0.64	9.5		5.1	5.0E + 03	Concentration and density
So et al.	(He + Air)/Air	275	0.1	275	0.08	0.64	9.5		6.4	5.0E + 03	Concentration and density
Richards and Pitts	He into Air	275	0.1	275	0.44	0.138	6.35	~50	20–80	4.0E + 03	Mass fraction
Richards and Pitts	C ₃ H ₈ into Air	275	0.1	275	0.02	1.56	6.35	~50	40–120	2.5E + 04	Mass fraction

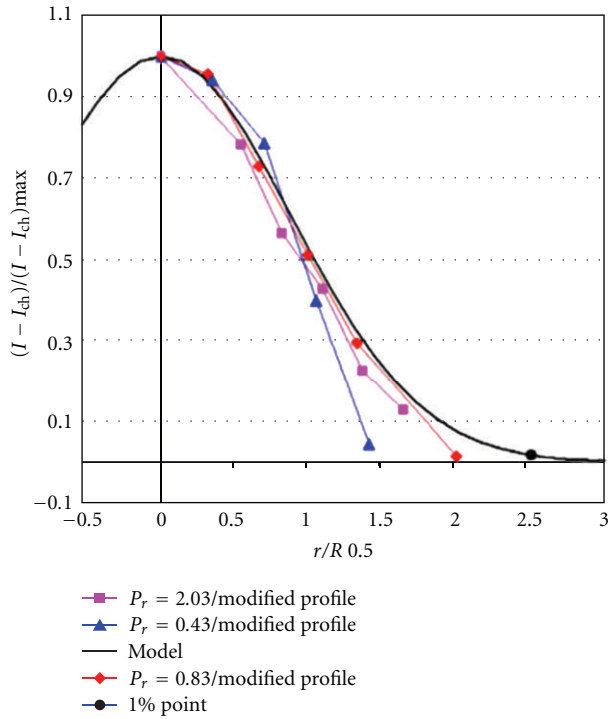


FIGURE 11: Plots of normalized intensity versus normalized radius for a single LN₂ jet injected into GN₂, at $x/D = 12.2$, at subcritical, near-critical, and supercritical pressures (Chehroudi et al. [20]). The solid curve is the self-similar model that represents data from a gaseous jet injected into a gaseous environment. I and I_{ch} symbols are measured intensities in the jet and in the chamber far away from the jet, respectively. Chehroudi et al. [20].

a remarkably similar form. For example, Reitz and Bracco [7] proposed that the growth rate of isothermal steady liquid sprays could be expressed as

$$\theta \approx 0.27 \left[0 + \left(\frac{\rho_g}{\rho_l} \right)^{0.5} \right]. \quad (1)$$

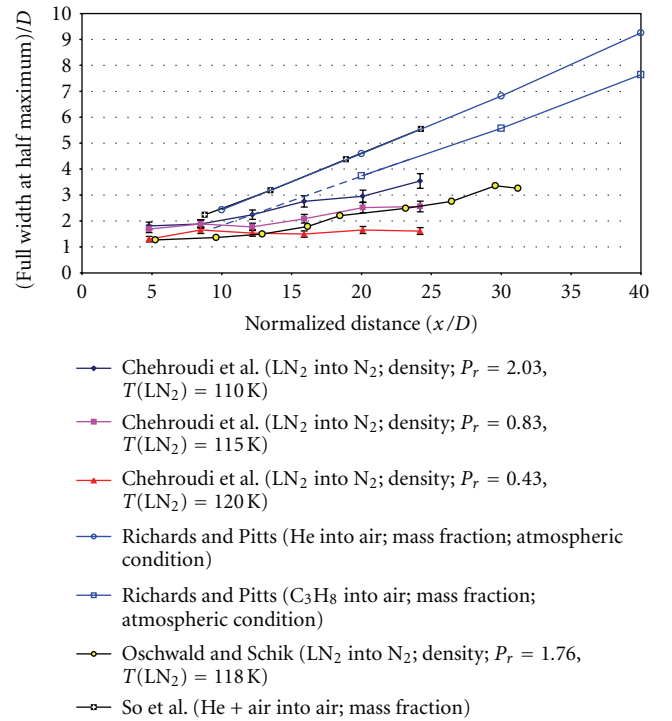


FIGURE 12: Normalized FWHM of the density-surplus radial profiles of single jets plotted as a function of the normalized axial distance from the injector exit plane. From Chehroudi et al. [20].

The first term in the bracket is the number zero. This zero term was purposely kept to enable a comparison with other equations Chehroudi et al. [5, 10] discussed. They also referred to an equation proposed by Papamoschou and Roshko [17] for incompressible, but variable-density, turbulent gaseous jets:

$$\theta \approx 0.212 \left[1 + \left(\frac{\rho_g}{\rho_l} \right)^{0.5} \right]. \quad (2)$$

The similarity in the form of these equations is quite astonishing considering vast differences between the cases. Chehroudi then suggested a linkage between the two cases. This is how Chehroudi et al. [5, 10] explained their case.

Imagine a jet that is being injected into a subcritical pressure environment similar to the ones shown in frame 4 of Figure 1 (or the left image in Figure 2). Clearly there are drops, ligaments, and interface “bulges” testifying existence of a surface tension. Chehroudi’s group also reported evidence of a thermodynamic phase change under this condition. Hence, one appropriate characteristic time of the problem (at subcritical, $P_r < 1$) is the “bulge” formation/separation time (τ_b) on the interface of the turbulent liquid jet. This time scale, according to Chehroudi et al. [5, 10], characterizes the formation and separation event of bulges from the liquid jet which subsequently produce isolated ligaments and drops. Then they referred to a suggestion made by Tseng et al. [33] that this time scale was equal to $(\rho_l L^3/\sigma)^{1/2}$ for the primary breakup in turbulent liquid jets, where ρ_l , L , and σ are liquid density, characteristic dimensions of turbulent eddies, and surface tension, respectively. The second relevant characteristic time (for subcritical jets) that Chehroudi considered was the gasification time (τ_g). Here, an estimate of this time was calculated through the so-called D -squared law of spherical drop evaporation which is equal to D^2/K , where D and K are drop diameter and vaporization constant, respectively. In addition, Chehroudi also proposed a hypothesis as follows: if the aforementioned characteristic times (calculated for appropriate length scales) were nearly equal in magnitude, then the interface bulges are not able to separate as unattached entities from the jet interface to form ligaments and drops. This is because they are gasified as fast as they desire to be detached. This condition was then defined as the onset of the gas-jet-like behavior. Therefore, the transition between liquid-spray-like and gas-jet-like behaviors would be governed by finding the point at which these characteristic times are approximately equal. The scenario just explained is also supported by the “comb-like” structures seen in the middle image of Figure 2.

Using the above physical description, a model equation was then proposed for the N_2/N_2 system as

$$\theta = 0.27 \left[\frac{\tau_b}{(\tau_b + \tau_g)} + \left(\frac{\rho_g}{\rho_l} \right)^{0.5} \right]. \quad (3)$$

In the limit when $\tau_g \gg \tau_b$ and $\tau_g \rightarrow \infty$, this equation collapses to the isothermal liquid spray case. This equation agrees well with the Chehroudi et al. [5, 10] experimental data at subcritical pressures for $\tau_b/(\tau_b + \tau_g) < 0.5$. A constant value of 0.5 was used for this term to predict the spreading rate at higher chamber pressures, including supercritical pressures.

For injection of N_2 into N_2 , the characteristic time ratio, $\tau_b/(\tau_b + \tau_g)$, was computed from the experimental measurements of bulge and droplet sizes and calculations of the relevant properties. For N_2 injection into other gases, however, reliable information about the mixture properties at the interface, particularly the surface tension, prevented

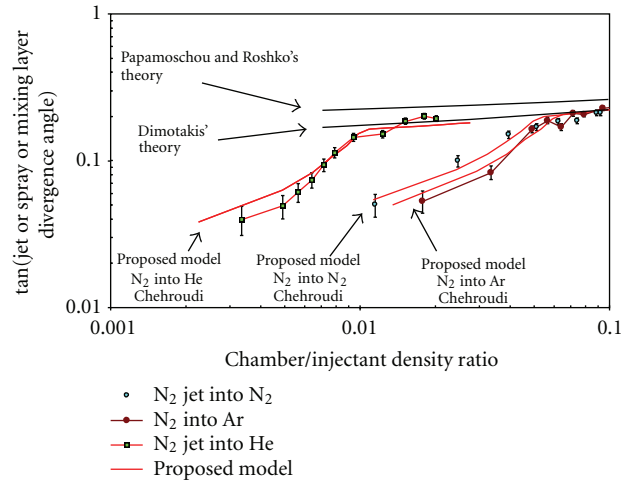


FIGURE 13: Comparison of the Chehroudi’s proposed growth rate model with experimental data for single jets. Chehroudi et al. [5, 10].

such a calculation from being performed; see Chehroudi et al. [5, 10]. To model these cases though, they further hypothesized that the characteristic time ratio term is a dominant function of the density ratio; that is, $\tau_b/(\tau_b + \tau_g) = F(\rho_g/\rho_l)$. Chehroudi then referred to the work by Brown and Roshko [15] in which they indicated that such a hypothesis is reasonable. This is because at low Mach numbers, there is no distinction between mixing layers where the two streams have different molecular weights, temperatures, or compressibility effects. Measurements and calculations of $\tau_b/(\tau_b + \tau_g)$ provided a shape of the function “ F ” for the N_2/N_2 system which is given as a plot in Chehroudi et al. [5, 10]. A curve fit of that plot generates the following equation:

$$F\left(\frac{\rho_g}{\rho_l}\right) = 5.325\left(\frac{\rho_g}{\rho_l}\right) + 0.0288 \quad \text{when } \frac{\rho_g}{\rho_l} < 0.0885 \quad (4)$$

$$= 0.5 \quad \text{when } \frac{\rho_g}{\rho_l} \geq 0.0885.$$

It was found that the same function, F , calculated from measurements of the N_2/N_2 system could be made to work for other cases, provided that a case-dependent transformation was made to the density ratio at which the function F is evaluated. The final form of the Chehroudi proposed equation is

$$\theta = 0.27 \left[F\left(x \left(\frac{\rho_g}{\rho_l}\right)\right) + \left(\frac{\rho_g}{\rho_l}\right)^{0.5} \right], \quad (5)$$

where $x = 1.0$ for N_2 into N_2 , $x = 0.2$ for N_2 into He, and $x = 1.2$ for N_2 into Ar.

The quality of the agreement with experimental data is demonstrated in Figure 13. Hence there are no major changes in the form of the proposed model equation, even for an extreme arrangement such as injection of N_2 into He gas. It is also important to indicate that spreading angle

under supercritical condition using modeling and computer simulation work by Zong and Yang [34] also agrees with Chehroudi's equation.

3. Single Jet with External Excitation

3.1. Effects of External Acoustic Field. Substantial evidences accumulated in the past attributed combustion instability to a complex interaction of the external acoustic field with the fuel injection processes, leading to incidences of instability in liquid rocket engines. For example, Oefelein and Yang [35] indicated that the near-injector processes in the thrust chamber were generally more sensitive to velocity fluctuations parallel to the injector face than normal to it. For this and other reasons, controlled experimental, analytical, and computational studies have been conducted in the past focusing on the effects of acoustic waves on both gaseous and liquid jets from a variety of injector designs. However, as indicated earlier, with a few exceptions, the scope of this paper is limited to experimental work which covers injection into supercritical conditions.

Chehroudi and Talley [36] used a piezo-siren design capable of generating sound waves with a sound power level (SPL) of up to 180 dB. This was used at three chamber pressures of 1.46, 2.48, and 4.86 MPa (reduced pressures of 0.43, 0.73, and 1.42, resp.). The experimental setup consisted of an acoustic driver and a high-pressure chamber, forming a cavity which resonated at several frequencies. The strongest ones were reported at 2700 and 4800 Hz. This basic setup was also used as the backbone for many of their future studies on coaxial injectors albeit with some improvements in data acquisition and facility plumbing. Chehroudi and Talley [36] injected LN₂ into GN₂ at room temperature under sub- and supercritical chamber pressures. Three different flow rates were considered, and the nature of the aforementioned interaction was documented via a high-speed imaging system using a CCD camera.

Figure 14 shows some sample results from this study where images of the jet are shown at two different perpendicular directions. These pair images at two different angles were taken on different test runs, but the operating conditions were as close as possible to each other. Each composite jet image consists of a mosaic of several images taken from the same test run but at different times and jet axial locations.

Chehroudi and Tally [36] reported that the acoustic field constricted the jet in the wave propagation direction, as seen in Figure 14, and consequently stretched the jet in the direction perpendicular to the propagation. They found that the impact of the acoustic waves on the jet structure was indeed strong at subcritical and near-critical pressures, but weakest at supercritical pressures. This is quite evident in Figure 14. They also observed that the externally imposed acoustic field interacted strongly at low injectant flow rates. The weakest effect was observed at supercritical pressures. This suggests that the mechanisms governing the coupling between acoustic waves and jets may be significantly different for jets injected under supercritical and subcritical conditions. This observation is important and its implications are discussed later in this writing.

To search for a plausible reason for the observed minimal impact at supercritical chamber pressures, Chehroudi and Talley [36] used the information mentioned earlier that at supercritical pressures, the unperturbed-jet spreading rate is the same as that by an incompressible variable-density gaseous jet; see Chehroudi et al. [5, 10]. For this reason, one expects the existence of vortices similar to what has been described, for example, by Rockwell [37] in which transverse disturbances were generated by an externally oscillating plate at a fixed amplitude but different frequencies (1000 to 10000 Hz). A synopsis of Rockwell's conclusions is useful in the context of the discussion here and hence is presented in the next two paragraphs.

A relatively large planar nozzle was designed by Rockwell [37] to inject water and investigate the details of vortex formation and their interactions near the exit area. The effects of the frequency of oscillations on the natural vortex coalescence were classified based on a Strouhal number ($St = fd/U$, where f , d , and U are the externally imposed excitation frequency, jet diameter, and mean jet velocity) versus Reynolds number ($Re = \rho Ud/\mu$, where ρ and μ are the injectant density and viscosity) plot, see Figure 15. For the range of Re investigated (1,860 to 10,800), natural breakdown of the jet (i.e., with no external disturbances) was observed to be within a few nozzle widths. The dimensionless frequency (St_N) of natural vortices was found to change with Re number as $St_N = 0.012 (Re)^{0.5}$. Four regimes were distinguished based on the observed effects of the external disturbance on the nature of the vortex interaction. The reference regime was that which corresponds to the natural breakdown of the jet. The four regimes were named, in order of decreasing St number, as "upper zone," "preservation," "matched excitation," and "forced fusion" regimes. A plot of these regimes is shown in Figure 15 and compared with the values estimated for Chehroudi's study using LN₂ injection into a GN₂ chamber.

In the "upper zone" regime of Figure 15 where the excitation frequencies were higher than about 3 to 4 times the natural breakdown frequency ($St > 3 St_N$), no effects were observed. In the "preservation" regime, the core flow of the jet tended to be preserved followed by the induction of smaller vortices, the time-averaged velocity profile was narrowed, and the longitudinal turbulence was decreased (relative to undisturbed case). When the excitation frequency was matched with the natural break-down frequency ("matched" regime), the effect was to accelerate the process of vortex formation and growth relative to the undisturbed case. Also, transverse distortion of the jet core was seen due to the vortex growth and coalescence. For the symmetrical jet work of Becker and Massaro [38], symmetrical ring vortices were produced and highest time-averaged widening of the jet has occurred. This was in contrast to the planar jet case in which vortices on the two sides of the jet were 180 degrees out of phase with each other. This regime merges to the "preservation" regime at higher Re number ($\sim 10,000$). In the "forced fusion" regime (frequencies $\sim 1/3$ of natural jet breakdown), the natural break-down vortices were forced to fuse early as a result of the formation of large-diameter applied disturbance vortices. Vaslov and Ginevskiy

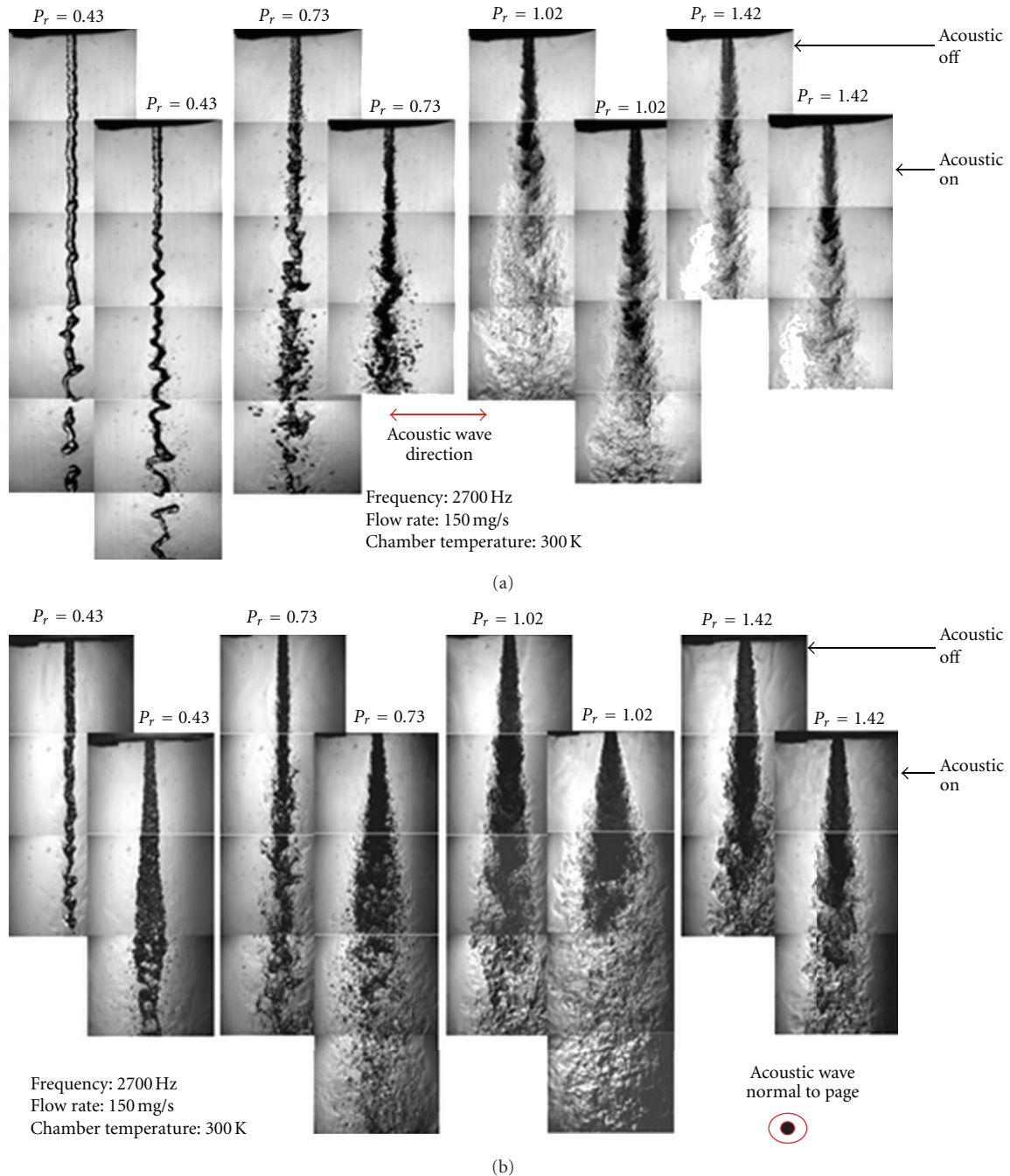


FIGURE 14: Interaction of acoustic waves with a single round liquid nitrogen jet injected into gaseous nitrogen at a range of chamber pressures from sub- to supercritical conditions. (a) Top images show front view; only one acoustic driver located at the left of the jet. The set of images shifted downward are when the acoustic field is turned on as indicated. (b) Bottom images show side views of the same jet (the same acoustic driver is located behind this page). P_r is the reduced chamber pressure (i.e., chamber pressure divided by the critical temperature of the injected nitrogen). Chehroudi and Talley [36].

[39] found that in this regime the time-averaged velocity profile of the jet was broadened. Finally, in the “lower zone” regime (frequencies $< 1/10$ of natural jet breakdown), the vortex growth was unaffected in their formation region. In the limit, however, as St approaches zero, the jet experienced a quasi-steady deflection process. Rockwell [37] stated that a fallacious averaged jet widening is detected if a time-averaged

measurement technique is used downstream the injector, when in reality the jet is being deflected by the applied transverse disturbance.

To see how the results of Chehroudi and Talley [36] relate with Rockwell [37], their supercritical data is superimposed on the plot by Rockwell indicating different regimes discussed in the previous paragraph. Figure 15 shows a

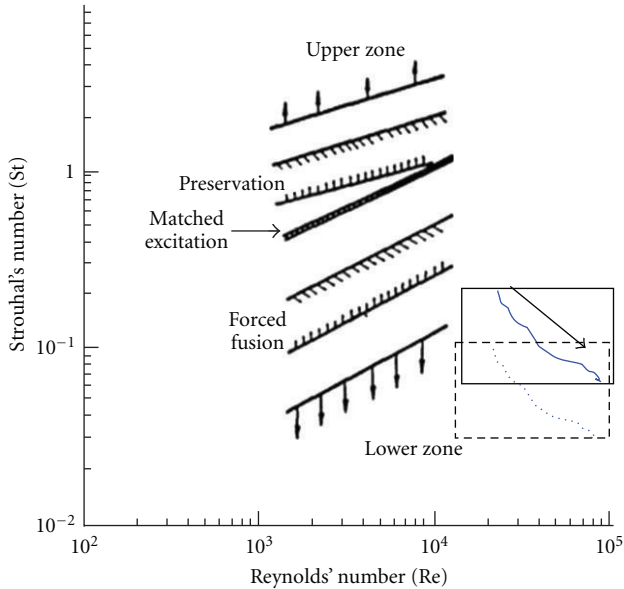


FIGURE 15: Regimes discussed by Rockwell [37] shown on an excitation Strouhal number versus the jet Reynolds number plot. The small solid rectangle to the right indicates the approximate region in which the Chehroudi LN₂ jet data lies when excitation is at 4800 Hz. The curve within this rectangle shows the approximate path as flow rate is increased from the lowest to the highest values, all at supercritical chamber pressures. Similar region for the 2700 Hz excitation is shown as a dashed rectangle. Chehroudi and Talley [36].

plot of the Strouhal number as a function of the Reynolds number. The curve marked as “matched excitation” is the same equation proposed by Becker and Massaro [38] for the natural breakdown of the jet. It can be seen that results from Chehroudi’s study are beyond the regions studied by Rockwell [37]. With the caveats of extrapolating Rockwell’s results, Figure 15 suggests that the frequencies used by Chehroudi’s group are not expected to bring about noticeably large effects of the acoustic waves on supercritical jet because they lie in the region identified by Rockwell [37] as the “lower zone.” No effects of the transverse disturbance on the jet were observed in the studies conducted by Rockwell [37] in this regime as described earlier. Note that the lowest flow rate case studied by Chehroudi’s group in Figure 15 tends to enter into the “forced fusion” regime where stronger interaction is expected.

4. Coaxial Jets without External Excitation

Coaxial jets injectors have been used in liquid rocket engines since the 1940s and are found in the present-day hardware such as the Space Shuttle Main Engine (SSME); see Hulka and Hutt [40]. Rocket engines such as the SSME use liquid oxygen (LOX) and hydrogen (H₂) as propellants with the LOX flowing through an inner tube (or a center post) of a coaxial injector design and H₂ through an outer annular region. The inner jet goes through the break-up process after it exits the injector and then mixes in the shear

layer between the inner and outer streams. Subsequently, combustion and heat release occur to generate the desired engine thrust.

Often the combustion processes are controlled by, or at least intimately related to, the jet breakup and mixing of the oxidizer and fuel streams. Certain aspects of these processes can safely and inexpensively be studied using chemically inert fuel and oxidizer simulants. Moreover, attempts are made for as many parameters as possible, such as velocity ratio, mass flow rate ratio, density ratio, Reynolds’ number (*Re*), Weber’s number (*We*), and Ohnesorge’s number (*Oh*), to represent similar values obtained in real engines. This scaling exercise, to the extent possible, allows reasonable inferences and evaluation of different injector designs before ever being tested under hot fire conditions.

Investigations targeted at enhanced and fundamental understanding of the injection processes and combustion stability, although desirable to be performed under operating engine conditions, are practically problematic and costly for many reasons, including the need for an optically accessible full-scale liquid rocket engine, special material choices, and optical diagnostic limitations. For example, a single-element noncombusting test rig having as much of the key features of a real cryogenic rocket engine as possible, such as cryogenic temperatures, transcritical temperature ranges, supercritical pressures, realistic velocity ratios, and activation of an acoustic field inside its test chamber, is as close as one can get to the actual engine, yet avoiding indicated complications associated with the combustion in a full-scale setup. Therefore, test rigs have been designed in many studies to have such desired characteristics. Combination of the cryogenic liquid N₂ and gaseous N₂ (to eliminate mixture critical phenomena) and N₂/helium (He) system (to better simulate the LOX/H₂ injection issues) were considered in most of these studies.

4.1. Coaxial LN₂/He Injection. Telaar et al. [41] experimentally investigated the influence of the ambient pressure on the atomization phenomena from subcritical to supercritical pressures in a coaxial LN₂/He injection. They used a coaxial injector design with an inner diameter of $d_{LN_2} = 1.9$ mm for the cryogenic nitrogen flow and an annular slit width of 0.2 mm with an outer diameter of 2.8 mm for helium. Two examples of the flow visualization by shadowgraphy near the injector region are shown in Figure 16. The changes in the break-up mechanism at a reduced surface tension are quite evident. At the low chamber pressure of 1 MPa in Figure 16(A), a liquid spray is formed, whereas at the supercritical pressure of 6 MPa in Figure 16(B), a gas-like turbulent mixing of the dense and light fluids is seen. At 6 MPa, the initial temperature of the center LN₂ jet was 97 K, whereas the critical mixing temperature of He/N₂ mixtures at this pressure is 125.7 K. Thus, in the mixing layer between the LN₂ and He gas, transcritical zones may exist. The visual boundary of the LN₂ jet as shown in this figure is assumed to be the layer at which the temperature reaches the critical mixing temperature. At this interface then, the influence of the surface tension forces as compared to the shear forces appears to be negligible.

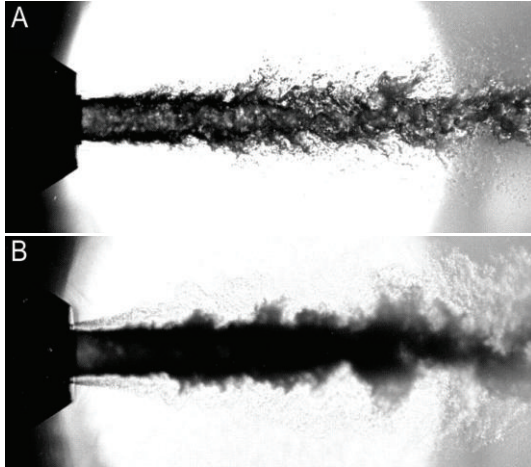


FIGURE 16: Binary coaxial liquid N_2/GHe system at (A) chamber pressure of 1.0 MPa, (B) chamber pressure of 6.0 MPa. Inner-tube hole diameter, $d_{LN_2} = 1.9$ mm; liquid nitrogen injection velocity, $v_{LN_2} = 5$ m/s; helium gas injection velocity, $v_{He} = 100$ m/s; liquid nitrogen injection temperature, $T_{LN_2} = 97$ K; gaseous helium injection temperature, $T_{He} = 280$ K (from Telaar et al. [41]).

4.2. *Visualization of a Liquid Nitrogen/Gaseous Nitrogen Coaxial Injector.* Davis and Chehroudi [42] used a coaxial injector designed to inject a liquid nitrogen, with a coflow of gaseous nitrogen in its annular region, as a part of a program to better understand the nature of the interaction between acoustic waves and liquid fuel jets in cryogenic rocket engines. In their test setup, injection was into a chamber filled with gaseous nitrogen at a supercritical temperature and different pressures spanning from sub- to super critical conditions. However, prior to presenting Davis and Chehroudi's results on acoustic forcing investigations, they provided a wealth of new information on dynamics of the jets (with no acoustic excitations), specifically focusing on the dark-core length of the inner jet in their coaxial injector. This is discussed next.

Davis and Chehroudi [42] argued that in their coaxial injector design, or in any generic one, the outer-jet flow rate played two key roles. First, it assisted the inner-jet breakup at the subcritical condition and enhanced mixing for the supercritical case. Second, because of the temperature differences between the inner jet and the outer jet, there was a heat exchange between the two, both inside and outside the injector. Evidences for the heat transfer behavior were given by examination of the results from jet temperature measurements. Figure 17 shows normalized temperature measurements within the inner jet and at the injector exit plane plotted versus normalized outer-jet mass flow rate at four different chamber pressures covering sub-, near-, and super-critical chamber pressures. Figure 18 shows images indicating typical jet characteristics taken at these same three-chamber reduced pressures. Evidences on the impact of the heat transfer are shown in Figure 17. For instance, at the lowest (subcritical) chamber pressure of 1.4 MPa, Davis and Chehroudi [42] found that the inner-jet exit-plane temperature was fairly insensitive to changes in the

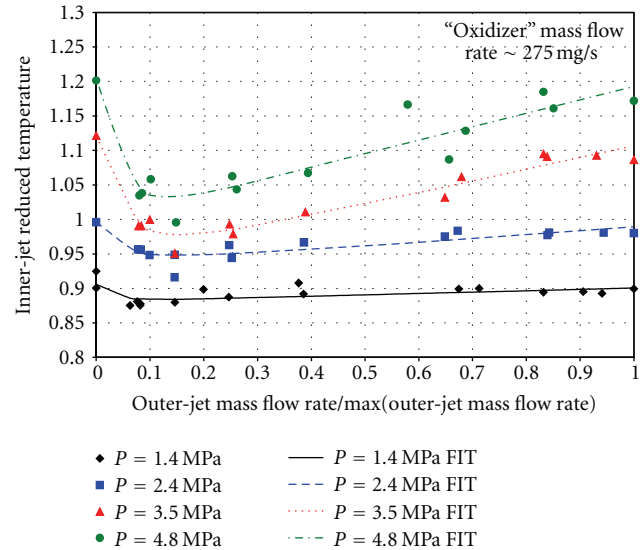


FIGURE 17: The inner-jet reduced temperature for a coaxial injector plotted versus the annular outer-jet mass flow rate, normalized by its maximum mass flow rate, at four different chamber pressures. Inner-jet mass flow rate is fixed at about 275 mg/s. The lines, called "FIT" on the inset, are curve fits to the raw data. The maximum outer-jet mass flow rates for 1.4, 2.4, 3.5, and 4.8 MPa are 2,995, 2,985, 2,974, and 2,918 mg/s, respectively, Davis and Chehroudi [42].

annular outer-jet flow rate; see Figure 17. However, at all other elevated pressures, particularly at the supercritical one, an increase in inner-jet exit temperature was measured.

Under zero or no outer-jet flow rate condition in Figure 17, the annular passage of the injector was filled with the warm chamber nitrogen, hence strongly affected the heat transfer not only inside but also outside the injector. Clear evidence for the high heat transfer rate inside the injector was shown from the exit temperature measurements under this no-flow condition; see the y -axis in Figure 17. Here, the observed elevated temperature was reported to be the effects of the warm chamber gases present inside the annular space of the injector. Hence, referring to Figure 18, even though no atomizing (outer-jet) mass flow was at work in frames 11 and 21, one sees a shorter dark-core axial length than those seen in other images presented in frames 13 and 23. A small flow of the colder-than-chamber gaseous nitrogen in the annular passage, though may not assist the jet breakup, lowers the inner-jet exit temperature. Davis and Chehroudi [42] reported that the two processes (i.e., gas-assist liquid atomization and heat transmission) worked in such a way that the net effect was an apparent longer dark core in most cases. For example, compare the images in column one and two (from the left) in the last two rows as shown in Figure 18.

Clearly, the jet behaved differently at different outer-jet mass flow rates. Considering that the outer-jet mass flow rate acted as an atomizing gas, thus accelerating the breakup mechanism, then as the mass flow rate of the outer jet increased slightly (~ 487 mg/s, frame 3, Figure 18), the inner jet began to break up into relatively large droplets and

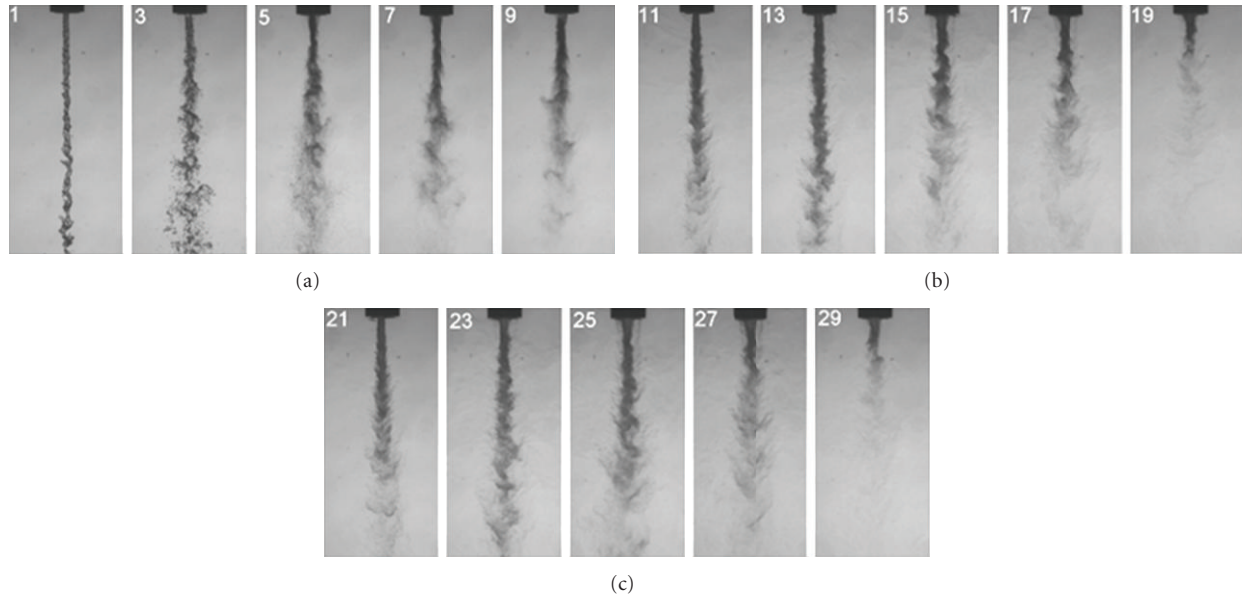


FIGURE 18: Images of a coaxial jet at approximately the same inner-jet mass flow rates (~ 275 mg/s). Columns are at about the same outer-annular-jet mass flow rates. For each row, the annular mass flow rate starts at a zero value to 2800 mg/s and increases from the left column to the right. The chamber pressure levels for images 1–9 are subcritical (~ 1.41 MPa), for 11–19 are near-critical (~ 3.46 MPa), and for 21–29 are supercritical (~ 4.77 MPa). Inner- and outer-tube flow average temperatures at injector exit are 170 K and 112 K, respectively. Davis and Chehroudi [42].

ligaments resulting from its interaction with the atomizing outer-jet flow. When the outer-jet flow rate was increased even further, finer droplets and ligaments were reported forming from the inner jet fluid, and more of its mass from the intact core was converted into droplets and ligaments. This consequently produced a shorter and less dark core for the inner jet. Moreover, as the outer flow rate increased, the heat transfer from the outer jet to the inner one intensified outside the injector, thus lowering the average density of the inner core in the injector near-field area. Under the subcritical condition, Davis and Chehroudi [42] reported that this combined outer-jet-assisted atomization of the inner jet and heat transfer processes created a dark core region more susceptible to external excitations.

4.3. Density Measurements in a Coaxial LN_2/GH_2 Jet.

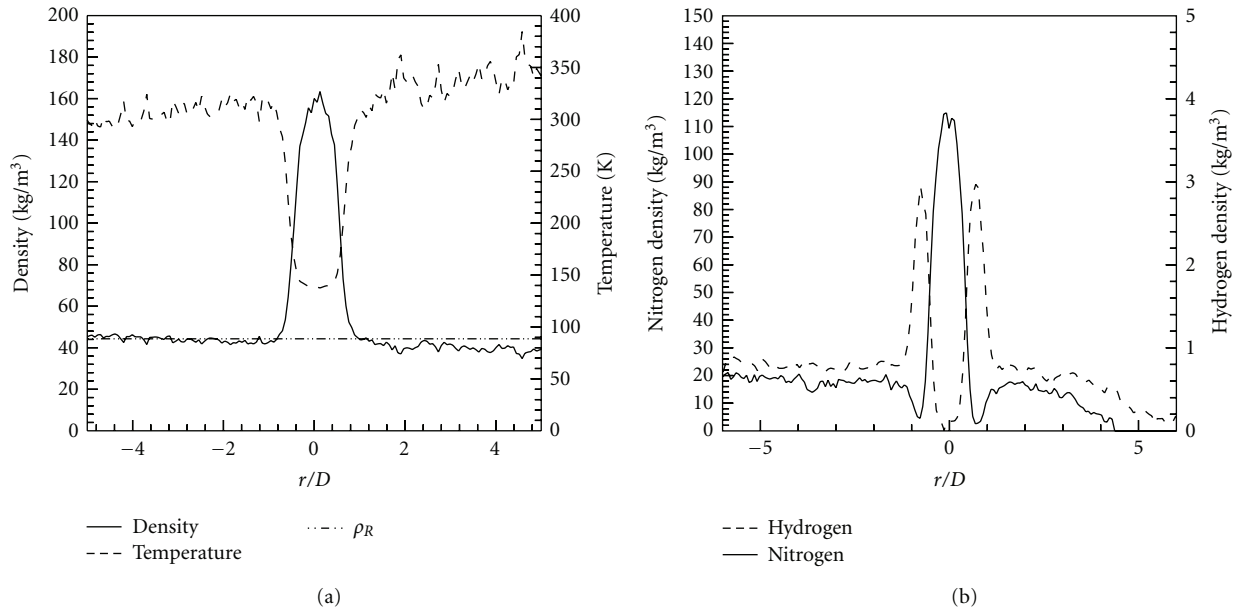
Although use of the Raman scattering is straightforward for a liquid N_2 injection into a gaseous N_2 , in a mixture of N_2 and H_2 the Raman signals of the N_2 and H_2 are generated at two different wavelengths. Thus, in principle, utilizing an appropriate filtering technique, the signals from both species can be analyzed independently and the partial densities of each species can be determined.

This diagnostic method has been used to investigate the atomization and mixing of coaxial LN_2/H_2 injection at pressures which were supercritical with respect to the critical pressure of pure nitrogen in the inner jet; see Oswald et al. [32]. During all the tests, the fluids were injected into a flow channel filled with N_2 at near atmospheric temperature and a pressure of 4 MPa ($P_r = P/P_{\text{crit}} = 1.17$). Results from a coaxial LN_2/H_2 injection are shown in Figure 19(b) and are contrasted with a single-jet case presented in Figure 19(a).

The decrease of the measured densities at large positive r/D values was reported to be due to refraction of the laser beam experienced as a result of density gradients existing at the H_2/LN_2 interface. Similar radial profiles have also been obtained for a range of axial distances from the injector. Based on these data, two-dimensional species distributions were reconstructed for both H_2 and N_2 . For the D4 test case described in Figure 19, such a distribution pertaining to the H_2 is shown in Figure 20.

The maximum of the radial nitrogen density distribution at each axial distance was plotted as a function of the normalized distance (x/D) from the injector; see Oswald et al. [32]. This was then used to ascertain the evolution of the injection process for the LN_2 jet downstream of the injector, as well as to assess the mixing effectiveness between the H_2 and N_2 species. Compared to the test case without the H_2 coflow, the existence of the coflow decreased the measured nitrogen density much faster from its initial injection value near the injector exit area to a plateau which was a value for the far-field background level. The x/D value at which this plateau occurred was then interpreted as representing a complete mixing of the jet with its background gas.

It was shown in Oswald et al. [32] that when the inner-jet temperature at the injector exit was above the pseudoboiling temperature, it had a shorter decay distance (x/D) than a jet with an injection temperature initially below it. In both cases, the injected nitrogen was at a supercritical pressure. They also reported that the nitrogen inner jet above the pseudoboiling temperature exhibited a gas-like density; whereas below this temperature it possessed a liquid-like density value. Interestingly, their data suggested that



	Test case	V_{N_2} [m/s]	T_{N_2} [K]	V_{H_2} [m/s]	T_{H_2} [K]
single N ₂ jet	A4	5	140	—	—
	B4	5	118	—	—
	D4	5	140	60	270
coaxial N ₂ /H ₂ jet	E4	5	118	120	270
	F4	5	118	60	270

FIGURE 19: (a) Radial N₂ density profile for test case A4 (single jet), 2 mm ($x/D = 1.05$) downstream of the coaxial injector exit. (b) Radial N₂ and H₂ density profiles for coaxial LN₂/H₂ injection for test case D4, 2 mm ($x/D = 1.05$) downstream the injector exit. Laser beam direction is from left to right. Oswald et al. [32].

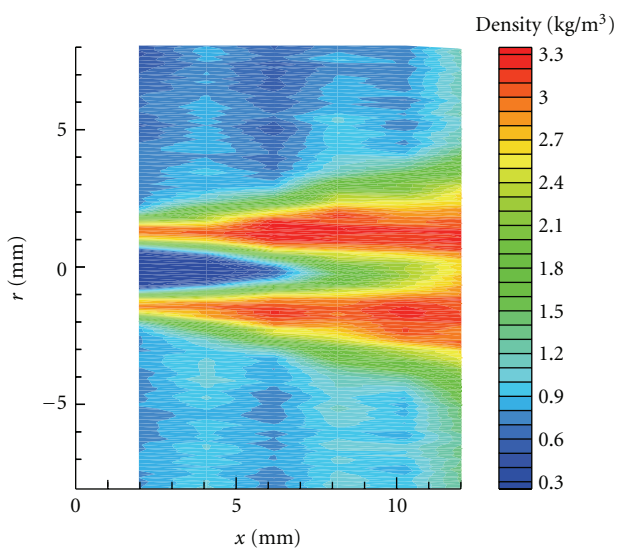


FIGURE 20: Hydrogen density for a coaxial LN₂/H₂ injection for the test case D4 in Figure 19 ($T_{N_2} = 140$ K, $T_{H_2} = 270$ K). Oswald et al. [32].

the effect of higher H₂ velocity was found not to be as pronounced as this effect of the initial N₂ density.

4.4. Spreading Angle and Core Length Measurements. Two important, and less difficult to measure, geometrical characteristics of such coaxial injectors are the spreading angle of the (combined inner and) outer jet and the length of a dark inner-core of the injected jet. They are readily determined through the high-speed shadowgraphy approach. Both the length of the dark core and the spreading angle provide good measures for mixing characteristic of the jets in coaxial injectors.

Mixing of the propellant streams, if not controlling, is at least intimately related to the combustion process. To a first-order approximation, one measure of the mixing process is the length of the inner jet's liquid and/or dark core, which has been extensively studied by many researchers in the past. For details see Davis and Chehroudi [43]. Experimental core-length correlations, semiempirical theories, and other data for shear coaxial injector studies involving core length were competently summarized by Davis and Chehroudi [42]. Many of the correlations and semiempirical theories

reviewed by them indicated dependencies of the core length with parameters such as outer-jet-to-inner-jet velocity ratio (V_r), outer-jet-to-inner-jet momentum flux ratio (M), density ratio (ρ_o/ρ_i), Reynolds' number (Re), and Weber's number (We). One difficulty Davis and Chehroudi reported with applying these relationships at supercritical pressures is that the predicted core length was very small or zero in magnitude. This is because one of the parameters in the equation was (We) and surface tension diminished greatly or vanishes all together. To overcome the difficulty in core length prediction associated with large (We) number, one group of researchers, proposed that M can be used to describe the scaling of the core length for shear-coaxial injectors and need not include (We) number if it was sufficiently high; see Davis and Chehroudi [42, 43] for details.

But before moving forward, it should be mentioned that confusion does exist in the literature especially when vague definitions are used to characterize the core length. The terms potential-core, potential-cone, intact length, intact-liquid length, and break-up length have all been used along with various measurement techniques. To be clear and to remove any possible ambiguities from the data, the dark-core length was defined as the connected dark fluid region between the injector exit area and the first break in the core as defined by an adaptive thresholding procedure; see Davis [44] or Davis and Chehroudi [42] for more details.

A plot of the dark-core length values for a coaxial injector measured by Davis and Chehroudi [43, 44] versus momentum flux ratio is shown in Figure 21. They used liquid nitrogen (in inner jet) with gaseous nitrogen (in outer annular jet) injected into a chamber filled with gaseous nitrogen at various pressures spanning sub- to supercritical values. The chamber temperature was always at a supercritical value. A clear distinction between the subcritical dark-core length (diamond symbols) and this length at the near-critical and supercritical chamber pressures is seen in Figure 21. Subcritical data suggests a much longer length than that at supercritical pressures for a given momentum flux ratio. Davis and Chehroudi indicated that both the near-critical and supercritical pressure conditions produced an appearance of a single-phase coaxial jet even though liquid nitrogen was injected through the inner tube of the coaxial jet. Recall that earlier in the single-jet part of this paper, Chehroudi and his coworkers [5, 10, 26] also found that two-phase-appearing jets were solely observed at subcritical chamber pressures. However, at supercritical chamber pressures, the spreading rate and fractal dimension values were the same as those seen for gaseous jets injected into a gaseous environment (i.e., single phase); that is, these supercritical single jets can be considered as variable-density, single-phase, gaseous jets. This conclusion presented earlier for the single-jet injection is something Davis and Chehroudi [43, 44] also showed to be mostly valid when it comes to the dark-core length observations in coaxial jet injectors. Evidences in support of such a behavior for coaxial injectors are presented in the next few paragraphs.

The dashed line in Figure 21 is a least-square curve fit to the subcritical data, and the dotted line is a similar

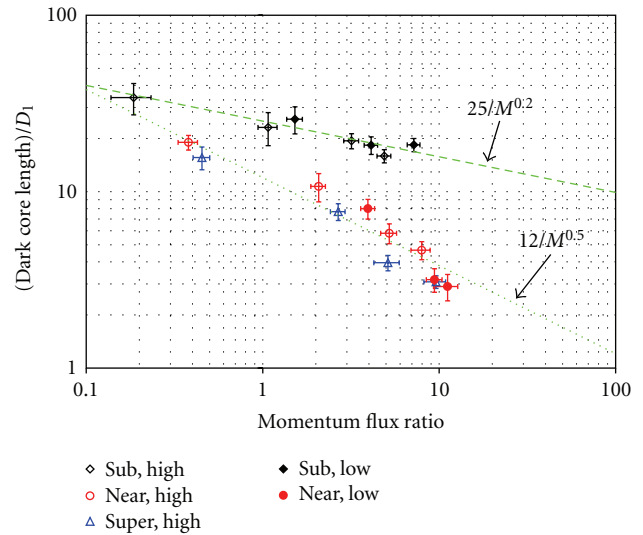


FIGURE 21: Plots of the dark-core length versus momentum flux ratio for a coaxial injector. Liquid nitrogen (inner jet) and gaseous nitrogen (outer annular jet) injected into chamber filled with gaseous nitrogen. The diamond, circle, and up-triangle symbols represent sub-, near-, and supercritical chamber pressure, respectively. The hollow symbols are at a “high” outer-jet temperature (~ 190 K) and solid symbols are at a “low” outer-jet temperature (~ 140 K). The dashed line is $25/M^{0.2}$ and the dotted line is $12/M^{0.5}$. Davis and Chehroudi [43, 44].

fit to the near-critical and supercritical data. As indicated by the equations in this figure from Davis and Chehroudi [42, 43], the single-phase-appearing (i.e., at near-critical and supercritical pressures) data has a $M^{-0.5}$ dependence on momentum flux ratio. However, they indicated that the two-phase-appearing subcritical data had a weaker dependence, $M^{-0.2}$, than the single-phase dark-core length at near- and super-critical chamber pressures. Other quantitative differences between the subcritical and supercritical cases have been reported before. They also reported that the $M^{-0.5}$ form of the dependency on M parameter under near- and supercritical pressures is not only valid for gas-gas shear-coaxial jets, but is also for any single-phase (gas-gas or liquid-liquid) shear-coaxial jet.

Figure 22 was constructed by Davis and Chehroudi [42, 43] aiming at a comprehensive comparison of the dark-core length they measured for the LN_2/GN_2 with all other comparable single-phase and two-phase data available in the literature for the potential-core length, intact-core length, and break-up length. This unique figure represents all relevant data in the literature concerning core length spanning 5 orders of magnitude in momentum flux ratio. They also noted that as M approaches zero, one reaches a limit which defines a single round jet configuration because the outer-jet velocity becomes zero. From the information shown in Figure 22, it seems that for $M < 1$, the data points converge and approach the core length range expected for single round jets reported by Chehroudi et al. [27] and Oswald et al. [45]. The single-phase data by others (i.e., injectants and chamber content all are in one phase, either all gaseous or all liquids) along with the Davis and Chehroudi's

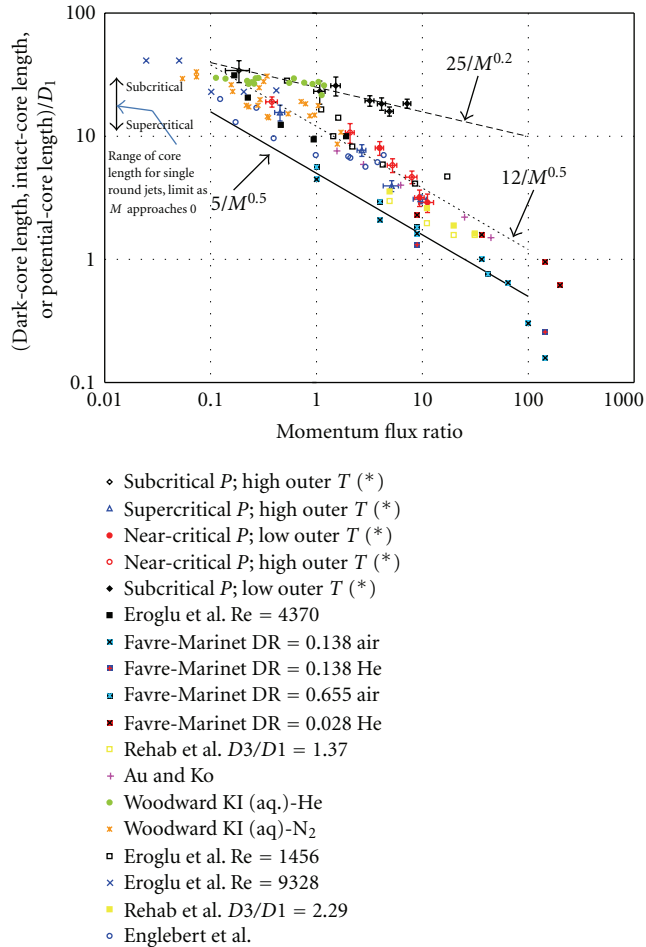


FIGURE 22: This figure shows comparison of the present coaxial-jet dark-core length measurements with all other relevant core length data available in the literature versus momentum flux ratio. Amongst the data reported by others, Eroglu et al. [47], Englebort et al. [48], and Woodward [50] are two-phase flows and the rest are single phase. The range of core length for cryogenic single jet (LN₂/GN₂) is also shown at the left margin. Davis and Chehroudi [42, 43].

LN₂/GN₂ supercritical results are all seen in Figure 22 to follow a dependence close to $L/D_1 = AM^{-0.5}$, where the constant A is between 5 and 12. This information combined with the clear separation of all the two-phase data, including the subcritical core length data seen in Figure 22, essentially suggests a two-phase behavior at subcritical and a single-phase conformance at supercritical chamber pressures.

Even though best efforts were made to use the most relevant data by other investigators, some shortcomings were reported. For example, at $M > 100$ in Figure 22, the experiments of Favre-Marinet and Camano Shettini [46] exhibited a recirculation bubble at the end of the core, and thus the core length decreases as depicted in this figure. The injectors used to produce the two-phase coaxial jets of Eroglu et al. [47] and Englebort et al. [48] had apparently much larger outer-jet gap widths than what is typical of rocket injectors. Additionally, the apparatus of Eroglu et al. [47], reported in Faragó and Chigier [49], did not produce fully

turbulent inner jet until $Re > 10^4$. Davis and Chehroudi [42, 43] explained that the lack of a fully turbulent inner jet and the significant differences between their injector and shear-coaxial ones used in rockets could be the reason why the core length measured by Eroglu et al. [47] is shorter than those observed in their work. Englebort et al. [48] reported that the core length scaled with $M^{-0.3}$. The two-phase core length by Woodward [50] for the water potassium iodide solution with helium, however, obeyed very nearly the trends for the subcritical data points (i.e., $25M^{-0.2}$). Considering that the momentum flux ratios near or higher than 10 are of importance for liquid rocket engines (LRE), Davis and Chehroudi [42, 43] indicated that the data for the subcritical (two-phase) case was the only reported information in the neighborhood of the $M = 10$.

Outer-to-inner jet velocity ratio, V_r , has been a design parameter for shear-coaxial injectors, particularly, as a criterion to ensure stable operation of liquid rocket engines (LRE). For LOX/H₂ engines, the design rule of thumb has been to keep the velocity ratio greater than about 10 in order to maintain stable engine operation, as is discussed by Hulka and Hutt [40]. Although this stability criterion has been suggested by the experimental data, no physical explanation has been provided. Related to this is a method to rate a LRE for combustion instability, known as the *temperature ramping*. The temperature ramping of a fired H₂/O₂ LRE is accomplished by lowering the temperature of the H₂ (in the outer jet of the coaxial injector) while maintaining its mass flow rate at a constant value. The lower the H₂ temperature when the onset of the combustion instability is detected, the broader the stability margin of that particular LRE. The temperature ramping is related to and affects the velocity ratio. This is because one of the outcomes of lowering H₂ temperature at constant mass flow rate is the increased density and consequently, lowered injection velocity values. Davis and Chehroudi [42, 43] therefore investigated the impact of the velocity ratio on their nonreacting LN₂/GN₂ coaxial jets, hoping that results may shed some light on the effects of velocity ratio observed in fired production engines. This is explained next.

To determine the effects of the outer-jet temperature (which is GN₂ in Davis and Chehroudi's work) on the coaxial jet, Davis and Chehroudi [42, 43] studied two nominal temperatures of ~ 190 K and ~ 140 K, called "high" and "low," respectively. Recognizing that the dark-core length is a dynamic quantity, its basic characterization required measurements of both the average and root mean square (RMS) of length fluctuations. The averaged dark-core lengths were then measured and are shown in Figures 23(a) and 24(a) as a function of velocity ratio for sub-, near-, and super-critical chamber pressures. The RMS of the variations of the dark-core length is also shown in Figures 23(b) and 24(b). Note that Figures 23 and 24 present results for conditions when the external acoustic field is both turned on and off for "high" and "low" outer-jet temperatures. However, it is important to emphasize that in this section only the results when the acoustic field is turned off are discussed, deferring the impact of the externally imposed acoustic field to the next part of this paper.

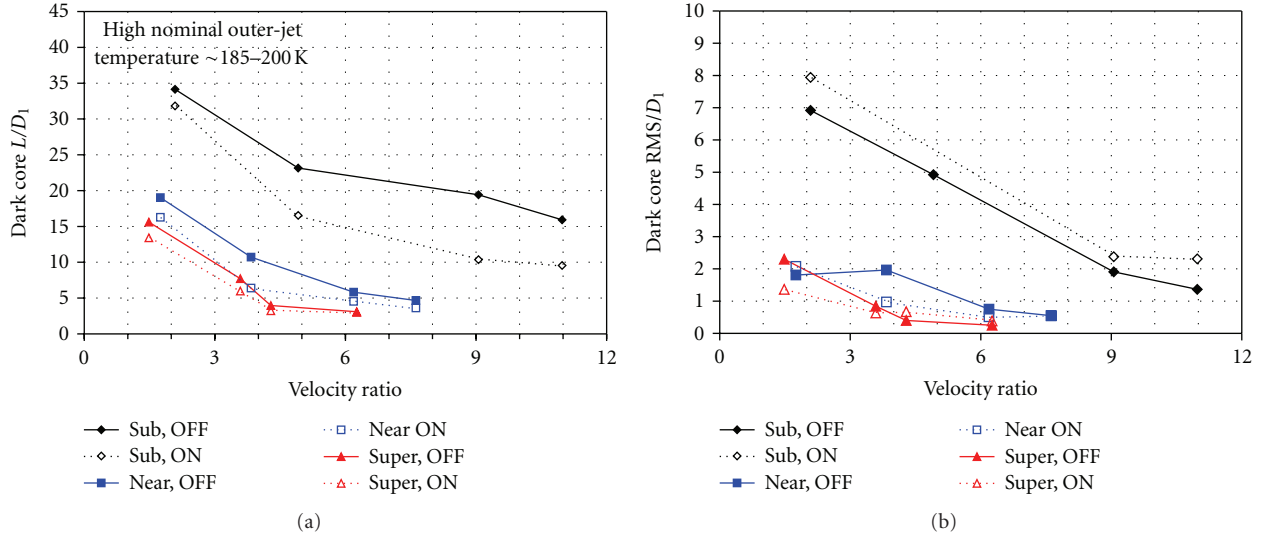


FIGURE 23: Plot of the averaged dark-core length (a) and the root mean square (RMS) of the length variations (b) normalized by the inner diameter of a LN_2/GN_2 coaxial jets injector. The solid symbols and lines represent the data when the acoustic driver is off, and the hollow symbols and dotted lines show the data when the acoustic driver was operated at ~ 3 kHz. The diamond, square, and up-triangle symbols are sub-, near-, and supercritical chamber pressures, respectively. All cases are for the high nominal outer-jet temperature of ~ 190 K. In the inset, the words sub, near, and super refer to subcritical, near critical, and supercritical chamber pressures, respectively, and the words OFF and ON refer to the acoustic driver being off and on at ~ 3 kHz, respectively. Davis and Chehroudi [42, 43].

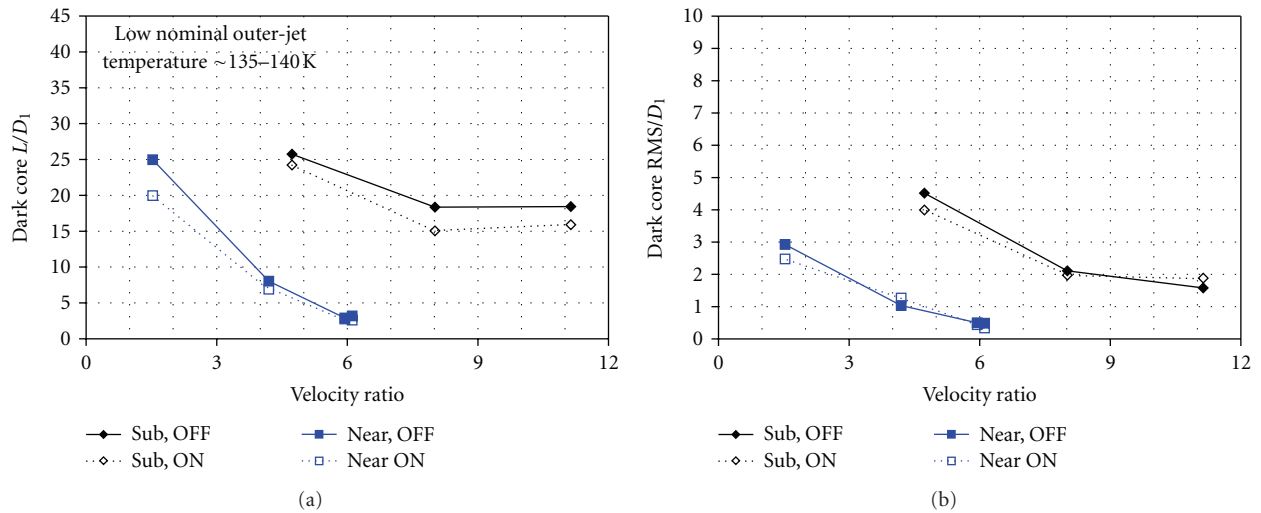


FIGURE 24: Plot of the averaged dark-core length (a) and the root mean square (RMS) of the length variations (b) normalized by the inner diameter of a LN_2/GN_2 coaxial jets injector. The solid symbols and lines represent data when the acoustic driver is off, and the hollow symbols and dotted lines show results when the acoustic driver is operated at ~ 3 kHz. The diamond and square symbols are for sub- and near-critical chamber pressures, respectively. All cases are for the low nominal outer-jet temperature of ~ 140 K. In the inset, the words sub and near refer to subcritical and near-critical chamber pressures, respectively, and the words OFF and ON refer to the acoustic driver being off and on at ~ 3 kHz, respectively. Davis and Chehroudi [42, 43].

Evident in Figures 23(a) and 24(a) is the fact that the length of the dark core decreases as the chamber pressure is increased from sub- to super-critical conditions. The dark core provides an indication of high-density regions of the flow. At a given fixed chamber pressure, as V_r is increased, the length of the dark core decreases and appears approaching a constant value. The RMS values of the dark-core length fluctuations, shown in Figures 23(b) and 24(b), exhibit

somewhat similar trends to those seen for the averaged values, that is, substantially lowered at near- and super-critical chamber pressures.

It is known that for a liquid-fueled rocket, atomization and break-up processes, interactions between the propellant jets, droplet formation, and vaporization are all affected by the pressure and, particularly, velocity fluctuations. Also, for any chemically reacting system, it is expected that, to certain

but different degrees, the rate at which energy is released be sensitive to the rate of changes in temperature, density, pressure, and, of course, particularly mixture ratio. It is then intuitive to relate, in some form, the RMS values of the dark-core length fluctuations to mixture ratio variations. On the other hand, a low RMS value can be interpreted as the coaxial jet's "inherent steadiness" (or insensitivity to external stimuli) and vice versa. Examination of Figures 23(b) and 24(b) clearly shows that this property is drastically reduced as the velocity ratio is increased. Although these results are for one injector (i.e., no interinjector interaction), Davis and Chehroudi [42, 43] proposed a linkage between these nonreacting results and production-engine combustion instabilities observed at low velocity ratios. They stated that "it is then quite possible that the observed improvement in combustion stability at higher values of velocity ratio is a result of the inability of the jet to generate large mass flow rate fluctuations under these conditions, thus weakening a key feedback mechanism for the self-excitation process."

As indicated earlier, in temperature ramping exercises for stability rating of LOX/H₂ engines, the mass flow rate of the outer-jet hydrogen is maintained at a constant value. Davis and Chehroudi [42, 43] also attempted to provide a linkage between the temperature ramping and their experimental data. They said that as the temperature of the H₂ is decreased during a ramping episode, the H₂ becomes more dense, which decreases the injector velocity ratio at a constant mass flow rate. The RMS plots shown in Figures 23(b) and 24(b) suggest that such a decline in this ratio amplifies the jet's inherent unsteadiness (i.e., higher RMS values), providing a possible explanation for the engine's eventual arrival into an unstable zone as a temperature ramping test proceeds.

On the spreading angle or growth rate of the coaxial jets, Figure 25 is a compilation of experimental measurements reported earlier by Chehroudi et al. [5, 10] on single jets along with those newly acquired from a coaxial injector and other data. The tangent of the total jet divergence angle is plotted against the chamber-to-injectant (for single jets) or chamber-to-inner-jet (for coaxial jets) density ratio. The data taken by Chehroudi for single jets in the same facility is marked by (*) in the legend. Note that there are also some theoretical expressions presented in this figure for comparison purposes. The coaxial injector data follows the direction of the arrow as chamber pressure is changed from sub- to near- and to super-critical condition. Interestingly, the data for coaxial injection at subcritical condition conforms with the classical incompressible variable-density shear layer (Dimotakis' theory) which is also what is observed for the single jet, but at supercritical chamber pressures. This suggests that under such a condition the outer jet in Chehroudi's coaxial injector grows similar to a variable-density gaseous jet. Coaxial data, although stays nearly at a constant value, departs from the rest in this figure as chamber pressure is raised towards the supercritical condition.

5. Coaxial Jets with External Excitation

Cold flow studies investigating the interaction of acoustic waves with single-jet injectors have recently been extended

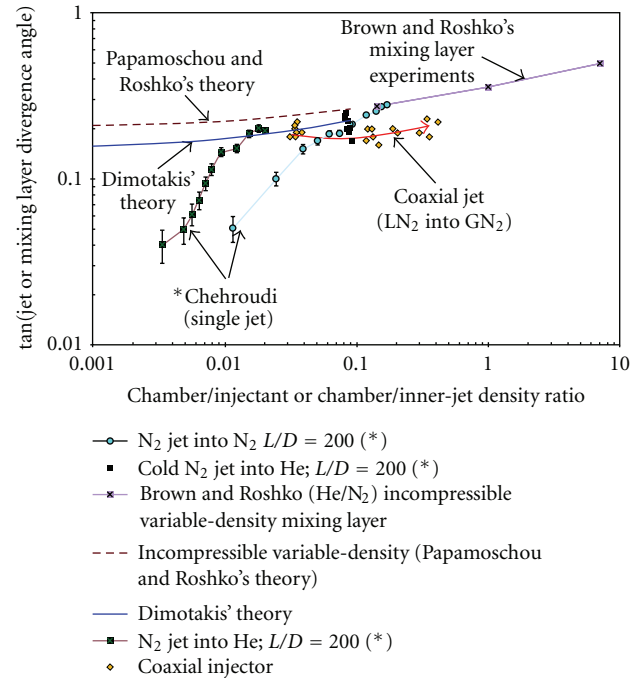


FIGURE 25: Spreading rate of the shear layer versus the chamber/injectant or chamber/inner-jet density ratio for single and coaxial jets compared with different predictions for planar shear layers. For the coaxial data, the chamber pressure increases from sub- to near- and to supercritical conditions in the direction of the arrow.

to include coaxial injectors by Chehroudi et al. [51], Davis and Chehroudi [42] and Leyva et al. [52]. Their objective was to characterize the coaxial jets response and understand how nonreacting injector results are related to historical liquid rocket engine combustion instability data. As it will be shown in the next few paragraphs, the aforementioned observation that the single-jet interaction with the externally imposed acoustic waves was stronger at subcritical pressures than at supercritical pressures appears to remain generally true for the coaxial-jet injector as well, although some influences of the mass flow ratio and initial temperature were observed. Efforts by Chehroudi's group continue in order to better understand how various parameters control the coupling mechanisms.

Figure 26, taken by Davis and Chehroudi [42], shows a sample of ten consecutive images at sub- (rows one and two from top), near- (rows three and four), and supercritical (rows five and six) chamber pressures from a LN₂/GN₂ coaxial injector. Rows one, three, and five are when the acoustic driver was off and the remaining ones are when it was activated at ~3 kHz. The evolution of the jet in time is from left to right in this figure and the time interval between frames is about 55.6 μs. Prominent in all images of the jet is the existence of a dark central region. After close examination of many images at different magnifications, Davis and Chehroudi [42] reported that the dark core under the unexcited subcritical pressures (Figure 25, row one) can be approximated as a cylinder-like structure with unstable

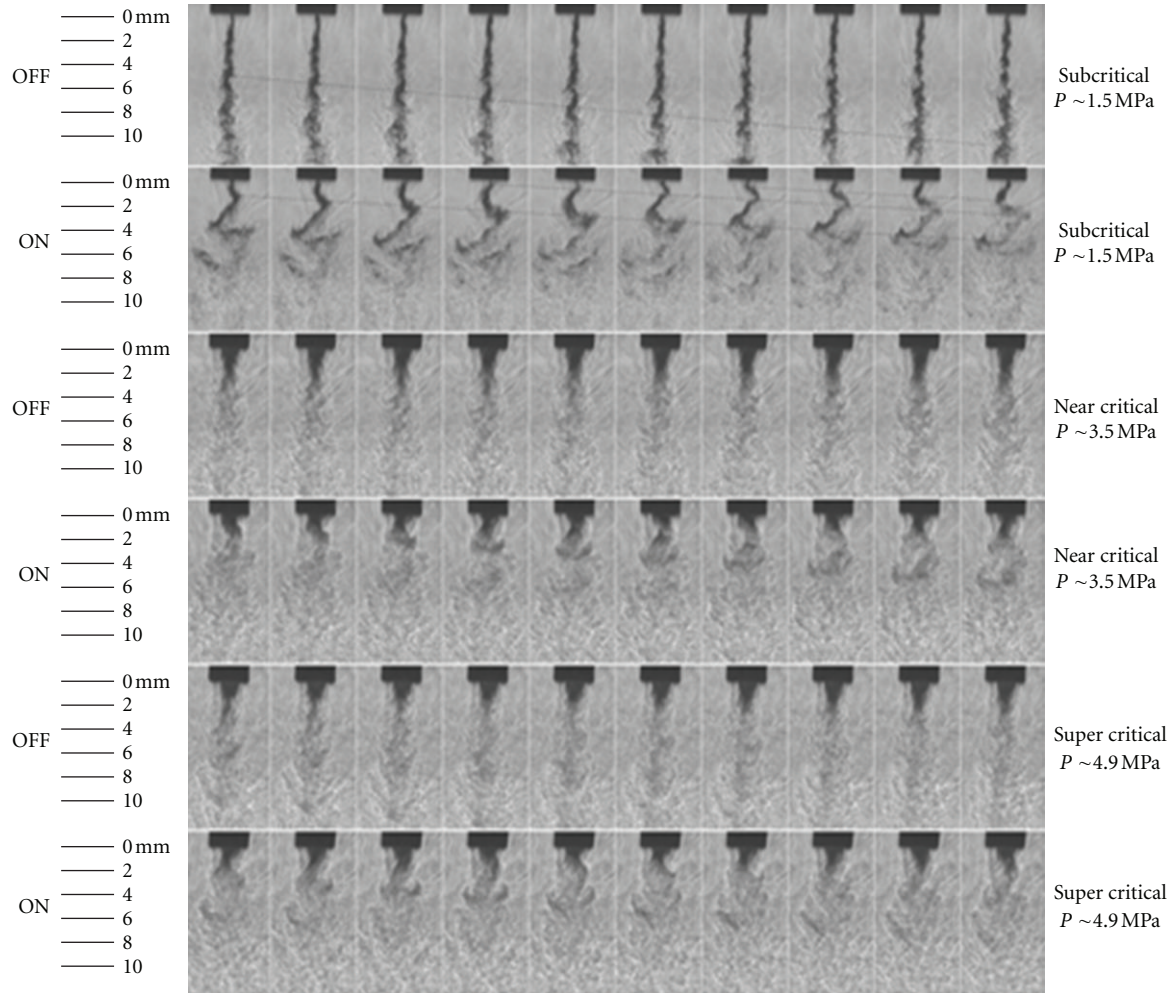


FIGURE 26: Consecutive frames from high-speed shadowgraph movies of a coaxial injector (LN_2/GN_2 into N_2 -filled chamber) with the acoustic driver turned off (in rows 1, 3, and 5) and on (in rows 2, 4, and 6) at ~ 3 kHz. Time increases from left to right with an interval of 55.6 ms between frames. The first two rows are at a subcritical chamber pressure (~ 1.5 MPa), the third and fourth rows are at a near-critical chamber pressure (~ 3.5 MPa), and the fifth and sixth rows are at a supercritical chamber pressure (~ 4.9 MPa). The acoustic driver is turned off for the first, third, and fifth rows and on for the second, fourth, and sixth at ~ 3 kHz. The light gray lines in the first and second rows connect fluid structure as they evolve in time. Davis and Chehroudi [42].

surface waves of low amplitudes. However, when they increased the chamber pressure to near- and supercritical pressures (rows three and five), the dark-core length became shorter (as indicated earlier) and the structure changed to a more conical shape near the injector exit area. The conical structure of the dark core has been reported before for single-phase coaxial jets by Lasheras and Hopfinger [53] but not at supercritical conditions.

Excitation of the jet with an acoustic driver yielded significantly different behavior of the dark core compared to that of the unexcited one. The strongest effect was observed under subcritical pressures and made clear in Figure 26. Note that the direction of the acoustically induced velocity oscillations is horizontal (towards left and right) in images presented in Figure 26. It is seen that the core of the jet forms large-scale sinusoidal structures as a result of this imposed velocity field oscillations. From the movies

they acquired, Davis and Chehroudi [42, 43] explained an observed dominant pattern which is also shown in Figure 26. They said that as a piece of fluid left the injector tip, the momentum from the acoustically induced motion caused a transverse displacement pushing the core of the jet into the higher-speed annular jet area. Then the dense fluid from the core experienced acceleration in the axial direction, which was caused by the high-speed annular jet motion. Upon reversal of the acoustic field, the dense fluid, which was initially from the core but now in the high-speed annular flow, appeared to maintain its transverse component of the momentum imparted upon leaving the injector and hence the dense fluid particle did not reverse its direction. The dense fluid parcel then slowed (both in the axial and transverse directions) as it arrived at the shear layer between the outer jet and the chamber fluid farther downstream, where a “cusp-shaped” structure was formed from the dense

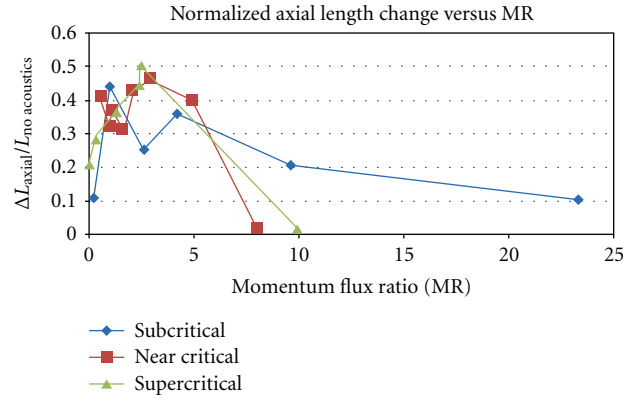


FIGURE 27: Maximum length change between dark-core length without acoustics and dark-core length with acoustics (ΔL_{axial}) divided by the dark-core length without acoustics ($L_{no\ acoustics}$) for each momentum flux ratio case. Results for a coaxial injector. Rodriguez et al. [54].

fluid originating in the core of the jet. Subsequent mixing and heat transfer from the outer-jet to the inner-jet core fluid ultimately cause the fluid parcel to be indistinguishable from the outer-jet fluid.

Figures 23(a) and 24(a) also show the impact of the outer-jet-to-inner-jet velocity ratio (V_r) on the mean dark-core length at three different chamber pressures but under externally imposed acoustic excitation. On an average, when the dark core feels the imposed external acoustic field, its length is shorter than or equal to that when the acoustic driver is turned off. At the near-critical and supercritical chamber pressures, as the V_r increases, the difference between the lengths of the dark core, measured with and without the acoustic field, diminishes. One distinct feature of plots in Figures 23(b) and 24(b) is that, at any given velocity ratio, the RMS of the core fluctuations under subcritical condition is much higher than near- and, particularly, super-critical conditions. And equally important, is that this statement is true with or without the externally imposed acoustic excitation field. Using Davis and Chehroudi's [42, 43] interpretation of the RMS, it appears that the jets under supercritical conditions are more *inherently insensitive* to their environment even when an acoustic field is imposed. Another important feature here is the fact that the magnitude of this RMS of fluctuations drastically declines for all cases, more so for the subcritical case, when velocity ratio is increased. Implications of these unique and important observations for the combustion instability in liquid rocket engines are provided later in this writing.

Rodriguez et al. [54] initiated a set of experiments to analyze the impact of the transverse acoustic wave phase variations on the magnitude of the inner-jet dark-core length. The chosen coaxial jet was exposed to different acoustic conditions by varying the phase between two acoustic sources which faced each other while the jet was located at the midpoint between the two sources, all being inside a high-pressure chamber. The coaxial jet was exposed to a subcritical and a near-critical pressure environment. The measurements were performed on backlit images of the

coaxial jet obtained with a high-speed camera. The outer-jet-to-inner-jet momentum flux ratio was varied from 1 to 20 for subcritical conditions and from 0.6 to 5 for near-critical conditions. The resonant frequency of the system was approximately 3 kHz and the maximum pressure variation with respect to total pressure was 3%. Figure 27 shows summary of their results. This figure presents the maximum dark-core length reduction between the case without the external acoustics and that with the acoustics for all phase angles, each normalized with the core length without the acoustics and then plotted as a function of M (momentum flux ratio). The analysis of this data showed a reduction of this length with acoustic excitation within the momentum flux ratio (M) range between 1 and 5 for all chamber pressures, except at the subcritical which extended up to M value of 10. The effect of the acoustic waves at lower or higher M values did not have significant influences on the behavior of the dark-core length.

Rodriguez [55] also examined effects of the injector geometry, specifically the impact of the inner-tube wall thickness on the jet behavior and its interaction with the acoustic field. A new injector design was considered with a thinner inner-tube wall thickness value which consequently produced an inner jet with larger diameter than the original one used in earlier studies. The highest reduction in the dark-core length for the tests with the new coaxial injector geometry took place at moderate M values which supports similar evidence obtained with the original injector possessing a larger inner-tube wall thickness. The results for the new injector also showed that for a given outer-to-inner jet momentum flux ratio, the normalized values of the dark core length between subcritical and nearcritical cases agree reasonably well.

6. Impinging Jets

To the best of this author's knowledge, there is only one impinging jet data set reported under both sub- and supercritical conditions; see Chehroudi [56]. However, the study conducted by Anderson et al. [57] is an example at

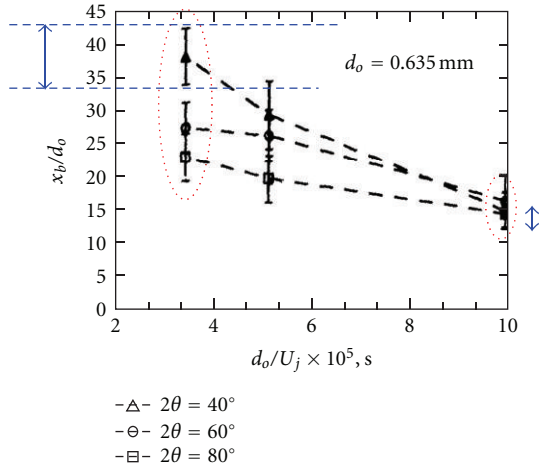


FIGURE 28: This figure shows *sheet break-up length* for an impinging injector as a function of instability parameter at three different impingement included angles. Much higher sensitivity of the *sheet break-up length* is seen with included angle (2θ) at low dn/V ($= d_o/U_j$, in the original article) values. Anderson et al. [57].

high-pressure subcritical chamber conditions which is of relevance to the discussion in this section.

Figures 28 and 29 taken from Anderson et al.'s [57] studies show measured data for the *sheet break-up length* in a doublet impinging jet injector design plotted against injector-hole-diameter (dn)-to-injection-velocity (V) ratio, that is, dn/V . The dn/V ratio is also called the *stability parameter*. This is because of the dependency of the rocket engine stability region (using this type of injector design) with the dn/V ratio. Large differences between the sheet break-up lengths for different pressures and different impinging-jet included angles (2θ) at low values of the stability parameter are seen in Figure 29. For example, Figure 29 strongly suggests higher sensitivity of the injector when dn/V is reduced through an increase in V (injection velocity) values. This is simply deduced by the enlarged size of the scatter bounds at any given pressure and sensitivity to pressure changes at low dn/V values. Although strictly speaking one should have its frequency response (amplitude and phase) measured, Chehroudi [56] interpreted these results as an indication of injector hypersensitivity under such conditions. At a given pressure or included angle, the *data scatter band* shown in Figures 28 and 29 is also largest at low dn/V values, again and consistently suggesting a more erratic/chaotic dynamic behavior.

The changes in the dark-core (break-up) length were also reported in Figure 30 by Chehroudi [56], showing a progressive increase in chamber pressure up to a supercritical condition for liquid nitrogen injection into gaseous nitrogen environment with no externally imposed acoustic field. The long preimpingement length seen along the jet is expected due to L/dn of about 100 which was intentionally designed to obtain a fully developed condition at the hole exit plane and also to accentuate the effects of chamber pressure on the nature of the impingement. Obviously, shorter dark core

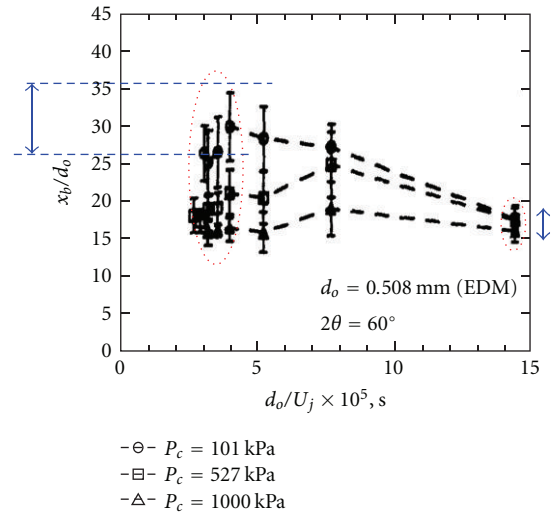


FIGURE 29: This figure shows *sheet break-up length* for an impinging injector as a function of instability parameter at three different chamber pressures. Much higher sensitivity of the *sheet break-up length* is seen with chamber pressure at low dn/V ($= d_o/U_j$, in the original article) values. Anderson et al. [57].

is achieved for lower (injector hole) L/dn values used in LRE. It is observed that not only the dark-core length of each individual jet is reduced as supercritical pressures are approached (as before and as expected), but the jet also thickens during this process. Clearly each jet is going through a very similar process discussed earlier in the context of single jet discussion. However, there are important implications as a result of such anatomical changes in an impinging injector which will briefly be discussed in the final part of this paper.

Aside from these results, the author is not aware of any published impinging jet data of relevance under supercritical chamber conditions. The situation is even worse as no systematic investigation or results are available on the impact of external excitation (imposed acoustic field) on impinging-jet injectors.

7. Implications for Combustion Instability

From the review of recent studies presented here, it is clear that our understanding of the jet behavior under transcritical and supercritical conditions has substantially improved in the past 20 years primarily due to pioneering experimental studies reviewed here. Computer simulations have also contributed heavily in the understanding and design process but are not within the scope of this short review. While experimental results have been very valuable for simulations and provided physics-based improvements in computational efforts, the implications of these results towards formulating “a big-picture” and efforts in constructing such an image through synergies amongst these pieces of information were needed and are just beginning. One relevant sketch of this *big picture* this author knows is that attempted by Chehroudi [56]. He, in his work, has made an effort to collect pieces of experimental information and offered a compelling

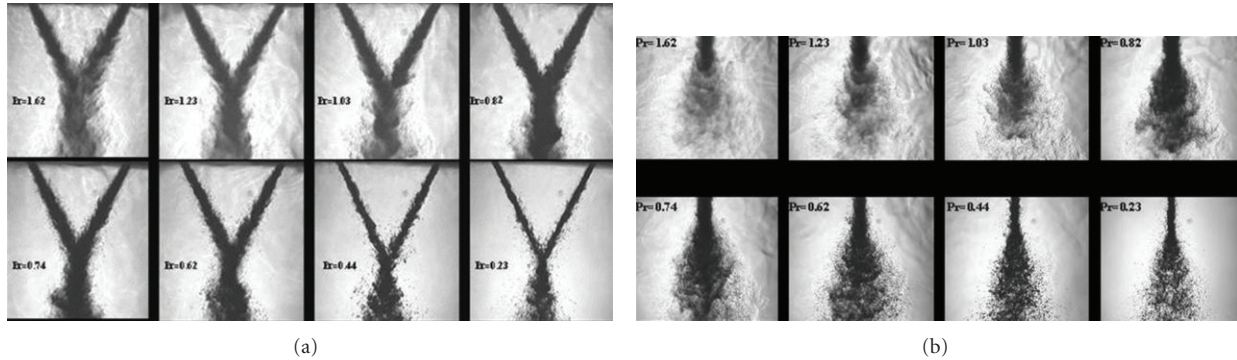


FIGURE 30: Instant images of sub-, near-, and supercritical impinging jets for LN_2 into GN_2 (room temperature) injection by Chehroudi. The last two rows show the same injector in the first two rows but viewed at a 90-degree angle. $P_{\text{ch}} = 0.8, 1.5, 2.1, 2.5, 2.8, 3.5, 4.2, 5.5$ MPa; from lower right to upper left, $P_{\text{ch}} = 100, 200, 300, 350, 400, 500, 600, 800$ psig. For nitrogen: $P_{\text{critical}} = 3.39$ MPa; $T_{\text{critical}} = 126.2$ K. $\text{Re} = 25,000$ to $70,000$; holes' length-to-diameter (L/d_n) of ~ 100 ; no cavitation; injection velocity: $10\text{--}15$ m/s. Chehroudi [56].

argument to link nonreacting cold-flow studies (in test rigs) to fired subscale engine information and to what occurs in production engine in the context of combustion instability. Of course, as the history of scientific discovery testifies, such efforts are mostly evolutionary in nature and, while they approach full understanding in time, are incomplete in every step taken. Nevertheless, they are important in order to continuously improve the “sketch” and hopefully soon converge to a colorful big picture. Therefore, in this section, the work by Chehroudi [56] published in such a context is summarized to present a sample of an important attempt to tackle the problem through placement of pieces of jigsaw puzzle. But before doing so, a concise description of the combustion instability in liquid rocket engine is offered to provide a context and sufficient background for Chehroudi's work.

Acoustic combustion instability has been one of the most complex phenomena in liquid rocket engines and therefore difficult to fully understand, control, and predict particularly in the design of high-power rockets. The difficulty arises from the emergence of oscillatory combustion with rapidly increasing and large pressure amplitudes. This leads to local burnout of the combustion chamber walls and injector plates which is caused through extreme heat-transfer rates by high-frequency pressure and gas velocity fluctuations; see Harrje and Reardon [58] and Yang and Anderson [59]. It is thought that resonance acoustic modes of the thrust chamber, amongst them the transverse modes being the most troublesome, are excited through the energy provided by the combustion. The amplification process is thought to include a feedback of information from the acoustic field to the injector or near-injector phenomena which in turn tends to reinforce the combustion-to-acoustic-field energy transfer processes.

This energy transfer reasoning alone is the widely cited general principle by Lord Rayleigh [60]. In essence, he made a phasing argument and stated that the interaction between the combustion heat release and the acoustic field is the strongest if heat is added in a region of space and at the time when the acoustic amplitude is the highest.

Although this view has been useful to understand a part of the big picture, evidences gathered by past investigations attributed combustion instability to a complex interaction of the external acoustic field with the fuel injection or near-injector processes as a feedback mechanism, thereby leading to incidences of instability in rocket engines. See, for example, Heidemann and Groeneweg [61], Anderson et al. [57], and Hulka and Hutt [40]. For this and other reasons, controlled studies have been conducted probing into the effects of acoustic waves on gaseous and liquid jets from a variety of injector hole designs. A series of investigations concentrated on disturbances induced from within the injection system. They considered the effects of acoustic fields on many phenomena such as flow structure, vortex pairing, and shear layer growth rate in the initial region of the jet (e.g., see a short review article by Kiwata et al. [62]). More relevant to the work reported here are a few reports and articles on gaseous and (in particular) liquid jets under the influence of external (transverse and longitudinal) acoustic fields. The experimental work under high-pressure supercritical condition has already been reviewed here. More information on this and others can be found in Chehroudi and Tally [39] and Davis and Chehroudi [42, 43].

In Davis and Chehroudi's [63, 64] experimental work on a cryogenic nonfired coaxial injector at sub- and supercritical pressures, they have offered a plausible explanation of why in temperature ramping stability rating exercises an engine becomes unstable. In such tests, which are usually conducted in LOX/H_2 cryogenic liquid rocket engines (LRE), they proposed that a progressive reduction of the propellant (H_2) temperature decreases the outer-to-inner jet velocity ratio for shear coaxial injectors and therefore pushes the engine into an unstable operating zone. As indicated earlier, this velocity ratio was found to be a key parameter defining the stability of the engine; see Hulka and Hutt [40]. But what this velocity ratio does to the jet itself and how the connection to combustion instability comes about are explained in the next paragraph. Moreover, in Chehroudi's work, in which an externally imposed acoustic field was used to simulate certain key aspects of their interaction in real engines, it was shown

that at subcritical conditions the root mean square (RMS) fluctuation values of the dark-core length were much higher than those at near-critical and supercritical conditions by a factor of 4 to 6 at all velocity ratios; see Figures 23(b) and 24(b). Also, as the outer-to-inner jet velocity ratio declined, the RMS value increased from 1-2 to values of about 7-8 inner-jet hole diameters at subcritical pressures.

Chehroudi [56] interpreted the RMS of the dense dark core as a reflection of mass fluctuations to a first-order approximation; combining it with measurements of a core dominant oscillation frequency consistent with the imposed acoustic field's resonant mode frequency, he then suggested that a connection to rocket combustion instability may be obtained from these data through examination of the RMS of the dark-core length fluctuations. Decreases in the dark-core length fluctuation levels (quantified through the RMS) were then interpreted as the *reduced intrinsic sensitivity* of the jet. Chehroudi [56] then stated the possibility that decreases in the dark-core length fluctuation levels could weaken a key feedback mechanism for the self-excitation process that is believed to drive the combustion instability in cryogenic LRE. This was offered as a possible explanation for the combustion stability improvements experienced in production engines under higher outer-to-inner jet velocity ratios (see also Figures 23 and 24). The effect of temperature ramping was linked to its impact on the outer-to-inner velocity ratio and hence was also explained. More details can be found in Davis and Chehroudi [63, 64], Davis [44], and Leyva et al. [65]. In other words, *the dynamic behavior of the dark-core, specifically its axial length, was considered by Chehroudi [56] to be the culprit for coaxial jet injectors.*

Chehroudi [56] has then compared some of his results (from nonreacting test rigs) with those taken in single-element fired rocket engines and demonstrated consistency of results pertaining to the dark-core dynamics. For example, he noted that measured mean intact or dark-core length for SSME-like momentum flux ratios by Woodward et al. [66] in a LOX/GH₂-fired single-element rocket engine agreed with those of Davis and Chehroudi's [63, 64] nonreacting case. Additionally, Chehroudi [56] referred to the existence of the dark-core length fluctuations reported by Woodward et al. [66]. He also pointed at a recent work by Yang et al. [67] in which they performed tests in a fired single-element rocket equipped with a coaxial LOX/CH₄ injector. Their measurements of the dark core length indicated an increasing trend in the level of fluctuations when the outer-to-inner velocity ratio was decreased and the core oscillation spectra showed more high-frequency contents in jet oscillation at lower velocity ratios. Finally, Chehroudi [56], by referring to the work of Smith et al. [68] where subcritical-to-supercritical sweeps were carefully conducted in a fired rocket engine, indicated that very low RMS values of the dark-core length at near- and super-critical conditions and high RMS values at subcritical pressures, both measured by Davis and Chehroudi [63, 64] in their *nonreacting* experimental setup, were consistent with the *fired-engine* experimental observations by Smith et al. [68]. Hence, Smith et al. [68]'s reported unstable combustion behavior at subcritical pressures with high core unsteadiness correlates with Davis

and Chehroudi's high RMS values at subcritical conditions, which was then interpreted as conditions leading to highly "sensitive" dark-core dynamic response to its surrounding. In short, Chehroudi indicated that these results in such fired engines were consistent with the Davis and Chehroudi [63, 64] conclusions cited above.

Leveraging the observation that some of the key findings in cold nonreacting jets were consistent with subscale fired rocket engine, all using coaxial injectors, Chehroudi [56] then attempted to employ these, particularly the single-jet's, information to offer a compelling argument in addressing the combustion instability in engines using impinging-jet injector designs. Whereas RMS of the core fluctuations was a key factor for coaxial injectors, Chehroudi [56] proposed that both the mean and RMS of the dark core fluctuations in each jet of an impinging-jet injector were key parameters.

On the engine side, Chehroudi [56] used the information that when the so-called stability parameter (dn/V) was reduced in production engines possessing impinging-jet injectors, combustion instability emerged at some point within this change. This stable-to-unstable transition boundary has been discussed in details by Anderson et al. [57] and is referred to as the Hewitt correlation. To offer a possible explanation, Chehroudi [56] had to propose a hypothesis (explained in the next paragraph) which although intuitively acceptable, requires further verification. However, he, by using data from impinging-jet injector designs in production engines and the dark-core lengths measured from single jets reported here (Figure 9), was able to provide some initial support for the hypothesis. Next, the hypothesis itself and some of his supporting information are explained.

For example, Chehroudi [56] showed that a reduction in the dn/V (stability parameter) through changes in either dn or V leads to shortening of the mean dark-core (or break-up) length for each jet in an impinging jet injector. He then stated that it was quite possible that as dn/V was reduced in an engine, the mean dark core length reached a critical value ($L_{C,Ph}$) where one intuitively expects *inherently high sensitivity (high RMS)* for an impinging-jet injector "system" to its environmental acoustic field. *Here, Chehroudi [56] hypothesized that the Hewitt stable-to-unstable transition point (or line), which is usually observed as dn/V is reduced, was at or near a condition where the distance from the holes exit plane of the impinging injector to the impinging point (i.e., pre-impingement length) reached a critical value ($L_{C,Ph}$), creating a situation somewhat similar to what is shown in Figure 31.* The arrangement shown in this figure was considered to be most sensitive to the ambient acoustic field. Chehroudi [56] also demonstrated that a situation shown in Figure 31 could easily take place in the thrust chamber of production engines during operation considering typical geometrical dimensions of impinging jet injectors for these engines. He also provided experimental evidence by Anderson et al. [57] (Figures 28 and 29) from tests of nonreacting impinging jets conducted at elevated chamber pressures suggesting high level of sensitivity for the arrangement shown in Figure 31.

Considering what was discussed for the coaxial jet injector, one implication of the hypothesis Chehroudi proposed is that an impinging jet injector engine should be more

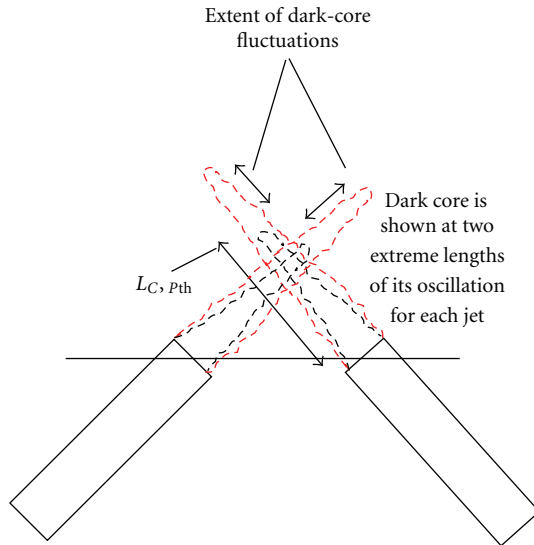


FIGURE 31: This figure shows the extent of the dark-core (or break-up) length fluctuations for individual jets of an impinging injector design for a situation when the average length ($L_{C,Pth}$) is of the same order as (or less than) the distance from each hole to the impinging point. Chehroudi [56].

stable at sufficiently high pressures, such as supercritical conditions. This is because not only the RMS of the core length fluctuations declines substantially (see Figures 23(b) and 24(b)), but also the length of the core may become adequately shorter than the pre-impingement length depending on the geometrical dimensions of the impinger. The changes in the dark-core (break-up) length can also be inferred by examination of Figure 30, showing a progressive increase in chamber pressure up to a supercritical condition for liquid nitrogen injection into gaseous nitrogen environment with no externally imposed acoustic field. The long pre-impingement length seen along the jet is expected due to L/d_n of about 100 which was intentionally designed to obtain a fully developed condition at the hole exit plane and also to accentuate the effects of chamber pressure on the nature of the impingement. Obviously, shorter dark core is achieved for lower (injector hole) L/d_n values used in LRE. Not only the dark core length of each individual jet is reduced as supercritical pressures are approached (as before and expected), but the jet also becomes thicker. The impinger is expected to pass through a situation described in Figure 31 as chamber pressure is increased. Hypersensitivity is anticipated at that condition according to Chehroudi's hypothesis. Progressive increase of chamber pressure beyond this point sufficiently thickens each jet and shortens the dark-core length to a situation where the two dark-core lengths are shorter than the preimpingement distance and a gas-like jet is impinging another gas-like jet with enlarged cross-section areas. Based on Chehroudi's hypothesis and given that RMS of the dark core is much lower at supercritical than subcritical conditions, a more robust (targeting and mixing) and less sensitive impinging jet system would be expected at supercritical chamber pressures. However, it is likely that

the dynamic behavior of the *potential core* plays a somewhat similar but weaker role under this latter gas-like condition.

Chehroudi's [56] attempt should be considered as the first step, but an important one, towards construction of a "big picture" through linkage of the increasing amount of experimental information made available. Essentially he was able to connect pieces of information from nonreacting test rigs, fired subscale engines, and production engines to provide an initial sketch. The sketch proposed by Chehroudi [56] has the advantage, simplicity, and the beauty as well, of identifying the possible weak link in the combustion stability assessment regardless of the design of the injector at least for the two popular cryogenic impinging and coaxial cases described. Much, of course, remains to be investigated, amongst them is the close examination of the historical data on the *dynamic characteristics* of the dark-core (or break-up) length and width for the circular jets forming the impinging injector for the propellant of interest and under the realistic thrust chamber conditions (which are quite rare or nonexistent) to further substantiate that a critical value, $L_{C,Pth}$, is reached when the onset of instability is detected in an engine. Also, the *dynamic* characterization of each jet forming the impinging injector and when the two jets meet, in the presence of an externally imposed acoustic field, is highly desirable to assess sensitivity of the dark-core or break-up length of the jet to relevant design and operating variables.

8. Conclusions

It is evident from this relatively short and targeted review that much has been learned on jet breakup and relevant processes involved in cryogenic liquid propellant injection into high-pressure supercritical condition over the past twenty years. In a quest to understand coaxial jet injectors used in H_2/O_2 cryogenic liquid rocket engines, systematic research efforts have been initiated which consider a logical progression from single jet injected into a quiescent environment to such jets under externally imposed acoustic field and to coaxial injectors with and without acoustic forcing, all under nonreacting conditions.

It is now clear that the impact of progressively lowered surface tension, as environmental pressure approaches the injectant's critical pressure from subcritical and exceeds to supercritical condition, suppresses classical liquid breakup and drop/ligament formation processes and a gas-like jet behavior emerges at or above the critical pressure of the injectant. It is also shown, quantitatively, and for the first time by Chehroudi's group that single liquid jets injected into a supercritical pressure and temperature behave similar to variable-density incompressible jets in visual growth rate. The gas-like nature of these single jets under such conditions has also been demonstrated through fractal analysis of the injected jet boundary. Based on physical arguments and visualizations, an effective model, and the only one known to this author, for the growth rate of such jets was proposed by Chehroudi, a model which mimics the experimental data quite well from sub- to supercritical chamber pressures and for different fluids.

Visual length scales were measured which suggest conformance with the Taylor microscale. The Raman scattering measurements were conducted both for density profiles and growth rates. Based on this information, relationships between the same jet parameters when measured by shadowgraphy and by the Raman scattering were established. Similarity behavior in the radial density profile was demonstrated for the near- and super-critical single jets when the gas-like appearance emerged. Jet growth rates under supercritical pressures, as identified by density profiles, showed tendency to converge with those extrapolated for gaseous jets near the injector exit plane. Temperature estimates from the Raman data suggested existence of a pseudo-boiling behavior when the injection temperature is below the pseudo-boiling line at which the fluid-specific heat becomes very large (mathematical infinity). When the injected liquid possessing temperatures below the pseudo-boiling line warms up under supercritical chamber pressures, it eventually reaches this line, at which time most of the absorbed heat is taken up by the large specific heat value of the fluid, thus exhibiting a pseudo-boiling behavior.

Dark-core length dynamics of cryogenic single jets injected into both sub- and super-critical conditions were measured and compared with those of liquid fuel sprays and single-phase jets. At subcritical conditions, larger fluctuations of this length were reported than those under supercritical chamber pressures. Investigations on the response of the single jets to externally imposed acoustic waves indicated high sensitivity of the jet at subcritical pressures which then substantially diminished at supercritical pressures. Such a lack of response or jet's inherent insensitivity at supercritical pressures was explained through comparison with results extracted from similar studies conducted on single-phase (liquid and gaseous) jets.

Coaxial-jet studies revealed the existence of a dark core originating from the central hole exit area, similar to the single-jet case, but for the coaxial case it was surrounded by a cushion of the outer jet promoting liquid atomization at subcritical and mixing at supercritical pressures. The dark core interface assumed the appearance of a gaseous jet again under supercritical conditions similar to what was observed in a single-jet case. However, the possibility of delay in such a transition exists depending on the solubility of the inner jet and the critical mixing condition.

The mean dark-core length measurements in coaxial injectors with no externally imposed acoustic field exhibited a dual-character behavior depending on whether it experienced subcritical or supercritical chamber pressures. Results for the LN_2 injection to GN_2 were compared with a vast number of pertinent cases from single-phase gaseous and liquid flows to two-phase flows and found that the dark-core length scales with the outer-to-inner jet momentum flux ratio to the power of -0.2 , for the subcritical, and to -0.5 for supercritical pressures. Interestingly, as outer-to-inner jet momentum flux ratio approaches zero (i.e., turning into a single jet), the dark-core length approaches values corresponding to the single-jet measurements. The growth rate for the coaxial jets, as measured by the visual spreading angle of the outer (GN_2) jet, agreed with that of supercritical

pressures measured for the single jet but then declined below this value as one approached the supercritical pressures.

The impact of the external acoustic forcing on the coaxial jet was seen to be the highest at the subcritical pressures, similar to the single jet and substantially declined when reaching critical and supercritical chamber pressures. Effects of increases in outer-to-inner jet velocity ratio, an important design parameter for stable engine operation and recommended to be greater than 10, were seen to dramatically reduce the mean dark-core length at subcritical pressures while having a minimal impact on this length under supercritical pressures. The dynamic behavior of the core was examined by measurements of the RMS of the core length fluctuations and interpreted as a factor influencing or contributing towards the propellant mass flow oscillations in a rocket thrust chamber. This too behaved very similar to the dark-core length mean value and was distinctively much higher at subcritical pressures than any others. This RMS behavior was then used to offer possible explanations for the empirical observation that stable engine operation required higher outer-to-inner jet velocity ratios (greater than about 10) and also for temperature ramping stability rating tests. Finally, for the injector used, the overall impact of the acoustic field was seen to be important only within a certain region of momentum flux ratios from about 1 to 5.

Implications of a subset of these results were discussed in the context of the rocket combustion instability. Essentially, evidences were shown which suggest that the RMS of the dark-core length and its mean value are important for dynamic behavior of an impinging jet injector. It appears that for the coaxial jets, only RMS values are of relevance in this context.

A hypothesis was proposed that associates the stable-to-unstable transition border in the Hewitt stability plot (for liquid rockets using impinging jets designs) to an event which is defined as an arrangement seen at a moment when the mean core length of one or more of the single jets in an impinging-jet injector design reaches the pre-impingement distance. Some evidences were presented in support of this hypothesis. Essentially, a new alternate and compelling explanation for the Hewitt transition border was offered.

References

- [1] T. J. Bruno and J. F. Ely, *Supercritical Fluid Technology: Review in Modern Theory and Applications*, CRC Press, 1991.
- [2] R. S. Lazar and G. M. Faeth, "Bipropellant droplet combustion in the vicinity of the critical point," in *Proceedings of the 30th Symposium (International) on Combustion*, p. 801, The Combustion Institute, 1971.
- [3] A. Umemura, "Supercritical droplet gasification combustion," in *Proceedings of the IUTAM Symposium on Theories Combustion on Droplets and Sprays*, Taiwan, December 1994.
- [4] J. A. Newman and Brzustowski, "Behavior of a liquid jet near the thermodynamic critical region," *AIAA Journal*, vol. 9, no. 8, pp. 1595–1602, 1971.
- [5] B. Chehroudi, D. Talley, and E. Coy, "Initial growth rate and visual characteristics of a round Jet into a sub- to supercritical

- environment of relevance to rocket, gas turbine, and diesel engines,” in *Proceedings of the 37th AIAA Aerospace Science Meeting and Exhibit*, Reno, NV, USA, January 1999, AIAA 99-0206.
- [6] W. Mayer, A. Schik, C. Schweitzer, and M. Schaffler, “Injection and mixing processes in high pressure LOX/GH₂ rocket combustors,” in *Proceedings of the 32nd AIAA/ASME/SAE/ASEE Joint Propulsion Conference & Exhibit*, Lake Buena Vista, Fla, USA, 1996, AIAA Paper no. 96-2620.
- [7] R. D. Reitz and F. B. Bracco, “On the dependence of spray angle and other spray parameters on nozzle design and operating condition,” in *Proceedings of the SAE International Congress and Exposition*, Detroit, MI, USA, February-March 1979, SAE Paper no. 790494.
- [8] W. Mayer, A. Ivancic, A. Schik, and U. Homung, “Propellant atomization in LOX/GH₂ rocket combustors,” in *Proceedings of the 34th AIAA/ASME/SAE/ASEE Joint Propulsion Conference & Exhibit*, Cleveland, Ohio, USA, July 1998, Paper no. 98-3685.
- [9] A. Roy and C. Segal, “Experimental study of subcritical to supercritical jet mixing,” in *Proceedings of the 47th AIAA ASM Meeting, Paper AIAA-2009-809*, Orlando, Fla, USA, January 2008.
- [10] B. Chehroudi, D. Talley, and E. Coy, “Visual characteristics and initial growth rates of round cryogenic jets at subcritical and supercritical pressures,” *Physics of Fluids*, vol. 14, no. 2, pp. 850–861, 2002.
- [11] C. J. Chen and W. Rodi, *Vertical Turbulent Buoyant Jets: A Review of Experimental Data*, Pergamon Press, 1980.
- [12] P. N. Papanicolaou and E. J. List, “Investigations of round vertical turbulent buoyant jets,” *Journal of Fluid Mechanics*, vol. 195, pp. 341–391, 1988.
- [13] R. Branam and W. Mayer, “Characterization of cryogenic injection at supercritical pressure,” *Journal of Propulsion and Power*, vol. 19, no. 3, pp. 342–355, 2003.
- [14] G. N. Abramovich, *The Theory of Turbulent Jets*, MIT Press, Cambridge, UK, 1963.
- [15] G. L. Brown and A. Roshko, “On density effects and large structure in turbulent mixing layers,” *Journal of Fluid Mechanics*, vol. 64, no. 4, pp. 775–816, 1974.
- [16] G. Brown, “The entrainment and large structure in turbulent mixing layers,” in *Proceedings of the 5th Australian Conference on Hydraulics and Fluid Mechanics*, pp. 352–359, 1974.
- [17] D. Papamoschou and A. Roshko, “The compressible turbulent shear layer: an experimental study,” *Journal of Fluid Mechanics*, vol. 197, pp. 453–477, 1988.
- [18] P. E. Dimotakis, “Two-dimensional shear-layer entrainment,” *AIAA Journal*, vol. 24, no. 11, pp. 1791–1796, 1986.
- [19] C. D. Richards and W. M. Pitts, “Global density effects on the self-preservation behaviour of turbulent free jets,” *Journal of Fluid Mechanics*, vol. 254, pp. 417–435, 1993.
- [20] B. Chehroudi, R. Cohn, D. Talley, and A. Badakhshan, “Raman scattering measurements in the initial region of sub- and supercritical jets,” in *Proceedings of the 36th Joint Propulsion Conference*, Huntsville, AL, USA, 2000, AIAA 2000-3392.
- [21] M. Oswald and M. M. Micci, “Spreading angle and centerline variation of density of supercritical nitrogen jets,” *Atomization and Sprays*, vol. 12, no. 1–3, pp. 91–106, 2002.
- [22] B. B. Mandelbrot, *The Fractal Geometry of Nature*, W. H. Freeman and Company, San Francisco, Calif, USA, 1983.
- [23] K. R. Sreenivasan and C. Meneveau, “The fractal facets of turbulence,” *Journal of Fluid Mechanics*, vol. 173, pp. 357–386, 1986.
- [24] J. J. Taylor and J. W. Hoyt, “Water jet photography—techniques and methods,” *Experiments in Fluids*, vol. 1, no. 3, pp. 113–120, 1983.
- [25] B. Chehroudi, D. Talley, and E. Coy, “Fractal geometry and growth rate of cryogenic jets near critical point,” in *Proceedings of the 35th AIAA/ASME/SAE/ASEE Joint Propulsion Conference*, Los Angeles, Calif, USA, June 1999, AIAA Paper 99-2489.
- [26] B. Chehroudi and D. Talley, “The fractal geometry of round turbulent cryogenic nitrogen jets at subcritical and supercritical pressures,” *Atomization and Sprays*, vol. 14, no. 1, pp. 81–91, 2004.
- [27] B. Chehroudi, S.-H. Chen, F. V. Bracco, and Y. Onuma, “On the intact core of full-cone sprays,” SAE Transaction 850126, 1985.
- [28] M. Oswald and A. Schik, “Supercritical nitrogen free jet investigated by spontaneous Raman scattering,” *Experiments in Fluids*, vol. 27, no. 6, pp. 497–506, 1999.
- [29] I. Wygnanski and H. E. Fiedler, “The two-dimensional Mixing region,” *Journal of Fluid Mechanics*, vol. 41, no. 2, pp. 327–361, 1970.
- [30] R. M. C. So, J. Y. Zhu, M. V. Ötügen, and B. C. Hwang, “Some measurements in a binary gas jet,” *Experiments in Fluids*, vol. 9, no. 5, pp. 273–284, 1990.
- [31] N. Zong, H. Meng, S.-Y. Hsieh, and V. Yang, “A numerical study of cryogenic fluid injection and mixing under supercritical conditions,” *Physics of Fluids*, vol. 16, no. 12, pp. 4248–4261, 2004.
- [32] M. Oswald, A. Schik, M. Klar, and W. Mayer, “Investigation of coaxial LN₂/GH₂-injection at supercritical pressure by spontaneous raman scattering,” in *Proceedings of the 35th AIAA/ASME/SAE/ASEE Joint Propulsion Conference and Exhibit*, Los Angeles, Calif, USA, June 1999.
- [33] L.-K. Tseng, G. A. Ruff, P.-K. Wu, and G. M. Faeth, “Continuous- and dispersed-phase structure of pressure-atomized sprays,” in *Proceedings of the Progress in Astronautics and Aeronautics: Recent Advances in Spray Combustion*, 1995.
- [34] N. Zong and V. Yang, “Cryogenic fluid jets and mixing layers in transcritical and supercritical environments,” *Combustion Science and Technology*, vol. 178, no. 1-3, pp. 193–227, 2006.
- [35] J. C. Oefelein and V. Yang, “Comprehensive review of liquid-propellant combustion instabilities in F-1 engines,” *Journal of Propulsion and Power*, vol. 9, no. 5, pp. 657–677, 1993.
- [36] B. Chehroudi and D. Talley, “Interaction of acoustic waves with a cryogenic nitrogen jet at sub- and supercritical pressures,” in *Proceedings of the 40th Aerospace Sciences Meeting and Exhibit*, Reno, NV, USA, 2002, AIAA 2002-0342.
- [37] D. O. Rockwell, “External excitation of planar jets,” *Journal of Applied Mechanics*, vol. 39, no. 4, pp. 883–891, 1972.
- [38] H. A. Becker and T. A. Massaro, “Vortex evolution in a round jet,” *Journal of Fluid Mechanics*, vol. 31, pp. 435–448, 1968.
- [39] Y. V. Vaslov and A. S. Ginevskiy, “Acoustic effects on aerodynamic characteristics of a turbulent jet,” Tech. Rep. FTD-MT-24-232-68, Foreign Technology Division, Air Force Systems Command, 1968.
- [40] J. Hulka and J. J. Hutt, “Instability phenomena in liquid oxygen/hydrogen propellant rocket engines,” in *Liquid Rocket Engine Combustion Instability*, V. Yang and W. E. Anderson,

- Eds., AIAA Progress in Astronautics and Aeronautics, pp. 39–71, 1995.
- [41] J. Telaar, G. Schneider, and W. Mayer, *Experimental Investigation of Breakup of Turbulent Liquid Jets*, ILASS-Europe 2000, Darmstadt, Germany, 2000.
- [42] D. Davis and B. Chehroudi, “The effects of pressure and acoustic field on a cryogenic coaxial jet,” in *Proceedings of the 42nd AIAA Aerospace Sciences Meeting and Exhibit*, pp. 10741–10759, January 2004.
- [43] D. Davis and B. Chehroudi, “Behaviour of a rocket-Like coaxial injector in an acoustic field, ILAS america,” in *Proceedings of the 19th Annual Conference on Liquid Atomization and Spray Systems*, Toronto, Canada, May 2006.
- [44] D. W. Davis, *On the behavior of a shear-coaxial Jet, spanning sub- to super-critical pressures, with and without an externally imposed transverse acoustic field [Ph.D. thesis]*, Department of Mechanical and Nuclear Engineering, The Pennsylvania State University, 2006.
- [45] M. Oswald, J. J. Smith, R. Branam et al., “Injection of fluids into supercritical environments,” *Combustion Science and Technology*, vol. 178, no. 1–3, pp. 49–100, 2006.
- [46] M. Favre-Marinet and E. B. Camano Schettini, “Density field of coaxial jets with large velocity ratio and large density differences,” *International Journal of Heat and Mass Transfer*, vol. 44, no. 10, pp. 1913–1924, 2001.
- [47] H. Eroglu, N. Chigier, and Z. Farago, “Coaxial atomizer liquid intact lengths,” *Physics of Fluids A*, vol. 3, no. 2, pp. 303–308, 1991.
- [48] C. Englebert, Y. Hardalupas, and J. H. Whitlaw, “Article usage statistics center,” *Proceedings of the Royal Society A*, vol. 451, pp. 189–229, 1995.
- [49] Z. Faragó and N. Chigier, “Morphological classification of disintegration of round liquid jets in a coaxial air stream,” *Atomization and Sprays*, vol. 2, pp. 137–153, 1992.
- [50] R. D. Woodward, *Primary atomization of liquid jets issuing from rocket engine coaxial injectors [Ph.D. thesis]*, Pennsylvania State University, Department of Mechanical Engineering, University Park, Pa, USA, 1993.
- [51] B. Chehroudi, D. Davis, and D. Talley, “Initial results from a cryogenic coaxial injector in an acoustic field,” in *Proceedings of the 41st Aerospace Sciences Meeting and Exhibit*, Reno, NV, USA, 2003, AIAA 2003-1339.
- [52] I. A. Leyva, J. I. Rodriguez, B. Chehroudi, and D. Talley, “Preliminary results on coaxial jet spread angles and the effects of variable phase transverse acoustic fields,” in *Proceedings of the 46th AIAA Aerospace Sciences Meeting and Exhibit*, Reno, NV, USA, January 2008.
- [53] J. C. Lasheras and E. J. Hopfinger, “Liquid jet instability and atomization in a coaxial gas stream,” *Annual Review of Fluid Mechanics*, vol. 32, pp. 275–308, 2000.
- [54] J. I. Rodriguez, I. A. Leyva, B. Chehroudi, and D. Talley, in *Proceedings of the 21st Annual Conference on Liquid Atomization and Spray Systems (ILASS '08)*, Orlando, Fla, USA, May 2008.
- [55] J. I. Rodriguez, *Acoustic excitation of liquid fuel droplets and coaxial jets [Ph.D. thesis]*, University of California at Los Angeles, 2009.
- [56] B. Chehroudi, “Physical hypothesis for the combustion instability in cryogenic liquid rocket engines,” *Journal of Propulsion and Power*, vol. 26, no. 6, pp. 1153–1160, 2010.
- [57] W. E. Anderson, H. M. Ryan, R. J. Santoro, and R. A. Hewitt, “Combustion instability mechanisms in liquid rocket engines using impinging jet injectors,” in *Proceedings of the 31st AIAA/ASME/SAE/ASEE Joint Propulsion Conference and Exhibit*, San Diego, Calif, USA, July 1995, Paper AIAA-95-2357.
- [58] T. D. Harrje and H. F. Reardon, “Propellant rocket combustion instability,” NASA Report, 1972, NASA SP-194.
- [59] “Liquid rocket engine combustion instability,” in *Proceedings of the AIAA Progress in Astronautics and Aeronautics*, V. Yang and W. E. Anderson, Eds., vol. 169, p. 577, 1995.
- [60] L. Rayleigh, “The explanation of certain acoustical phenomena,” in *Proceedings of the Royal Institution*, vol. 8, pp. 536–542, London, UK, 1878.
- [61] M. F. Heidemann and J. F. Groeneweg, “Analysis of the dynamic response of liquid Jet atomization to acoustic oscillations,” NASA Technical Note, 1969, NASA TN D-5339.
- [62] T. Kiwata, A. Okajima, and H. Ueno, “Effects of excitation on plane and coaxial jets,” in *Proceedings of the 3rd Joint ASME/JSME Fluid Engineering Conference*, pp. 18–22, San Francisco, Calif, USA, 1999.
- [63] D. W. Davis and B. Chehroudi, “Measurements in an acoustically-driven coaxial jet under supercritical conditions,” *Journal of Propulsion and Power*, vol. 23, no. 2, pp. 364–374, 2007.
- [64] D. W. Davis and B. Chehroudi, “Shear-coaxial jets from a rocket-like injector in a transverse acoustic field at high pressures,” in *Proceedings of the 44th AIAA Aerospace Sciences Meeting*, pp. 9173–9190, Reno, Nv, USA, January 2006, Paper No. AIAA-2006-0758.
- [65] I. A. Leyva, B. Chehroudi, and D. Talley, “Dark core analysis of coaxial injectors at sub-, near-, and supercritical pressures in a transverse acoustic field,” in *Proceedings of the 43rd AIAA/ASME/SAE/ASEE Joint Propulsion Conference and Exhibit*, pp. 4342–4359, Cincinnati, Ohio, USA, July 2007.
- [66] R. D. Woodward, S. Pal, S. Farhangi, G. E. Jensen, and R. J. Santoro, “LOX/GH₂ shear coaxial injector atomization studies: effect of recess and non-concentricity,” in *Proceedings of the 45th AIAA Aerospace Sciences Meeting and Exhibit*, pp. 6925–6946, Reno, Nv, USA, January 2007.
- [67] B. Yang, C. Francesco, L. Wang, and M. Oswald, “Experimental investigation of reactive liquid Oxygen/CH₄ coaxial sprays,” *Journal of Propulsion and Power*, vol. 23, no. 4, pp. 763–771, 2007.
- [68] J. J. Smith, M. Bechle, D. Suslov, M. Oswald, O. J. Haidn, and G. M. Schneider, “High pressure LOx/H₂ combustion and flame dynamics preliminary results,” in *Proceedings of the 40th AIAA/ASME/SAE/ASEE Joint Propulsion Conference & Exhibit*, Fort Lauderdale, Fla, USA, July 2004, AIAA-2004-3376.

Research Article

Solid Rocket Motor Design Using Hybrid Optimization

Kevin Albarado, Roy Hartfield, Wade Hurston, and Rhonald Jenkins

Department of Aerospace Engineering, Auburn University, Auburn, AL 36849, USA

Correspondence should be addressed to Kevin Albarado, albarkm@tigermail.auburn.edu

Received 16 February 2012; Accepted 30 April 2012

Academic Editor: Valsalayam Sanal Kumar

Copyright © 2012 Kevin Albarado et al. This is an open access article distributed under the Creative Commons Attribution License, which permits unrestricted use, distribution, and reproduction in any medium, provided the original work is properly cited.

A particle swarm/pattern search hybrid optimizer was used to drive a solid rocket motor modeling code to an optimal solution. The solid motor code models tapered motor geometries using analytical burn back methods by slicing the grain into thin sections along the axial direction. Grains with circular perforated stars, wagon wheels, and dog bones can be considered and multiple tapered sections can be constructed. The hybrid approach to optimization is capable of exploring large areas of the solution space through particle swarming, but is also able to climb “hills” of optimality through gradient based pattern searching. A preliminary method for designing tapered internal geometry as well as tapered outer mold-line geometry is presented. A total of four optimization cases were performed. The first two case studies examines designing motors to match a given regressive-progressive-regressive burn profile. The third case study studies designing a neutrally burning right circular perforated grain (utilizing inner and external geometry tapering). The final case study studies designing a linearly regressive burning profile for right circular perforated (tapered) grains.

1. Introduction

The ability to perform the optimization phase of design in a timely manner can be key to the ultimate success of the design. With recent developments in computing efficiency and modeling techniques, a computer can evaluate thousands of candidate designs for a complex system on the preliminary design level that it once took an engineer to evaluate a handful of designs. In the case of the rocket motor, engineers now have the capability to design motors that can match a specified pressure-time curve, motor specs such as weight, and optimally fit motors into missile systems [1, 2].

Numerous tools have been developed for modeling solid rocket motors. Industry tools such as solid performance program (SPP) [3] and simpler tools developed for preliminary design use [4–7] perform the burnback by approximating the grain cross sections as 2D and 3D shapes that have analytical burnback solutions. These tools can provide a wide range of information in a relatively short amount of time, making them suitable candidates for optimization schemes. The motor modeling scheme

employed for this study is an extension of the method outlined in reference [5]. The prediction results from this code has been compared to space shuttle booster data with favorable results. In this model, the internal geometry can taper along the grain length as well as the outer mold line. This brings about numerous advantages from a vehicle design standpoint, whether it be that the outer mold line needs to be tapered as part of a booster set within a ramjet combustor, or the rocket motor needs to take advantage of vehicle aerodynamics while still producing the burn profile desired.

The HyStrike (high speed strike missile) fast hawk low-cost missile was one such system designed to incorporate a solid booster into the ramjet combustor. The vehicle was designed to fire the booster to accelerate up to cruise speed, then switch to ramjet power for cruise. Due to the design, the rocket motor had tapered outer geometry to adhere to the ramjet combustor design (see Figure 1). In order to produce the desired thrust profile for the vehicle, the inner geometry had to be tapered to accommodate this design criteria. While the project eventually was scrubbed, the problem itself is still very relevant in designing new systems. To design for such

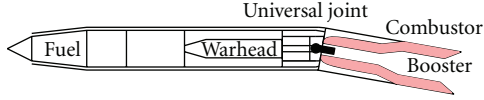


FIGURE 1: HyStrike fast hawk missile conceptual design.

a problem, population based optimization is the most practical and robust driver for the design code.

Holland [8] originally suggested simulation population-based biological processes such as evolution and reproduction for use in genetic algorithms for optimization. Eberhart and Kennedy [9] developed the first particle swarm optimization method in 1995, mimicking crowd behavior. These two ideas have paved the way for optimization because the methods do not require the calculation of partial derivatives of the function. Instead, they rely on communication between members in a generation to develop new populations. The optimizer employed in this investigation is a state-of-the-art combination of a population-based approach and an efficient gradient method. A particle swarm optimizer based on the method described in [10] was used in conjunction with a pattern search method. Perhaps one of the earliest uses of the pattern search method in optimization of a solid motor problem can be found in reference [11], where Woltosz used a pattern search method to reduce the weight of a solid rocket motor while still achieving a desired total impulse.

2. Optimization Methodology

In this study, a hybrid optimizer was implemented for solving common solid rocket motor problems. The strategy developed combines a particle swarm optimization technique with a direct search method known as pattern search, and is largely based on the optimizer developed by Jenkins and Hartfield [12].

2.1. Particle Swarm. Particle swarm optimization was first suggested as a useful optimization strategy by Eberhart and Kennedy [9]. Particle swarm is a population-based optimization method utilizing aspects of crowding or flocking behavior observed in nature. Particle swarm begins with an initial population of members (particles or designs) defined by some set of independent variables, in this case design variables describing solid rocket motor geometry. Each particle moves through the design space with a nonconstant velocity, searching for the position that either maximizes or minimizes the objective function (optimum position). The particles interact and communicate to determine which particles are performing the best and in which direction to travel next. Each particle is influenced by the best position that particle has seen thus far, the best position seen by any particle, and its own previous movement (momentum). The equations of motion for a particle as modified by Mishra [10] can be seen below in (1) and (2). Shown in Figure 2 is a depiction of how each term influences the particle. The stochastic nature of the particle swarm algorithm appears in

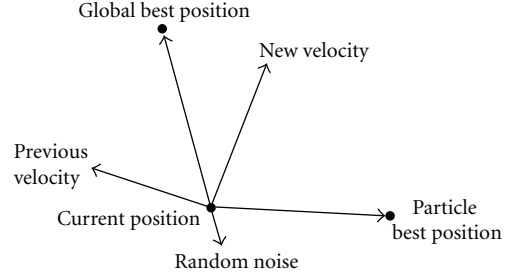


FIGURE 2: Influences on a particle.

the random numbers in the first two terms and the random noise added to the equation of motion in the third term.

$$v_{i+1} = \alpha R_1 \omega (\hat{x}_m - x_i) + \beta R_2 (\hat{x}_i - x_i) + \gamma R_3 + \omega v_i, \quad (1)$$

$$x_{i+1} = x_i + v_{i+1}. \quad (2)$$

Unlike most evolutionary algorithms, the particle swarm technique is not bounded to some resolution on the independent parameters. This allows for a virtually infinite number of solutions possible. Also, particle swarming does not rely on the objective function to be differentiable nor smooth in nature. Unlike gradient methods, the particle swarm method can and will move particles off of local optima if better positions are found by other particles. Particle swarming's largest downside however, is that the best solution in the population will not feel influence from the first two terms in (1) leaving only the particle's previous velocity and a random (small) inertial term to influence the movement. This point makes finding the global optima difficult for the particle swarm optimizer and hinders the efficiency of the optimizer [13]. The particle swarm method works well for finding optimal the optimal area of the design space, but does in fact struggle to find the optimal point. For this reason, the particle swarm optimizer was combined with the gradient evaluation method known as pattern search.

2.2. Pattern Search. Pattern search is a direct search method technique originally offered by Hooke and Jeeves [14]. It imposes the logic that is individual changes in parameters improve the objective function, then a pattern move of all parameters will also improve the objective function. An illustration of this concept is shown in Figure 3. The following methodology is implemented into the algorithm developed.

- (1) Initialize a case design.
- (2) Perform an exploratory move on a single variable, holding all others constant.
- (3) Evaluate fitness function using exploratory move.
- (4) If the fitness improves, store the exploratory move.
- (5) Repeat 2, 3, and 4 for all variables.
- (6) Perform a pattern move, simultaneously altering all variables with the appropriate stored exploratory moves.
- (7) Reevaluate fitness function with pattern move.

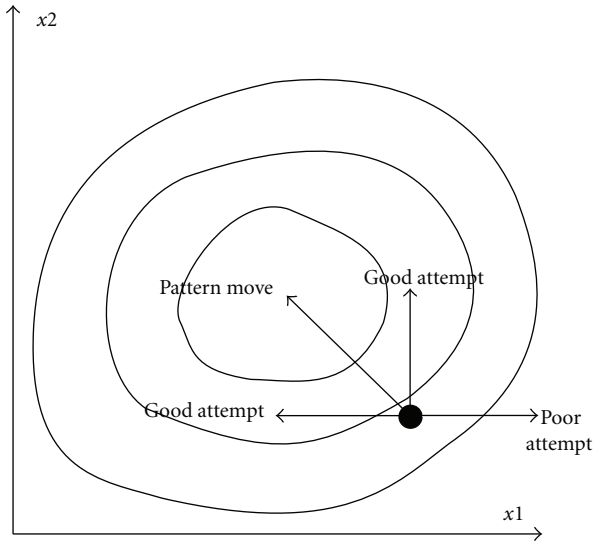


FIGURE 3: Pattern search diagram.

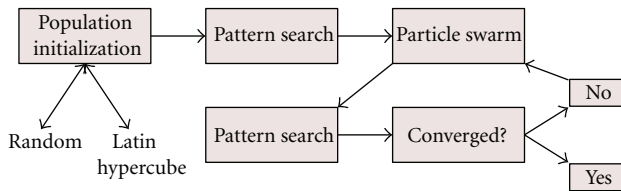


FIGURE 4: Hybrid optimizer flow chart.

- (8) If fitness improves, change the case design.
- (9) If fitness gets worse, keep initial design and reduce size of exploratory move.

Figure 3 could best be thought of as a topological map of a design space with independent variables x_1 and x_2 . From the figure, moving in the negative x_1 direction and positive x_2 direction will send the particle directly to the high point (inner ring). When positioned properly within the design space, the pattern search method can find local optima rapidly. However, the pattern search is only as good as its initial guess, making the pattern search a weak optimization method when working alone in a complex design space.

2.3. Hybrid Optimizer. There are two methods for combining the particle swarm technique with the pattern search algorithm. The simple method would be to piggyback the pattern search method onto the particle swarm optimizer (i.e., implement them in series). However, this would fail to take advantage of each optimization strategy during each iteration of the routine. Instead, the two methods were implemented in parallel. In other words, a single iteration of the optimizer required one particle swarm maneuver and at least one pattern search maneuver (the number of iterations of pattern search per generation is a variable to be chosen by the user). The program flow for the complete optimizer is shown below in Figure 4. Jenkins and Hartfield [12] proved that a combination of a population-based scheme with

a gradient-based scheme achieves a lower total fitness in fewer function calls for a variety of aerospace propulsion problems. In particular, the optimizer they developed performed better than both genetic algorithms and the particle swarm optimizer alone.

3. Modeling Scheme

The modeling scheme for solid motors used in this study is a modified version of the method described by Hartfield et al. [5]. The program calculates the burn perimeter and port area in terms of burn distance using a series of analytical equations described in detail in [5]. A motor of uniform cross-section can be theoretically fully described using the grain length, six parameters for the cross section, the throat area, and the nozzle exit area. The modified code used in this study however, requires scale factors for three different motor sections, to determine how the grain cross-section tapers from section to section linearly. The six parameters that describe the cross section are the outer grain radius, R_0 , the maximum inner radius with no fillet, R_p , the minimum inner radius, R_i , which can be determined by the angular opening of the star point, θ , the fraction of the angle allowed for a single star point taken up by the structure of the star point (angular fraction) ϵ , and the fillet radius, f . Each of these parameters is labeled in Figure 5, which represents one-half of a single star point. For more information on Figure 5 and the equation set used, see [5].

The six parameters plus the three grain lengths and three scale factors are the independent variables selected for this problem, giving a total of 12 independent variables. Figure 6 represents a simplified sketch of the side view of the rocket motor with tapered grains. In addition to having the ability to taper the inner grain design, the model is also capable of tapering the outer mold-line. In its present state, the outer radius can be tapered linearly between three sections. However, this ability could easily be applied to modeling motors that have characteristic curves describing the outer mold line to take advantage of vehicle aerodynamics.

4. Results and Discussion

The first case attempted for this study was to match a pressure-time curve. The first case serves as a proof that the optimization scheme is in fact a viable approach to solving this problem. For this reason, the pressure time curve chosen, shown in Figure 7, has three distinct phases: a regressive burn, a progressive burn, and a regressive burn phase. This adds a level of complexity to the solution space. In order to determine mathematically how well a candidate motor's performance compares to the desired performance in Figure 7, an error was calculated based on (3). Minimization of (3) is ultimately the goal for the optimizer.

$$e = \frac{\sum_{i=1}^n (\hat{P}_i - P_i)^2}{n^2}. \quad (3)$$

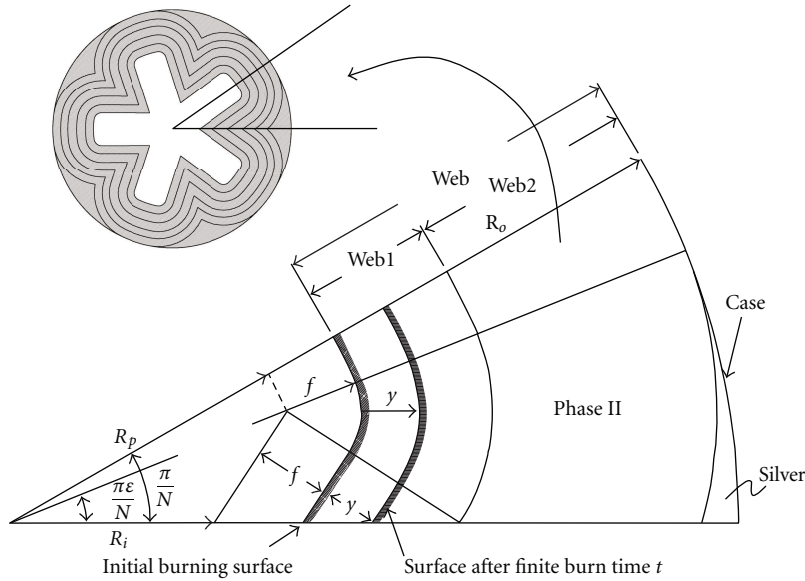


FIGURE 5: One-half of a single star point.

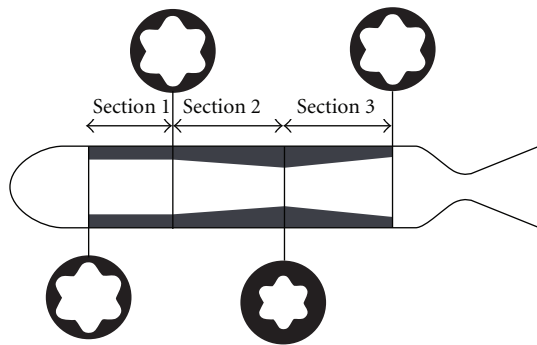


FIGURE 6: Tapered grain sections.

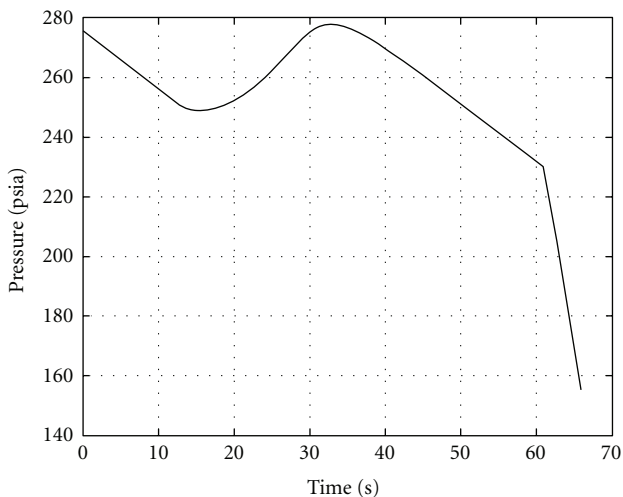


FIGURE 7: Desired regressive-progressive-regressive pressure-time curve.

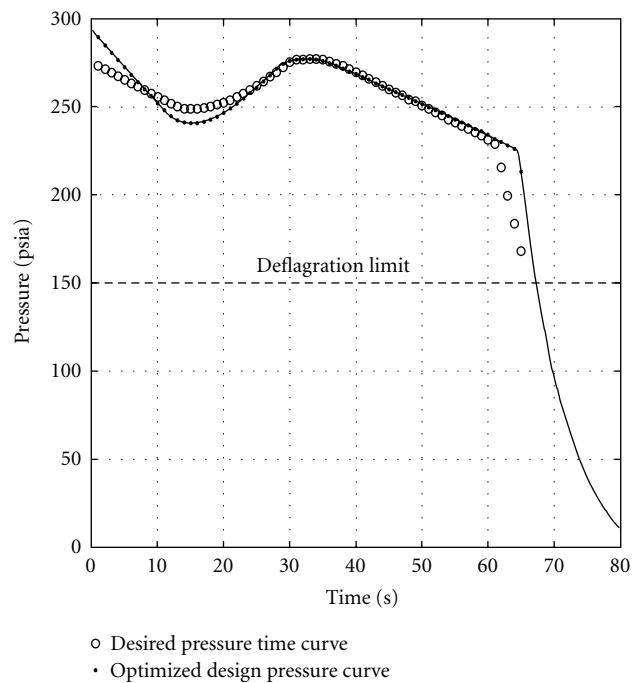


FIGURE 8: Optimized pressure-time curve for regressive-progressive-regressive profile.

In order to match the pressure-time curve in Figure 5, the 12 independent variables mentioned previously were systematically altered using the particle swarm/pattern search method. Approximately 100,000 motor designs were tested to arrive at the solution. While this number may seem high, this problem is fairly complex (12 design variables with a multivalued objective function), and to perform this many function evaluations manually would be considered exhaustive and inefficient. The results from the optimization are shown in Figures 8 and 9.

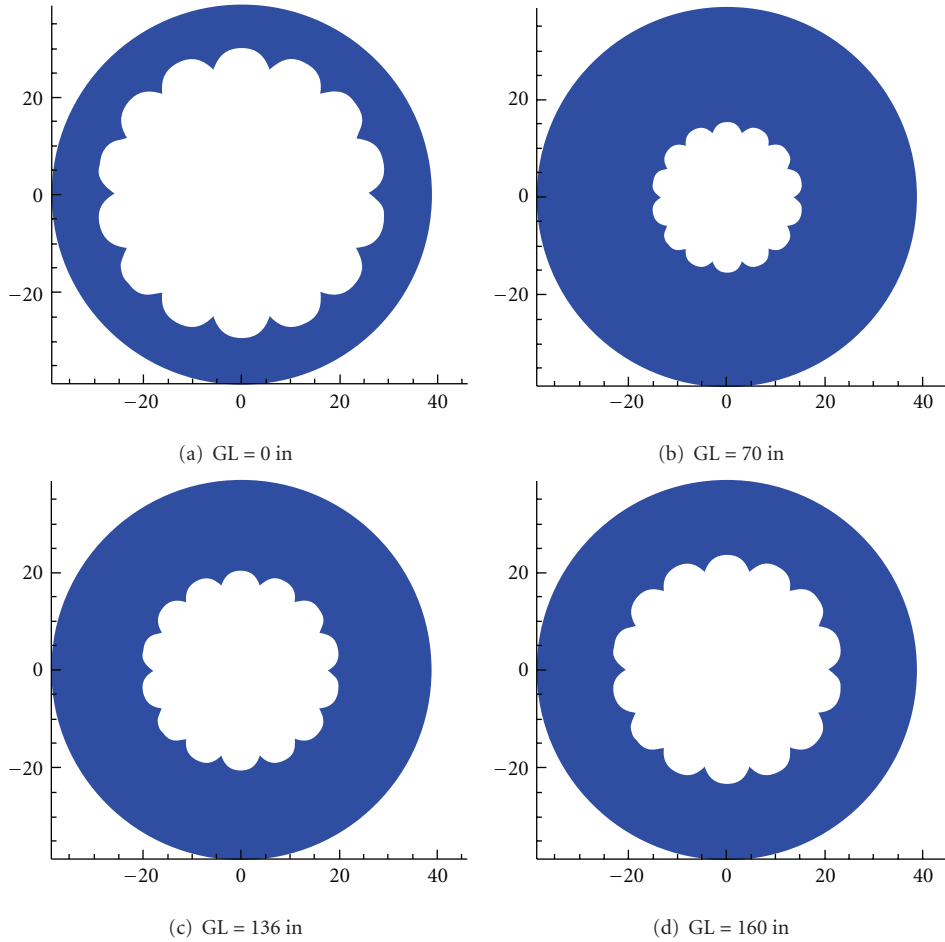


FIGURE 9: Grain cross section for regressive-progressive-regressive profile.

It is believed that the motor shown in Figure 9 is the optimal design for the desired pressure-time curve. It should be noted that at a burn time of around 70 seconds, the pressure reaches the deflagration limit where it is believed that the motor will actually burn out. This effect is not currently modeled in the program used for this study. The final solution relied heavily on the tapering of the grain in order to achieve the final solution. This was an expected result because right circularly perforated star and wagon wheel grains are not capable of producing the desired curve. The tapering of the motor allows for producing regressive burn profiles late in the burning of the motor due to the propellant burning out at the walls in some sections before it burns out in other sections. This method for designing star and wagon wheel motors could allow for designing almost any desired pressure curve. This would allow a designer to specify a pressure-time profile for a vehicle with certainty that a motor exists and can be designed for that profile. An additional ability of this approach to grain design is the ability to taper the outer mold line as well as internal geometry. An attempt to match the same pressure-time curve given in Figure 7 was made using the same techniques as before only this time the outer radius was allowed to vary. Presented in Figures 10 and 11 are the results of this case.

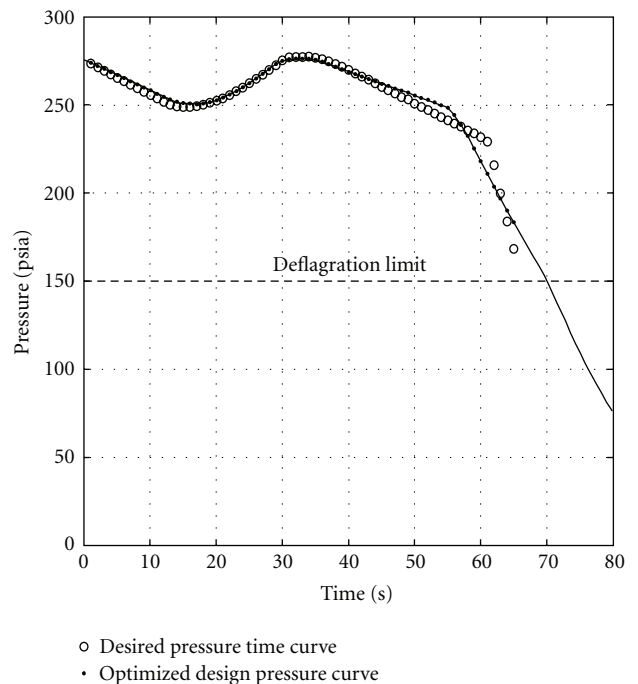


FIGURE 10: Optimized pressure-time curve for regressive-progressive-regressive profile allowing outer-mold line to vary.

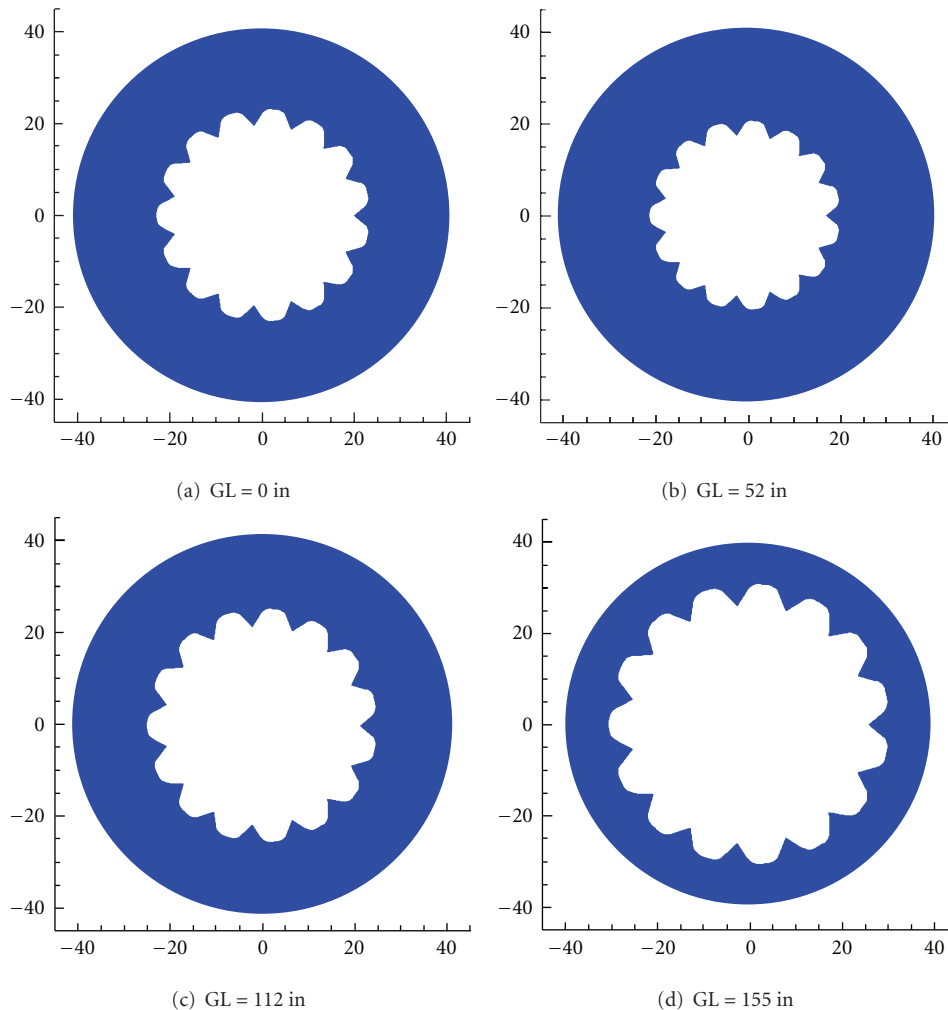


FIGURE 11: Optimized grain cross section for regressive-progressive-regressive profile allowing outer-mold line to vary.

Figures 9 and 11 have numerous similarities such as a large number of star points, a body radius of around 40 inches, grain lengths around 160 inches, and tapering of the inner geometry to achieve the results shown in Figures 8 and 10. One similarity to focus on further is the large number of star points, and the relatively small star point structure (i.e., the value for R_i is very close to that of R_p). From Figure 5, this would imply that the optimizer is attempting to drive the solution to circular perforated grains. This result implies that simpler CP grain motors could utilize tapering of the inner and outer radii to produce pressure-time curves similar to that a right circular perforated star or wagon wheel could produce.

This result leads to the second study performed. In some designs it is either impractical or not cost effective to design a tapered star grain. For that reason, simpler motor designs are often employed to avoid cost buildup. But what if a simpler design, say a circular perforated grain, could be tapered in sections as shown before? Better yet, what if the outer radius of the motor was tapered for aerodynamic reasons? With the setup described, a motor can be designed to take advantage of the simplicity of CP motors, take advantage of outer mold line aerodynamics, and can still be relatively simple

in design complexity. Two profiles were examined: a neutral burning tapered CP motor and a linearly regressive tapered CP motor. Both of these design cases are not possible with a uniform right circular perforated grain (which produces a highly progressive burn profile). For the first CP grain optimization, the optimizer searched for a motor that could match a 400 psia constant pressure for 10 seconds. The inner radius parameter, R_i , was set equal to R_p , and the fillet radius was set to zero. The outer radius was allowed to taper linearly between the sections. Shown in Figures 12 and 13 are the results of this case study.

As can be seen from Figure 12, the optimizer was able to find a motor that nearly (within 3%) match the constant 400 psia over a ten second burn time. From Figure 13, the optimizer apparently chose a design with the web thickness to be roughly a constant; however, it tapered the outer radius significantly between the sections. In fact, section three (Figure 13(c)) tapers up from a radius of 23 inches to over 43 inches (almost 100%). For the second case study involving only CP grains, the optimizer was set to design a motor that could match a linearly regressive burn curve beginning at 600 psia over 10 seconds and burning out at 400 psia. Shown in Figures 14 and 15 are the results.

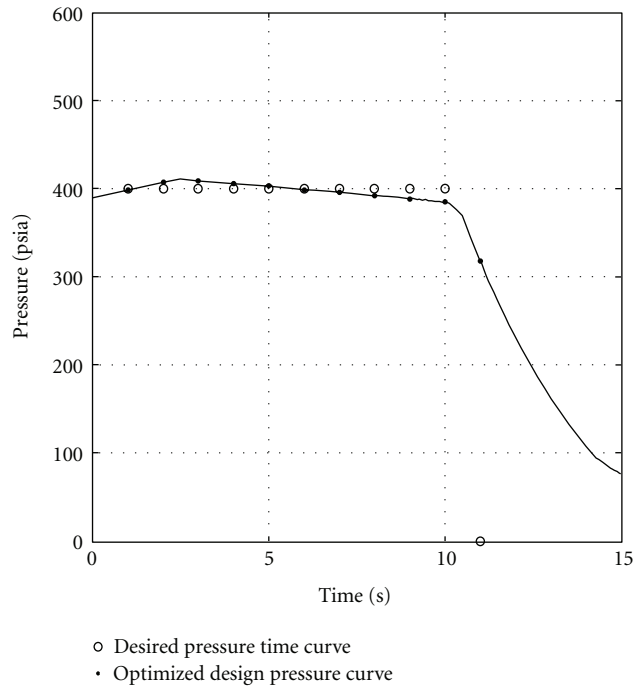


FIGURE 12: Optimized pressure-time curve for neutral burning CP grain.

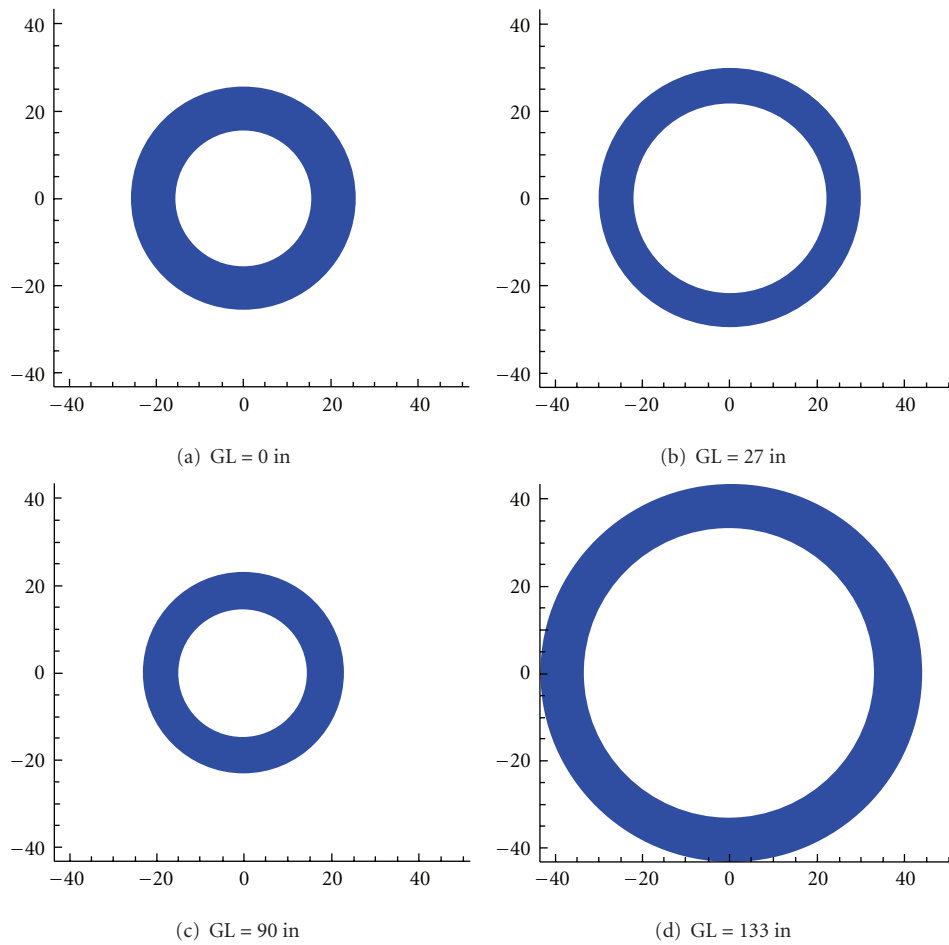


FIGURE 13: Optimized grain cross section for neutral burning CP grain.

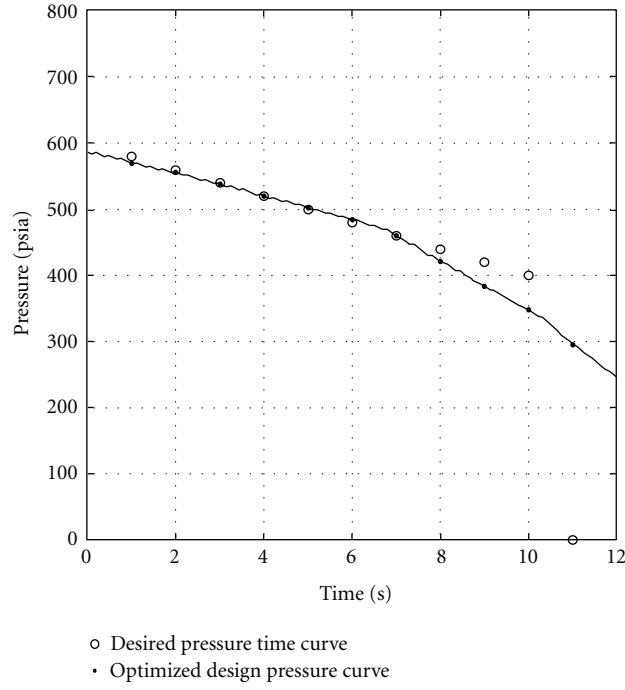


FIGURE 14: Optimized pressure-time curve for linearly regressive CP grain.

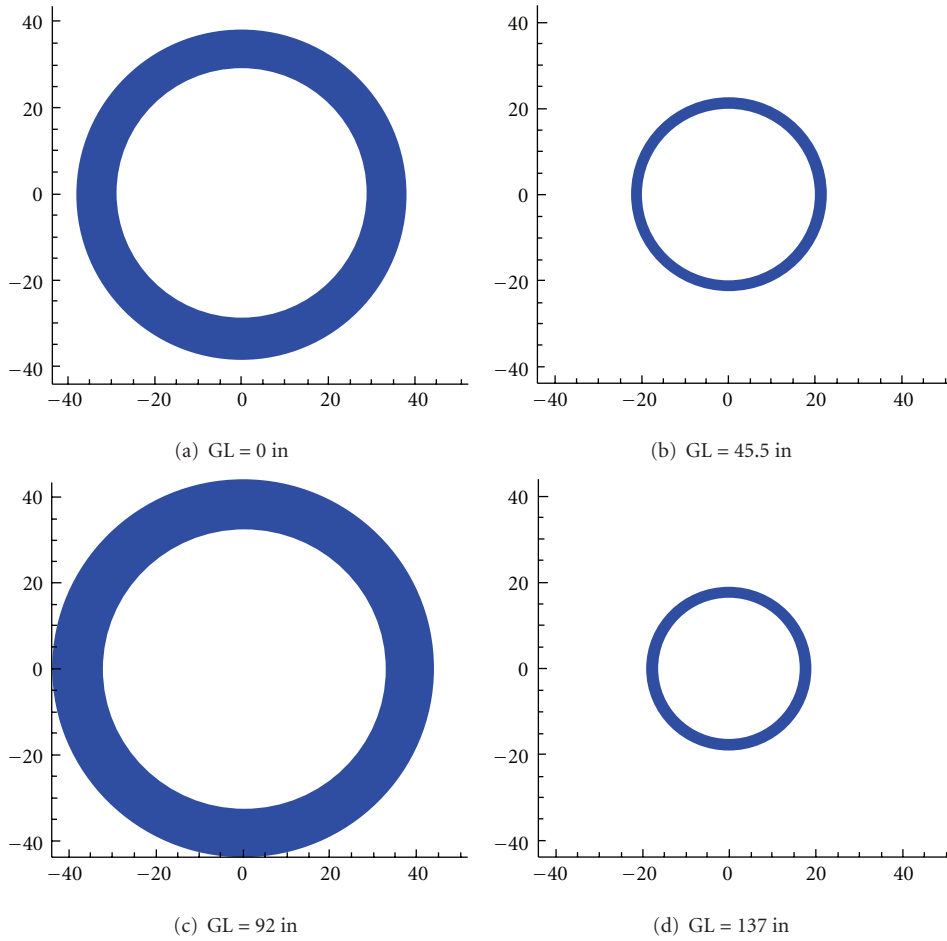


FIGURE 15: Optimized grain cross section for linearly regressive CP grain.

In order to generate the necessary regressive burn profile, the optimizer used tapering of both the inner and outer geometry as illustrated in Figure 15. From the neutral burning CP study, it was apparent that the web thickness should be somewhat constant and the outer geometry tapered to in order to keep a constant burn area. But here, the motor essentially tapers the web thickness so that parts of the motor burn out before others so the burn area is constantly decreasing. It should be noted that while the curve does not completely line up with the desired profile, the final result is within 10% of the desired solution.

5. Conclusion

The particle swarm/pattern search optimizer coupled with the modified solid propulsion modeling code proved to be a proficient simulation and optimization tool, capable of finding a solution to the regressive/progressive/regressive burn curve given. It was clear from the results that the tapering of the motor sections proved vital in finding solutions to the problems proposed. For simple star grains, the tapering was essential in providing burning behavior not found in right perforated grains. This effect was enhanced by showing not only how internal tapering of the grains can produce complex, multiphase burn profiles, but also how outer mold line tapering can be utilized to achieve the same effects. This has implications in both booster design for air breathing missiles and vehicle designs with considerations in outer mold line for aerodynamics or vehicle architecture. Both a neutral and linearly regressive burn profile were created using circular perforated grains by tapering the inner and outer radii. This has strong implications in design problems where manufacturing limitations require the need to keep designs simple and cost effective, yet complex pressure profiles are required.

Nomenclature

e :	RMS error
P :	Predicted pressure
\hat{P} :	Desired pressure
$R_{1,2,3}$:	Random number between 0 and 1
v_i :	Current particle velocity
v_{i+1} :	Next particle velocity
x_i :	Current particle position
x_{i+1} :	Next particle position
\hat{x}_i :	Particle best position seen
\hat{x}_m :	Global best position seen
α :	Inertial constant acting on global best position influence
β :	Inertial constant acting on particle best position influence
γ :	Inertial constant acting on random noise
ω :	Inertial repulsive constant.

References

- [1] M. B. Anderson, J. E. Burkhalter, and R. M. Jenkins, "Design of a guided missile interceptor using a genetic algorithm," *Journal of Spacecraft and Rockets*, vol. 38, no. 1, pp. 28–35, 2001.
- [2] D. Riddle, R. Hartfield, J. Burkhalter, and R. Jenkins, "Genetic Algorithm Optimization of Liquid Propellant Missile Systems," AIAA paper 2007-362, 2007.
- [3] S. Dunn, D. Coats, and J. French, *SPP'02: 3D Grain Design User's Manual*, Software & Engineering Associates Inc., 2002.
- [4] R. Sforzini, "An Automated Approach to Design of Solid Rockets Utilizing a Special Internal Ballistics Model," AIAA paper 1980-1135, 1980.
- [5] R. Hartfield, R. Jenkins, J. Burkhalter, and W. Foster, "A Review of analytical methods for predicting grain regression in tactical solid-rocket motors," *AIAA Journal of Spacecraft and Rockets*, vol. 41, no. 4, pp. 689–692, 2004.
- [6] A. Ricciardi, "Generalized geometric analysis of right circular cylindrical star perforated and tapered grains," *AIAA Journal of Propulsion and Power*, vol. 8, no. 1, pp. 51–58, 1992.
- [7] R. Sforzini, *Notes on Solid-Propellant Rocket Motors Including Jet Propulsion Fundamentals*, Auburn University, 1980.
- [8] J. Holland, *Adaptation in Natural and Artificial Systems*, MIT Press, 1992.
- [9] R. Eberhart and J. Kennedy, "New optimizer using particle swarm theory," in *Proceedings of the 6th International Symposium on Micro Machine and Human Science*, pp. 39–43, October 1995.
- [10] S. Mishra, "Repulsive particle swarm method on some difficult test problems of global optimization," In press.
- [11] W. Woltoz, *The application of numerical optimization techniques to solid-propellant rocket motor design [M.S. thesis]*, Auburn University, 1977.
- [12] R. Jenkins and R. Hartfield, "Hybrid particle swarm-pattern search optimizer for aerospace applications," AIAA paper 2010-7078, 2010.
- [13] J. Badyrka, R. Jenkins, and R. Hartfield, "Aerospace design: a comparative study," AIAA paper 2010-1311, 2010.
- [14] R. Hooke and T. Jeeves, "Direct search solution of numerical and statistical problems," *Journal of Association of Computing Machinery*, vol. 8, no. 2, pp. 212–229, 1961.

Research Article

Testing and Modeling Fuel Regression Rate in a Miniature Hybrid Burner

Luciano Fanton, Christian Paravan, and Luigi T. De Luca

SPLab, Aerospace Engineering Department, Politecnico di Milano, 34 Via La Masa, 20156 Milan, Italy

Correspondence should be addressed to Luciano Fanton, luciano.fanton@gmail.com

Received 10 February 2012; Accepted 7 May 2012

Academic Editor: Dario Pastrone

Copyright © 2012 Luciano Fanton et al. This is an open access article distributed under the Creative Commons Attribution License, which permits unrestricted use, distribution, and reproduction in any medium, provided the original work is properly cited.

Ballistic characterization of an extended group of innovative HTPB-based solid fuel formulations for hybrid rocket propulsion was performed in a lab-scale burner. An optical time-resolved technique was used to assess the quasisteady regression history of single perforation, cylindrical samples. The effects of metalized additives and radiant heat transfer on the regression rate of such formulations were assessed. Under the investigated operating conditions and based on phenomenological models from the literature, analyses of the collected experimental data show an appreciable influence of the radiant heat flux from burnt gases and soot for both unloaded and loaded fuel formulations. Pure HTPB regression rate data are satisfactorily reproduced, while the impressive initial regression rates of metalized formulations require further assessment.

1. Introduction

HREs are propulsive systems combining chemical reactants in both a solid and a fluid (liquid or gaseous) state. In particular, the direct hybrid configuration studied in this work is characterized by a solid fuel reacting with a gaseous oxidizer. The main points of interest of this architecture include high specific impulse, relative construction simplicity, intrinsic handling safety, operational flexibility, minimal environment impact, and possible cost effectiveness compared to other systems, notably solid and liquid rocket engines [1, 2]. On the other hand, a serious drawback of HREs is the low regression rate of the gasifying solid fuel surface that yields low thrust levels if simple grain geometries are implemented. The main reason of such behavior is the complex diffusive nature of the flame, as described by several investigators [3–6].

The development of novel energetic additives renewed the interest for hybrid rocket propulsion and brought a new generation of hybrid solid fuels, aiming at improving the relatively low regression rates of conventional HTPB-based formulations [7–9]. The main target for research activities on hybrid systems should be to improve the fuel regression rate and, subsequently, enhancing combustion efficiencies, while

granting adequate mechanical properties, and commercial availability of the ingredients.

SPLab of Politecnico di Milano has developed a variety of experimental techniques and diagnostics in order to investigate ballistics of hybrid fuels and to achieve a relative grading of different fuel formulations in terms of regression rate. The present study is focused on a time-resolved technique for regression rate measurements. Collected data were considered to investigate the effects of radiant heat transfer on regression rate of loaded and nonloaded HTPB-based fuel formulations.

2. Literature Survey

In a direct HRE, the oxidizer flow over the solid fuel grain generates a boundary layer. After the ignition, the vaporized fuel diffuses into the oxidizer flow. Thus a flame is established in the boundary layer, where the mixture *O/F* reaches the flammability limits of the reactants. Heat transfer from the flame to the solid fuel grain gasifies new fuel thus sustaining the process. Fundamentals of hybrid combustion were investigated by Marxman et al. [3, 4], who identified convective heat transfer as the driving phenomenon for solid

fuel regression. The r_f of solid grains was evaluated as a strong function of the total mass flux $G = G_f + G_{ox}$, and, more precisely, $r_f \propto G^{0.8}$. Similar results were achieved by Smoot and Price [10]. In most experimental studies, r_f was evaluated by TOT techniques. In recent research activities conducted at Pennsylvania State University, instantaneous regression rate measurements were performed and $r_f \propto G^{0.61}$ was found for tests on HTPB burning in GOX [7].

The presence of soot and solid fuel fragments leads to a contribution of radiant heat transfer on r_f [1, 7]. The purely convective model was extended by Marxman et al. in order to take into account the radiant heat transfer [3]: the total heat flux to the solid grain was considered as the sum of convective and radiant heat fluxes. Radiation effects on regression rate were investigated also by Strand et al. [11], Estey et al. [12], and the research team of Pennsylvania State University [13]. The work by Strand et al., in particular, suggested that radiant heat flux due to combustion gaseous products such as CO, CO₂, H₂O, and soot particles could significantly influence hybrid combustion process. According to their results, radiant heat transfer accounts for nearly 50% of the total heat flux and is reduced by increasing O/F . The Pennsylvania State University research team observed a regression rate dependence on p_c , under the investigated conditions, leading to semiempirical correlations for combustion data interpolation. The contribution of radiant heat flux was found to mainly depend on the presence of soot, the radiation of combusted gases being quite low; hence, under the investigated conditions, convection has a high relative weight in the initial part of the combustion process, while radiation is more effective at lower values of the oxidizer mass flux.

One of the most promising ways to obtain r_f enhancement in hybrid systems is to increase the heat feedback from the flame to the solid fuel, by including highly energetic additives in the fuel matrix. Various ingredients have been tested in the recent past. Significant r_f enhancements were observed by adding nAl or boron-based composite metals [9]. This can be explained by the fact that these metalized ingredients combine high energy release and high reactivity, as shown by their large specific energy (~ 30 kJ/g for Al and ~ 59 kJ/g for B, the highest among nonhazardous metals or metalloids) with large specific surface values (~ 10 m²/g for nAl versus ~ 1 m²/g for conventional micron-sized additives). These characteristics favor short ignition delays and intense heat release near the regressing surface. Adding high-energy metal powders to the polymeric binder also increases the fuel density and therefore the engine volumetric specific impulse [9, 14, 15].

Among the undesirable characteristics of metal additives, one can recognize the tendency of both aluminum and boron to create an oxide layer during storage and fuel manufacturing. This implies a marked decrease of the particle reactivity (at least until the oxide is removed during the combustion phase) and a lower active metal content in the powders. An additional shortcoming of nanosized additives is their tendency to create clusters [9]. This requires proper manufacturing procedures in order to disperse the

nano-sized additives down to the nanoscale. Micron-sized additives do not require any dedicated dispersion technique.

3. Experimental Setup and Data Handling

3.1. Experimental Rig. The SPLab 2D radial burner utilized in this work enables a relative ballistic grading of different fuel formulations under controlled operating conditions (see Figure 1). The tested strands have a cylindrical shape and a single central port perforation. Each solid fuel grain is accommodated in a stainless steel case with 30 mm length. The strand outer diameter is 18 mm, while its nominal initial port diameter is 4 mm, thus yielding a solid fuel web thickness of 7 mm. Different cases enable testing of samples with different outer diameters (thus reducing the solid grain web thickness for a given D_0). Use of different mandrels enables the testing of strands with different D_0 .

The implemented experimental rig provides a continuous visualization of the head-end of the tested strand, thus it is possible to track the central port diameter during combustion. Video recording of the combustion processes enables r_f measurement by an optical, nonintrusive technique. Independent regulations of \dot{m}_{ox} and p_c are possible by a variable area flowmeter and by a pressure regulator driving a set of electric valves. The maximum values of the operating parameters are 6 g/s for \dot{m}_{ox} and 20 bar for pressure. Sample burning is initiated by a pyrotechnic primer charge. The latter is in turn ignited by a CO₂ laser. Video acquisition was operated with a dedicated analog camera (burning visualization at 25 fps, video resolution 640 × 480 pixels).

3.2. Time-Resolved Regression Rate. The main observable of interest for solid fuel ballistics is r_f . Thanks to the original design of the 2D radial burner, the latter parameter can be measured sampling the central port diameter of the visible head-end section of the cylindrical strand [16]. The diameter measurement starts when the central port perforation becomes visible following the primer charge ignition. For each sampling time, the space-average central port diameter is defined starting from local diameters measured along different radial directions, as shown in Figure 2. For a given sampling time, the so measured single diameters are averaged as in (1). Average diameters are obtained from the recorded combustion visualization with a sampling frequency of some Hz depending on the r_f . The resulting set of sampled $\bar{D}_i(t)$ is a discrete information in time. The latter becomes a continuous information in time by a proper data interpolation of the discrete $\bar{D}_i(t)$ thanks to (2), [17, 18]:

$$\bar{D}_i(t_i) = \frac{D_{1,i} + D_{2,i} + D_{3,i} + D_{4,i}}{4}, \quad (1)$$

$$\bar{D}(t) - D_0 = a_D \cdot (t - t_0)^{n_D}, \quad t \geq t_{\text{ign}} > t_0. \quad (2)$$

The latter (2) is valid starting from t_{ign} . This parameter is defined adhoc as the one maximizing the data fitting of

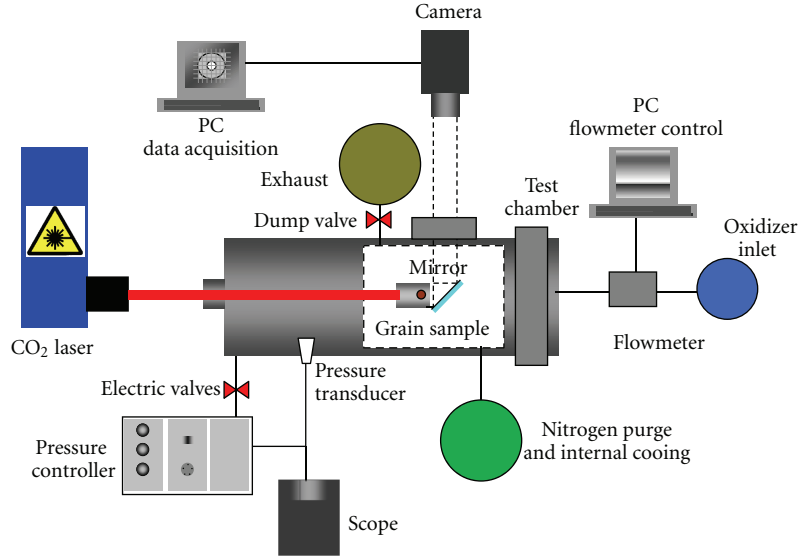


FIGURE 1: Experimental setup scheme highlighting the axial oxidizer inlet, the laser ignition apparatus, and the data acquisition hardware [16]. Note the 45° mirror enabling sample head-end visualization.

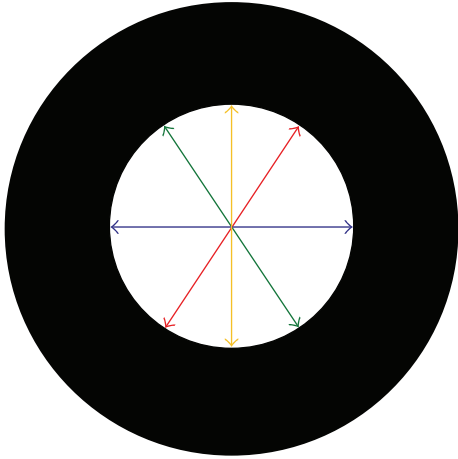


FIGURE 2: Single diameters measured along different radial directions.

(2) when associated with the discrete sampling of space-average port diameters. A straightforward time derivative of (2) allows defining $r_f(t)$ as

$$\begin{aligned} r_f(t \geq t_{\text{ign}}) &= \frac{d}{dt} \left(\frac{\bar{D}(t) - D_0}{2} \right) \\ &= \frac{1}{2} a_D n_D (t - t_0)^{n_D - 1}, \quad r_f(t < t_{\text{ign}}) = 0. \end{aligned} \quad (3)$$

The above expressions make it possible to determine all of the ballistic parameters of interest. The definitions of

the time-resolved $G_{\text{ox}}(t)$, $\dot{m}_f(t)$, and $O/F(t)$ are respectively obtained as

$$G_{\text{ox}}(t \geq t_{\text{ign}}) = \frac{\dot{m}_{\text{ox}}(t)}{\pi \bar{D}^2(t)/4} = \frac{\dot{m}_{\text{ox}}(t)}{\pi [D_0 + a_D(t - t_0)^{n_D}]^2/4}, \quad (4)$$

$$\dot{m}_f(t \geq t_{\text{ign}}) = \rho_f A_f(t) r_f(t) = \rho_f \pi \bar{D} L_s r_f(t), \quad (5)$$

$$\frac{O}{F}(t \geq t_{\text{ign}}) = \frac{\dot{m}_{\text{ox}}(t)}{\dot{m}_f(t)} = \frac{\dot{m}_{\text{ox}}(t)}{\rho_f \pi \bar{D}(t) L_s r_f(t)}. \quad (6)$$

In order to check the consistency of the time-resolved data reduction technique, all collected results are verified by the conventional TOT technique often used in the literature. The main advantage of the TOT technique is its formal independency from the ignition transient, as shown by (7) and (8). On the other hand, TOT results are intrinsically affected by relatively large errors especially when evaluated over small time intervals [17], being

$$r_{f,i+1/2} = \frac{1}{2} \frac{\bar{D}_{i+1} - \bar{D}_i}{t_{i+1} - t_i}, \quad (7)$$

$$G_{\text{ox},i+1/2} = \frac{\dot{m}_{\text{ox}}}{\pi \cdot (\bar{D}_{i+1} + \bar{D}_i)^2 / 16}. \quad (8)$$

In particular, a consistency test on the time-average regression rate is easily achieved by comparing the overall TOT regression rate (9) with the time-average analytical regression rate (10). The corresponding expressions for

the consistency check on G_{ox} are reported in (11) and (12) as follows:

$$\langle r_f \rangle_{\text{TOT}} = \frac{1}{2} \frac{\bar{D}_{\text{end}} - \bar{D}_{\text{ign}}}{t_{\text{end}} - t_{\text{ign}}}, \quad (9)$$

$$\langle r_f \rangle_{\text{an}} = \frac{1}{t_{\text{end}} - t_{\text{ign}}} \int_{t_{\text{ign}}}^{t_{\text{end}}} r_{fi}(t) dt, \quad (10)$$

$$\langle G_{\text{ox}} \rangle_{\text{TOT}} = \frac{\dot{m}_{\text{ox}}(t)}{\pi \cdot \left[(\bar{D}_{\text{end}} + \bar{D}_{\text{ign}})^2 / 16 \right]}, \quad (11)$$

$$\langle G_{\text{ox}} \rangle_{\text{an}} = \frac{1}{t_{\text{end}} - t_{\text{ign}}} \int_{t_{\text{ign}}}^{t_{\text{end}}} G_{\text{ox}}(t) dt. \quad (12)$$

A consistency test on the measured initial regression rate is achieved comparing the time-resolved experimental initial regression rate (reported in (13)) with the corresponding value calculated as shown in the following (14):

$$r_f(t_{\text{ign}}) = \frac{1}{2} a_D n_D (t_{\text{ign}} - t_0)^{n_D - 1}, \quad (13)$$

$$r_{fi} = \frac{1}{2} n_D \frac{\bar{D}_{\text{ign}} - D_0}{t_{\text{ign}} - t_0}. \quad (14)$$

The consistency of the adhoc defined ignition delay ($t_{\text{ign}} - t_0$) is checked comparing its value with the corresponding time based on a purely convective regime as suggested by Ohlemiller and Summerfield [19]:

$$t_{\text{ign, convective}} = \frac{\pi}{4} \alpha \left[\frac{\rho_f \cdot C_s \cdot \Delta T_s}{h^* \cdot \Delta T_g} \right]^2. \quad (15)$$

In this expression, the term ΔT_s represents the difference between final and initial solid fuel surface temperatures, while ΔT_g represents the difference between the flame temperature and the solid fuel temperature throughout the ignition transient (defined as the average value between ambient temperature and $T_s = 820$ K). The flame temperature was determined by thermochemical equilibrium calculations carried out with the NASA CEA code. The required convective heat exchange coefficient h^* was determined by the Gnielinski empirical correlation [20]:

$$\text{Nu}_D = \frac{(f/8)(\text{Re}_D - 1000)\text{Pr}}{1 + 12.7(f/8)^{1/2}(\text{Pr}^{2/3} - 1)}. \quad (16)$$

In the frame of the implemented time-resolved technique, each burning test yields an instantaneous r_f curve, and this is subjected to several consistency checks (9)–(14) before acceptance. The different $\bar{D}(t)$ of the single tests performed for a given formulation, under the same set of operating conditions (strand geometry, \dot{m}_{ox} and p_c), are then used to extract the corresponding ensemble average by a single power law interpolation of the kind of (2). The data reduction technique is finalized by constructing the cumulative time-average trends for both instantaneous and ensemble average curves. In order to evaluate the error bars for a given ensemble, a proper time (or G_{ox}) range is

identified considering the limits where the curves of all the performed single tests are defined. Over this latter interval, the error bars are evaluated by confidence intervals centered on the average value resulting from single test diameters at a given time (for (2)) or regression rates at a given G_{ox} . Confidence intervals are evaluated with 95% accuracy.

3.3. Tested Formulations and Ingredients. After testing the pure HTPB baseline, an extensive set of metallized HTPB-based formulations, including a variety of high-energy ingredients (e.g., aluminum, magnesium, boron, and magnesium hydride), was examined with the intent of evaluating the resulting increase in regression rate. Composition and properties of the HTPB baseline solid fuel are reported in Table 1. This inert polymeric binder is extensively used in full-scale engines and lab-scale testing because of its good mechanical properties, resistance to ageing, ease of production, and relative cost effectiveness.

Most loaded formulations concern nAl particles: both ALEX and L-ALEX powders were tested. While having identical nominal diameter (100 nm), the two powders differ because ALEX is uncoated (passivation in air), while L-ALEX is coated with a palmitic acid layer [21–23]. The ALEX powder was also combined with carbon or titanium oxide, in order to assess possible effects on powder dispersion. Likewise, a formulation containing ALEX, carbon, and magnesium (mass mean diameter of 44 μm) was tested, in order to exploit the magnesium flammability to ignite the aluminum particles.

Boron-based composite metals were also tested (Section 2). Since boron ignition is rather difficult to achieve because of the high temperatures needed for a sustained combustion process, a compound of magnesium and boron (MgB) was used. Mass composition of tested MgB composite is 20% Mg and 80% B, the latter component has a purity of 90%; therefore, the composite can be referenced as MgB90 (20% Mg). Particle size of MgB composite results submicrometric (mass mean diameter of 5.2 μm). Magnesium hydride (mass mean diameter of 47 μm) was also tested. Unfortunately this ingredient turns out to be particularly reactive with the HTPB polymeric binder, quickly oxidizing and reacting with the OH chemical groups. This way, macromolecules of polymeric binder are free to form a disorderedly reticulated compound with greatly increased viscosity. These unwanted effects limit the addition of magnesium hydrides powder to low mass percentages [24].

4. Ballistic Characterization: Results and Discussion

All results reported in this section were obtained under GOX at the same operating conditions: $p_c = 10$ bar and $m_{\text{ox}} = 1.67$ g/s (corresponding to an initial $G_{\text{ox}} = 140$ kg/(m²s)). For a matter of space, other results are not reported since they do not affect the general trends emerging at 10 bar.

4.1. HTPB Baseline. The ignition delay data are presented first and are reported in Figure 3. The numerically optimized

TABLE 1: Baseline (HTPB) solid fuel formulation and ingredients density.

Component (shorthand notation)	Mass fraction, % wrt fuel mass	Density (kg/m ³)	Supplier
HTPB-R45	79.0	901	Avio
DOA	13.1	920	Carlo Erba
IPDI	7.67	1061	Carlo Erba
TIN	0.23	1321	Carlo Erba
HTPB binder	100	915	—

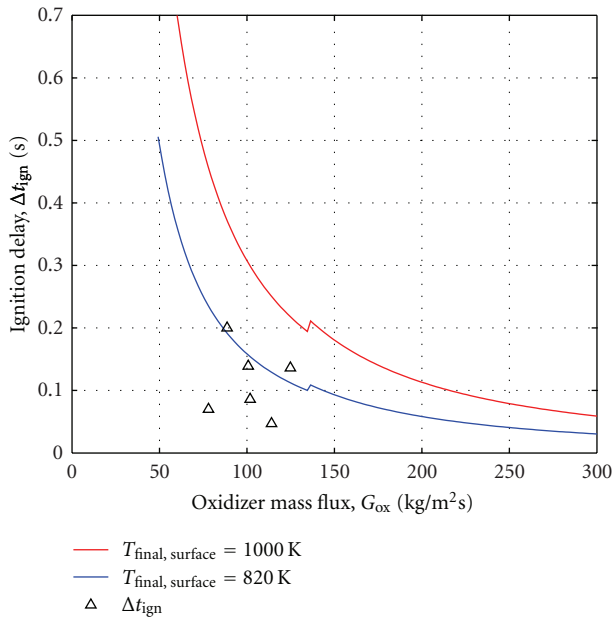


FIGURE 3: HTPB baseline: ignition delay. Experimental data and purely convective model by Ohlemiller and Summerfield [19], for two different final surface temperatures [25, 26].

ignition delays (see (2)) exhibit a general agreement with $(t_{\text{ign,convective}} - t_0)$ defined by (15).

After this step, the data-reduction procedure presented in Section 3.2 was carried out and produced the results presented in Figures 4 and 5. The instantaneous diameter change in time (2) is first determined, then the instantaneous regression rate is evaluated. This plot underlines the strong dependence of the hybrid combustion on the process fluid-dynamic properties, showing the highest regression rate in the initial combustion instants, when the oxidizer mass flux reaches its highest value. Notice that the oxidizer mass flux is maximum at ignition and then decreases in time, implying that, for all figures with oxidizer mass flux in the x -axis, time increases from right to left.

Figure 5 points out, with some data scattering, a similar ballistic response for all the HTPB tests: most of the curves show a steep initial slope and then a monotonic decrease in the final part of the combustion process.

In Figure 6, the instantaneous ensemble data are compared to the corresponding power law approximation, showing that a constant power does not provide a satisfactory estimate of the regression rate response in the initial part of

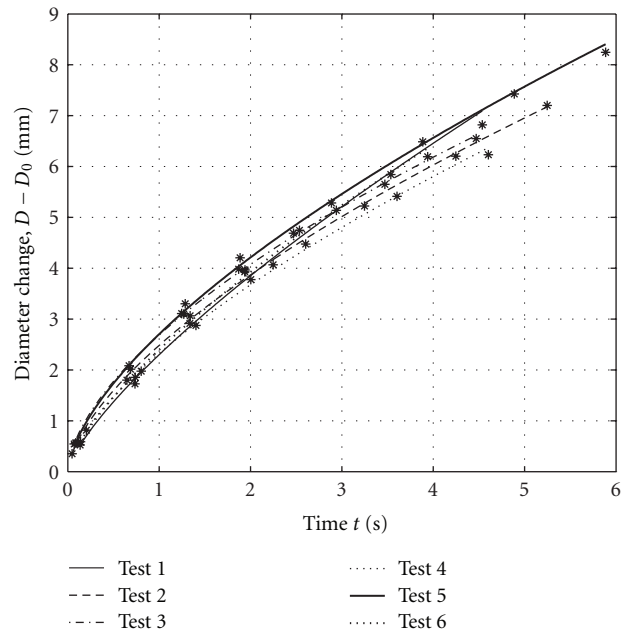


FIGURE 4: HTPB baseline: diameter change in time for all performed tests.

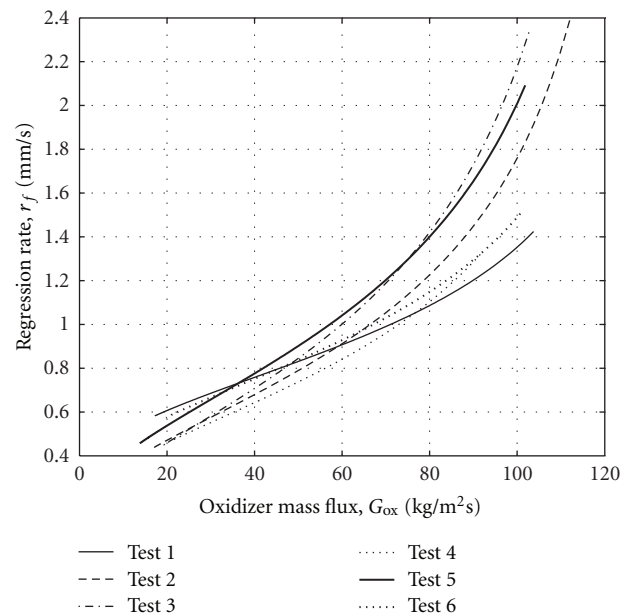


FIGURE 5: HTPB baseline: regression rate versus oxidizer mass flux for all performed tests.

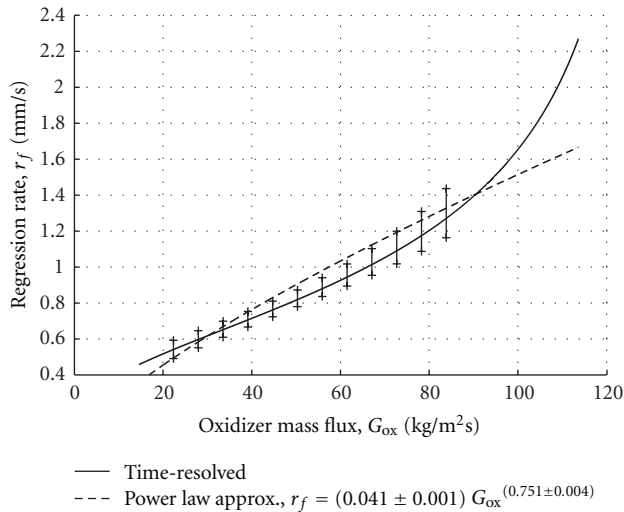


FIGURE 6: HTPB baseline: ensemble average, experimental data $r_f(G_{ox})$ and power law approximation, highlighting the diverging trends for $G_{ox} > 100$ kg/m²s.

the combustion process (say, $90 \leq G_{ox} \leq 110$ kg/(m²s)). In fact, while the TOT analysis and its power law approximation show a comparable pattern, the experimental data reduction brings to light a curve concavity opposite to the convexity of the power law approximation curve. The lack of agreement in the initial combustion instants is due to transient effects in the earlier phases of the combustion process, related to the establishment of the reacting turbulent boundary layer (see discussion in Section 6). A comparison between time-resolved and TOT data is reported in Figure 7. Discrete TOT values of r_f are in agreement with corresponding time-resolved data. The consistency check results for the HTPB baseline tests are shown in Tables 2 and 3. The percent variation between the different regression rate definitions are well below 5% for all presented tests, thus justifying the overall data handling procedure implemented in this work. In addition, the low variations in terms of mean regression rates show that the initial differences between the experimental data and their power law approximations do not lead to marked discrepancies in the mean values.

Finally, Figure 8 shows the actual trends of Re and O/F in G_{ox} . The parameters needed for Re evaluation are defined by the experimental O/F history during test. Note that the turbulent regime is lost for the low and final values of G_{ox} (say, $G_{ox} < 25$).

4.2. Effects of Metallized Additives. Once the HTPB baseline is fully characterized, it is possible to proceed with the evaluation of the ballistic characteristics of the innovative metallized formulations listed in Table 4. The same data handling procedure previously illustrated for HTPB was implemented yielding the experimental results shown in Figure 9 (nAl-containing formulations) and 10 (magnesium/boron-containing formulations), and compared to HTPB baseline.

As one can see also from Table 5, most of the tested metallized formulations show an increase in regression rate,

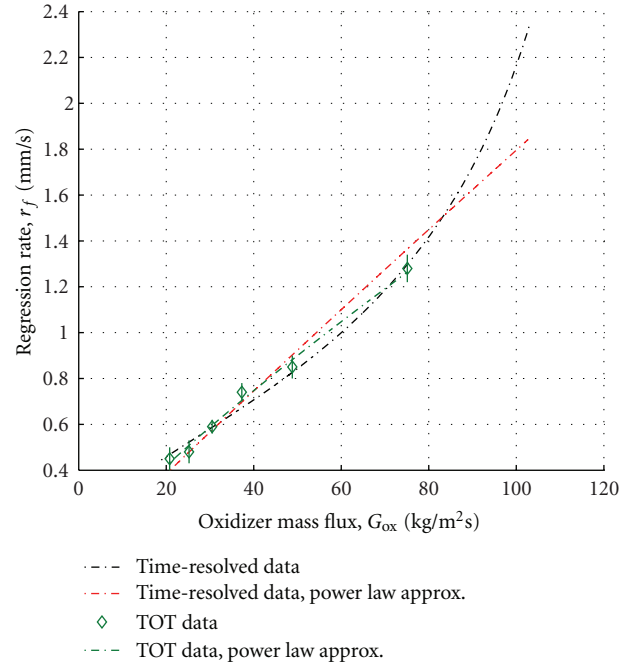


FIGURE 7: HTPB baseline, Test 3: example of experimental data $r_f(G_{ox})$ and TOT analysis results showing the different paths and concavities characterizing the two techniques.

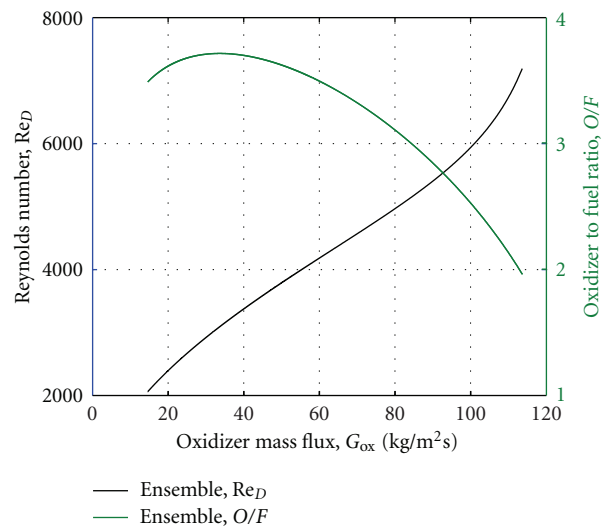


FIGURE 8: HTPB baseline: actual $Re(G_{ox})$ and $O/F(G_{ox})$ for the ensemble average.

with respect to pure HTPB, especially in the initial combustion instants, when the oxidizer mass flux is maximum; in the final part of the combustion process the metallized formulations exhibit regression rates closer—and sometimes even lower—than the HTPB baseline. This trend is probably explained by the fact that metal combustion is favored by the high oxidizer mass flux and turbulence level at the beginning of the test. Table 6 presents the regression coefficients for the constant power law approximation of the loaded formulations, while the corresponding data for

TABLE 2: HTPB baseline: optimization procedure comparing the initial regression rates $r_f(t_{\text{ign}})$ (13) and r_{f_i} (14).

Test number	Regression rate at ignition (13), $r_f(t_{\text{ign}})$, (mm/s)	Regression rate at ignition (14), r_{f_i} , (mm/s)	Percent variation $r_{f_i} - r_f(t_{\text{ign}})r_{f_i}$
1	1.424	1.436	0.8
2	2.389	2.390	0.1
3	2.334	2.337	0.1
4	1.319	1.323	0.3
5	2.092	2.102	0.5
6	1.506	1.509	0.2

TABLE 3: HTPB baseline: optimization procedure. Comparison between the two different techniques implemented to obtain the experimental mean regression rate.

Test number	Overall TOT regression rate (9), $\bar{r}_{f_{\text{TOT}}}$, (mm/s)	Integral time-average regression rate (10), \bar{r}_f , (mm/s)	Percent variation $\bar{r}_{f_{\text{TOT}}} - \bar{r}_f$ % $\bar{r}_{f_{\text{TOT}}}$
1	0.715	0.747	4.4
2	0.659	0.656	0.4
3	0.682	0.690	-1.0
4	0.616	0.632	-2.6
5	0.662	0.676	-2.1
6	0.737	0.760	-3.0

HTPB baseline are presented in Figure 6: the metal-loaded formulations show a great sensibility to the oxidizer mass flux variation, due to the occurrence of more complex phenomena than convection, as proven by the presence of exponent values greater than 1.

Contrary to expectations, coated L-ALEX showed lower regression than the uncoated ALEX, matching the baseline results. This behavior may be due to the fact that the coating process took place after the formation of cohesion clusters, thus involving groups of particles and subsequently deteriorating the powder characteristics. Literature sources also suggest that nonreactive coating layers do not radically modify the powder ignition temperature. Among the nAl augmented formulations, the one loaded with uncoated ALEX and carbon showed the highest increase in regression rate compared to the baseline, probably due to the great reactivity of ALEX and the simultaneous contribution of carbon to good powder dispersion in the matrix. In addition, carbon tends to reduce the thermal radiation penetration, hence avoiding decrease in regression rate results. Addition of TiO_2 to ALEX-loaded formulations shows a lower regression rate under low oxidizer mass flux, with a marked increase in regression rate under higher fluxes.

Addition of Mg or MgH_2 to ALEX-loaded formulations produced comparable results in increasing the regression rate, but without reaching the same results as the ALEX/carbon formulation. Results obtained for the formulations containing Mg or Boron, are shown in Figure 10. The first visible difference from the ALEX-containing ones is that, in this case, regression rates are faster than those of the baseline even under low levels of the oxidizer mass flux. Furthermore, one can see that the MgB compound is able to effectively overcome the well-known boron ignition problems. Indeed, the formulation containing only MgB

shows the best ballistic response, with a remarkable increase in regression rate, particularly under high oxidizer mass flux. As expected, magnesium hydride does not show impressive ballistic properties, thus supporting the experimental evidence regarding its reactivity with HTPB and the subsequent rheological properties change of the polymeric matrix. In particular, the addition of MgH_2 tends to worsen the characteristics of MgB-loaded formulations, enhancing its ignition problems and therefore decreasing its regression rate under high oxidizer mass flux. The simple addition of MgH_2 (in different percents) and the addition of Mg and MgB lead to comparable intermediate results: anyway, it seems to be preferable to add low percents of MgH_2 , in order to lessen the binder properties decline.

A comprehensive summary of the metallized formulations percent differences (both in terms of regression rate and fuel mass flow rate) compared to the baseline is presented in Table 5. One can verify that the formulations that show the highest improvement in regression rate under high values of the oxidizer mass flux are those loaded with ALEX/carbon and those loaded with Mg and/or MgB. But while Mg- and MgB-loaded formulations exhibit a regression rate improvement also under low flux levels, the one containing ALEX and carbon shows good properties only under the highest oxidizer mass flux levels, with rapidly decreasing regression rate and fuel mass flow rate in the final portion of the combustion run.

Figures 9 and 10 also show how the Mg- and MgB-containing formulations combustions start earlier and therefore at greater oxidizer mass flux levels than ALEX. The initial regression rate is particularly high, thus explaining why those formulations are particularly interesting, but it does not appear in Table 5 for lack of comparable baseline and ALEX-containing formulations data.

TABLE 4: Overview of the tested metal-loaded formulations.

Formulation	Number of samples	Port diameter (mm)	External sample diameter (mm)
HTPB + 10% ALEX + 2% C	4	4	18
HTPB + 10% ALEX + 2% TiO ₂	6	4	18
HTPB + 10% ALEX + 2% C + 2% Mg	3	4	18
HTPB + 10% L-ALEX	4	4	18
HTPB + 2.5% MgH ₂ + 1.4% MgB	4	4	18
HTPB + 2.5% MgH ₂	4	4	18
HTPB + 7.5% MgH ₂	8	4	18
HTPB + 5% MgH ₂ + 5% ALEX + 1% C	4	4	18
HTPB + 2.27% Mg + 1.4% MgB	4	4	18
HTPB + 2.8% MgB	2	4	18

TABLE 5: Metal-loaded formulations: regression rate and fuel mass flow rate percent differences at discrete values of oxidizer mass flux, compared to baseline.

Formulation	Regression rate percent difference (%)			
	Oxidizer mass flux (kg/(m ² s))			
	40	60	80	100
HTPB + 2.5% MgH ₂	8.25	16.47	25.39	37.19
HTPB + 7.5% MgH ₂	2.19	8.13	14.48	22.72
HTPB + 2.8% MgB	31.90	37.00	42.33	49.10
HTPB + 2.27% Mg + 1.4% MgB	28.63	33.53	38.67	45.19
HTPB + 2.5% MgH ₂ + 1.4% MgB	19.70	20.55	21.42	22.48
HTPB + 10% ALEX + 2% C	-22.57	3.58	38.87	—
HTPB + 10% ALEX + 2% TiO ₂	-32.49	-23.31	-12.80	1.96
HTPB + 10% L-ALEX	-11.82	-5.12	2.14	—
HTPB + 10% ALEX + 2% C + 2% Mg	-0.15	15.90	34.67	61.67
HTPB + 5% MgH ₂ + 5% ALEX + 1% C	-7.06	9.44	29.03	—
Formulation	Fuel mass flow rate percent difference (%)			
	Oxidizer mass flux (kg/(m ² s))			
	40	60	80	100
HTPB + 2.5% MgH ₂	9.31	17.62	26.63	38.54
HTPB + 7.5% MgH ₂	5.09	11.21	17.73	26.21
HTPB + 2.8% MgB	34.20	39.39	44.82	51.70
HTPB + 2.27% Mg + 1.4% MgB	31.16	36.16	41.40	48.05
HTPB + 2.5% MgH ₂ + 1.4% MgB	21.79	22.66	23.54	24.63
HTPB + 10% ALEX + 2% C	-16.51	11.69	49.74	—
HTPB + 10% ALEX + 2% TiO ₂	-26.51	-16.52	-5.08	10.99
HTPB + 10% L-ALEX	-5.65	1.52	9.28	—
HTPB + 10% ALEX + 2% C + 2% Mg	9.35	26.91	47.47	77.04
HTPB + 5% MgH ₂ + 5% ALEX + 1% C	-1.67	15.78	36.51	—

Finally, the effects of the ignition delay optimization procedure are shown in Figures 11 and 12: it is possible to see the consistent behavior of the various tested formulations and how almost all the data are comprised in a narrow range of times and oxidizer mass fluxes.

5. Effects of Radiant Heat Transfer

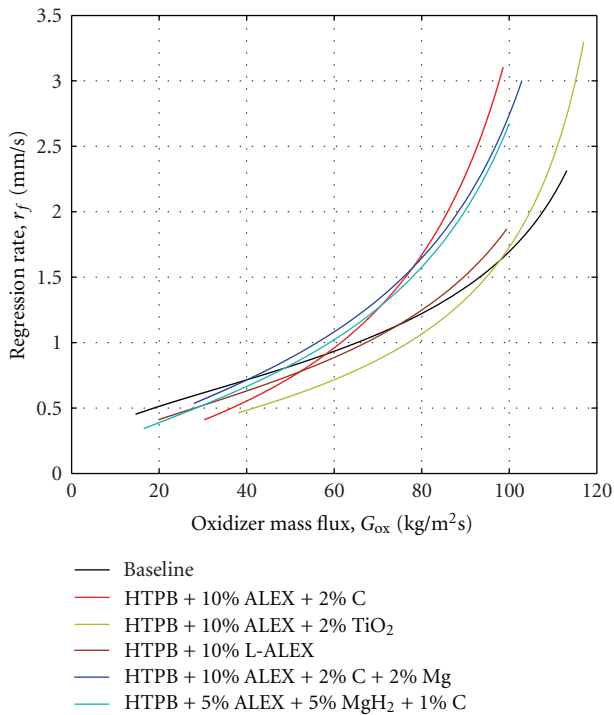
As recalled in Section 2, the recognized reference for hybrid rocket combustion is the diffusion-limited, purely convective ballistic model proposed by Marxman et al. [3, 4]. Data collected during this experimental investigation

show that the power law relationship for $r_f(G_{ox})$ identified by Marxman and coworkers is not fully consistent with the trend of instantaneous time-resolved data. The latter exhibits a different concavity with respect to its power law approximation, yielding a markedly larger r_f for high G_{ox} values (see Figure 6). This effect was reported also by Evans et al. during similar investigation on HREs combustion [27–29]. On the other hand, approximation of time-resolved data reported in Figure 6 shows $r_f \propto G_{ox}^{0.7}$.

Next, how important might be radiation in reproducing the obtained experimental results and explaining the previously mentioned differences was investigated. The original

TABLE 6: Additivated formulations: coefficients and uncertainties for constant power law approximation of the regression rate. For baseline data, see Figure 6.

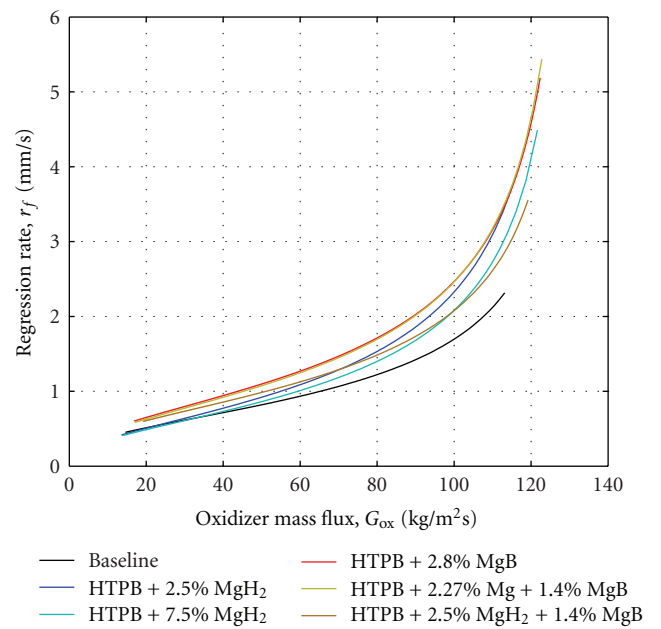
Formulation	a_r	n_r	R^2
HTPB + 2.5% MgH ₂	0.031 ± 0.001	0.901 ± 0.005	0.956
HTPB + 7.5% MgH ₂	0.028 ± 0.001	0.918 ± 0.006	0.940
HTPB + 2.8% MgB	0.002 ± 0.001	0.981 ± 0.013	0.897
HTPB + 2.27% Mg + 1.4% MgB	0.032 ± 0.001	0.930 ± 0.006	0.935
HTPB + 2.5% MgH ₂ + 1.4% MgB	0.043 ± 0.001	0.825 ± 0.005	0.946
HTPB + 10% ALEX + 2% C	0.001 ± 0.001	1.687 ± 0.008	0.976
HTPB + 10% ALEX + 2% TiO ₂	0.001 ± 0.001	1.639 ± 0.009	0.952
HTPB + 10% L-ALEX	0.026 ± 0.001	0.883 ± 0.004	0.972
HTPB + 10% ALEX + 2% C + 2% Mg	0.006 ± 0.001	1.272 ± 0.006	0.970
HTPB + 5% MgH ₂ + 5% ALEX + 1% C	0.013 ± 0.001	1.088 ± 0.005	0.971

FIGURE 9: ALEX-loaded formulations: ensemble average, experimental data $r_f(G_{ox})$ compared to baseline. Error bars are not reported to improve readability.

convective model requires modifications in order to include radiant heat flux contributions. To this purpose, the model proposed by Greatrix [30] was considered due to its simplified treatment of the reacting boundary layer with respect to the original work by Marxman and coworkers.

5.1. The Regression Rate Model by Greatrix. The model proposed by Greatrix aims at predicting the fuel regression rate, provided that the fundamental thermodynamic and fluid-dynamic properties are given. Starting point of the model is an energy balance at the gasifying fuel surface where only convective heat transfer is considered:

$$\rho_f r_f [C_s(T_s - T_i) - \Delta H_s] = h(T_f - T_s). \quad (17)$$

FIGURE 10: Magnesium-loaded formulations: ensemble average, experimental data $r_f(G_{ox})$ compared to baseline. Error bars are not reported to improve readability.

In (17), the overall r_f can be considered as the flux-depending regression, while the pressure-depending part can be neglected for hybrid systems; the convective fuel regression rate can thus be estimated as:

$$r_f = \frac{h(T_f - T_s)}{\rho_f [C_s(T_s - T_i) - \Delta H_s]}. \quad (18)$$

Changes of the thermodynamic and fluid-dynamic quantities are incorporated in the definition of the convective heat exchange coefficient, whereas all other parameters can be considered constant throughout the combustion process. The occurrence of gasified fuel blowing towards the reaction zone [3, 4] is taken into account thanks to

$$h = \frac{\rho_f r_f C_p}{\exp(\rho_s r_f C_p / h^*) - 1}. \quad (19)$$

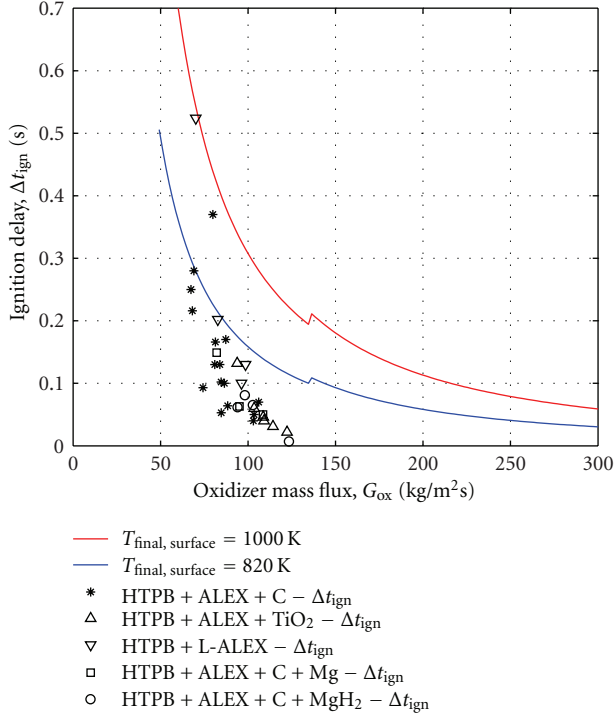


FIGURE 11: Ignition delay for aluminum-containing formulations. Comparison with the purely convective model by Ohlemiller and Summerfield [19], for two different final surface temperatures [25, 26].

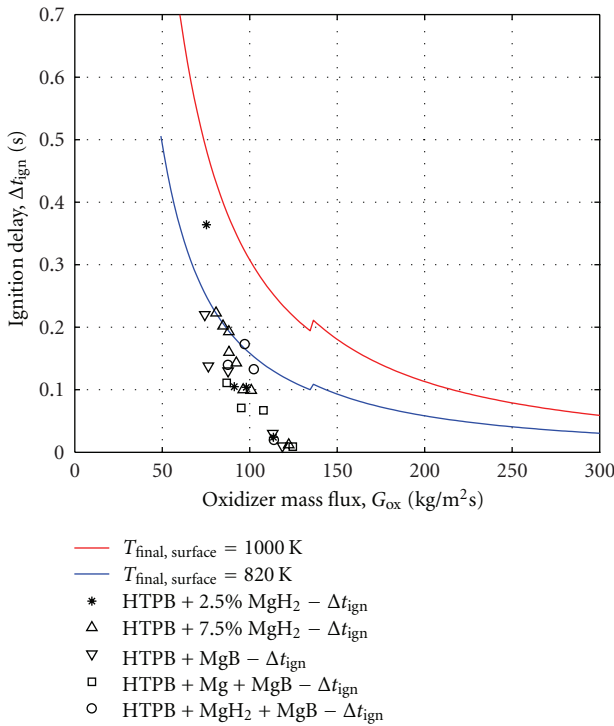


FIGURE 12: Ignition delay for magnesium-containing formulations. Comparison with the purely convective model by Ohlemiller and Summerfield [19], for two different final surface temperatures [25, 26].

From the Reynolds analogy, coupled with the definition of the Darcy-Weisbach friction factor (calculated with the Colebrook semiempirical correlation as reported in [20]), one obtains

$$(f^*)^{-1/2} = -2 \log_{10} \left[\frac{2.51}{\text{Re}_d(f^*)^{1/2}} + \frac{\epsilon/d}{3.7} \right]. \quad (20)$$

Therefore, the convective heat exchange coefficient without blowing can be evaluated as

$$h^* = \frac{k^{2/3} C_p^{1/3} G \cdot f^*}{\mu^{2/3} \cdot 8}. \quad (21)$$

The implicit (20), depending on the instantaneous values of the fluid-dynamic properties, can be resolved with the Newton numerical method; for HTPB-based fuels, the duct roughness ϵ is defined equal to $5 \mu\text{m}$ [30]. The regression rate can thus be defined as

$$r_f = \frac{h^*}{\rho_s C_p} \ln \left[1 + \frac{(T_f - T_s)}{(T_s - T_i - \Delta H_s/C_s)} \right]. \quad (22)$$

5.2. Extending the Regression Rate Model by Greatrix. In this section the work done to extend the original Greatrix model is discussed.

5.2.1. Effective Values of Thermodynamic and Transport Properties. The thermodynamic and transport properties of (22) require a proper evaluation. In particular, in the original Greatrix model, T_f , k , C_p , and μ are defined by values close to the ones characterizing the stoichiometric condition for the considered propellants. In the present study, a phenomenological approach is chosen for the r_f determination. Experimental, time-resolved data are considered as input for evaluating the effective values of thermodynamic and transport properties. In particular, experimental $\bar{D}(t)$ and $O/F(t)$ are considered. For each time-step of the combustion process, the associated O/F is used to determine the effective values of T_f , k , C_p , and μ , by thermochemical calculations by the NASA CEA code. As shown in Figure 8, the overall O/F exhibits values in the range from 1 to 4.5 under the investigated conditions. For the determination of the parameters defining h^* (21), knowing the histories of $\bar{D}(t)$ and $O/F(t)$ enables evaluating the histories of Re_D , and f^* (20) and (21).

The term ΔH_s appearing in (22) is defined according to literature data. As suggested by Lengellé et al., the net surface enthalpy is defined equal to -430 cal/g , [25]. This datum refers to the degradation process of reference HTPB. Surface temperature is considered equal to 820 K , from a previous work of Risha et al. on HTPB burning under pure oxygen [31]. In this first effort, the same values of ΔH_s and T_s were used for modeling of loaded formulations, in spite of the possible changes induced by energetic additives.

5.2.2. Radiant Heat Transfer Contributions. The experimental correlations available in the literature were reviewed.

In particular, Chiaverini et al. [13, 32] and Risha et al. [9, 31] reported detailed analyses comparing theoretical and experimental results. These approaches, while very promising and sufficiently accurate, in general are not valid for every formulation under every operating condition. Within this framework, the radiant heat transfer contribution was estimated for a variety of sources spanning from the gaseous combustion products to soot formation from the polymeric binder and to metal particulate dispersed in the gaseous phase. In-depth conduction in the solid fuel grain was not considered in this study.

The flame zone can be considered a source of thermal radiation, while the adjoining areas are not taken into account, as proposed by [13]: indeed, the flame zone represents the highest temperature zone in the gaseous flow and in the diffusion zone, where the highest concentration of gaseous combustion products (CO_2 , CO , and H_2O) can be detected. The emissivity of burnt gases can be determined according to (23), where $\Delta\epsilon$ is the negative contribution due to the possible overlapping of emissivity bands of CO_2 and H_2 [13]:

$$\epsilon_{\text{gas}} = \epsilon_{\text{H}_2\text{O}} + \epsilon_{\text{CO}_2} + \epsilon_{\text{CO}} - \Delta\epsilon. \quad (23)$$

A first correlation taking into account the radiant heat transfer due to combusted gases can thus be identified, as originally proposed by Marxman and coworkers to correct their purely convective model [3]:

$$q''_{r,g} = \sigma\epsilon_s(\epsilon_g T_f^4 - \alpha_g T_s^4), \quad (24)$$

where according to [13, 33]:

- (i) $\epsilon_s = 0.95$;
- (ii) $\epsilon_g = 1 \cdot 10^{-2} - 4 \cdot 10^{-2}$;
- (iii) $\alpha_g \cong \epsilon_g$.

Gas emissivity, according to [13], can be approximated as linearly varying from $1 \cdot 10^{-2}$ to $4 \cdot 10^{-2}$ in the range of $1.5 \leq O/F \leq 2.5$, while maintaining the highest value for $O/F > 2.5$.

Due to the large difference between surface temperature and flame temperature, it is plausible to suppose that radiant heat transfer towards the flame is negligible.

An alternative model for the gas-phase radiation was proposed by Strand et al. [11]. In this latter work, an explicit contribution from pressure was included as

$$q''_{r,g} = \sigma T_g^4 (1 - e^{k_s \cdot p_c \cdot D}). \quad (25)$$

In (25), the gas absorption coefficient is defined as reported in (26)

$$k_g = 9.33 \cdot 10^{-4} - 6.19 \cdot 10^{-6} \cdot p_c + 1.79 \cdot 10^{-8} \cdot p_c^2. \quad (26)$$

Since, under the investigated conditions, p_c exerts a limited influence on r_f , in spite of the explicit pressure dependence, (25) is not considered very relevant.

It is important to point out that the main radiant heat source, about 80% of the total value, is due to soot (partially unburned solid fuel particles in the gas phase). An approximation of this contribution [7, 13], considering experimental data, is given as

$$q''_{r,\text{soot}} = \sigma T_g^4 (1 - e^{k_s}). \quad (27)$$

In the latter (27), the soot absorption coefficient can be defined as

$$k_s = 0.51 - 0.113 \frac{O}{F}, \quad \left(1.5 \leq \frac{O}{F} \leq 3.5\right), \quad (28)$$

where the absence of pressure dependences and the appearance of an explicit dependence on O/F can be noted.

For Al-containing formulations, an additional radiant heat flux emission is defined taking into account the radiation effects due to the presence of $\text{Al}/\text{Al}_2\text{O}_3$ particles [28]:

$$q''_{r,\text{Al}} = \sigma\epsilon_{\text{Al}/\text{Al}_2\text{O}_3} (T_b^4 - T_s^4). \quad (29)$$

In (29), T_b is the boiling temperature of aluminum (2792 K) and the emissivity of $\text{Al}/\text{Al}_2\text{O}_3$ is taken equal to 0.1, [34].

5.3. Extended Greatrix Regression Rate Model. The original purely convective Greatrix model was extended to include radiation effects by writing the surface energy balance of (17) as

$$\rho_s r_f [C_s (T_s - T_i) - \Delta H_s] = h (T_f - T_s) + q''_r. \quad (30)$$

The radiant heat flux term q''_r refers to the sum of several single contributions defined in Section 5.2.2. As for thermodynamic and thermal properties, also the radiant heat transfer terms for combustion gases and soot are evaluated for each time step of the burning process, considering the experimental O/F history as input. Under the considered circumstances, the extended phenomenological model of the regression rate gives

$$r_f = \frac{h (T_f - T_s) + q''_r}{\rho_s [C_s (T_s - T_i) - \Delta H_s]}. \quad (31)$$

This latter form was implemented for the time-resolved ballistic analysis as shown in the next section.

6. Results

Three different fuel formulations are considered in this part of the study: HTPB baseline, HTPB loaded with 2% C and 10% ALEX, and HTPB loaded with 2.8% MgB90 (20% Mg). The three fuel formulations are characterized by different contributions to the radiant heat flux. In particular, for all of the tested formulations the combustion gases and soot contributions given by (24) and (27) are present. Under the investigated conditions, the latter (27) is considered valid

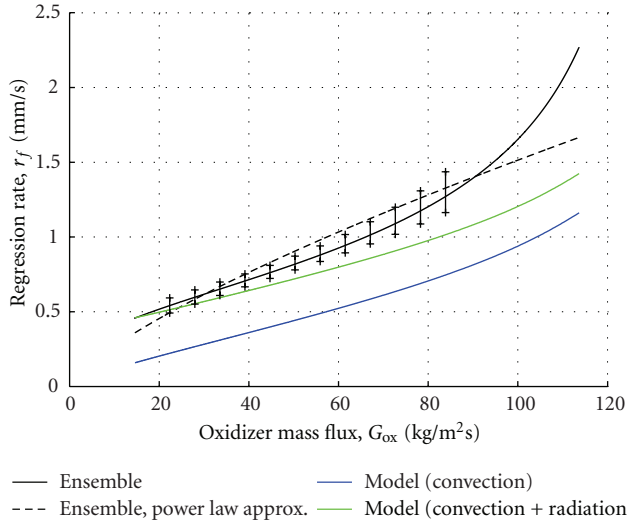


FIGURE 13: HTPB baseline: ensemble average of experimental data for $r_f(G_{ox})$ with its power law approximation and extended Greatrix model.

over the tested O/F range. When dealing with HTPB loaded with ALEX, the additional term accounting for emissivity of Al/Al_2O_3 particles (29) is considered.

Overall, the results obtained show a quite different behavior from the original purely convective model.

In Figure 13, the results achieved for HTPB baseline considering a pure convection regime and the extended model (31) are reported in terms of $r_f(G_{ox})$. Time-resolved instantaneous, ensemble average r_f and its power law approximation are reported in the same Figure 13. Resorting to the effective values of thermal and transport properties yields $r_f(G_{ox})$ curves with a similar concavity with respect to the experimental data for both convective and extended models. This result is unlikely by a conventional approach based on fixed values of thermal and transport properties. Considering the radiant heat transfer term, the $r_f(G_{ox})$ behavior provides a better representation of the experimental data, in spite of a marked difference for $G_{ox} \geq 100 \text{ kg}/(\text{m}^2\text{s})$. In this region one can speculate about possible transient effects due to the development of the reacting boundary layer, determining a marked regression rate increase, such as high oxidizer mass flux, high turbulence level, and probably other reasons as well.

The results concerning the $r_f(G_{ox})$ response including radiant heat transfer for HTPB loaded with ALEX and MgB90 (20% Mg) are reported in Figures 14 and 15 respectively. For these formulations, the extended Greatrix model shows a good agreement in $r_f(G_{ox})$ with experimental data but limited to the low G_{ox} region.

Differences between experimental and model results for metallized formulations are mainly related to the assumption of the same ΔH_s value used for HTPB baseline. Loading the solid fuel grain with metals enhance solid fuel reactivity. An evidence of this is the reduced ignition delay of metallized fuel formulations with respect to HTPB baseline (see Figures 3, 11, and 12). As a consequence of the enhanced reactivity,

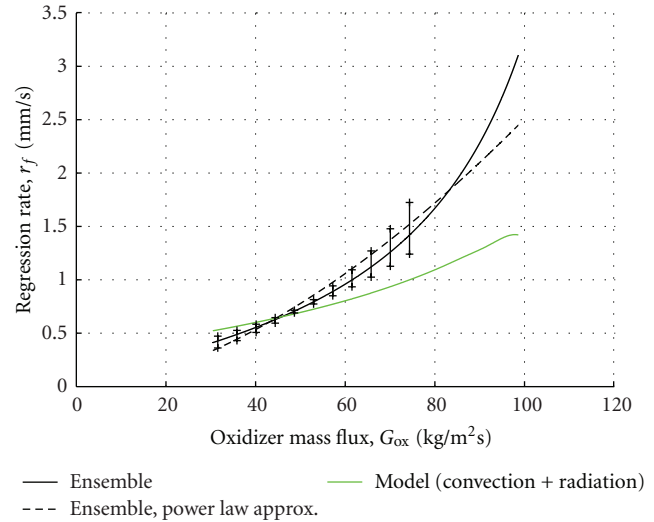


FIGURE 14: HTPB, loaded with ALEX and Carbon: ensemble average of experimental data for $r_f(G_{ox})$ with its power law approximation and extended Greatrix model.

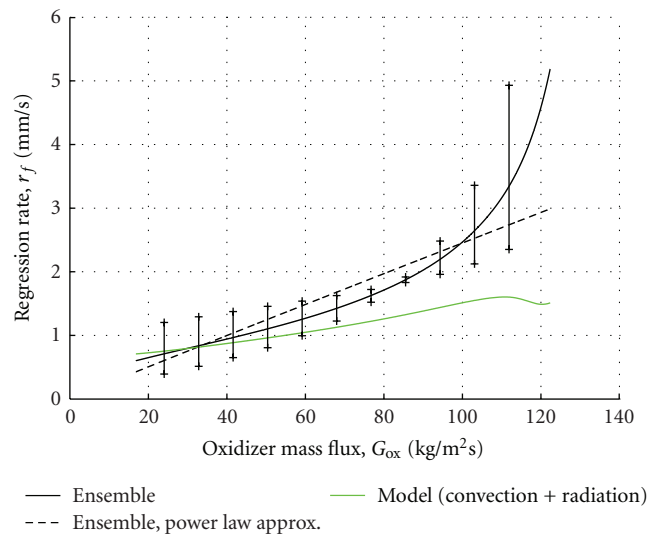


FIGURE 15: HTPB, loaded with MgB90 (20% Mg): ensemble average of experimental data for $r_f(G_{ox})$ with its power law approximation and extended Greatrix model. Note model r_f results for $G_{ox} \geq 100 \text{ kg}/(\text{m}^2\text{s})$ exhibiting a non-monotonic trend.

particular attention should be given to ΔH_s . This parameter should exhibit a less endothermic behavior for metal-loaded fuel formulations than inert binder, thus providing a r_f increase with respect to the currently achieved behavior.

Model data for metallized fuel formulations, and notably MgB-loaded HTPB, exhibit nonmonotonic behavior of r_f for decreasing G_{ox} in the earlier phases of the combustion. This result is mainly related to the marked nonmonotonic and nonlinear behavior of thermodynamic and transport properties for the relatively low O/F values characterizing the initial phases of burning.

In spite of the discussed effects, the proposed approach enable to define in all cases a $r_f(G_{ox})$ curve characterized by a similar trend with respect to the experimental time-resolved data.

7. Conclusions and Future Developments

A systematic ballistic characterization of innovative HRE solid fuels was performed, by implementing an optical time-resolved technique able to provide the instantaneous regression rates and other relevant ballistic parameters. All experiments were conducted for HTPB-based solid fuels under GOX, with $p_c = 10$ bar and $\dot{m}_{ox} = 1.67$ g/s (corresponding to an initial $G_{ox} = 130$ kg/(m²s)), but extension to a wider set of operating conditions is already in progress. The performed measurements clearly point out that $r_f(G_{ox})$ exhibits a peculiar monotonic growth with G_{ox} (e.g., see Figure 5), whose power law approximation however features an exponent close to the 0.8 value predicted by Marxman [3, 4]. The performed measurements also show that adding ALEX or MgB to HTPB speeds up the regression rate of solid fuels especially under the highest oxidizer mass fluxes and turbulence levels.

The Greatrix convective regression rate model was revised and extended to include the actual *O/F* history in time with the corresponding thermophysical properties of the burned mixture. Moreover, radiant flux contributions from both the hot gases and soot particles were accounted for HTPB-based formulations resorting to optical properties from the literature [7, 13]. Considering radiant heat transfer, a better agreement between model results and experimental data is achieved in terms of r_f for HTPB baseline, while metallized formulations still show discrepancies that will be addressed in future works.

Recommended developments are to determine experimentally radiant heat fluxes for high-energy ingredients under a wider set of operating conditions (e.g., extending the G_{ox} and p_c ranges). Moreover, specific attention will be given to the value of ΔH_s needed to implement the extended model.

Nomenclature

Abbreviations

2D:	Two-dimensional
ALEX:	Aluminum exploded (100 nm, uncoated)
an:	Analytical
B90:	Boron with 90% purity
CEA:	Chemical equilibrium with application
DOA:	Dioctyl adipate
GOX:	Gaseous oxygen
HRE:	Hybrid rocket engine
HTPB:	Hydroxyl-terminated polybutadiene
IPDI:	Isophorone diisocyanate
L-ALEX:	Aluminum exploded (100 nm, coated with palmitic acid)
MgB:	Magnesium-boron composite
nAl:	Nanosized aluminum

NASA:	National Aeronautics and Space Administration
OD:	Outer diameter, mm
Re _D :	Reynolds number (based on diameter)
TIN:	Dibutyltin diacetate
TOT:	Thickness over time
wrt:	With reference to.

Chemical Symbols

Al:	Aluminum
B:	Boron
C:	Carbon
Mg:	Magnesium
MgH ₂ :	Magnesium hydride
TiO ₂ :	Titanium oxide.

Latin Symbols

a_D :	Multiplier factor in(2)
A_f :	Port regressing surface area, mm ²
C_p :	Constant pressure specific heat (gas phase), J/kg·K
C_s :	Solid phase specific heat, J/kg·K
D :	Diameter, mm
D_0 :	Nominal initial port diameter, mm
\bar{D} :	Space-average mean diameter, mm
\bar{D}_{end} :	Space-average diameter at measurement completion, mm
\bar{D}_{ign} :	Space-average diameter at ignition, mm
\bar{D}_i :	Sampled space-average diameter (ith value), mm
f^* :	Friction factor without blowing
G :	Total mass flux, kg/(m ² · s)
G_f :	Fuel mass flux, kg/(m ² s)
G_{ox} :	Oxidizer mass flux, kg/(m ² s)
h :	Convective heat transfer coefficient with blowing, W/(m ² · K)
h^* :	Convective heat transfer coefficient without blowing, W/(m ² · K)
k :	Conductive heat transfer coefficient (of the gas phase), W/(m · K)
k_g :	Gas absorption coefficient
k_s :	Soot absorption coefficient
L_s :	Fuel sample length, mm
\dot{m}_f :	Fuel mass flow rate, g/s
\dot{m}_{ox} :	Oxidizer mass flow rate, g/s
n_D :	Time exponent in (2)
<i>O/F</i> :	Oxidizer-to-fuel ratio
p_c :	Chamber pressure, bar
$q''_{r,Al}$:	Radiant heat flux due to Al/Al ₂ O ₃ , W/m ²
$q''_{r,g}$:	Radiant heat flux due to burnt gases, W/m ²
$q''_{r,soot}$:	Radiant heat flux due to soot, W/m ²
r_f :	Regression rate, mm/s
$\langle r_f \rangle$:	Time-average regression rate, mm/s
r_{fi} :	Measurement initial regression rate, mm/s
r_u :	Mass flux-depending regression rate, mm/s
R^2 :	Correlation index
t :	Time, s

t_i : Sampling time (i th value), s
 t_0 : Reference time in (2), s
 t_{end} : Measurement completion time, s
 t_{ign} : Ignition time, s
 T_b : Boiling temperature, K
 T_i : Initial fuel temperature, K
 T_f : Flame temperature, K
 T_g : Gas temperature, K
 T_s : Fuel surface temperature, K.

Greek Symbols

α : Thermal diffusivity m^2/s
 α_g : Gas phase adsorption coefficient
 ΔH_s : Solid-phase vaporization enthalpy balance, cal/g
 ϵ : Regressing surface roughness, μm
 $\epsilon_{\text{Al/Al}_2\text{O}_3}$: Al/Al₂O₃ emissivity, W/m^2
 ϵ_s : Solid-phase emissivity
 ϵ_g : Gas-phase emissivity
 μ : Gas-phase viscosity, $\text{kg}/(\text{m}\cdot\text{s})$
 ρ_f : Solid fuel density, kg/cm^3
 σ : Stefan-Boltzmann constant, $\text{W}/(\text{m}^2 \cdot \text{K}^4)$.

Acknowledgments

This work was partially supported by ORPHEE (Operational Research Project on Hybrid Engine in Europe), European FP7 Program. Theme 9: Space, Area: SPA-2007.2.2.02–Space Transportation, Grant Agreement 218830 and SPARTAN (SPAcE exploration Research for Throttleable Advanced eNginE), Research Area: SPA.2010.2.1-04—Space Transportation for Space Exploration. MACH I (King of Prussia, PA, USA) and Advanced Powder Technology LLC (Tomsk, Russia) are acknowledged for the supplied materials and the precious collaboration.

References

- [1] L. T. de Luca, *Energetic Problems in Aerospace Propulsion*, chapter 12, Politecnico di Milano, 1st edition, 2007.
- [2] G. P. Sutton, *Rocket Propulsion Elements*, John Wiley & Sons, 6th edition, 1992.
- [3] G. Marxman and M. Gilbert, “Turbulent boundary layer combustion in the hybrid rocket,” *Symposium (International) on Combustion*, vol. 9, no. 1, pp. 371–383, 1963.
- [4] G. A. Marxman, “Fundamentals of hybrid boundary layer combustion,” in *Heterogeneous Combustion Conference*, December 1963.
- [5] D. Altman, “Highlights in hybrid rocket propulsion,” in *Proceedings of the 10th International Workshop on Combustion and Propulsion*, p. 17, Lerici La Spezia, Italy, September 2003.
- [6] D. Altman and A. Holzmann, “Overview and history of hybrid rocket propulsion,” in *Fundamentals of Hybrid Rocket Combustion and Propulsion*, M. J. Chiaverini and K. K. Kuo, Eds., vol. 218, chapter 1, pp. 1–36, AIAA Progress in Astronautics and Aeronautics, 2007.
- [7] M. J. Chiaverini and K. K. Kuo, *Fundamentals of Hybrid Rocket Combustion and Propulsion*, AIAA, 2006.
- [8] R. A. Yetter, G. A. Risha, and S. F. Son, “Metal particle combustion and nanotechnology,” *Proceedings of the Combustion Institute*, vol. 32, no. 2, pp. 1819–1838, 2008.
- [9] G. A. Risha, B. J. Evans, E. Boyer, R. B. Wehrmann, and K. K. Kuo, “Nano-sized aluminum- and boron-based solid-fuel characterization in a hybrid rocket engine,” in *Proceedings of the 39th AIAA/ASME/SAE/ASEE Joint Propulsion Conference*, July 2003.
- [10] L. D. Smoot and C. F. Price, “Regression rates of non-metallized hybrid fuels systems,” *AIAA Journal*, vol. 3, pp. 1408–1413, 1965.
- [11] L. D. Strand, M. D. Jones, R. L. Ray, and N. S. Cohen, “Characterization of hybrid rocket internal heat flux and HTPB fuel pyrolysis,” in *Proceedings of the 30th AIAA/ASME/SAE/ASEE Joint Propulsion Conference*, June 1994.
- [12] P. Estey, D. Altman, and J. McFarlane, “An evaluation of scaling effects for hybrid rocket motors,” in *Proceedings of the 27th AIAA/ASME/SAE/ASEE Joint Propulsion Conference*, June 1991.
- [13] M. J. Chiaverini, K. K. Kuo, A. Peretz, and G. C. Harting, “Regression-rate and heat-transfer correlations for hybrid rocket combustion,” *Journal of Propulsion and Power*, vol. 17, no. 1, pp. 99–110, 2001.
- [14] A. Gany, “Comprehensive consideration of boron combustion in airbreathing propulsion,” in *Proceedings of the 42nd AIAA/ASME/SAE/ASEE Joint Propulsion Conference*, pp. 2592–2603, July 2006.
- [15] L. T. DeLuca, L. Galfetti, G. Colombo et al., “Innovative solid fuels and propellants loaded with metals and hydrides,” SPLab Report to CNES under Commande No. 4700028003/DLA094, 2009.
- [16] L. T. DeLuca, L. Galfetti, G. Colombo et al., “Time-resolved burning of solid fuels for hybrid rocket propulsion,” in *Advances in Propulsion Physics*, vol. 2, pp. 341–362, Taurus Press, Moscow, Russia, 2011.
- [17] T. J. Houser and M. V. Peck, “Research in hybrid combustion,” in *AIAA Progress in Astronautics and Aeronautics, Heterogeneous Combustion*, H. G. Wolfhard, I. Glassman, and L. Green Jr., Eds., pp. 559–581, 1964.
- [18] B. Evans, N. A. Favorito, E. Boyer, G. A. Risha, R. B. Wehrman, and K. K. Kuo, “Characterization of nanosized energetic particle enhancement of solid-fuel burning rates in an x-ray transparent hybrid rocket engine,” in *Proceedings of the AIAA/ASME/SAE/ASEE Joint Propulsion Conference and Exhibit*, Fort Lauderdale, Fla, USA, July 2004.
- [19] T. J. Ohlemiller and M. Summerfield, “A critical analysis of arc image ignition of solid propellants,” *AIAA Journal*, vol. 6, no. 5, pp. 878–886, 1967.
- [20] F. P. Incropera and D. de Witt, *Fundamentals of Heat and Mass Transfer*, John Wiley & Sons, 3rd edition, 1990.
- [21] Y. S. Kwon, A. A. Gromov, A. P. Ilyin, and G. H. Rim, “Passivation process for superfine aluminum powders obtained by electrical explosion of wires,” *Applied Surface Science*, vol. 211, no. 1–4, pp. 57–67, 2003.
- [22] Y. F. Ivanov, M. N. Osmonoliev, V. S. Sedoi et al., “Productions of ultra-fine powders and their use in high energetic compositions,” *Propellants, Explosives, Pyrotechnics*, vol. 28, no. 6, pp. 319–333, 2003.
- [23] A. A. Gromov, A. P. Il’In, U. Foerter-Barth, and U. Teipel, “Effect of the passivating coating type, particle size, and storage time on oxidation and nitridation of aluminum powders,” *Combustion, Explosion and Shock Waves*, vol. 42, no. 2, pp. 177–184, 2006.

- [24] P. Selvam, B. Viswanathan, C. S. Swamy, and V. Srinivasan, "Magnesium and magnesium alloy hydrides," *International Journal of Hydrogen Energy*, vol. 11, no. 3, pp. 169–192, 1986.
- [25] G. Lengellé, J. C. Gordon, B. Fourest, and C. Guin, "Condensed-phase behavior and ablation rate of fuels for hybrid propulsion," in *Proceedings of the 9th Joint Propulsion Conference and Exhibit*, June 1993.
- [26] M. A. Karabeyoglu, D. Altman, and B. J. Cantwell, "Combustion of liquefying hybrid propellants: part 1, General theory," *Journal of Propulsion and Power*, vol. 18, no. 3, pp. 610–620, 2002.
- [27] D. A. Kearney and W. W. Geiman, "Accounting for planned fuel expulsion by hybrid rockets," in *Proceedings of the 41st AIAA/ASME/SAE/ASEE Joint Propulsion Conference and Exhibit*, Tucson, Ariz, USA, July 2005.
- [28] B. Evans, N. A. Favorito, E. Boyer, and K. K. Kuo, "Characterization of solid fuel mass-burning enhancement utilizing an x-ray translucent hybrid rocket motor," in *Proceedings of the 7th International Symposium on Special Topics in Chemical Propulsion*, pp. 705–724, 2005.
- [29] B. Evans, N. A. Favorito, and K. K. Kuo, "Oxidizer-type and aluminum-particle addition effects on solid-fuel burning behavior," in *Proceedings of the 42nd AIAA/ASME/SAE/ASEE Joint Propulsion Conference*, pp. 3538–3547, Sacramento, Calif, USA, July 2006.
- [30] D. R. Greatrix, "Model for predicting fuel regression rate in hybrid rocket engines," in *Proceedings of the 43rd AIAA/ASME/SAE/ASEE Joint Propulsion Conference*, pp. 3436–3443, July 2007.
- [31] G. A. Risha, G. C. Harting, K. K. Kuo et al., "Pyrolysis and combustion of solid fuels in various oxidizing environments," in *Proceedings of the 34th AIAA/ASME/SAE/ASEE Joint Propulsion Conference*, pp. 98–3184, Cleveland, Ohio, USA, July 1998.
- [32] M. J. Chiaverini, N. Serin, D. K. Johnson, Y. C. Lu, K. K. Kuo, and G. A. Risha, "Regression rate behavior of hybrid rocket solid fuels," *Journal of Propulsion and Power*, vol. 16, no. 1, pp. 125–132, 2000.
- [33] M. F. Modest, *Radiative Heat Transfer*, McGraw-Hill, New York, NY, USA, 1993.
- [34] M. Q. Brewster and D. M. Taylor, "Radiative properties of burning aluminum droplets," *Combustion and Flame*, vol. 72, no. 3, pp. 287–299, 1988.

Research Article

Feasibility Study and Demonstration of an Aluminum and Ice Solid Propellant

Timothee L. Pourpoint, Tyler D. Wood, Mark A. Pfeil, John Tsohas, and Steven F. Son

School of Aeronautics and Astronautics, Purdue University, 500 Allison Road, West Lafayette, IN 47907, USA

Correspondence should be addressed to Timothee L. Pourpoint, timothee@purdue.edu

Received 11 March 2012; Accepted 25 May 2012

Academic Editor: Valsalayam Sanal Kumar

Copyright © 2012 Timothee L. Pourpoint et al. This is an open access article distributed under the Creative Commons Attribution License, which permits unrestricted use, distribution, and reproduction in any medium, provided the original work is properly cited.

Aluminum-water reactions have been proposed and studied for several decades for underwater propulsion systems and applications requiring hydrogen generation. Aluminum and water have also been proposed as a frozen propellant, and there have been proposals for other refrigerated propellants that could be mixed, frozen in situ, and used as solid propellants. However, little work has been done to determine the feasibility of these concepts. With the recent availability of nanoscale aluminum, a simple binary formulation with water is now feasible. Nanosized aluminum has a lower ignition temperature than micron-sized aluminum particles, partly due to its high surface area, and burning times are much faster than micron aluminum. Frozen nanoscale aluminum and water mixtures are stable, as well as insensitive to electrostatic discharge, impact, and shock. Here we report a study of the feasibility of an nAl-ice propellant in small-scale rocket experiments. The focus here is not to develop an optimized propellant; however improved formulations are possible. Several static motor experiments have been conducted, including using a flight-weight casing. The flight weight casing was used in the first sounding rocket test of an aluminum-ice propellant, establishing a proof of concept for simple propellant mixtures making use of nanoscale particles.

1. Introduction

Aluminum powder is a common ingredient in conventional solid rocket propellants. It is used to increase specific impulse, I_{sp} , as well as stability. The properties and recent availability of nanoscale aluminum (nAl) have motivated recent efforts in new solid propellant formulations. For example, Kuo et al. [1] discussed the potential use of nanosized powders for rocket propulsion in a recent paper. Many of the potential advantages listed for these particles are short ignition delay, fast burning times, and the possibility to act as an energetic gelling agent. Using nAl has been shown to produce a significant increase in performance with conventional solid propellants [2, 3]. Researchers showed that replacing 50 μm particles with the same amount of nominally 100 nm particles in AP-based propellants could result in a burning rate increase of up to 100% [4]. Most of these characteristics can be attributed to the high-specific surface area of the nanoscale particles [1, 5]. The possible

drawbacks of nAl are the reduction in active aluminum content, electrostatic discharge (ESD) sensitivity when dry, and poor rheological properties. Other research has been conducted pairing this increased reactivity of nAl with less reactive oxidizers such as water in addition to conventional oxidizers [6, 7]. Aluminum and water propellants may prove to be suited for deep space exploration in that propellants could be made in situ from available water and aluminum. Also, the products of this propellant, mainly H_2 and Al_2O_3 , are relatively nontoxic, making it a “greener” propellant [8, 9].

The objectives of this paper are to present results of nAl/ice (ALICE) small-scale static experiments, along with the launch of a sounding rocket powered by ALICE. Another objective was to develop larger scale (kilogram scale) mixing procedures that produce a consistent material. A classical mixer and a newly available Resodyn mixer were considered. The burning rate was characterized for these propellants in

a strand burner. Results of the static test firings are also compared against internal ballistic predictions.

2. Background

While bulk commercial nAl has only recently been developed, the water-aluminum reaction received attention as early as the 1940s. In 1942, Rasor and Portland [10] filed a patent, which proposed to use seawater and aluminum to propel a submarine. While thermodynamically this reaction would be viable, the kinetics of the available aluminum would not yield complete reaction. This was evident by work done by Elgert and Brown [11] who used U235 to melt the aluminum but could only react 0.2% of the aluminum, even though temperatures reached $\sim 1200^\circ\text{C}$. Even work done by Leibowitz and Mishler [12], who tried igniting aluminum with a laser, found that if the melting temperature of the aluminum oxide was not reached, ignition would not occur.

Several studies investigated the use of micron-sized Al powders with water for underwater propulsion [13, 14]. In 2004, Ingenito and Bruno [8] also published a paper discussing the potential uses for an aluminum-water mixture for space propulsion. Using the NASA CEA equilibrium code, they calculated the theoretical specific impulse values of mixtures over a range of oxidizer-to-fuel (O/F) ratios. Assuming an expansion ratio of 100, the calculated vacuum I_{sp} at an O/F of ~ 1.2 is greater than 300 s and higher than that of most solid propellants [15]. Ingenito and Bruno also proposed the idea of adding hydrogen peroxide (H_2O_2) to increase performance. Indeed, many other propellant formulations are possible [8].

Nanoscale aluminum can dramatically increase the reaction rates of aluminum and water. Ivanov et al. [16] reported the earliest combustion work with stoichiometric mixtures of nAl and water. They reported needing 3% polyacrylamide to thicken (or gel) the water and enable the nAl-water reaction. In 2006, Risha et al. [17] reported, for the first time, the combustion of nAl and water without the use of a gelling agent. Risha's successful results were likely attributable to a higher surface area nAl than previously used. Risha et al. found that stoichiometric mixtures of nAl-water propellant have a pressure dependence of around 0.47 and have densities of around 1.5 g/cm^3 . While the burning rate for a fuel-lean mixture was lower than a stoichiometric mixture, the pressure exponents were similar. This suggests that the propellant has the same pressure dependence, regardless of the amount of excess water.

Upon production by manufacturers, such as Novacentrix Inc. and Argonide Corp, aluminum powders form a passivation layer of alumina. Even with this passivation layer, nAl-water can have a short shelf life, on the order of weeks, when exposed to moist air due to the high affinity of nAl for oxygen [18]. The inert alumina shell adversely affects the performance of the mixture [5, 17]. Due to the smaller size of the aluminum particles (from micron to nano), the alumina layer accounts for more of the mass in nAl particles. Dokhan et al. [19] estimate that active aluminum content of micron aluminum is 99.5% or better, while the active aluminum

content of passivated nAl typically ranges from 50% to 95% [18, 20, 21].

Franson et al. [22] performed perhaps the first work on the implementation of ALICE in a rocket motor configuration. The outer diameter of the grain was 86 mm, with an inner perforation diameter of 60 mm and a length of 157 mm. The total mass of the grain using a combination of micron and nanoscale aluminum was 550 g. Postinspection of the motor revealed large amounts of alumina residues in the chambers. Analysis of the slag showed that $\sim 17\%$ of the initial aluminum did not participate in the reaction. This helped explain the observed maximum pressure of 1.6 MPa compared to the 3 MPa expected value.

In previous work by our group, we examined the aging characteristics of aluminum and water mixtures. One method to increase shelf life is to freeze the aluminum water mixture to form ALICE. Sippel et al. [18] showed that nAl and water stored at -25°C retained its original active aluminum content after 40 days, following a procedure by Cliff et al. [21]. This was a significant increase from the previous findings that had a value less than 10% after the same time period in liquid water. In addition, Sippel et al. found that over the course of six months, the active aluminum content was unchanged within the uncertainty of the measurement [18].

Safety testing was also performed on the experimental propellant. Impact sensitivity testing showed that a mixture of frozen nAl using nominally 80 nm powder and water (ALICE) has a drop height greater than the capacity of the experiment apparatus (>2.2 meters), while dry $200\text{ }\mu\text{m}$ AP has a drop height of 38.5 cm. ESD testing showed that stoichiometric ALICE mixtures have an energy threshold greater than 1.5 J, over one thousand times the amount of energy typically released in a human ESD event. Shock sensitivity was performed to determine whether the propellant would propagate a detonation wave. The results displayed the stability of the frozen propellant using 80 nm nAl, with no indication of damage to a witness plate [18].

3. Mixing Techniques

Early mixtures in this work were mixed by hand or using a Ross DPM-1Q dual planetary mixer (Charles Ross & Son Company, Hauppauge, New York). However, inconsistencies in mixing and packing densities motivated other approaches. A Resodyn LabRAM resonating mixer (Resodyn Acoustic Mixer Inc., Butte, Montana) was ultimately selected to mix the ALICE propellant. The LabRAM mixer is designed to operate at the resonant frequency of the system being mixed, using the user-specified intensity (ranging from 0 to 100) [23]. The density and viscosity of the system will change as it mixes causing the resonant frequency of the system and the energy put into the mixture (measured by the acceleration level) to change with time.

The changes in acceleration and frequency provide important information related to the completeness of the mixing process. In a typical mix, the frequency of the mixer increases initially and then drops, while the acceleration

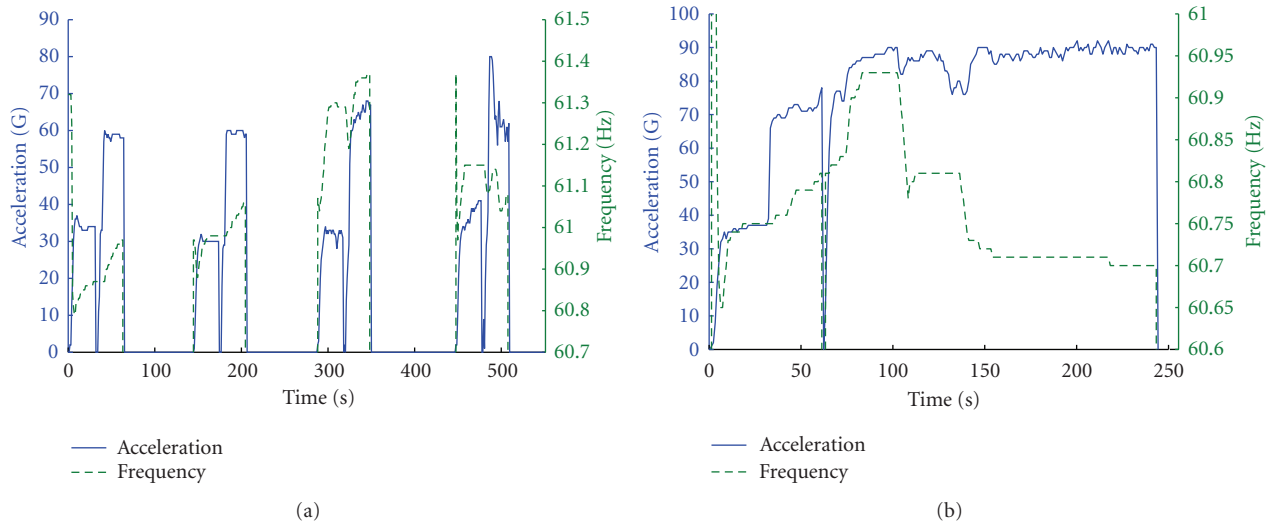


FIGURE 1: Traces from the Resodyn mixer: (a) acceleration and frequency of consecutive multiple mixing cycles; (b) acceleration and frequency of single mixing cycle of near constant intensity.

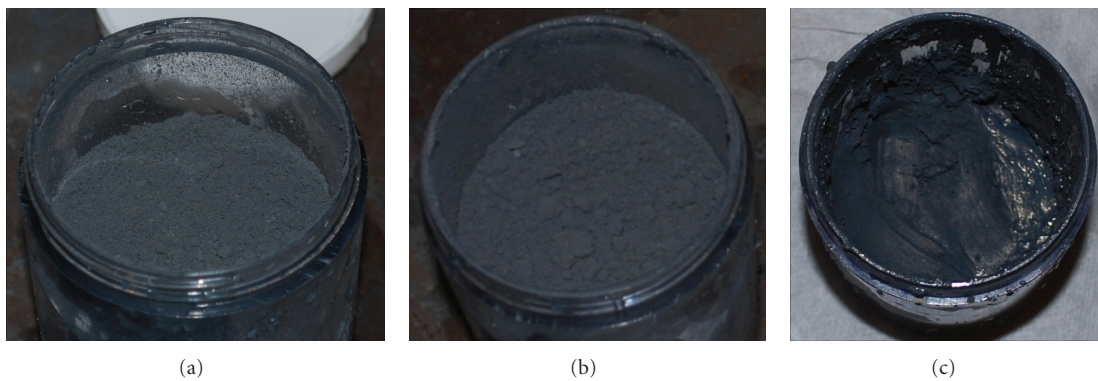


FIGURE 2: Images of various stages of mixing in 7.6 cm (3'') diameter jar: (a) mixing consistency after first cycle; (b) mixing consistency after second cycle; (c) mixing consistency after final cycle.

exhibits a general continual increase. These fluctuations occur due to the changing mixture properties throughout mixing (Figure 1).

As shown in Figure 2(a), ALICE starts out as a mixture of deionized water and 80 nm aluminum powder from Novacentrix Inc. (Product no.: M2666, properties listed in Table 1). Upon mixing, the mixture begins to form clumps until it becomes a uniform paste-like substance (Figure 2(b)). The properties of the propellant then reach a uniform state; in other words the propellant is fully mixed, when the acceleration and the frequency level off for a period of time (Figure 2(c)).

4. Burning Rate Measurements Technique and Results

In previous work with the Ross dual planetary mixer, stoichiometric mixtures proved to be too viscous for the size of nAl used. The propellant became too thick to mix effectively with the Ross mixer. This viscous behavior

prompted the final ALICE mixtures to be fuel-lean with a target equivalence ratio, ϕ , of 0.75. Fuel-lean mixtures had an overall decrease in burning rate when compared to stoichiometric mixtures, but Risha et al. show similar pressure exponents for both the fuel-lean and stoichiometric mixtures [17].

Mixing procedures used with the Resodyn mixer evolved and improved throughout the project. Initial procedures were developed based on the equivalence ratio of 0.75. However, safety concerns related to the reactive nature of the nanoaluminum powder led to the decision of passivating the powder in air for two days prior to mixing. This passivation step lowered the active aluminum content by about 4% leading to an equivalence ratio closer to 0.71 and providing for a less reactive propellant. Again, the formulation studied here is far from optimum.

Strand burn experiments were performed using material from each mixing batch used to produce static fire grains. Each strand consisted of an 8 mm ID \times 5 cm L tube filled with the $\phi = 0.71$ mixture. The frozen strand samples were

TABLE 1: Properties of 80 nm aluminum powder (Novacentrix Inc., product no. M2666).

Mean particle diameter, D_{av} (nm)			Lognormal probability distribution parameters		Oxide layer thickness, t_{av} (nm)		
D_{av} , BET ^(a)	D_{av} , SAS ^(b)	D_{av} ^(c)	Mean ^(c)	Std. Dev. ^(c)	t_{av} , SAS ^(b)	t_{av} , SSA ^(d)	t_{av} ^(c)
70	71 ± 7	79	4.25	0.481	2.4	2.34	2.54

^(a) Per BET analysis as reported by Mang et al. [24].

^(b) Per Small Angle Scattering analysis as reported by Mang et al. [24].

^(c) Per SEM and TEM images analysis as reported by Sippel [25].

^(d) Calculated from BET surface area and reported by Sippel [25].

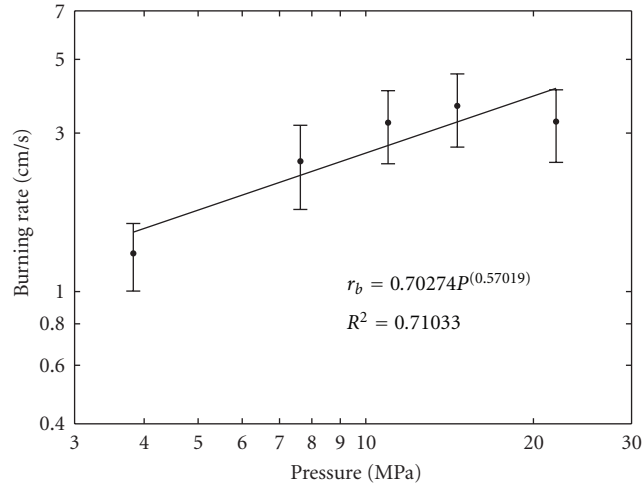


FIGURE 3: Burning rate data of ALICE propellant mixed with the Resodyn mixer.

burned in an argon pressurized and optically accessible combustion bomb. Burning rate measurements were repeated over a range of pressures leading to the power law estimate shown in Figure 3. Over 25 tests were performed and averaged in the results shown. The pressure exponent for this mixing procedure is 0.57, which is somewhat larger pressure dependency than the Al-water propellant tested by Risha et al. [17].

5. Motor Performance Prediction

An internal ballistics analysis of the combustive ALICE motor grain was developed using a lumped-parameter model. The control volume considered in this model takes into account the geometry of the experimental grains. These configurations are summarized in Table 2.

While a simple approach, the assumptions inherent to a lumped-parameter model are quite appropriate in the present application as the experimental grains had low aspect ratios L/D ranging from 1.2 for the 3.5'' long grains to 2.3 for the 7'' long grains, and, therefore, the pressure variations along the chamber length can be neglected [15]. Furthermore, while propellant and motor parameters are adjusted in the model, detail accounting of potentially important two-phase flow losses or nozzle flow losses is not within the scope of the present study. Instead, the model is used to predict the peak chamber pressure and thrust

developed by the ALICE grains and to indicate the history of both parameters based on the measured burning rate and the geometry of the grain.

The ALICE propellant formulation assumed in the model has an equivalence ratio of 0.71 and a characteristic velocity of 1360 m/s. Further, based on previous experimental results reported and theoretical performance calculations, specific impulse of 210 s is assumed for the thrust calculations [26].

The results presented below include that of two variants of the model. In the first variant, the aforementioned propellant characteristics and nozzle geometries are assumed as nominal. It is used to predict the maximum thrust and chamber pressure prior to experimental testing of a new grain or chamber geometry. In the second variant, combustion and flow losses in the combustion chamber and through the nozzle are evaluated with model. These losses are taken into account in two ways: first, since posttest examination of the experimental hardware reveals alumina deposition on the throat and the expansion section of the nozzle, a simple deposition model is included in the analysis. The thickness of the alumina deposit is assumed to increase linearly with time up to the deposit thickness measured upon examination of the hardware. Second, performance losses are included by reducing the nominal propellant characteristic velocity and specific impulse values until a reasonable agreement with the experimental data is obtained.

A final simplifying assumption included in both variants of the model is that the total impulse and mass flow rate produced by the igniter are negligible compared to that of the ALICE grain. The validity of this assumption is discussed in the following. At any given instant in a lumped-parameter model, all exposed surfaces in the control volume are assumed to contribute to amount of mass produced by the combustion of the propellant:

$$\dot{m}_{in} = r_b \rho_p A_b. \quad (1)$$

Conversely, the mass flow exiting the nozzle is given by

$$\dot{m}_{out} = P_c \frac{A_t}{c^*}. \quad (2)$$

Combining (1) and (2) with the conservation of mass equation under steady-state conditions leads to

$$\frac{dm}{dt} = 0 = \dot{m}_{in} - \dot{m}_{out} = r_b \rho_p A_b - P_c \frac{A_t}{c^*}. \quad (3)$$

TABLE 2: ALICE grain geometries.

Test	Grain dimensions			Casing dimensions	
	Outer diameter (cm/in)	Inner bore diameter (cm/in)	Length (cm/in)	Chamber length (cm/in)	Nozzle throat diameter (cm/in)
1 to 3	7.62/3	2.54/1	8.89/3.5	12.70/5	0.914/0.36
4 to 5	7.62/3	2.54/1	12.70/5	12.70/5	1.067/0.42
6	7.62/3	2.54/1	17.14/6.75	19.05/7.5	1.321/0.52
7	7.62/3	2.54/1	17.78/7	19.05/7.5	1.321/0.52

Equation (3) can then be solved for the chamber pressure using St-Robert's burning rate law, $r_b = aP_c^n$:

$$P_c = \left(\frac{a\rho_p A_b c^*}{A_t} \right)^{1/(1-n)}. \quad (4)$$

Since neither end of the grain is inhibited, the ALICE grain burning surface area is a function of the grain outer and inner bore diameter and the grain length as given by

$$A_b = 2\pi R_i L + 2\left(\frac{\pi}{4}(2R_o)^2 - \frac{\pi}{4}(2R_i)^2\right), \quad (5)$$

with both R_i and L functions of the web thickness consumed normal to the local burn surface. The web thickness, W , can therefore be defined as the integral of the burning rate history as given by

$$W = \int_0^{t_b} r_b(t) dt. \quad (6)$$

The theoretical mass flow rate and thrust can then be calculated based on (1) or (2) and

$$F = g \cdot I_{sp} \cdot \dot{m}_{in}. \quad (7)$$

Both variants of the lumped parameter model incorporate (1) to (7) using an Euler numerical integration method with an adequately small time step (typically 1 ms). The second model variant reflects the previously mentioned performance losses and the alumina deposition on the nozzle according to (8):

$$D_t = D_t - 2\epsilon dt, \quad (8)$$

where ϵ is the thickness of the alumina deposit measured around the circumference of the nozzle throat. The chamber pressure and thrust profiles calculated with both variants of the model are shown in Table 3 and Figure 5 for a 5'' long ALICE grains.

As shown in Table 3, a peak chamber pressure of ~14.5 MPa is calculated with both variants of the model. However, the peak pressure obtained with the second variant follows a longer chamber pressurization period and occurs a quarter of a second later than with the first variant (Figure 5). This delay is a result of the reduced characteristic velocity, assumed to be 85% of nominal in the second model variant. The peak pressures calculated with both variants are almost identical as a result of the assumed alumina deposition model.

Also shown in Table 3 is the reduction in peak thrust from ~2 to ~1.78 kN from the first to the second variant of the model. This reduction is the result of the lower specific impulse value assumed in the second variant of the model.

6. ALICE Battleship Static Thrust Stand Experiments

Several static rocket tests were conducted in the Purdue University Propulsion laboratory. The test cell for the static tests has a remote control room from which experiments are monitored and initiated. Pressure and thrust are recorded using LabView, and a 16-bit National Instruments, 32 channel data acquisition system. At least two video cameras are used to observe and record the experiments. One camera monitors the outside where the plume is expelled, and another high-speed camera, recording at 300 fps, monitors the side profile of the exhaust plume.

Based on the strand burn tests, the ALICE propellant combustion does not perform well at pressures below 7 MPa; therefore a thick steel "battleship" motor casing was used initially (see Figure 4). This casing was sized to withstand internal pressures up to 35 MPa. However, constraints in the design of the flight-weight casing influenced the operating pressure of ALICE to be below 20 MPa. To eliminate an additional variable between the battleship tests and the flight-weight tests, the same bolts were selected to secure the ALICE motor assembly together. These bolts are designed to fail around 22 MPa, so overpressurization does not result in the failure of the casing. With the anticipation that variations in mixing and casting will affect performance, the nozzle throat diameter was varied to provide a peak chamber pressure of 10–14 MPa.

The battleship casing was attached horizontally to a metal stand frame. The metal framing is attached to a pair of flexures, which transfers the thrust to a 4.5 kN load cell (Interface, Scottsdale, Arizona). Chamber pressure is measured using two PMP 1260 diaphragm pressure transducers, (Druck, GE Electric, Billerica, MA) with a 0.25% full-scale accuracy.

Following a few experimental tests with various igniter motor sizes, the igniter of choice in all test configurations was a commercially available Aerotech H180 motor [27]. A summary of the motor specifications of interest in the present study is provided in Table 4. The reported I_{sp} of 178 s is not unexpected for small motors such as these. As listed in Table 4, the Aerotech H180 motor has a total impulse of

TABLE 3: Modeling summary for 5'' long grain.

Model assumptions	Total impulse (N-s)	Peak P_c (MPa)	Peak thrust (kN)
No losses for 5'' long grain	1484	14.68	1.98
With deposit and losses for 5'' long grain	1336	14.82	1.78

TABLE 4: Aerotech H180 motor specifications [27].

Parameter	Value	Unit
Outer diameter	29.0	mm
Total length	23.8	cm
Total weight	252	g
Propellant weight	124	g
Average thrust	180.0	N
Maximum thrust	228.5	N
Total impulse	217.7	N-s
Burn time	1.3	s
I_{sp}	178	s

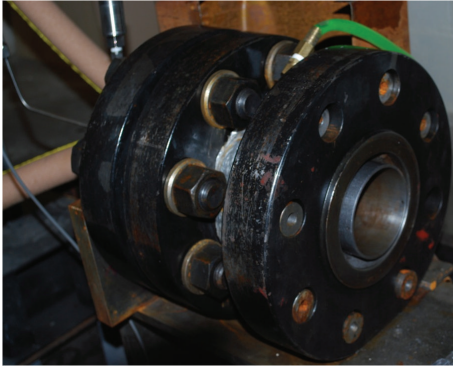


FIGURE 4: Photograph of the battleship motor casing for 3'' diameter propellant grains.

218 N-s or about 15% of the total impulse predicted with the first variant of the lumped parameter model for a 5'' long ALICE grain (Table 3). While a smaller igniter would be highly desirable, the selected igniter size was necessary for reliable and fast ignition of the ALICE formulation evaluated in the study.

Several runs were performed with the battleship motor. Initial runs started with 3.5'' long grains. The results of these experiments are not presented herein for conciseness. Following three successful runs with the 3.5'' long grains, the length of the grain was increased to 5'' to provide more thrust and better approximate the scale required for the sounding rocket. The experimental results of the two runs performed with 5'' long grains (Tests 4 and 5) are presented and compared with the modeling results in Figure 5 and Table 5.

Although the two tests are not precisely replicated, there are several key features to note. First, the length and packing densities of both 5'' long grains varied by 2.3% and 4.8%, respectively, with the first 5''-class grain about 0.25 inches longer than the second one. Second, while

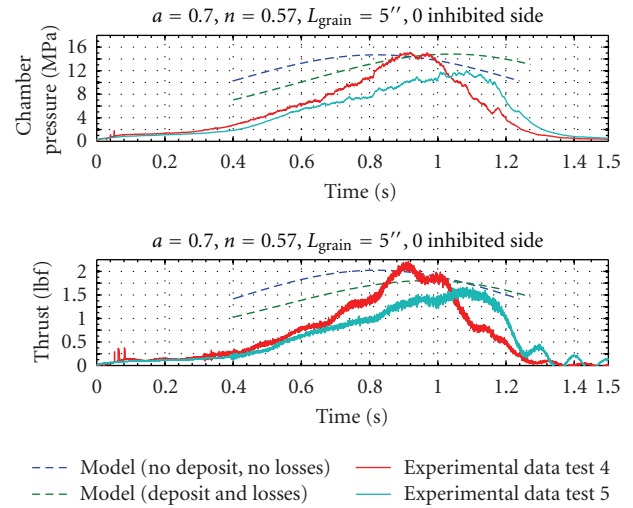


FIGURE 5: Comparison of 5'' long ALICE motor tests with lumped parameter models.

aluminum agglomeration on the nozzle or variations in casting could explain the differences in peak pressure, the experimental peak pressures and peak thrusts compare well with the modeling results thus providing an increased level of confidence for performance prediction of longer grains. The experimental and modeling results obtained for the 5''-class grains are provided in Table 5 including the calculated total impulse values which are of particular interest for the sounding rocket trajectory predictions.

Shown on Figure 6 is the recorded thrust profile for Test 4 and images of the plume at selected time stamps during the burn. The first picture (Figure 6(A)) is the start of the igniter flame and initial chamber pressurization. As the H-180 igniter motor burns, gases expand in the ALICE casing and exit the nozzle as a dark smoke. Based on the recorded data (pressure and thrust), it is believed that ALICE begins to burn in the second picture (Figure 6(B)). This is evident from the sudden oscillatory change in thrust from the load cell, that has been consistent throughout the battleship tests. As the pressure increases further, the flame continues to increase in size until the peak pressure is reached (Figures 6(B) to 6(F)). The pressure and thrust decay rapidly following the consumption of the ALICE grain.

7. Rocket Design and Launch

The demonstration flight of the ALICE propellant with an unguided experimental rocket was a proof of concept for more advanced rockets using similar nanoenergetic material-based propellants. The flight followed a rigorous design

TABLE 5: Comparison of modeling and experimental results for 5'' long grains.

	Total impulse (N-s)	Peak P_c (MPa)	Peak thrust (kN)
Model with no losses (5'' long grain)	1484	14.68	1.98
Model with deposit & losses (5'' long grain)	1336	14.82	1.78
5'' Long experimental grain (Test 4)	970	14.89	2.13
5'' Long experimental grain (Test 5)	890	11.72	1.56

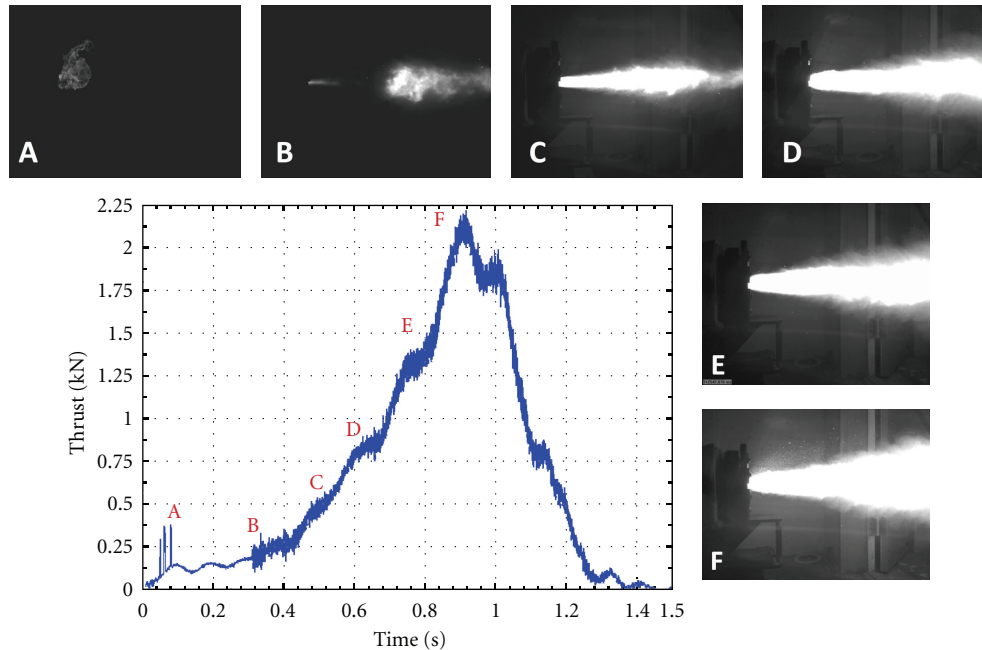


FIGURE 6: Thrust profile of Test 4 and corresponding plume images recorded by the high-speed camera.

process and extensive ground testing of the ALICE rocket motor thus minimizing the likelihood of ignition issues or motor structural failure.

The experimental rocket chosen for the flight is an all-carbon-fiber, minimum diameter, 98 mm high-power rocketry kit known as a Mongoose 98. Two launches were performed with this rocket; the first flight used a K-780 commercially available rocket motor to test the avionics bay and deployment of the parachutes, and the second used the flight-weight motor casing with an ALICE propellant grain. All launch operations were carried out at a remote area located approximately 12 miles southwest of West Lafayette. Known as Scholer Farm, this land is owned by Purdue University and managed by the Animal Sciences Research and Education Center (ASREC). The first flight, with the K780 commercial motor, took place on June 14th, 2009. The demonstration flight of the ALICE propellant took place approximately two months later on August 7th, 2009. For both test flights, we used a commercial ballistic trajectory simulation code (Rocsim-PRO, [28]) to calculate flight-vehicle performance (altitude, range, velocity, and acceleration). This code simulates flight with the addition of wind speed and direction, atmospheric thermal gradients, pressure, location latitude/longitude, launch rail azimuth/elevation, and more. In addition it incorporates the

NASA SPLASH code in order to perform 6-DOF Monte-Carlo simulations based on the uncertainty values in physical parameters such as mass properties (moment of inertia, center-of-gravity), aerodynamics (drag coefficient, center-of-pressure, fin cant angle), propulsion (total impulse, propellant mass, thrust axis), wind direction/velocity, and launch guide angle uncertainties.

Shown in Figure 7, the ALICE flight-vehicle is composed of two fuselage sections, connected together by a carbon-fiber interstage coupler and an avionics bay which contain two redundant R-DAS (Rocket Data-Acquisition System) Tiny units (AED Electronics; The Netherlands). The R-DAS units are preprogrammed to eject a drogue parachute at apogee and a main parachute at a predetermined altitude. An ogive nose cone is placed on the forward end of the vehicle, and three carbon-fiber fins are attached to the aft end in order to provide aerodynamic stability. The fins are attached with carbon-fiber plain weave cloth by using a wet hand layup technique to apply the cloth from fin-tip to fin-tip. Following the layup process, vacuum bagging is used to provide pressure on the composite layer assembly in order to remove any excess resin and improve bond strength.

The flight weight motor and igniter casings shown schematically in Figure 8 are built out of solid rods of 7075-T6 aluminum. This method is preferred over welding on

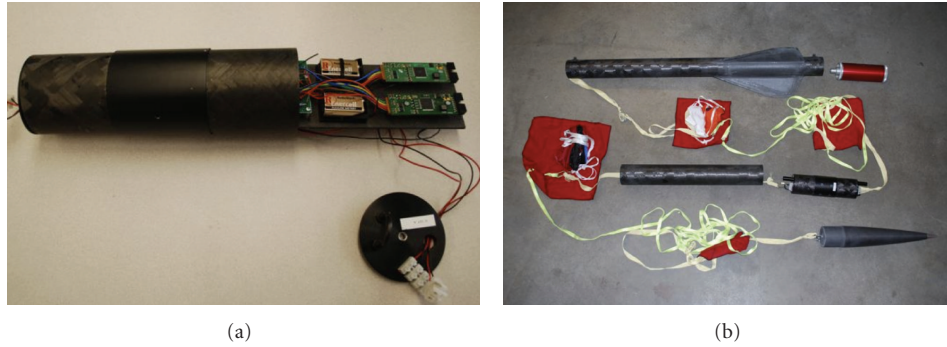


FIGURE 7: Images of the sounding rocket: (a) altimeter bay with RDAS units; (b) exploded view of Mongoose 98 Rocket. The entire length of the assembled rocket is about 8 feet 6 inches and the outside diameter is 4''.

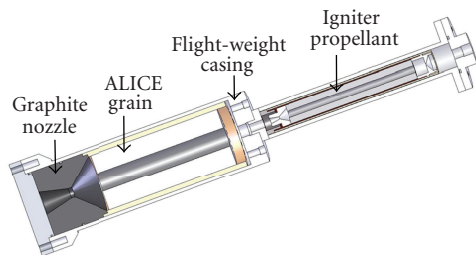


FIGURE 8: Schematic of the flight-weight motor casing.

flanges to the end of the casing, which could potentially cause changes in the mechanical properties of the aluminum. Bolts are threaded into steel threaded inserts located in the aluminum flange at the aft end of the motor casing. These steel inserts help to distribute the load evenly over the length of the thread. The bolts are the same ones used on the battleship motor, which were selected to fail at 22 MPa. The results of a structural analysis of the flight-weight motor using a 3D ProMechanica model with a solid mesh of 3512 elements and an 18 MPa internal pressure load lead to a failure index of 0.29 based on the tensile yield strength of aluminum 7075-T6 of 500 MPa. Upon completion of the casing, the vessel was hydrotested for several minutes at a pressure of 14 MPa. Passing this test allowed for the first static test with the ALICE propellant.

Two static fire tests were conducted with the flight-weight hardware prior to launch. The first test (Test no. 6 in Table 2) was performed with the horizontal configuration established with the battleship motor. The last static test prior to launch (Test no. 7 in Table 2) was performed with the motor installed vertically to assess how the grain and alumina slag would behave under the effects of gravity. These concerns ranged from questions on whether the grain would become dislodged from the walls of the phenolic tube and slide toward the nozzle or if the alumina slag would clog the nozzle. This vertical test was conducted using the same Aerotech H180 igniter as in prior tests. The grain was slightly longer, from 6.75'' to 7'', compared to the previous horizontal test but with a nearly identical packing density (within 2.2%). Figure 9 displays the experimental

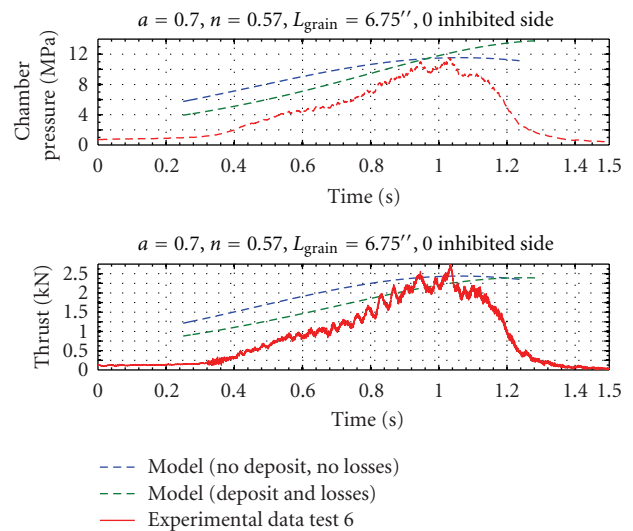


FIGURE 9: Comparison of 7'' long ALICE motor tests with lumped parameter models.

data of the vertical test and the predictions obtained with the performance prediction model. Using the previously described simplifying assumptions for alumina deposition, characteristic velocity and specific impulse losses, the second variant of the model reflects the progressive nature of the grain burning but overpredicts the peak chamber pressure.

Based on the thrust profile from the hot-fire test performed with the 7'' long ALICE grain, as well as the new flight-weight motor design, the Rocsim-PRO simulations predicted that the 30 lb flight vehicle would depart the launch rail in 0.9 seconds, achieving a velocity of ~ 20 m/s at rail exit. The simulations also predicted a maximum acceleration of 16 G's, maximum velocity of ~ 300 km/h (Mach 0.24), and a nominal altitude of ~ 365 m under no wind conditions.

Several constraints limited the achievable altitude with the current ALICE powered rocket. First, the combustion and flow losses observed during the last six static test firings lead to total impulse values of about 60% that of the predicted values. These losses are being addressed in ongoing work with improved propellant formulations

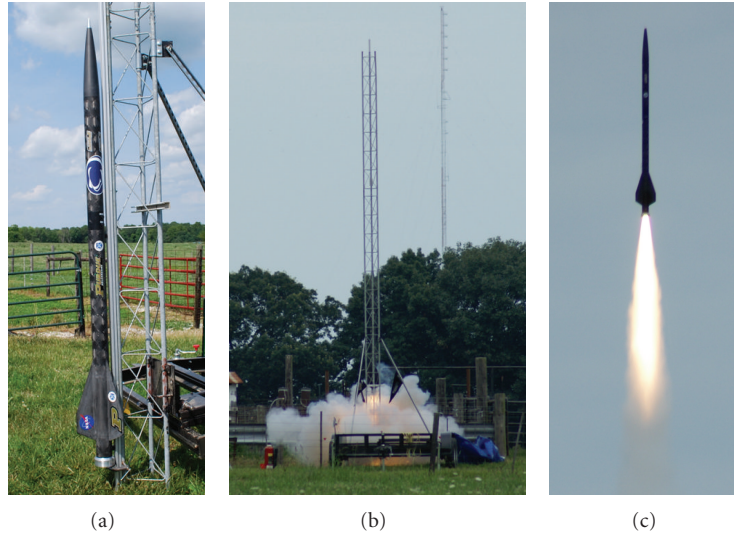


FIGURE 10: Images from the ALICE flight test: rocket on launch platform (a), ignition of the ALICE propellant (b), and rocket in flight (c).

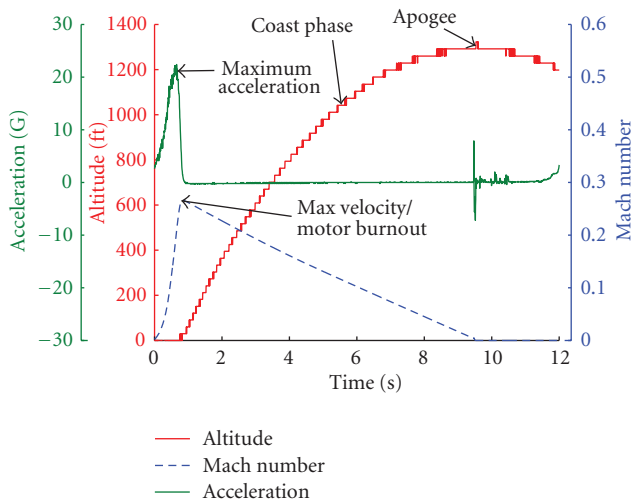


FIGURE 11: R-DAS flight-data from test launch of the flight vehicle powered by the ALICE motor.

including additives and alternative formulations to achieve higher specific impulse and lower the alumina content of the products. Second, the flight-weight casing for the ALICE propellant had to sustain pressures up to 14 MPa requiring thicker walls, thus increasing vehicle weight compared to a traditional SRM. In addition, the energy required for igniting the current ALICE propellant formulation is significantly higher than that required for a standard solid propellant. This leads to added weight for an igniter casing and an interface with the ALICE casing capable of sustaining high pressures and designed in such a way that the combustion gases do not impact the aluminum walls. Weights were also added just below the nose cone to yield a higher stability margin. While designed for flight with safety factors around 1.5, the heavier casing reduced the maximum altitude achievable with the rocket. Finally, the burning rate of the

current ALICE formulation is on the order of 2.5 cm/s at the nominal operating pressure of 10 MPa. This high burning rate means that a larger web thickness is required to sustain the ALICE combustion over sufficiently long durations. In turn, larger grains require heavier casings. The current design is a trade-off between the aforementioned constraints. Further improvements of the propellant formulation should address these constraints, thus reducing the weight of the flight-weight casing in an effort to achieve better flight performance.

The ALICE demonstration flight took place of a fairly cool ($\sim 21^\circ\text{C}$ ambient temperature) and calm (~ 3 km/h wind at launch site) day.

Figure 10 shows the ALICE vehicle on the stand ready for takeoff (left), soon after ignition (middle), and flying under ALICE soon after it cleared the launch tower (right).

The rocket coasted after the grain was depleted and reached a peak altitude of ~ 394 m (1292 ft). This altitude is very close to the estimate of 365 m (1200 ft) obtained from Rocsim-PRO assuming no wind. The data recorded from the R-DAS is shown in Figure 11.

This close agreement between recorded flight data and predictions indicates that the thrust profile and thrust magnitude experienced during flight were very similar to those recorded on the ground with the flight hardware. Similarly, it is observed that the peak I_{sp} of 210 s calculated from the ground test data is a good estimate for the flight I_{sp} .

8. Conclusions

We have shown that refrigerated solid propellants can be used for rocket motors, and the ALICE propellant has shown promise as a rocket propellant in static test firings. Six small-scale static experiments have shown consistent results when compared to the prediction codes. Although this current propellant formulation is far from optimized, improvements in the mixing procedure have produced a consistent and

homogeneous propellant. While the performance of ALICE is too low for practical use, the knowledge gained through formulating and experimenting with nanoscale particles in a simple mixture is of great interest for ongoing research activities on advanced propellants.

An internal ballistic model developed to support the experiments provides a simplified account of a complex series of events within the igniter and the main combustion chamber. The model is based on measured burning rate parameters and exact grain geometries tested at the Purdue Propulsion Laboratories. Perturbations to the model can be introduced to reflect the reduction of the nozzle throat diameter due to alumina deposition and to take into account losses in the combustion chamber and the nozzle. While the model overpredicts the total impulse of the ALICE propellant grains, it is a useful tool for peak chamber pressure and thrust predictions. Finally, based on consistency between model and experiment over several tests, the model is also a prediction tool for flight-weight motor performance and, therefore, rocket trajectory predictions.

Nomenclature

a, n :	Propellant burning rate coefficients
A_b :	Burning area
A_t :	Throat area
c^* :	Characteristic velocity
D_{av} :	Average particle diameter
D_t :	Throat diameter
dt :	Time increment
F :	Thrust
g :	Gravity
I_{sp} :	Specific impulse
L :	Length
m :	Mass
\dot{m} :	Mass flow rate
P_c :	Chamber pressure
r_b :	Burning rate
R_o :	Outer diameter
R_i :	Inner diameter
t_{av} :	Oxide layer thickness
t_b :	Burning time
W :	Web thickness
ε :	Thickness of alumina deposit
ρ_p :	Propellant density
ϕ :	Mixture ratio.

Subscript

in:	In
out:	Out
p:	Propellant.

Acknowledgments

The authors would like to thank Dr. Mitat Birkan of the Air Force Office of Scientific Research and NASA under contract numbers FA9550-09-1-0073 and FA9550-07-1-0582.

The authors would also like to thank Mr. T. L. Connell, Jr., Dr. Grant A. Risha and Dr. Richard A. Yetter of the Pennsylvania State University for their many contributions.

References

- [1] K. K. Kuo, G. A. Risha, B. J. Evans, and E. Boyer, "Potential usage of energetic nano-sized powders for combustion and rocket propulsion," *Materials Research Society Symposium Proceedings*, vol. 800, pp. 3–14, 2003.
- [2] A. Dokhan, E. W. Price, J. M. Seitzman, and R. K. Sigman, "The effects of bimodal aluminum with ultrafine aluminum on the burnign rates of solid propellants," *Proceedings of the Combustion Institute*, vol. 29, no. 2, pp. 2939–2946, 2002.
- [3] A. Shalom, H. Aped, M. Kivity, and D. Horowitz, "The effect of nanosized aluminum on composite propellant properties," in *Proceedings of the 41st AIAA/ASME/SAE/ASEE Joint Propulsion Conference and Exhibit*, July 2005.
- [4] L. Galfetti, F. Severini, L. T. De Luca, and L. Meda, "Nano-propellants for space propulsion," in *Proceedings of the 4th International Spacecraft Propulsion Conference*, vol. 4, Sardinia, Italy, June 2004.
- [5] M. A. Trunov, M. Schoenitz, and E. L. Dreizin, "Ignition of aluminum powders under different experimental conditions," *Propellants, Explosives, Pyrotechnics*, vol. 30, no. 1, pp. 36–43, 2005.
- [6] G. A. Risha, Y. Huang, R. A. Yetter, V. Yang, S. F. Son, and B. C. Tappan, "Combustion of aluminum particles with steam and liquid water," in *Proceedings of the 44th AIAA Aerospace Sciences Meeting and Exhibit*, January 2006.
- [7] V. G. Ivanov, M. N. Safronov, and O. V. Gavriluk, "Macrokinetics of oxidation of ultradisperse aluminum by water in the liquid phase," *Combustion, Explosion and Shock Waves*, vol. 37, no. 2, pp. 173–177, 2001.
- [8] A. Ingenito and C. Bruno, "Using aluminum for space propulsion," *Journal of Propulsion and Power*, vol. 20, no. 6, pp. 1056–1063, 2004.
- [9] E. Shafirovich, P. E. Bocanegra, C. Chauveau, and I. Gökalp, "Nanoaluminium—water slurry: a novel "green" propellant for space applications," in *Proceedings of the 2nd International Conference on Green Propellants for Space Propulsion*, vol. 2, Sardinia, Italy, June 2004.
- [10] O. Razor and O. R. Portland, U.S. Patent Application for a "Power Plant", 1939.
- [11] O. J. Elgert and A. W. Brown, *In Pile Molten Metal-Water Reaction Experiment*, U.S. Atomic Energy, 1956.
- [12] L. Leibowitz and L. W. Mishler, "A study of aluminum-water reactions by laser heating," *Journal of Nuclear Materials*, vol. 23, no. 2, pp. 173–182, 1967.
- [13] T. F. Miller and J. D. Herr, "Green rocket propulsion by reaction of Al and Mg powders and water," in *Proceedings of the 40th AIAA/ASME/SAE/ASEE Joint Propulsion Conference and Exhibit*, July 2004.
- [14] J. P. Foote, J. T. Lineberry, B. R. Thompson, and B. C. Winkelman, "Investigation of aluminum particle combustion for underwater propulsion applications," in *Proceedings of the 32nd AIAA/ASME/SAE/ASEE Joint Propulsion Conference and Exhibit*, 1996.
- [15] R. W. Humble, G. N. Henry, and W. J. Larson, *Space Propulsion Analysis and Design*, chapter 6, McGraw-Hill, New York, NY, USA, 1st edition, 1995.
- [16] V. G. Ivanov, O. V. Gavriluk, O. V. Glazkov, and M. N. Safronov, "Specific features of the reaction between ultrafine

- aluminum and water in a combustion regime,” *Combustion, Explosion and Shock Waves*, vol. 36, no. 2, pp. 213–219, 2000.
- [17] G. A. Risha, S. F. Son, R. A. Yetter, V. Yang, and B. C. Tappan, “Combustion of nano-aluminum and liquid water,” *Proceedings of the Combustion Institute*, vol. 31, no. 2, pp. 2029–2036, 2007.
- [18] T. R. Sippel, S. F. Son, G. A. Risha, and R. A. Yetter, “Combustion and characterization of nanoscale aluminum and ice propellants,” in *Proceedings of the 44th AIAA/ASME/SAE/ASEE Joint Propulsion Conference and Exhibit*, July 2008.
- [19] A. Dokhan, *The effects of aluminized particle size on aluminized propellant combustion [Ph.D. thesis]*, Aeronautics and Astronautics Department, Georgia Institute of Technology, Atlanta, Ga, USA, 2002.
- [20] Y. S. Kwon, A. A. Gromov, and J. I. Strokova, “Passivation of the surface of aluminum nanopowders by protective coatings of the different chemical origin,” *Applied Surface Science*, vol. 253, no. 12, pp. 5558–5564, 2007.
- [21] M. Cliff, F. Tepper, and V. Lisetsky, “Ageing characteristics of Alex nanosize aluminum,” in *Proceedings of the 37th AIAA/ASME/SAE/ASEE Joint Propulsion Conference and Exhibit*, 2001.
- [22] C. Franson, O. Orlandi, C. Perut et al., “Al/H₂O and Al/H₂O/H₂O₂ frozen mixtures as examples of new composite propellants for space application,” in *Proceedings of the 7th International Symposium on Launcher Technologies*, Barcelona, Spain, 2007.
- [23] LabRam Resonant Acoustic Mixer Manual, ResoDyn, Butte, Mont, USA, 2012 <http://www.resodynmixers.com/products/labram/>.
- [24] J. T. Mang, R. P. Hjelm, S. F. Son, P. D. Peterson, and B. S. Jorgensen, “Characterization of components of nano-energetics by small-angle scattering techniques,” *Journal of Materials Research*, vol. 22, no. 7, pp. 1907–1920, 2007.
- [25] T. R. Sippel, *Characterization of nanoscale aluminum and ice solid propellants [M.S. thesis]*, Mechanical Engineering Department, Purdue University, West Lafayette, Ind, USA, 2009.
- [26] R. A. Yetter, G. A. Risha, T. Connell et al., “Novel energetic materials for space propulsion,” in *Presentation, AFOSR/NASA Office of Chief Engineer Joint Contractors / strategic Planning Meeting in Chemical Propulsion*, Vienna, Va, USA, 2008.
- [27] ThrustCurve, John Coker, 2012, <http://www.thrustcurve.org/>.
- [28] “RockSim, Ver. 8.0,” Apogee Components, Inc., Colorado Springs, Colo, USA, 2009.

Review Article

Approaches to Low Fuel Regression Rate in Hybrid Rocket Engines

Dario Pastrone

Dipartimento di Ingegneria Meccanica e Aerospaziale, Politecnico di Torino, Corso Duca degli Abruzzi 24, 10129 Torino, Italy

Correspondence should be addressed to Dario Pastrone, dario.pastrone@polito.it

Received 10 February 2012; Accepted 5 April 2012

Academic Editor: David Greatrix

Copyright © 2012 Dario Pastrone. This is an open access article distributed under the Creative Commons Attribution License, which permits unrestricted use, distribution, and reproduction in any medium, provided the original work is properly cited.

Hybrid rocket engines are promising propulsion systems which present appealing features such as safety, low cost, and environmental friendliness. On the other hand, certain issues hamper the development hoped for. The present paper discusses approaches addressing improvements to one of the most important among these issues: low fuel regression rate. To highlight the consequence of such an issue and to better understand the concepts proposed, fundamentals are summarized. Two approaches are presented (multiport grain and high mixture ratio) which aim at reducing negative effects without enhancing regression rate. Furthermore, fuel material changes and nonconventional geometries of grain and/or injector are presented as methods to increase fuel regression rate. Although most of these approaches are still at the laboratory or concept scale, many of them are promising.

1. Introduction

Hybrid rocket engines (HREs) are chemical rockets which present interesting advantages over liquid rocket engines (LREs) and solid rocket motors (SRMs) and can provide a safe and affordable option for many applications. They have recently come to the fore as they have been chosen to power the second stage of the Tier One, the winner of the \$10 million X-Prize [1]. The Tier One (<http://www.scaled.com/projects/tierone/>) was the first privately-developed reusable vehicle able to perform a manned suborbital flight over 100 km. The first stage of the Tier One is a twin-turbojet carrier-launch aircraft, called the White Knight, which is able to bring the second stage to 15 km altitude. The second stage, the SpaceShipOne, is a reusable three-place manned space plane, powered by an N₂O/HTPB hybrid rocket engine. This HRE has a burning time of about 80 seconds and it is able to produce an average thrust of 75 kN with a vacuum specific impulse of about 250 s. The Tier One was retired after winning the X-Prize, but it remains proof that HREs may be the key propulsion system of the emerging space market [2].

In HREs, oxidizer and fuel are separated and stored in two different physical phases. In the most common configuration, a liquid or gaseous oxidizer and a solid-fuel grain are

employed (*direct* HRE). In the conventional configuration the grain is cylindrical with a circular port. Due to this propellant storage, HREs have a peculiar combustion process as shown Figure 1. A boundary layer is formed when the oxidizer is injected into the port of the fuel grain. After ignition a diffusion flame is formed inside this layer. The fuel deriving from the solid grain is gasified by the heat coming from the flame, which in turn is fed by the fuel. The gasified fuel blows from the surface and modifies the boundary layer, blocking the heat transfer.

The aforementioned propellant storage and combustion process determine both positive and negative effects. Many authors have discussed the advantages and the drawbacks of HREs. Characteristic hybrid rocket features are briefly summarized below. Benefits include the following.

- (i) Performance: HREs may deliver a higher specific impulse than SRMs. Due to the high-density solid they also may have higher density specific impulse than LREs. This latter benefit may be wasted by sliver or low grain volumetric efficiency.
- (ii) Safety: HREs are inherently safe and low cost mainly due to the use of a solid fuel grain which is classically inert. Since the fuel and oxidizer are separated by distance and phase, hybrids have almost no explosion

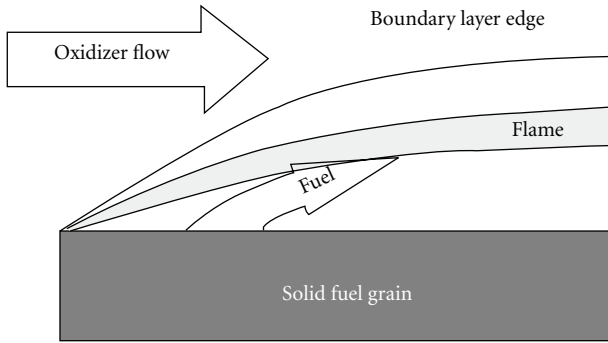


FIGURE 1: HRE combustion.

hazard and very few failure modes. The fluid oxidizer is usually depleted in the diffusion flame region. It can reach and attack the fuel surface only when gaseous chemical kinetics are slow (low pressures). No deflagration to detonation transition can be caused by pores, cracks, and imperfections, and inadvertent ignitions are avoided. Last, but not least, defining a maximum expected operating pressure is not a concern as HREs do not have the high temperature sensitivity which characterizes SRMs.

- (iii) Reliability and simplicity: feeding system hardware is reduced as only the oxidizer is liquid.
- (iv) Fuel versatility: additives for different purposes can be embedded in the fuel grain.
- (v) Oxidizer control: liquid propellant control allows for throttling, motor shutdown, and reignition.
- (vi) Environmental friendliness: compared to SRMs, oxidizers are chlorine free. Compared to LREs, storable propellants are available, which do not have noxious features such as MMH and nitrogen tetroxide.
- (vii) Low cost: hybrid rockets pose almost no explosion hazard during manufacture, transport, ground test, and storage. Low recurring costs are foreseen because of high levels of safety and minimal failure modes.

Classical HREs also present disadvantages which include the following.

- (i) Performance: HREs cannot reach the high specific impulse of cryogenic bipropellant LREs and have a lower density specific impulse compared to SRMs.
- (ii) Low fuel regression rate: the regression rate of conventional binders such as HTPB is typically an order of magnitude lower than solid propellants and hence a large fuel surface is needed to produce the required thrust level, as discussed later in Section 2. This limit is usually set by the physical phenomenon of heat transfer from the diffusion flame to the fuel surface. As a consequence, HREs may have poor fuel loading, low thrust densities, and large length-to-diameter ratios.
- (iii) Mixture ratio shifting: the regression rate primarily depends on the mass-flux, that is, on the ratio of

mass-flow and port area A_p . During combustion of classical side burning grains, A_p increases determining a regression rate reduction. On the other hand, the burning area A_b increases as well. These two competing effects are, in general, not balanced, leading to a change in the fuel mass flow, even when the oxidizer mass-flow is kept constant (see Section 2). The mixture ratio shifts and performance are worsened. Nonconventional injection systems may fix this issue but introduce complexity.

- (iv) Mixing inefficiencies: part of the fuel under the flame at the grain port exit may not mix with any oxidizer and thus exit the nozzle before releasing chemical energy. HREs have a lower overall combustion efficiency than LREs and SRMs. A mixer between the grain aft end and the nozzle inlet can enhance mixing, but the dry weight of the system is larger.
- (v) Slow transient/response to throttling: due to the thermal lag in the solid fuel, ignition and response to throttling is slow in comparison to LREs. Also, the chamber volume may be larger than in LREs, with large tail-off time.

One of the most important issues remains the very low regression rate of the fuel grain. Various methods for enhancing regression rate or, at least, for reducing negative effects of low fuel regression have been suggested in the past. The goal of this paper is to survey broadly some of the more significant approaches proposed. After summarizing some fundamentals (Section 2), two approaches are presented (Section 3) which aim at reducing the negative effects of regression rate without enhancing regression rate itself. Approaches which directly try to enhance regression rate are then presented: the modification of fuel is considered in Section 4, while approaches based on unconventional geometries for the grain and/or the injector are presented in Section 5.

2. Fundamentals

In this section the fundamentals are summarized in order to better understand the negative effects of low regression rate and in turn to allow one to consider approaches to mitigate this issue. An exhaustive treatment of this subject is beyond the scope of this work. Rudiments of regression rates behavior and models are first discussed. A ballistic model is then used to highlight that cylindrical single-port side-burning grain may have an unacceptable shape if large thrust levels are required. For further information consult [14].

2.1. Regression Rate Behavior and Modeling. Typical fuel regression rate behavior is depicted in Figure 2 as a function of mass flux G . Three different regions can be identified. For the medium G range the regression rate is diffusion dominated and is a function of the mass flux [15–17]. When G assumes high values, the combustion appears to be controlled by chemical kinetics and not by diffusion [18]. As a consequence, regression rate becomes pressure

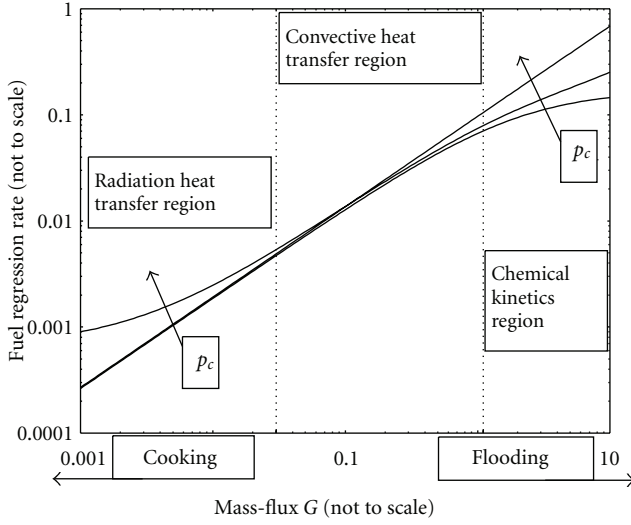


FIGURE 2: Typical regression rate behavior.

dependent. An upper bound for the mass flux exists, called the *flooding* limit, which depends on pressure level and propellant combination. When approaching this limit, the mass flux may become so high that the flame is extinguished due to small Damköhler numbers and/or very oxidizer-rich conditions. Finally, at low values of mass flux, the convective heat transfer diminishes and radiation from gaseous species may play a significant role. Consequently, the regression rate is enhanced depending on the partial pressure of emitting components and port diameter. In this regime a lower bound of the mass flux is also present. The regression rate is small, the fuel remains in the thermal layer of the grain a long time, and the solid fuel may be cooked/melt underneath the grain surface. Therefore, if the mass flux is too low (e.g., at the end of HRE operation with blowdown feed systems), chuffing instability may be produced by the perpetual repeating mechanical removal of this soft layer.

The well-known theory developed by Marxman and colleagues [15–17] set the basis for understanding and describing fuel regression rate. They assumed that the fuel regression rate is controlled by heat transfer to the grain and applied a flux balance at the fuel surface, finding

$$r\rho_F = \frac{q}{\Delta H_{v,\text{eff}}}, \quad (1)$$

where r is the fuel regression rate, ρ_F is the fuel density, q is the total heat flux received by the fuel grain, and $\Delta H_{v,\text{eff}}$ is the thermal energy required to change a unit mass of solid fuel into gas.

According to their studies, the regression rate is primarily governed by convective heat transfer, that is, by the local mass flux G . Modeling the heat transfer in a turbulent layer, they proposed a simplified regression rate expression for combustion with negligible radiation. Taking into account a refit of the data proposed by Altman Humble [19] this expression is

$$r\rho_F \propto B^{0.32} G^{0.8} x^{-0.2}, \quad 5 < B < 100. \quad (2)$$

The blowing parameter B is the ratio of the thermal energy of the main stream relative to the surface ΔH_{f_w} and $\Delta H_{v,\text{eff}}$. The weak negative dependence on axial position x reflects the effects of boundary layer growth on heat transfer. On the contrary, the total local mass flux increases with axial position along the fuel grain. These two competing effects usually determine a location of minimum regression rate along the grain axis. In any case, these difference are usually small. For these reasons the regression rate is assumed to be constant along the grain axis and semiempirical correlations based on the mass flow entering the port area, that is, $G_O = \dot{m}_O/A_p$ are widely used, that is,

$$r = aG_O^n, \quad (3)$$

where a and n are obtained by experimental data for a given G_O range and depend on engine dimensions (scale effect), port/grain geometry, injector geometry, and flow features. Correlation like the one presented in (3) well-describe the regression rate of conventional HREs in the intermediate range of G_O , where behavior is dominated by turbulent heat transfer.

Radiation from gas-phase products is usually small compared to convection. Nevertheless, convection itself becomes small at low values of G and radiation plays a role. Radiation effects are also important when the combustion products contain condensed matter, for example, soot and metal/oxides particles. Marxman and coworkers [16, 17] proposed a correction factor to take into account the radiation heat transfer. The total heat flux q in (1) becomes $q = q_c[(q_r/q_c) + \exp(-q_r/q_c)]$. This expression takes into account that there is a coupling effect between radiant flux q_r and convective heat q_c . In fact, the radiant flux enhances the blocking effect due to blowing thus depressing convective heat.

Other phenomena that affect fuel regression rate have been considered in later works [20–28]. Beside radiation, the most important mechanisms taken into account include variable fluid and transport properties across the boundary layer, and both gas-phase and heterogenous reaction kinetics.

The regression rate correlation of (3) should be modified consequently. As an example, Chiaverini et al. [28] proposed a modified relation for cases where kinetics effects can be disregarded. Variable fluid and transport properties into the boundary layer and radiation from soot are considered. The resulting model is

$$\frac{\rho_F r}{G} = 0.0155 \left(\frac{D_h}{L_g} \right)^{0.3} \theta^{0.6} \text{Re}_D^{-0.2} f \left[B, \frac{q_r}{q_c} \right], \quad (4)$$

where D_h is the port hydraulic diameter, L_g the grain length, and θ a temperature factor, representing the ratio of average flame to surface temperature [29].

Although correlations like (4) allow for a better fit of experimental data, (3) is often used. The reader should be aware that the values of a and n may be dependent on many factors such as G_O range, fuel formulation, grain production method, engine dimensions (scale effect), port/grain geometry, injector geometry, and flow features.

For example, if (3) is used to fit experimental data, r may be found to vary with G_O to the power of 0.6 instead of the theoretical 0.8 for turbulent flow over a flat plate used in (2). These findings imply that nonconvective processes, such as radiant heat flux and/or finite rate chemical kinetics, may influence the solid-fuel regression rates in this case.

2.2. Low Fuel Regression Rate Effects in Classical HREs. When the propellant combination is given, the characteristic velocity c^* is a function of the mixture ratio $\alpha = \dot{m}_O/\dot{m}_F$ (i.e., oxidizer to fuel mass flow ratio) [3]. Chamber pressure affects c^* to a lesser extent. The thrust coefficient C_F can be evaluated when the following data are provided: combustion gas properties (specific heat ratio), ambient pressure p_a , and expansion ratio $\epsilon = A_e/A_t$ (exit to throat area ratio) or p_e/p_c (exit to chamber pressure ratio). The corresponding effective exhaust velocity $c = c^*C_F$ or the specific impulse $I_s = c/g_0$ is consequently evaluated.

If a thrust level is assigned, the needed propellant mass flow m_p is

$$\dot{m}_p = (1 + \alpha)\dot{m}_F = \frac{F}{c^*C_F}, \quad (5)$$

and, using (3), the fuel mass flow m_F is

$$\dot{m}_F = a\rho_F \left(\frac{\dot{m}_O}{A_p} \right)^n A_b, \quad (6)$$

where ρ_F is the solid fuel density.

The mixture ratio is

$$\alpha = \frac{\dot{m}_O}{\dot{m}_F} = \frac{\dot{m}_O^{(1-n)} A_p^n}{a\rho_F A_b}. \quad (7)$$

This relation shows that α changes in proportion to A_b/A_p^n . In most cases A_b/A_p^n is a function of time and α changes even if \dot{m}_O is kept constant. This characteristic behavior of HREs is called mixture-ratio shifting. It is worthwhile to observe that mixture ratio shifting does not occur if a circular port is used and $n = 0.5$.

From (5) and (6):

$$A_b = \frac{1}{a\rho_F} \left(\frac{F}{c^*C_F} \right)^{(1-n)} \frac{A_p^n}{(1 + \alpha)^{(1-n)} \alpha^n}. \quad (8)$$

Equation (8) shows the relation of geometry (grain/nozzle) engine operation (mixture ratio) and mission requirements (thrust). Due to the low regression rate, the length-to-diameter ratio may be of concern. In fact, large values of A_b are required, while A_p must keep G_O in the appropriate range. Assuming a single-circular port, for given values of F , α , and c , the length-to-diameter ratio of the grain becomes $(L_g/D_p) \propto D_p^{(2n-1)}$, where L_g is the grain length, and D_p the port diameter. The outer diameter of the grain is $D_g = D_p + 2w$, where w is the web thickness. If $n > 0.5$ the length-to-diameter ratio of the grain may be reduced with a port diameter reduction. On the other hand, the overall length-to-diameter ratio L/D must be considered. The rocket length L includes the oxidizer tank length. The reduction of the port

area makes the ratio L/D worse if the oxidizer tank and grain have the same diameter [30]. On the contrary, if the diameter of the oxidizer tank may be larger than grain diameter, both L is reduced and D augmented thus improving the ratio L/D . Therefore, the reduction of A_p may be favorable [31]. However, this approach is limited as A_p has a lower bound due to flooding.

As a consequence, HREs are generally restrained to high length-to-diameter ratios and thus are long and skinny. The values of L/D become unacceptable when requiring high performance (e.g., upper stages and boosters), especially when compared to LREs and SRMs that are currently on the market. Solutions to this issue become necessary.

3. Mitigation Approaches

In this section two solutions which attempt to mitigate the negative effects of low regression rate are presented. Multiport grains allow for reducing L/D values with an almost constant fuel mass, while high mixture ratio aims at reducing the mass of the fuel grain.

3.1. Multiport Grains. Assuming that both A_b and A_p are constant, the grain length $L_g = A_b/P$ may be reduced by increasing the perimeter P . This result can be obtained using a multiport grain. The larger the number of ports, the more pronounced the length reduction. Also, volumetric efficiency is increased as the port volume is proportional to L_g . As an example, two possible multiport geometries are shown in Figure 5. In Figure 5(a) a triangular port [32] is shown. Sliver is a drawback which can be reduced using a wagon-wheel grain (Figure 5(b)) where a central circular port with initial radius R_{ci} is surrounded by a row of N quadrangular ports [33]. Grains with two or three rows of quadrangular ports have been tested [30]. Even with these more complicated geometries the unburned mass fraction is high. Furthermore, other drawbacks exist. The individual ports may behave in a different way and dedicated injector or a large prechamber would be required, compromising weight and simplicity. In addition, design and fabrication are complex and grain structural integrity may become an issue, especially towards the end of the burn.

Radial-flow/end-burning grains are other interesting geometry alternatives which may improve fuel section volumetric efficiency. Combination of end-burning with side-burning grains is possible. In this case the flow structure is modified and the regression rate may be enhanced too. Approaches which involve end burning grain or radial flows are left for the next sections which discuss regression rate enhancement.

Also more complicated geometries can be used which allow for a better use of volume. Rapid prototyping has been identified as a manufacturing technique for hybrid rocket fuel grains that enables the production of complex 3D grain shapes, which may improve hybrid rocket motor performance [34].

3.2. High Mixture-Ratio Values. If high mixture-ratio values are used, the regression rate is of minor concern, as the fuel

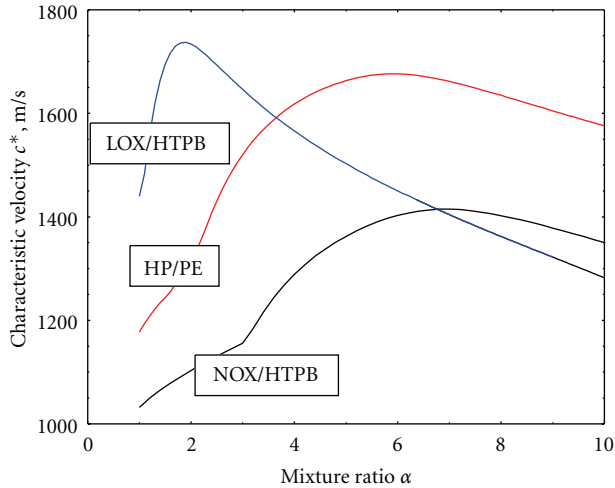


FIGURE 3: Theoretical values of characteristic velocity for different propellant combinations [3].

grain must give a minor contribution to the overall mass flow. Unfortunately, the propellant performance is a function of mixture ratio as well. Benefits may be obtained by adopting propellant combinations which present high values of c^* at high mixture ratios. Figure 3 shows c^* for three different propellant combinations: HTPB with liquid oxygen (LOX) or N_2O , and polyethylene (PE) with an 85% concentration solution of hydrogen peroxide (HP). The thrust coefficient C_F is primarily a function of the expansion ratio and is only slightly affected by α , reaching a maximum value in the stoichiometric region. As a result the maximum value of c is somehow shifted to the right of α which determines the maximum of c^* .

It is worthwhile to note here that proper tools are needed to perform a comparison [30, 31, 35–37]. In many applications thrust has a major influence since it affects both the propulsion system design and the trajectory performance; a compromise must be sought, as greater thrust levels reduce the gravitational losses but increase structural mass. Moreover, HREs are characterized by their peculiar combustion process and the consequent link between thrust level and mixture ratio. In order to efficiently perform a coupling of the HRE design parameter optimization with the trajectory optimization, a unique procedure has been developed at the Politecnico di Torino which uses a direct/indirect nested method.

As an example, the performance of a microgravity platform for three different propellant combination are compared [31]. Given rocket payload (100 kg) and initial mass (500 kg, comprising payload, fixed masses, propulsion system, and propellant), the time spent above 100 km ($t_{\mu g}$) is the performance index to be maximized. The optimization aims at finding the optimal mass split between propellant and propulsion system (i.e., tanks, combustion chamber, nozzle), the optimal grain geometry, and the corresponding optimal trajectory [31]. Single-port grains are considered and different propellant options are compared in Table 2. A simple blowdown feed system is adopted.

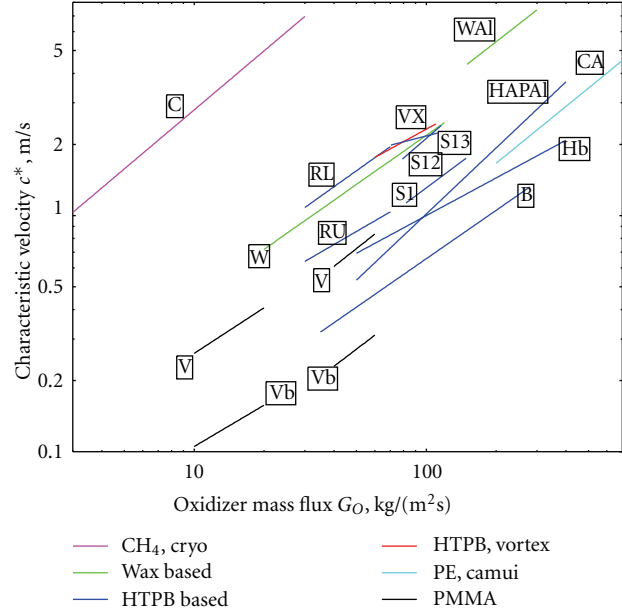


FIGURE 4: Regression rate for different systems and GOX/fuel combinations (see legend in Table 1).

Results show the superior performance of the HP/PE combination. Propellant consumption and propulsion system dry-mass are competing parameters. The LOX/HTPB propellant combination presents higher maximum values of c^* , but this maximum is reached for small values of α : large grains are required and the propulsion system mass penalty is higher than propellant savings. Also, LOX and HP have larger densities than HTPB, and higher values of density-specific impulse may be obtained with the HP/PE combination which adopts high values of α . On the other hand, N_2O is penalized by the low performance in terms of specific impulse. However, N_2O presents some interesting features, such as the reduced rocket length L and diameter D , as the large mixture ratio reduces the grain length. Also note that the initial required thrust for the same mission is lower.

4. Fuels with Enhanced Regression Rate

In this section approaches are considered based on the modification of the fuel. Possible approaches can be divided down into three categories: (1) adding energetic particles, (2) using energetic polymers (and/or plasticisers) instead of conventional inert components such as HTPB, (3) using fuels such as cryogenic fuels or paraffin-based fuels which exhibit new mass-transfer mechanisms. A combination of the aforementioned options is also possible.

4.1. Particle Additives in Solid Fuels. Several additives have been tested. Most researches considered metal additives in polymeric-based solid fuels [6, 8, 9, 27, 41–45]. More recently, metal additives in paraffin-based fuels have also been considered [8, 46–50].

Combustion of metals has inherent advantages as they help to increase both specific impulse and density specific

TABLE 1: Values of a and n to be used in (3) (r in m/s and G_0 in kg/m²s).

Legend	System	Propellants	a (m ¹⁺²ⁿ kg ⁻ⁿ s ⁿ⁻¹)	n	Note	Reference	G_0 (kg/m ² /s)
Fuel/additives							
B	Pure HTPB	GOX/HTPB	$2.85 \cdot 10^{-5}$	0.681	—	[4]	35–280
W	Paraffin	GOX/Wax	$9.10 \cdot 10^{-5}$	0.690	—	[5]	20–120
WAl	Paraffin/13% Silbal	GOX/fuel	$9.40 \cdot 10^{-5}$	0.766	—	[6]	150–300
C	Cryo	GOX/CH ₄	$4.14 \cdot 10^{-5}$	0.830	—	[7]	3–30
S1	Pure HTPB	GOX/fuel	—	—	baseline, [8, Figure 11]	[8]	80–150
S12	HTPB/13% Al325	GOX/fuel	—	—	[8, Figure 11]	[8]	80–120
S13	HTPB/13% ALEX	GOX/fuel	—	—	coated, [8, Figure 11]	[8]	70–120
Hb	Pure HTPB	GOX/HTPB	$8.7 \cdot 10^{-5}$	0.530	baseline	[9]	50–400
HAl	HTPB/Al	GOX/fuel	$1.4 \cdot 10^{-5}$	0.930	—	[9]	50–400
HAP	HTPB/AP	GOX/fuel	$3.8 \cdot 10^{-5}$	0.710	—	[9]	50–400
HAPAl	HTPB/Al/AP	GOX/fuel	$1.2 \cdot 10^{-5}$	0.97	—	[9]	50–400
Swirl/grain geometry							
VX	Vortex	GOX/HTPB	$1.93 \cdot 10^{-4}$	0.540	—	[10]	60–110
V	End-burning + Swirl	GOX/PMMA	$3.45 \cdot 10^{-5}$	0.778	—	[11]	40–60
Vb	End-burning + Swirl	GOX/PMMA	$1.45 \cdot 10^{-5}$	0.749	no swirl	[11]	40–60
V	End-burning + Swirl	GOX/PMMA	$5.96 \cdot 10^{-5}$	0.641	—	[11]	10–20
Vb	End-burning + Swirl	GOX/PMMA	$2.76 \cdot 10^{-5}$	0.581	no swirl	[11]	10–20
RU	Radial	GOX/HTPB	$9.20 \cdot 10^{-5}$	0.570	upper disk	[12]	30–70
RL	Radial	GOX/HTPB	$1.00 \cdot 10^{-4}$	0.700	lower disk	[12]	30–70
CA	CAMUI	GOX/PE	$2.40 \cdot 10^{-5}$	0.800	(11), $\alpha' = 3$	[13]	200–700

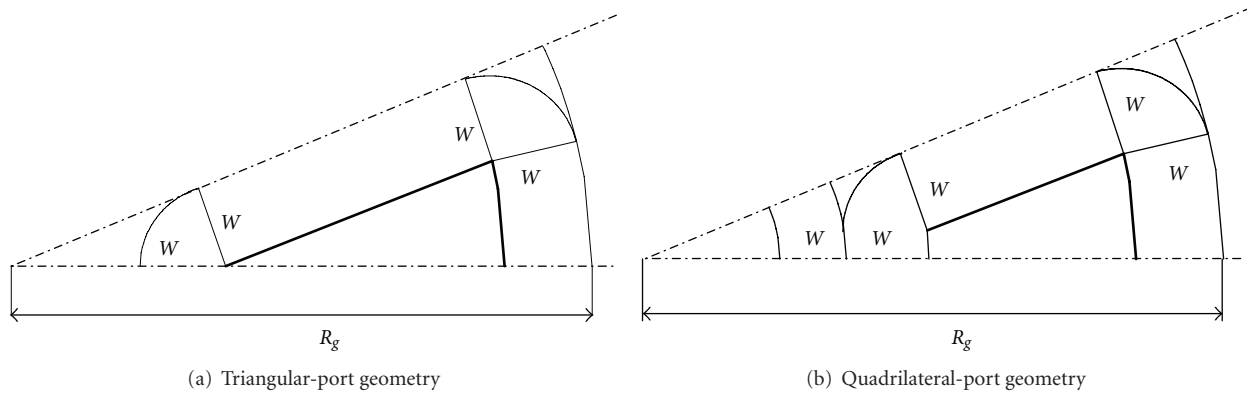


FIGURE 5: Multiport geometries.

impulse. In fact, even if their condensed combustion products determine multiphase losses, they have high reaction heat and high density. Being usually in powdered form they can easily be mixed in solid fuels. In the case of HREs it has been proven that metal additives may enhance regression rate. The addition of various types of metals (e.g., Al, LiH, B, W, Mg) into solid fuels has been tested. Most investigations considered aluminum, lithium, and boron.

Regression rate is influenced by component characteristics (e.g., reactivity, heat of oxidation, density) and particle features (e.g., shape, dimension, coating). Aluminum may be considered the most researched additive. It has a high heat of oxidation, high density and ease of ignition. Lithium-based particles are highly reactive, but the heat of oxidation

is low compared to more common particles such as aluminum. Finally, boron has a very high heat of combustion but is not so easy to ignite, which is of concern in limited volume propulsion systems. As far as dimension is concerned, micro-sized particles have been extensively tested. More recently nanosized particles have been used. Nanosized particles have a very high surface to volume ratio. Compared to micro-sized particles, nanosized particles present reduced ignition and burning time, present a more complete combustion (high c^* efficiency), and determine a larger increment of regression rate, but they are more expensive and complicate the grain production process.

Nonvolatile fuel particles (e.g., aluminum) in the grain have several effects, influencing both physical properties

TABLE 2: Optimal design and performance of sounding rocket for different propellant combinations.

Propellants	a ($\text{m}^{1+2n} \text{kg}^{-n} \text{s}^{-n-1}$)	n	Reference	F_i (kN)	α_i	m_p (kg)	D (m)	L (m)	t_{HG} (s)
HP/PE	$7.00 \cdot 10^{-6}$	0.800	[38]	24.8	8.57	339	0.42	5.01	299
LOX/HTPB	$9.24 \cdot 10^{-6}$	0.852	[39]	23.5	3.20	328	0.46	5.52	219
N ₂ O/HTPB	$1.87 \cdot 10^{-4}$	0.347	[40]	16.2	10.92	340	0.40	4.75	177

of the solid and the combustion process. Reasons behind some test results are currently under investigation. The main known effects due to nonvolatile particles are as follows.

- (i) Particles such as metals have higher density than fuel binders, and the grain mean density changes with the percentage of weight added k . It is useful to consider both the regression rate r and the mass burning rate $\rho_F r$ improvement. For example, if a weight fraction of 20% of ultrafine aluminum (UFAL) is added in HTPB, the regression rate is increased by about 40%, whereas the mass burning rate increases by almost 70% over that of pure HTPB [27].
- (ii) The blocking effect on surface heat transfer depends only on the gas blowing rate. Referring only to the volatile fuel mass flow, the density $\rho_v = (1 - k)\rho_F$ should be used instead of ρ_F in the previous equations (1) and (2). It follows that, disregarding other effects, the regression rate should be nearly inversely proportional to $(1 - k)$.
- (iii) The value of $\Delta H_{v,\text{eff}}$ (here evaluated on a volatile binder mass basis) is higher than the value of the volatile binder alone ΔH_v , as further energy is needed to heat the nonvolatile particle to the surface temperature. Nevertheless, due to the relatively low heat capacity of most metal additives, $\Delta H_{v,\text{eff}}$ does not differ much from ΔH_v . The new value of $\Delta H_{v,\text{eff}}$ should be used to evaluate B , but the resulting effect is mitigated by the low exponent of B in (2). (Note that a different point of view is often adopted in the literature: reference is made to the whole mass of the fuel grain. In this case $\Delta H_{v,\text{eff}}$ is decreased as the nonvolatile particle should be only heated to surface temperature and not gasified.)
- (iv) The radiant energy flux coming from condensed particles is large. This effect is mitigated by the coupling effect between radiant and convective heat fluxes.
- (v) Additives enhance flame temperature and $\Delta H_{f,w}$ increases. If particle size is large (some μm) the nonvolatile particles perform distributed combustion releasing some heat far from the fuel surface. On the contrary, nanometric particles burn more rapidly and closer to the fuel surface. Also microexplosions may be experienced. Moreover particle coating affects combustion. The new value of $\Delta H_{f,w}$ should be used to evaluate B , but the resulting effect is mitigated by the low exponent of B in (2).

(vi) The removal of solid from the grain surface may become the rate-limiting process for fuel rate regression [51]. The presence of flakes/agglomerates has been observed on the surface and in the combustion zone. Metals and their oxide may accumulate on the surface and leave it as agglomerates. At high mass fluxes the decomposition of fuel binders such as HTPB occurs very quickly and soot is formed, possibly due to desorption process of HTPB fragments at the grain surface.

(vii) Some of the oxidizer is consumed by metal particles burning and converted to solid oxides, thus reducing local gaseous mass-flux.

Beside metals, also oxidizer particles such as ammonium perchlorate (AP) have been used [52–55]. The presence of an oxidizer in the solid grain determines near-surface/heterogeneous reactions. In addition the flame in the boundary layer approaches the surface, thus further enhancing heat transfer. Consequently, the regression rate increases. Nevertheless, the inherently safe inert behavior of the solid grain is compromised.

4.2. Energetic Compounds. Energetic formulations can be used in solid fuels to replace low-energy conventional binders such as HTPB. Both polymers and/or plasticizers which contribute to the overall energy of the composition can be used.

High nitrogen ingredients (HiN) show great promise [56, 57]. Despite low decomposition temperatures, energetic materials such as triaminoguanidinium azotetrazolate (TAGzT) present positive heat of formation. Containing no oxygen, the dominant chemistry is more centered on condensed phase reactions and much faster decomposition rates are obtained when compared to HMX. A 25% increment in regression rate with respect to a similar HTPB grain has been observed using a 25% wt addition of TAGzT [58]. If nanoaluminum is added in addition to HiN ingredients, Al reacts with the high-temperature nitrogen liberated from the decomposition of HiN material to form AlN near the surface where oxygen is absent.

Azido-substituted polymers such as glycidyl azide polymer (GAP) [59], 3,3-bis-(azidomethyl)oxetane (BAMO) and 3-azidomethyl-3-methyl oxetane (AMMO) are effective as the polymer matrix. However, these compounds begin to transition the inert fuel to a fuel-rich solid propellant and the safe nature of classical HREs may be compromised.

4.3. Paraffin Fuels. Researchers at Stanford University [60] discovered that paraffin-based fuels exist which have regression rates that are 3–4 times than those of conventional

hybrid fuels. This is mainly due to the production of a thin liquid layer on the fuel grain surface which becomes instable: If this layer is characterized by low viscosity μ and low surface tension σ , instability driven by the oxidizer flow may arise and liquid fuel droplets are injected into the boundary layer [5, 61]. This mass-transfer mechanism is similar to a spray injection and does not depend on heat transfer. It enhances fuel mass flow without the blocking effect typical of gaseous fuel blowing. The entrained mass flow \dot{m}_{entr} depends on dynamic pressure p_{dyn} , layer thickness h , and liquid properties (i.e., μ and σ) at the temperature of the melt layer

$$\dot{m}_{\text{entr}} \propto \frac{p_{\text{dyn}}^{\beta} h^{\delta}}{\sigma^{\theta} \mu^{\lambda}}. \quad (9)$$

As shown in (9), entrainment occurs only when the liquid in the melt layer has low values of μ and σ . For example, high-density polyethylene (HDPE) does form a melt layer, but μ is four orders of magnitude larger than paraffin and droplet entrainment is not significant. In contrast, fuels such as paraffin waxes and polyethylene waxes have low viscosity. These fuels also present other advantages, as they are low-cost, easy to process, and environmentally benign. They may give a specific impulse similar to kerosene, but with higher density and without the combustion product toxicity typical of SRM grains. A blend of different components can be used to mitigate this issue and to tailor regression rate for a given mission. For example, ethylene-vinyl acetate copolymers have been mixed with paraffin-wax to change the melted-fuel viscosity [62]. According to experimental data, regression rate increases almost in proportion with $\mu^{-1/6}$. Beside all these advantages, one issue is the low mechanical strength. Additives may be used to improve this quality, but they may affect viscosity and surface tension adversely.

Additives to further enhance the regression rate have also been used. As an example high regression rate has been experienced adding Al particles in paraffin-based fuels: 13% wt of aluminum particles (Silberline) determine a 30% regression rate enhancement [8]. It is believed that aluminum particles coming from the surface may be encapsulated by the wax, thus helping ignition. Regression rate usually increases with loaded weight of additive. This is not the case of some tests with ammonia borane [48], where regression rate was enhanced with small weight fraction, while decreased for higher weight fractions.

4.4. Cryogenic Fuels. Many fuels such as methane, ethylene, pentane, and RP1 have been tested as solid cryogenic grains [63–65]. They proved to regress 2 to 10 times faster than storable fuels in the same operating conditions. Solid methane/gaseous oxygen (GOX) proved to regress at nearly 8 mm/s with an oxidizer mass flux of 20 kg/m²/s. Also, solid oxidizers such as CO and O₂ have been tested (*reverse* HRE configuration) [66]. The high regression rate obtained is explained by the theories developed to describe high regression rates in paraffin fuels [5, 61]. Results are encouraging, but complications arise due to the low temperatures, and the production of large grain is difficult.

5. Nonconventional Grain Geometries and Injectors

Methods can be used that modify classical flow structure in order to improve heat transfer. These approaches may be based on nonconventional grain geometry, nonconventional injector design, or both. Nonconventional geometries, for example, radial and/or end burning of the grain, may determine 3D flows with detachments and recirculation. Swirl injectors are able to reduce both thickness and growth of the boundary layer, thus enhancing heat transfer. The heat transfer variation is reduced and regression rate is more uniform.

5.1. Head-End Swirl in Side-Burning Grains. Several researchers tested swirl injector at the fore end of conventional cylindrical grains [11, 67]. For instance, Yuasa et al. [11] reports results for different grain length, geometric swirl factor, and G_O . Swirl strength and oxidizer mass flux were varied independently. An axial injector was also used to obtain a baseline correlation. A regression rate 2.7 times greater than that for the baseline case was experienced using GOX and PMMA. Using the correlation $r = aG_O^n$ it has been found that the exponent n is not affected significantly by the swirl number, but changes with the range of mass flux ($n \sim 0.8$ for large values of G_O according to the theoretical turbulent layer heat transfer, while $n \sim 0.6$ at lower G_O values, probably due to radiation effects). On the contrary, the value of a increases almost linearly with swirl factor.

Some researchers also modified the grain geometry [67, 68]. Lee et al. [67] considered grooves in the grain and swirl injectors. Separated and combined effects were analyzed. Swirl injectors alone are able to have double-regression rate, while grooves have a minor effect if used alone. Grooves are supposed to enhance the turbulence in the near-surface region and allow for an increased burning surface of more than 100%, but the complexity and the cost associated with grain manufacture must be taken into account. In [68] a tapered grain is proposed to avoid swirl decay along the grain axis. Conservation of angular momentum accelerates the tangential velocity because of section reduction and the swirl angle may be maintained.

It is to be pointed out that some effects of swirling must be addressed, including torque and effects of nonaxial flow in the nozzle (effective throat area and divergence losses). This holds for any of the concepts employing swirl oxidizer injection.

5.2. Aft-End Swirl in Side-Burning Grains: The Vortex Hybrid. The key characteristic of vortex hybrid [10, 69, 70] is a unique coaxial, coswirling, counterflowing vortex pair which has been found to improve regression rate. A classical cylindrical grain with circular port section is used. The vortex pair is obtained by injecting the oxidizer through a swirl injector located between the aft end of the fuel grain and the inlet of the exit nozzle. The oxidizer is prevented from directly flowing out of the nozzle by centrifugal forces and pressure gradients. An outer vortex is formed which spirals toward the engine head end. At the engine head end, the outer

vortex turns inward and transforms into an inner vortex that spirals toward the nozzle. This flow structure presents many advantages: the residence time is increased, mixing is enhanced, both thickness and growth of the boundary layer are reduced, thus augmenting the heat transfer to the fuel surface and making the regression rate very uniform. Tests have been carried out using GOX with HTPB and other proprietary fuels. HTPB shows a regression rate up to 6 times faster than those in HREs with classical head end injectors. Using the classical correlation of (3), it has been found [14]:

$$r = 0.193G_O^{0.54}. \quad (10)$$

The empirical power of 0.54 on mass flux, in conjunction with the single circular port and the uniform regression rate along the axis, guarantees a reduced mixture ratio shifting. On the other hand, the regression rate depends on the injection velocity of the oxidizer. Maximum mass flux tested [10] was about 100 kg/m² s. Scale effects must be investigated.

5.3. Radial-Flow HREs. An alternative, which may improve fuel section volumetric efficiency, is the radial flow hybrid rocket. Multiple fuel plates stacked on top of each other can provide very large burn surface areas and high volumetric efficiency if there is a little gap in between the plates. This configuration can be a good option when a small L/D is important as in launcher upper stages. It can be also used for space propulsion [71]. The flow can be injected from a central hole in a disk, or radially. The measured regression rates are greater than those observed in axial port designs at the same flux and chamber pressure levels [12]. However, detailed regression on both upper and lower fuel disks is very complex, being influenced by flow impingement, flow separation, and 3D flows that cause nonuniform regression rate, determining the presence of sliver. In addition, structural integrity may be of concern if multiple disks are used.

Swirl have been used in radial flow hybrids. One example is the so called vortex flow pancake (VFP) [72] where the swirl injectors are between two end-burning disks of fuel. It has been found that the regression rate is highly dependent on flux. The regression rate appears to be one order of magnitude larger than the one obtained in classical HRE for similar mass fluxes. Nevertheless, the mass flux used for these tests are small with respect to typical values in classical HRE tests: Scale effects must be evaluated.

5.4. Side/End-Burning Grains: The Cascaded Multistage Impinging-Jet. The cascaded multistage impinging-jet (CAMUI) is a method proposed to improve thrust level of hybrid rockets without changing fuel material or introducing nonconventional injectors [13, 73]. This concept is based on a unique geometry of the fuel grain which consists of several stages of cylindrical blocks with two axial ports. The jet of the combustion gas collides with the burning surfaces repeatedly, resulting in the high regression rate of the solid fuel. Both side burning and lateral end burning is used, thus reducing grain length for a given A_b . In fact, each block has three burning surfaces, namely, the port surfaces and

the two lateral ends (upstream and downstream end faces). To reduce sliver and avoid grain collapsing, the ports must reach the external grain diameter when the upstream face meets the downstream end face. The three surfaces have different regression and predicting grain geometry evolution and fuel flow rate is not an easy task. The development of accurate regression rate correlation is needed. Tests have been performed using GOX/PE propellant combination. The regression rate for port surface is similar to (3):

$$r = a(\alpha')G_p^n, \quad (11)$$

but in this case a is a function of the local mixture ratio α' and the propellant mass flux G_p is used. The regression rate of forward end faces depends on the spacing between blocks H and the port area diameter D_p of the upstream block:

$$\frac{r}{(H/D_p)^m} = a(\alpha')G_p^n. \quad (12)$$

The downstream end face has a more complicated behavior, presenting non uniform regression rates. Two different regression rate correlations are introduced as wall jets enhance the regression in the central part of the face. Due to the grain configuration low values of L/D can be obtained, but volumetric efficiency and sliver may be issues.

6. Final Remarks

The low regression rate of fuel grain is one of the most challenging issues for hybrid rockets. Many solutions have been presented in the literature, demonstrating the vital research activity in hybrid rocket propulsion. The most important principles and investigated solutions have been reviewed here. The challenge is to eliminate or, at least, mitigate the negative effects of the low regression rate, without compromising the appealing features of HREs (e.g., safety, low cost, simplicity, environmental friendliness).

Propellant combinations which require high mixture ratios reduce the contribution grain fuels make. In this case the choice of the oxidizer plays a significant role. Proper tools which couple engine design and trajectory optimization are needed to find the best propellant combination to be used. In order to have acceptable rocket geometries, multiport grains have to be adopted for missions requiring high performance. However, the drawbacks of multiport grains, such as sliver and structural concerns, drive the researchers to investigate means which enhance the regression rate.

Approaches which increase regression rate have been presented in two sections of this paper. A first section has been devoted to advanced fuels, considering both additives (mainly metal particles) and nonconventional fuels, that is, paraffin-based fuels and cryogenic grains. A second section considered methods which aim at increasing the heat transfer to the grain surface, modifying grain and/or injector geometry. Figure 4 and Table 1 compare the performance of approaches reviewed here. Dashed lines shows conventional HRE regression rate for comparison. Higher regression rates are usually obtained with respect to classical HREs at similar operating conditions. Most of the solutions presented remain

at a laboratory or concept scale and need further research efforts. Nevertheless, the data presented in the literature show that promising approaches do exist and may be adopted/combined to give HREs the opportunity to become a very competitive propulsion system.

Nomenclature

A_b :	Burning surface area, m ²
A_p :	Port area, m ²
A_t :	Nozzle throat area, m ²
a :	Regression constant, m ¹⁺²ⁿ kg ⁻ⁿ s ⁿ⁻¹
B :	Blowing parameter
D :	Rocket diameter, m
D_g :	Grain outer diameter, m
D_h :	Hydraulic diameter, m
D_p :	Port diameter, m
c :	Effective exhaust velocity, m/s
c^* :	Characteristic velocity, m/s
C_F :	Thrust coefficient
F :	Thrust magnitude, N
G :	Mass flux, kg/m ²
k :	Additive loading, % wt
L :	Overall length, m
L_g :	Grain length, m
m :	Mass, kg
n :	Mass-flux exponent
p_{dyn} :	Dynamic pressure, Pa
P :	Burning perimeter, m
q :	Total heat flux, W/m ²
q_c :	Convective heat flux, W/m ²
q_r :	Radiant heat flux, W/m ²
r :	Regression rate, m/s
Re_D :	Reynolds number
w :	Web thickness, m
x :	Axis abscissa, m
α :	Mixture ratio
$\Delta H_{f,w}$:	Energy of the main stream relative to the surface, J/kg
ΔH_v :	Binder (volatile) gasification heat, J/kg
$\Delta H_{v,\text{eff}}$:	Effective gasification heat, J/kg
ϵ :	Nozzle area-ratio
μ :	Dynamic viscosity, Pa s
ρ :	Density, kg/m ³
σ :	Surface tension, N/m.

Superscripts

·: Time derivative.

Subscripts

c :	Combustion chamber
e :	Nozzle exit
entr:	Entrained
F :	Fuel
i :	Initial
O :	Oxidizer
p :	Overall propellant (oxidizer + fuel).

References

- [1] M. A. Dornheim, "Reaching 100 km," *Aviation Week and Space Technology*, vol. 161, no. 6, pp. 45–46, 2004.
- [2] J. Benson, "Safe and affordable human access to LEO," in *Proceedings of the AIAA Space Conference & Exhibition*, pp. 1215–1216, September 2005, AIAA Paper 2005-6758.
- [3] S. Gordon and B. J. McBride, "Computer program for calculation of complex chemical equilibrium compositions and applications," NASA Reference Publication 1311, 1996.
- [4] G. Sutton, *Rocket Propulsion Elements: An Introduction to the Engineering of Rockets*, Wiley, New York, NY, USA, 6th edition, 1992.
- [5] M. A. Karabeyoglu, D. Altman, and B. J. Cantwell, "Combustion of liquefying hybrid propellants: part 1, General theory," *Journal of Propulsion and Power*, vol. 18, no. 3, pp. 610–620, 2002.
- [6] G. A. Risha, B. J. Evans, E. Boyer, and K. K. Kuo, "Metals, energetic additives, and special binders used in solid fuels for hybrid rockets," in *Fundamentals of Hybrid Rocket Combustion and Propulsion*, M. J. Chiaverini and K. K. Kuo, Eds., vol. 218 of *Progress in Astronautics and Aeronautics*, chapter 10, pp. 413–456, AIAA, Reston, Va, USA, 2007.
- [7] D. J. Gramer and E. E. Rice, "Experimental investigation of a metallized cryogenic hybrid rocket engine," in *Proceedings of the 34th AIAA/SAE/ASME/ASEE Joint Propulsion Conference and Exhibit*, July 1998, AIAA Paper 98-3509.
- [8] B. Evans, E. Boyer, K. K. Kuo, G. Risha, and M. Chiaverini, "Hybrid rocket investigations at penn state university's high pressure combustion laboratory: overview and recent results," in *Proceedings of the 45th AIAA/ASME/SAE/ASEE Joint Propulsion Conference and Exhibit*, August 2009.
- [9] P. George, S. Krishnan, P. M. Varkey, M. Ravindran, and L. Ramachandran, "Fuel regression rate in hydroxyl-terminated-polybutadiene/gaseous-oxygen hybrid rocket motors," *Journal of Propulsion and Power*, vol. 17, no. 1, pp. 35–42, 2001.
- [10] W. H. Knuth, M. J. Chiaverini, J. A. Sauer, and D. J. Gramer, "Solid-fuel regression rate behavior of vortex hybrid rocket engines," *Journal of Propulsion and Power*, vol. 18, no. 3, pp. 600–609, 2002.
- [11] S. Yuasa, K. Yamamoto, H. Hachiya, K. Kitagawa, and Y. Oowada, "Development of a small sounding hybrid rocket with a swirling-oxidizer-type engine," in *Proceedings of the 37th AIAA/ASME/SAE/ASEE Joint Propulsion Conference*, 2001, AIAA Paper 2001-3537.
- [12] J. R. Caravella Jr., S. D. Heister, and E. J. Wernimont, "Characterization of fuel regression in a radial flow hybrid rocket," *Journal of Propulsion and Power*, vol. 14, no. 1, pp. 51–56, 1998.
- [13] H. Nagata, S. Hagiwara, T. Totani, and T. Uematsu, "Optimal fuel grain design method for CAMUI type hybrid rocket," in *Proceedings of the 47th AIAA/ASME/SAE/ASEE Joint Propulsion Conference and Exhibit*, 2011, AIAA Paper 2011-6105.
- [14] M. J. Chiaverini, "Review of solid-fuel regression rate behavior in classical and nonclassical hybrid rocket motors," in *Fundamentals of Hybrid Rocket Combustion and Propulsion*, M. J. Chiaverini and K. K. Kuo, Eds., vol. 218 of *Progress in Astronautics and Aeronautics*, chapter 2, pp. 37–125, AIAA, Reston, Va, USA, 2007.
- [15] G. A. Marxman and M. Gilbert, "Turbulent boundary layer combustion in the hybrid rocket," in *Proceedings of the 9th International Symposium on Combustion*, pp. 371–383, Academic Press, 1963.

- [16] G. A. Marxman, C. E. Wooldridge, and R. J. Muzzy, "Fundamentals of hybrid boundary layer combustion," in *Heterogeneous Combustion*, H. G. Wolfhard, I. Glassman, and L. Green Jr., Eds., vol. 15 of *Progress in Astronautics and Aeronautics*, pp. 485–521, Academic Press, New York, NY, USA, 1964.
- [17] G. A. Marxman, "Combustion in the turbulent boundary layer on a vaporizing surface," in *Proceedings of the 10th International Symposium on Combustion*, pp. 1337–1349, Combustion Institute, 1965.
- [18] R. J. Muzzy, "Applied hybrid combustion theory," in *Proceedings of the 8th Joint Propulsion Specialist Conference (AIAA/SAE '72)*, 1972, AIAA Paper No. 72-1143.
- [19] D. Altman and R. Humble, "Hybrid rocket propulsion systems," in *Space Propulsion Analysis and Design*, R. W. Humble, G. N. Henry, and W. J. Larson, Eds., p. 379, The Mc Graw-Hill Companies, Primis Custom, New York, NY, USA, 1995.
- [20] P. J. Paul, H. S. Mukunda, and V. K. Jain, "Regression rates in boundary layer combustion," in *Proceedings of the 19th International Symposium on Combustion*, pp. 717–729, Combustion Institute, 1982.
- [21] P. N. Estey, D. Altman, and J. S. McFarlane, "An evaluation of scaling effects for hybrid rocket motors," in *Proceedings of the 27th Joint Propulsion Conference (AIAA/SAE/ASME '91)*, Sacramento, Calif, USA, June 1991, AIAA Paper 91-2517.
- [22] L. D. Strand, M. D. Jones, R. L. Ray, and N. S. Cohen, "Characterization of hybrid rocket internal heat flux and HTPB fuel pyrolysis," in *Proceedings of the 30th Joint Propulsion Conference*, June 1994, AIAA Paper 94-2876.
- [23] L. D. Smoot and C. F. Price, "Pressure dependence of hybrid fuel regression rates," *AIAA Journal*, vol. 5, no. 1, pp. 102–106, 1966.
- [24] F. J. Kosdon and F. A. Williams, "Pressure dependence of nonmetalized hybrid fuel regression rate," *AIAA Journal*, vol. 5, no. 4, pp. 774–777, 1967.
- [25] R. N. Kumar and D. B. Stickler, "Polymer-degradation theory of pressure-sensitive hybrid combustion," in *Proceedings of the 3th International Symposium on Combustion*, pp. 1059–1072, Combustion Institute, 1971.
- [26] E. Miller, "Hybrid rocket combustion regression rate model," *AIAA Journal*, vol. 4, no. 4, pp. 752–753, 1966.
- [27] M. J. Chiaverini, N. Serin, D. K. Johnson, Y. C. Lu, K. K. Kuo, and G. A. Risha, "Regression rate behavior of hybrid rocket solid fuels," *Journal of Propulsion and Power*, vol. 16, no. 1, pp. 125–132, 2000.
- [28] M. J. Chiaverini, K. K. Kuo, A. Peretz, and G. C. Harting, "Regression-rate and heat-transfer correlations for hybrid rocket combustion," *Journal of Propulsion and Power*, vol. 17, no. 1, pp. 99–110, 2001.
- [29] W. M. Kays and M. E. Crawford, *Convective Heat and Mass Transfer*, McGrawHill, New York, NY, USA, 2nd edition, 1980.
- [30] D. A. Kearney, K. F. Joiner, M. P. Gnau, and M. A. Casemore, "Improvements to the marketability of hybrid propulsion technologies," in *Proceedings of the AIAA Space Conference*, pp. 1674–1688, September 2007, AIAA Paper 2007-6144.
- [31] L. Casalino and D. Pastrone, "Optimal design of hybrid rocket motors for microgravity platform," *Journal of Propulsion and Power*, vol. 24, no. 3, pp. 491–498, 2008.
- [32] A. Ben-Yakar and A. Gany, "Hybrid engine design and analysis," in *Proceedings of the 29th Joint Propulsion Conference*, June 1993, AIAA Paper 93-2548.
- [33] L. Casalino, D. Pastrone, and F. Simeoni, "Hybrid rocket upper stage optimization: effects of grain geometry," in *Proceedings of the 47th AIAA/ASME/SAE/ASEE Joint Propulsion Conference and Exhibit*, 2011, AIAA Paper 2011-6024.
- [34] J. Fuller, P. Lu, R. Jansen, and J. Hoffman, "Advantages of rapid prototyping for hybrid rocket motor fuel grain fabrication," in *Proceedings of the 47th AIAA/ASME/SAE/ASEE Joint Propulsion Conference and Exhibit*, 2011, AIAA Paper 2011-5821.
- [35] L. Casalino and D. Pastrone, "Optimal design and control of hybrid rockets for access to space," in *Proceedings of the 41st AIAA/ASME/SAE/ASEE Joint Propulsion Conference and Exhibit*, July 2005.
- [36] L. Casalino and D. Pastrone, "Optimization of hybrid sounding rockets for hypersonic testing," in *Proceedings of the 45th AIAA/ASME/SAE/ASEE Joint Propulsion Conference and Exhibit*, August 2009.
- [37] L. Casalino and D. Pastrone, "Optimal design of hybrid rocket motors for launchers upper stages," *Journal of Propulsion and Power*, vol. 26, no. 3, pp. 421–427, 2010.
- [38] E. J. Wernimont and S. D. Heister, "Combustion experiments in hydrogen peroxide/polyethylene hybrid rocket with catalytic ignition," *Journal of Propulsion and Power*, vol. 16, no. 2, pp. 218–326, 2000.
- [39] M. Rocker, "Modeling of Nonacoustic Combustion Instability in Simulations of Hybrid Motor Tests," NASA/TP-000-209905, 2000.
- [40] E. Doran, J. Dyer, K. Lohner, Z. Dunn, B. Cantwell, and G. Zilliac, "Nitrous oxide hybrid rocket motor fuel regression rate characterization," in *Proceedings of the 43rd AIAA/ASME/SAE/ASEE Joint Propulsion Conference*, pp. 3485–3496, July 2007, AIAA Paper 2007-5352.
- [41] L. D. Smoot and C. F. Price, "Regression rates of metalized hybrid fuel systems," *AIAA Journal*, vol. 4, no. 5, pp. 910–915, 1965.
- [42] L. D. Strand, R. L. Ray, and N. S. Cohen, "Hybrid rocket combustion study," in *Proceedings of the 29th AIAA/ASME/SAE/ASEE Joint Propulsion Conference and Exhibit*, San Diego, Calif, USA, 1993, AIAA Paper 93-2412.
- [43] H. R. Lips, "Heterogeneous combustion of highly aluminized hybrid fuels," *AIAA Journal*, vol. 15, no. 6, pp. 777–778, 1977.
- [44] G. A. Risha, E. Boyer, R. B. WeHREan, and K. K. Kuo, "Performance comparison of HTPB-based solid fuels containing nano-sized energetic powder in a cylindrical hybrid rocket motor," in *Proceedings of the 38th AIAA/ASME/SAE/ASEE Joint Propulsion Conference*, 2002, AIAA Paper 2002-3576.
- [45] E. Farbar, J. Louwers, and T. Kaya, "Investigation of metallized and nonmetallized hydroxyl terminated polybutadiene/hydrogen peroxide hybrid rockets," *Journal of Propulsion and Power*, vol. 23, no. 2, pp. 476–486, 2007.
- [46] A. McCormick, E. Hultgren, M. Lichtman, J. Smith, R. Sneed, and S. Azimi, "Design, optimization, and launch of a 3" diameter N₂O/aluminized paraffin rocket," in *Proceedings of the 41st AIAA/ASME/SAE/ASEE Joint Propulsion Conference and Exhibit*, 2005, AIAA Paper 2005-4095.
- [47] B. Evans, A. Favorito, and K. Kuo, "Study of solid fuel burning-rate enhancement behavior in an X-ray translucent hybrid rocket motor," in *Proceedings of the 41st AIAA/ASME/SAE/ASEE Joint Propulsion Conference and Exhibit*, Tucson, Arizona, 2005, AIAA Paper 2005-3909.
- [48] M. R. Weismiller, T. L. Connell Jr., G. A. Risha, and R. A. Yetter, "Characterization of ammonia borane (NH₃BH₃) enhancement to a paraffin fueled hybrid rocket system," in *Proceedings of the 46th AIAA/ASME/SAE/ASEE Joint Propulsion Conference and Exhibit*, 2010, AIAA Paper 2010-6639.

- [49] L. Galfetti, L. Merotto, M. Boiocchi, F. Maggi, and L. De Luca, "Ballistic and rheological characterization of paraffinbased fuels for hybrid rocket propulsion," in *Proceedings of the 47th AIAA/ASME/SAE/ASEE Joint Propulsion Conference and Exhibit*, 2011, AIAA Paper 2011-5680.
- [50] D. B. Larson, E. Boyer, T. Wachs et al., "Characterization of the performance of paraffin / LiAlH₄ solid fuels in a hybrid rocket system," in *Proceedings of the 47th AIAA/ASME/SAE/ASEE Joint Propulsion Conference and Exhibit*, San Diego, Calif, USA, 2011, AIAA Paper 2011-5822.
- [51] L. D. Strand, R. L. Ray, F. A. Anderson, and N. S. Cohen, "Hybrid rocket fuel combustion and regression rate study," in *Proceedings of the AIAA, SAE, ASME, and ASEE, Joint Propulsion Conference and Exhibit*, July 1992, AIAA Paper 1992-3302.
- [52] B. N. Raghunandan, E. R. Ravichandran, and A. G. Marathe, "Combustion related to solid-fuel ramjets," *Journal of Propulsion and Power*, vol. 1, no. 6, pp. 502–504, 1985.
- [53] P. George, S. Krishnan, P. M. Varkey, M. Ravindran, and L. Ramachandran, "Fuel regression rate in hydroxyl-terminated-polybutadiene/gaseous-oxygen hybrid rocket motors," *Journal of Propulsion and Power*, vol. 17, no. 1, pp. 35–42, 2001.
- [54] L. R. Knox, M. D. Moser, and R. A. Frederick Jr., "Mixed hybrid propellants," in *Proceedings of the 39th AIAA/ASME/SAE/ASEE Joint Propulsion Conference and Exhibit*, 2003, AIAA Paper 2003-4745.
- [55] R. A. Frederick Jr., J. J. Whitehead, L. R. Knox, and M. D. Moser, "Regression rates study of mixed hybrid propellants," *Journal of Propulsion and Power*, vol. 23, no. 1, pp. 175–180, 2007.
- [56] D. E. Chavez and M. A. Hiskey, "1,2,4,5-tetrazine based energetic materials," *Journal of Energetic Materials*, vol. 17, no. 4, pp. 357–377, 1999.
- [57] S. F. Son, H. L. Berghout, C. A. Bolme, D. E. Chavez, D. Naud, and M. A. Hiskey, "Burn rate measurements of HMX, TATB, DHT, DAAF, and BTATz," in *Proceedings of the Combustion Institute*, vol. 28, pp. 919–924, 2000.
- [58] A. Risha, A. G. Miller, R. A. Glass, V. A. Yeager, M. J. Chiaverni, and B. C. Tappan, "Regression rates of solid fuels containing high nitrogen (HiN) materials," in *Proceedings of the 47th AIAA/ASME/SAE/ASEE Joint Propulsion Conference and Exhibit*, August 2011, AIAA Paper 2011-5912.
- [59] K. Hori et al., "Combustion characteristics of hybrid rocket motor using GAP as a solid fuel (II)," in *Proceedings of the 47th AIAA/ASME/SAE/ASEE Joint Propulsion Conference and Exhibit*, 2011, AIAA Paper 2011-5819.
- [60] M. A. Karabeyoglu, B. J. Cantwell, and D. Altman, "Development and testing of paraffin-based hybrid rocket fuels," in *Proceedings of the 37th AIAA/ASME/SAE/ASEE Joint Propulsion Conference and Exhibit*, July 2001, AIAA Paper 2001-4503.
- [61] M. A. Karabeyoglu and B. J. Cantwell, "Combustion of liquefying hybrid propellants: part 2, Stability of liquid films," *Journal of Propulsion and Power*, vol. 18, no. 3, pp. 621–630, 2002.
- [62] I. Nakagawa and S. Nikone, "Study on the regression rate of paraffin-based hybrid rocket fuel," *Journal of Propulsion and Power*, vol. 27, no. 6, pp. 1276–1279, 2011.
- [63] P. G. Carrick and W. C. Larson, "Lab scale test and evaluation of cryogenic solid hybrid rocket fuels," in *Proceedings of the 31st AIAA/ASME/SAE/ASEE Joint Propulsion Conference and Exhibit*, 1995, AIAA Paper 95-2948.
- [64] M. E. De Rose, K. L. Pfeil, P. G. Carrick, and W. C. Larson, "Tube burner studies of cryogenic solid combustion," in *Proceedings of the 33rd AIAA/ASME/SAE/ASEE Joint Propulsion Conference and Exhibit*, 1997, AIAA Paper 97-3076.
- [65] E. E. Rice, M. J. Chiaverini, C. P. St.Clair, W. H. Knuth, and R. J. Gustafson, "Mars ISRU CO/O₂ hybrid engine development status," in *Proceedings of the 38th Aerospace Sciences Meeting*, 2000, AIAA Paper 2000-1066.
- [66] C. P. St.Clair, E. E. Rice, W. H. Knuth, and D. J. Gramer, "Advanced cryogenic solid hybrid rocket engine developments: concept and testing," in *Proceedings of the 34th AIAA/ASME/SAE/ASEE Joint Propulsion Conference and Exhibit*, 1998, AIAA Paper 98-3508.
- [67] C. Lee, Y. Na, and G. Lee, "The enhancement of regression rate of hybrid rocket fuel by helical grain configuration and swirl flow," in *Proceedings of the AIAA/ASME/SAE/ASEE Joint Propulsion Conference and Exhibit*, 2005, AIAA Paper 2005-3906.
- [68] R. Wilkinson, K. Hart, R. Day, and I. Coxhill, "Proof-of-concept testing of a sustained vortex-flow configuration for hybrid rocket motors," in *Proceedings of the 46th AIAA/ASME/SAE/ASEE Joint Propulsion Conference and Exhibit*, July 2010, AIAA Paper 2010-6782.
- [69] W. H. Knuth, M. J. Chiaverini, D. J. Gramer, and J. A. Sauer, "Numerical simulation of vortex-driven, hybrid rocket engines," in *Proceedings of the 34th AIAA/ASME/SAE/ASEE Joint Propulsion Conference and Exhibit*, 1998, AIAA Paper 98-3351.
- [70] J. Madjalani, "Vortex injection hybrid," in *Fundamentals of Hybrid Rocket Combustion and Propulsion*, M. J. Chiaverini and K. K. Kuo, Eds., vol. 218 of *Progress in Astronautics and Aeronautics*, chapter 6, pp. 247–276, AIAA, Reston, Va, USA, 2007.
- [71] R. Jansen and E. Teegarden, "Characterization of a vortex-flow end-burning hybrid rocket motor for nanosatellite applications," in *Proceedings of the AIAA/ASME/SAE/ASEE Joint Propulsion Conference and Exhibit*, 2012, AIAA Paper 2012-0125.
- [72] G. Haag, M. Sweeting, and G. Richardson, "An alternative geometry hybrid rocket for spacecraft orbit transfer manoeuvres," in *Proceedings of the International Astronautical Federation (IAF '00)*, 2000, IAF Paper 00-W.2.07.
- [73] H. Nagata, "New fuel configurations for advanced hybrid rockets," in *Proceedings of the International Astronautical Federation (IAF '98)*, Paris, France, 1998, IAF-98-S.3.09.

Research Article

Burning Characteristics of Ammonium-Nitrate-Based Composite Propellants with a Hydroxyl-Terminated Polybutadiene/Polytetrahydrofuran Blend Binder

Makoto Kohga, Tomoki Naya, and Kayoko Okamoto

Department of Applied Chemistry, National Defense Academy, Hashirimizu 1-10-20, Yokosuka, Kanagawa 239-8686, Japan

Correspondence should be addressed to Makoto Kohga, kohga@nda.ac.jp

Received 5 December 2011; Accepted 24 January 2012

Academic Editor: Valsalayam Sanal Kumar

Copyright © 2012 Makoto Kohga et al. This is an open access article distributed under the Creative Commons Attribution License, which permits unrestricted use, distribution, and reproduction in any medium, provided the original work is properly cited.

Ammonium-nitrate-(AN-) based composite propellants prepared with a hydroxyl-terminated polybutadiene (HTPB)/polytetrahydrofuran (PTHF) blend binder have unique thermal decomposition characteristics. In this study, the burning characteristics of AN/HTPB/PTHF propellants are investigated. The specific impulse and adiabatic flame temperature of an AN-based propellant theoretically increases with an increase in the proportion of PTHF in the HTPB/PTHF blend. With an AN/HTPB propellant, a solid residue is left on the burning surface of the propellant, and the shape of this residue is similar to that of the propellant. On the other hand, an AN/HTPB/PTHF propellant does not leave a solid residue. The burning rates of the AN/HTPB/PTHF propellant are not markedly different from those of the AN/HTPB propellant because some of the liquefied HTPB/PTHF binder cover the burning surface and impede decomposition and combustion. The burning rates of an AN/HTPB/PTHF propellant with a burning catalyst are higher than those of an AN/HTPB propellant supplemented with a catalyst. The beneficial effect of the blend binder on the burning characteristics is clarified upon the addition of a catalyst. The catalyst suppresses the negative influence of the liquefied binder that covers the burning surface. Thus, HTPB/PTHF blend binders are useful in improving the performance of AN-based propellants.

1. Introduction

Solid propellants are contained and stored in the combustion chamber of a solid rocket motor and are sometimes hermetically sealed in the chamber for long-term storage. Upon ignition, the propellants react to form hot gases within the chamber, which in turn are accelerated and ejected at a high velocity through a supersonic nozzle, thereby imparting momentum to the rocket motor. Solid rocket motors offer the advantage of having few moving parts. Therefore, they are used as propulsion systems for launch vehicles, spacecrafts, missiles, and other applications.

There are various types of solid propellants, and a suitable propellant is selected to meet the requirements of each rocket motor application. A composite propellant is a solid propellant in the form of heterogeneous propellant grains composed of oxidizer crystals held together in a matrix of a synthetic or plastic binder. Ammonium perchlorate

(AP) and hydroxyl-terminated polybutadiene (HTPB) are widely used as an oxidizer and a binder, respectively, because AP/HTPB-based propellants have excellent burning and mechanical characteristics. One of the few serious drawbacks of AP-based propellants are the products of combustion, such as HCl, chlorine, and chlorine oxides, which cause atmospheric pollution.

Recently, ammonium-nitrate-(AN-) based composite propellants, that is, propellants prepared with AN as the oxidizer, have become popular, although there are some major problems associated with their use. These problems include a low burning rate, poor ignitability, and low energy output compared to AP-based propellants [1, 2]. Despite these problems, AN-based propellants are popular because they are chlorine-free, present a small hazard, and have low observable emissions (minimum smoke). Numerous approaches have been adopted to improve the burning characteristics of AN-based propellants, including the use of

catalysts [3–9], the addition of metals [10–13], and the use of energetic binders based on azide polymers [14–20].

Applying an energetic binder is an effective approach toward AN-based propellants. However, the synthesis processes of energetic binders are complicated and costly; therefore, it is difficult to manufacture these binders industrially. To date, such energetic binders have not yet been used for practical applications because they are expensive.

Polytetrahydrofuran (PTHF) is used as an ingredient in making rubber products. This inexpensive polymer is mass-produced commercially in several molecular weights. Table 1 shows the chemical properties of PTHF and HTPB. Although PTHF is not an energetic material, it could be a useful binder to improve the burning characteristics of composite propellants because oxygen is present in the repeating unit of PTHF as opposed to HTPB in which oxygen is not present [21–23]. The chemical structure of PTHF is similar to that of HTPB, and therefore, PTHF should mix easily and uniformly with HTPB.

The curing behavior, mechanical properties, and thermal decomposition behavior of HTPB binders are improved by the addition of a small amount of PTHF. PTHF is an effective plasticizer in the preparation of high-performance composite propellants [24, 25]. Furthermore, compared to HTPB, HTPB/PTHF blends have preferable curing behaviors and tensile properties for use as binders [26]. Therefore, it is expected that a HTPB/PTHF blend will prove to be a useful binder ingredient for improving the performance of AN-based composite propellants.

The thermal decomposition behaviors of AN-based composite propellants with a HTPB/PTHF-blend binder are provided in [27]. The thermal decomposition of AN/HTPB/PTHF propellants occurs at lower temperatures than that of AN/HTPB propellants according to the results of thermogravimetry/differential thermal analysis (TG-DTA). According to a visual observation of the decomposition phenomena, the propellants had decomposed significantly and the generation of smoke was more vigorous in the temperature range of 530–550 K. The size of the black residue after decomposition was smaller than that of the propellant sample before heating. The AN in the propellant decomposed completely, and the quantity of liquefied or decomposed binder increased with an increase in the mass ratio (ξ) of PTHF in the binder. AN/HTPB/PTHF propellants were found to have unique thermal decompositions. In this study, the burning characteristics of AN/HTPB/PTHF propellants were examined and reported.

2. Experimental

2.1. Sample Ingredients. AN was ground in a vibration ball mill (for 5 min) for use as an oxidizer. The weight mean diameter of AN was 125 μm . PTHF and HTPB were used as binder materials. HTPB is a widely used binder and composite propellant, while PTHF is produced in several molecular weights. In this study, three types of PTHF with sample molecular weights of 650, 1400, and 2900 designated as PTHF1, PTHF2, and PTHF3, respectively, were used. The value of the symbol increased with increasing molecular

weight. Isophorone diisocyanate (IPDI) was used as the curing agent. The ratio of the NCO group of IPDI to the OH group of HTPB and PTHF was 1.2.

The values of ξ were 0, 0.2, 0.4, 0.6, and 0.8. Table 2 shows the binder formulations. A binder at $\xi = 1$ was not prepared in this study because the burning rate characteristics of an AN-based propellant at $\xi = 1$ are provided in [23]. PTHF did not become solid by using IPDI alone, but it did become sufficiently rubbery by adding glycerin as a crosslinking modifier such that it could be used as a binder. In this study, the burning characteristics of an AN-based propellant with a HTPB/PTHF blend binder were not compared with those of a propellant at $\xi = 1$ because the addition of glycerin would make the comparison inconsistent.

Ammonium dichromate (ADC) was used as a burning catalyst and added to the propellant at 6% [8]. The weight mean diameter of ADC was 61 μm .

2.2. Burning Rate Measurement. Each of the prepared propellant strands were 10 mm in diameter and 40 mm in length. The burning behavior was investigated in a chimney-type strand burner that was pressurized with nitrogen. Each strand was ignited by applying 10 V to an electrically heated wire threaded into the top of the strand. The temperature of the wire was above 1200 K. Each propellant strand was combusted within a pressure range of 0.5–7 MPa. The burning phenomenon of the propellant was recorded by a high-speed video recorder, and the burning rate was measured from the images obtained. The combustion phenomenon was recorded at a shutter speed of 30–125 frames s^{-1} . All measurements were checked in triplicate at each pressure, and the average values were used in the data analysis.

3. Results and Discussion

3.1. Theoretical Performance. The specific impulse (I_{sp}) and adiabatic flame temperature (T_f) of the propellants at 70% and 80% AN were calculated using the NASA CEA program [28] with a combustion pressure of 7 MPa, an exit pressure of 0.1 MPa, and an initial temperature of 298 K. Table 3 shows the values of I_{sp} and T_f . The values of I_{sp} and T_f increase with an increase in ξ , and at constant ξ , these values slightly increase with a decrease in the molecular weight of PTHF. The propellant performance is theoretically dependent upon the ξ value and the molecular weight of PTHF. In particular, the increases in the values of the propellant at 80% AN are greater than those of the propellant at 70% AN. For example, the maximum difference in I_{sp} between $\xi = 0$ and 0.8 at 80% AN is 5 s, whereas that at 70% AN is 3 s. The maximum difference in T_f between $\xi = 0$ and 0.8 at 80% AN is 200 K, whereas that at 70% AN is 31 K. These values were obtained for an AN/HTPB/PTHF1 propellant. These results suggested that the effect of PTHF on propellant performance would be enhanced by the use of a smaller molecular weight of PTHF at 80% AN.

The mass fraction of IPDI in the binder increases with decreasing molecular weight of PTHF, as shown in Table 2. For example, at $\xi = 0.8$, the mass fraction of IPDI for the PTHF1 binder is 25.6% and that for the PTHF3 binder is

TABLE 1: Chemical properties of PTHF and HTPB.

Binder ingredient	PTHF	HTPB
Molecular structure	HO-($-\text{CH}_2-\text{CH}_2-\text{CH}_2-\text{CH}_2-\text{O}-$) $_n$ -H	HO-($-\text{CH}_2-\text{CH}=\text{CH}-\text{CH}_2-$) $_n$ -OH
Density (g cm^{-3})	0.970–0.981	0.902
Heat of formulation (kJ mol^{-1})	-219.2	-21.1

TABLE 2: Binder formulations.

Binder	ξ (—)	Mass fraction (%)		
		HTPB	PTHF	IPDI
PTHF1	0	92.5	0.0	7.5
	0.2	69.7	17.4	12.8
	0.4	49.5	32.9	17.6
	0.6	31.3	46.9	21.8
	0.8	14.9	59.5	25.6
PTHF2	0	92.5	0.0	7.5
	0.2	72.5	18.1	9.4
	0.4	53.3	35.6	11.1
	0.6	34.9	52.3	12.8
	0.8	17.1	68.5	14.4
PTHF3	0	92.5	0.0	7.5
	0.2	73.8	18.5	7.7
	0.4	55.3	36.8	7.9
	0.6	36.8	55.2	8.1
	0.8	18.4	73.4	8.2

8.2%. For the 80% AN propellant at $\xi = 0.8$, the difference in I_{sp} and T_f between the AN/HTPB/PTHF1 propellant and the AN/HTPB/PTHF3 propellant is 1 s and 35 K, respectively. This indicates that the influence of the IPDI fraction on propellant performance is negligible.

The value of I_{sp} theoretically increases with the use of PTHF, indicating that PTHF would be effective in enhancing the performance of an AN-based propellant. The increase in T_f would also accelerate the propellant combustion reactions. Therefore, the burning rate of the AN/HTPB propellant would be expected to increase with increasing ξ .

Table 4 shows the theoretical mole fraction of the main combustion products from the AN/HTPB/PTHF2 propellants; these products were scarcely dependent on the molecular weight of PTHF. For the 70% AN propellant, the mole fraction of graphite notably decreases with the addition of PTHF as a binder, and the fraction of other products increases with an increase in ξ . For the 80% AN propellant, no graphite is produced. The mole fraction of H_2O increases with an increase in ξ , whereas the fractions of CH_4 , CO , CO_2 , H_2 , and N_2 decrease, indicating that the hydrogen produced by the propellant decomposition would react with the oxygen in PTHF. The oxygen contained in PTHF was found to influence the reaction product compositions and cause an increase in I_{sp} and T_f .

A subsequent experiment investigated the thermal decomposition behavior and burning characteristics of propellants at 80% AN, because the influence of the HTPB/PTHF binder on the theoretical performance of a

propellant at 80% AN is greater than that of a propellant at 70% AN.

3.2. Burning Rate of Propellant. Figure 1 shows the burning rate characteristics of AN/HTPB/PTHF propellants. These propellants only burned at pressures above 2 MPa. The burning rates are seen to increase linearly on the logarithmic scale. The pressure exponent of these propellants is in the range of 0.7–0.8, and the values are not correlated with ξ and the molecular weight of PTHF. There is no obvious difference in the burning rates of the AN/HTPB/PTHF and AN/HTPB propellants.

The thermal decomposition behavior of the AN/HTPB/PTHF propellant ($\xi = 0.2$ – 0.8) was preferable for creating a high burning rate propellant because the decomposition temperature ranges of the AN/HTPB/PTHF propellant were lower than those of the AN/HTPB propellant ($\xi = 0$) [26]. The T_f for the AN/HTPB/PTHF propellant was higher than that for the AN/HTPB propellant, as described in the previous section. These results suggest that the burning rate would increase by the use of PTHF as a binder; however, the burning rates of the AN/HTPB/PTHF propellant were not significantly different from those of the AN/HTPB propellant, as shown in Figure 1.

The burning propellant at 7 MPa was quenched by a depressurization of approximately -1 MPa s^{-1} . Figure 2 shows photographs of the AN/HTPB/PTHF2 propellant at $\xi = 0$ and 0.6 after quenching. With the AN/HTPB propellant ($\xi = 0$), there was solid residue on the burning surface, and the shape of the residue was almost the same as that of the propellant. Theoretically, the propellant with 80% AN should not generate graphite, as described in Section 3.1. However, in actual, this propellant did produce a residue after the burning test, indicating that the actual propellant combustion is inferior to the theoretical one. This is because the theoretical values were calculated for an adiabatic process, while in actual combustion the propellant sample burned in a nitrogen gas flow, resulting in heat loss and mass transfer into/from the system.

On the other hand, the propellant containing PTHF did not leave a solid residue at $\xi = 0.6$, as shown in Figure 2(b). A small amount of solid residue was generated by burning, but this was removed from the burning surface and discharged from the combustion chamber along with nitrogen.

When a solid residue is produced in the combustion chamber of a rocket motor, it interferes with the combustion of the propellant and the mass ratio of the rocket decreases. Furthermore, the presence of a solid residue results in erosion of the nozzle and an exhaust plume is produced. Thus, the generation of a solid residue is undesirable. The use of PTHF as a binder ingredient prevents the generation of a solid

TABLE 3: Theoretical values of I_{sp} and T_f .

Propellant AN content (%)	AN/HTPB/PTHF1		AN/HTPB/PTHF2		AN/HTPB/PTHF3	
	70	80	70	80	70	80
ξ (—)	I_{sp} (s)					
0	189	198	189	198	189	198
0.2	190	199	189	199	189	199
0.4	190	201	190	200	190	200
0.6	191	202	191	201	191	201
0.8	192	203	191	203	191	202
ξ (—)	T_f (K)					
0	1186	1353	1186	1353	1186	1353
0.2	1194	1403	1191	1393	1190	1388
0.4	1200	1456	1197	1438	1195	1429
0.6	1208	1507	1203	1485	1200	1473
0.8	1217	1553	1210	1531	1207	1518

TABLE 4: Theoretical mole fraction of main combustion products of AN/HTPB/PTHF2 propellants.

ξ (—)	70% AN						
	Mole fraction (—)						
	CH ₄	CO	CO ₂	H ₂	H ₂ O	N ₂	Graphite
0	0.0843	0.0358	0.1270	0.2397	0.2086	0.1653	0.1393
0.2	0.0852	0.0364	0.1338	0.2411	0.2156	0.1681	0.1198
0.4	0.0862	0.0368	0.1406	0.2423	0.2227	0.1709	0.1005
0.6	0.0873	0.0371	0.1473	0.2433	0.2299	0.1737	0.0814
0.8	0.0885	0.0374	0.1541	0.2440	0.2371	0.1765	0.0624
ξ (—)	80% AN						
	Mole fraction (—)						
	CH ₄	CO	CO ₂	H ₂	H ₂ O	N ₂	Graphite
0	0.0662	0.0507	0.1719	0.2642	0.2371	0.2099	0
0.2	0.0581	0.0469	0.1700	0.2636	0.2521	0.2093	0
0.4	0.0506	0.0434	0.1680	0.2620	0.2672	0.2088	0
0.6	0.0437	0.0401	0.1659	0.2596	0.2822	0.2085	0
0.8	0.0373	0.0370	0.1637	0.2564	0.2974	0.2082	0

residue for the AN/HTPB propellant, although the burning rate of the propellant does not increase, indicating that PTHF improves the propellant performance.

Figure 3 shows scanning electron microscopy (SEM) photographs of the burning surface of a propellant quenched at $\xi = 0$ and 0.6. In Figure 3(a), the burning surface of the quenched AN/HTPB propellant ($\xi = 0$) has a sponge-like appearance. What appear to be voids in the sponge are traces of AN particles caused by the HTPB binder being barely liquefied just before decomposition [23–27]. The AN particles exposed at the burning surface decomposed and disappeared during the depressurization event. A trace amount of AN was observed at the bottom. The HTPB at the burning surface barely liquefied and maintained its shape just before decomposition. Because the shape of the binder

was preserved, the AN particles were exposed at the burning surface and decomposition gases were emitted in the gas phase.

Figure 3(b) shows the burning surface of the quenched AN/HTPB/PTHF2 propellant ($\xi = 0.6$), which is basically smooth and wavy. When the melted AN at the burning surface was cooled to the surrounding temperature, the AN crystallized and numerous cracks were generated in the AN crystals owing to phase transitions. As described above, the burning surface was smooth, indicating that a majority of materials at the burning surface were binder ingredients. The depressions depict the traces of the decomposition of AN particles and also some projections at the burning surface. The AN particles were below the surface of these projections; small holes were produced by ejection of the decomposed

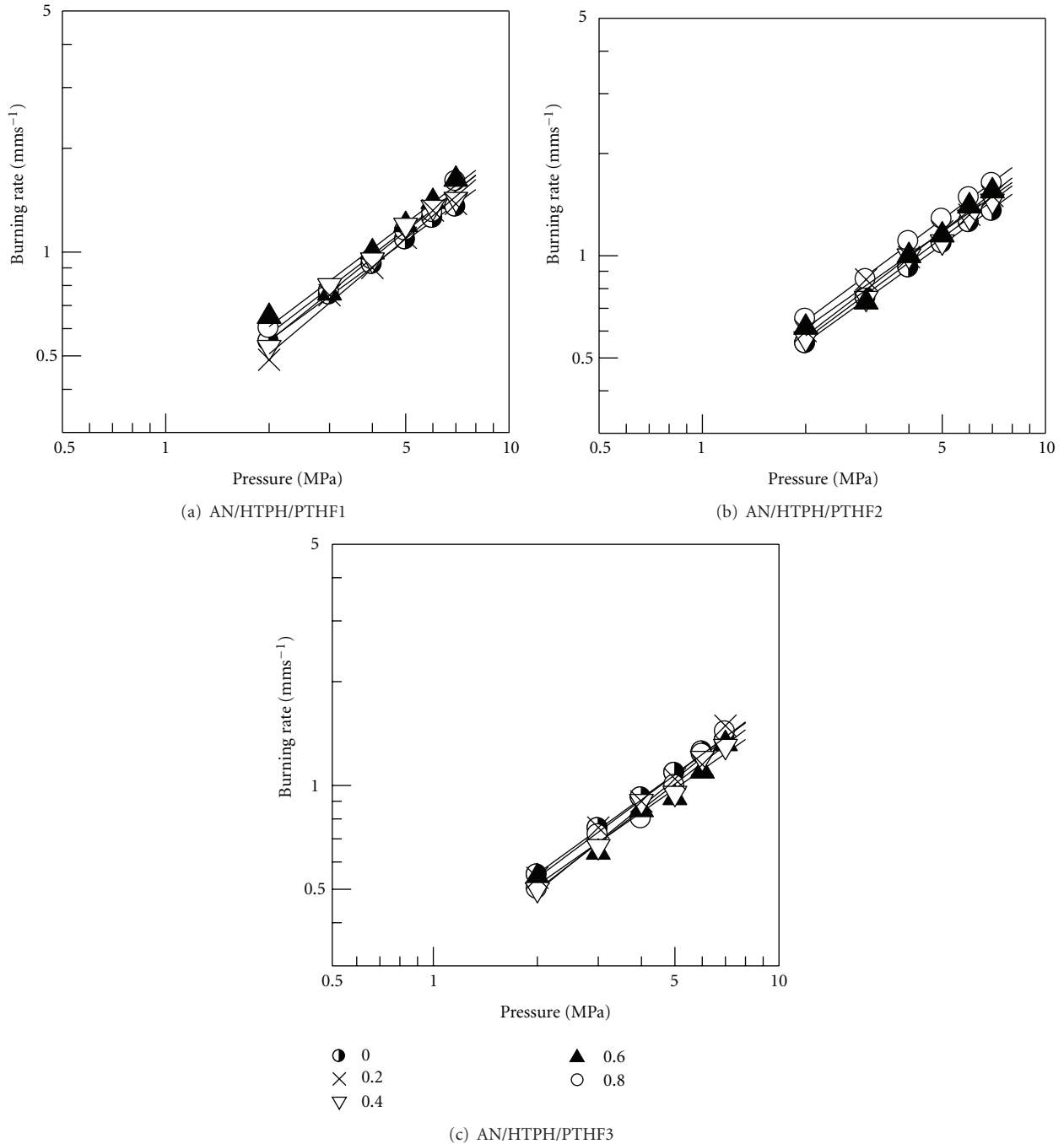


FIGURE 1: Burning rate characteristics of propellants.

gases of AN trapped under the surface. Part of the AN particles was observed at the surface of the projections.

As described in Section 3.1, the value of T_f was increased by adding PTHF. The increase in T_f accelerates the propellant combustion reaction and enhances the temperature gradient just above the burning surface; the burning rate of the AN/HTPB propellant would therefore be expected to increase by the addition of PTHF. It was hypothesized that the burning rates of the AN/HTPB/PTHF propellant

were not noticeably different from those of the AN/HTPB propellant for physical rather than chemical reasons.

The combustion process of the AN/HTPB propellant is as follows [23]. At the burning surface, AN melts and decomposes, while the HTPB binder barely liquefies and retains its shape until just before decomposition. A condensed phase is formed by the melted AN and the solid HTPB binder just below the burning surface. The decomposition gases of the AN and HTPB binder are diffused in the gas phase

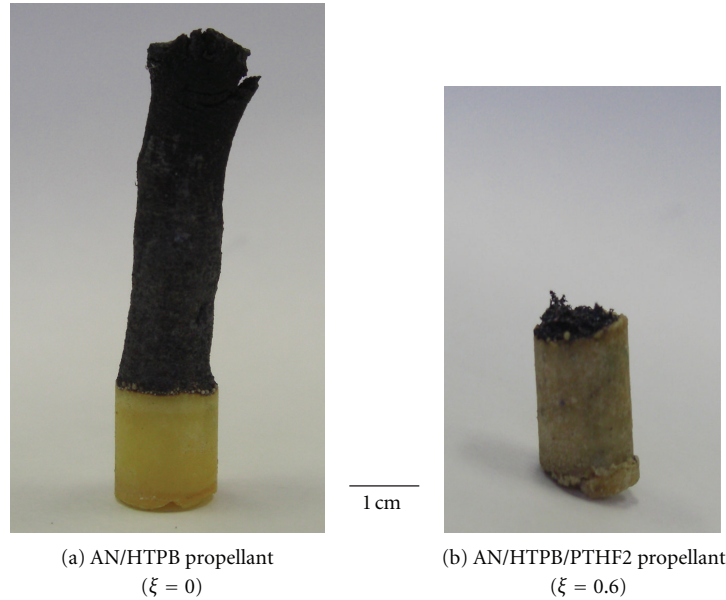


FIGURE 2: Photograph of propellant quenched at 7 MPa.

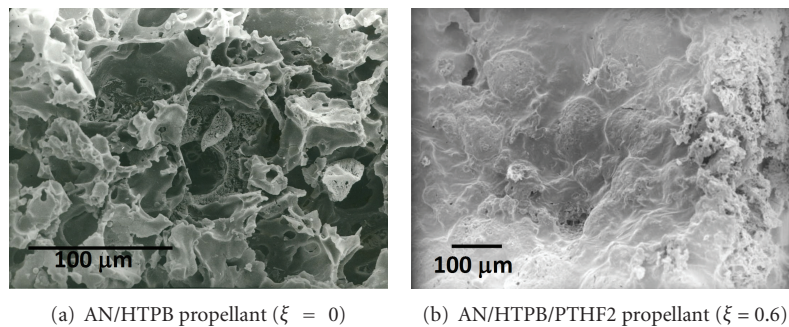


FIGURE 3: SEM photographs of burning surface of propellant quenched at 7 MPa.

and burned. A large quantity of heat is produced by the combustion of the decomposition gases, and this heat is fed back to the burning surface of the propellant, thus increasing the surface temperature even more. Combustion of the AN/HTPB propellant is maintained by this sequence of processes. During this sequence of events, AN is continually exposed on the burning surface.

For the AN/PTHF/glycerin propellant, the liquefied binder covering the burning surface interferes with the evolution of the AN decomposition gases and the heat flux feedback from the flame to AN, and therefore, the AN/PTHF/glycerin propellant does not ignite [23]. It was found that an AN-based propellant does not burn when the burning surface is covered with a liquefied binder, which prevents AN from being exposed.

In a previous study [27], at $\xi = 0.6$ and 0.8 , a small quantity of HTPB/PTHF-blended binders liquefied at approximately 474 K, and that of AN/HTPB/PTHF propellants liquefied at approximately 500 K. As described above,

most of the materials at the burning surface are binder ingredients. This suggests that the burning rates of the AN/HTPB/PTHF propellant are not higher than those of the AN/HTPB propellant because some portion of the liquefied HTPB/PTHF binder covered the burning surface.

3.3. Burning Rate of Propellant Supplemented with ADC.

The effect of a PTHF/glycerin binder on improving the burning characteristics of an AN/PTHF/glycerin propellant was clarified by adding ADC, which suppressed the negative influence of the liquefied binder covering the burning surface [23]. The AN/HTPB/PTHF propellants were supplemented with ADC, and the burning rates of these propellants were measured.

Figure 4 shows the burning rate characteristics of AN/HTPB and AN/HTPB/PTHF propellants with ADC. These propellants were successfully burned above 0.5 MPa by the addition of ADC and the burning rates increased linearly on the logarithmic scale. The pressure exponent of these

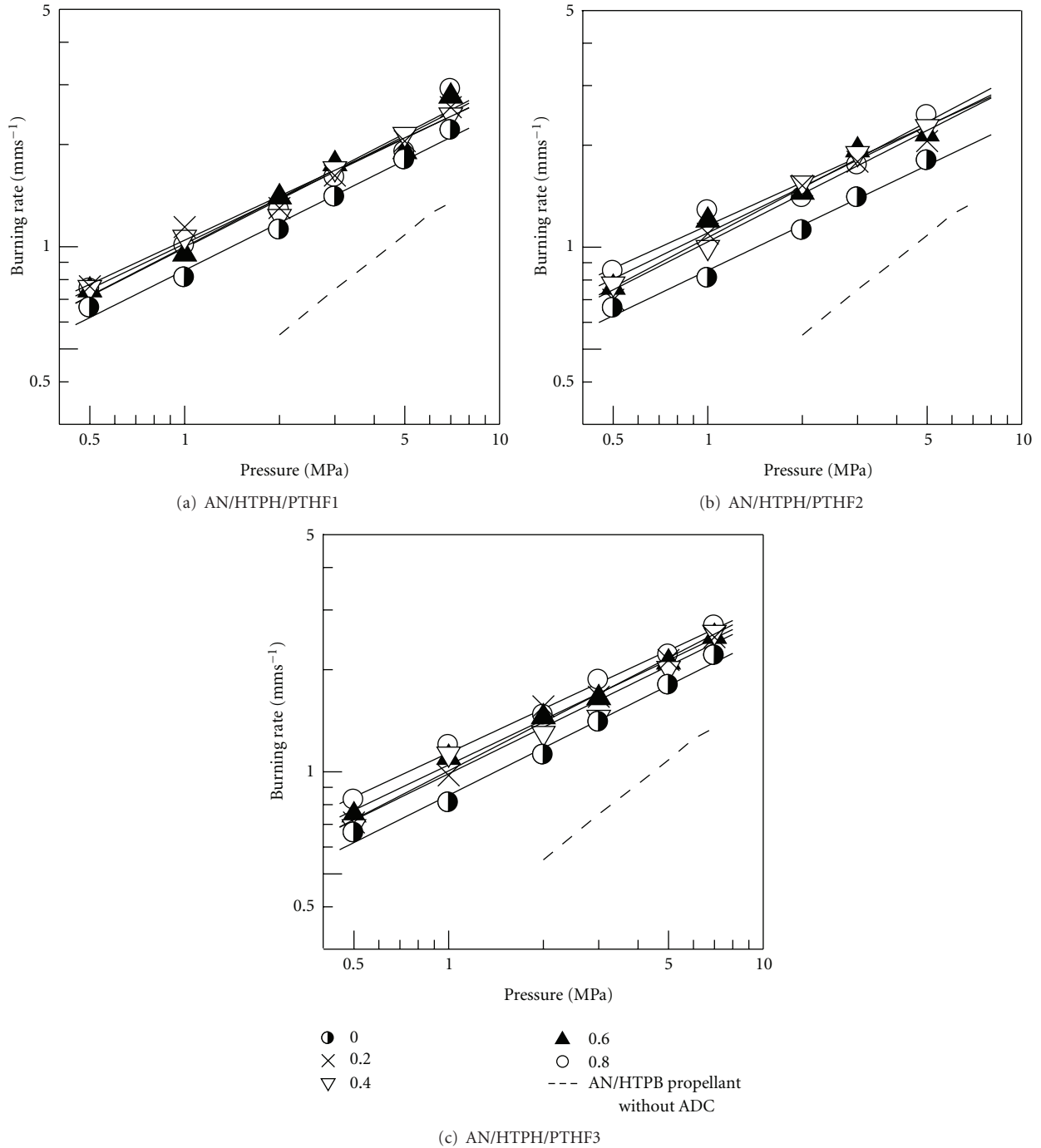


FIGURE 4: Burning rate characteristics of propellants with ADC.

propellants was approximately 0.6 and the type of binder did not influence the values. As described above, the pressure exponent of the propellants without ADC was in the range of 0.7-0.8. The pressure exponent of the propellant with ADC was lower than that of the propellant without it.

The burning rates of an AN/HTPB propellant without ADC, as shown in Figure 1, are also illustrated in

Figure 4 with broken lines for comparison. The burning rates of propellants with ADC were higher than those of propellants without ADC. Furthermore, the burning rates of AN/HTPB/PTHF propellants with ADC were approximately 1.3 times those of AN/HTPB propellants with ADC. The effect of the HTPB/PTHF blend on the improvement of the burning characteristics is clarified by adding ADC because

it suppressed the negative influence of the liquefied binder covering the burning surface. However, the burning rate of the AN-based propellant with the HTPB/PTHF blend as a binder was clearly not dependent on ξ and the molecular weight of PTHF.

4. Conclusions

The burning characteristics of an AN-based propellant with a HTPB/PTHF blend binder were investigated. The use of a HTPB/PTHF blend is theoretically effective in enhancing the specific impulse and adiabatic flame temperature of an AN-based propellant. The AN/HTPB propellant left a solid residue on the burning surface, and the shape of the residue was almost the same as that of the propellant. On the other hand, an AN/HTPB/PTHF propellant did not leave a solid residue, and the burning rates of the AN/HTPB/PTHF propellant were almost the same as those of the AN/HTPB propellant. This was because some of the liquefied HTPB/PTHF binder covered the burning surface of the AN/HTPB/PTHF propellant. The burning rates of AN/HTPB/PTHF propellants with ADC were higher than those of AN/HTPB propellants with ADC. The addition of ADC to the AN/HTPB/PTHF propellant was required to clarify the effect of the blend binder on the improvement of the burning characteristics. The effect of the HTPB/PTHF blend on the increase of the burning rate was independent of the mass ratio of PTHF in the blend.

Nomenclature

I_{sp} : Specific impulse, s
 T_f : Adiabatic flame temperature, K
 ξ : Mass ratio of PTHF in binder, —.

Abbreviations

AN: Ammonium nitrate
 AP: Ammonium perchlorate
 DTA: Differential thermal analysis
 HTPB: Hydroxyl-terminated polybutadiene
 IPDI: Isophorone diisocyanate
 PTHF: Polytetrahydrofuran
 TG: Thermogravimetry.

References

- [1] G. P. Sutton, *Rocket Propulsion Element*, John Wiley & Sons, New York, NY, USA, 1992.
- [2] C. Oommen and S. R. Jain, "Ammonium nitrate: a promising rocket propellant oxidizer," *Journal of Hazardous Materials*, vol. 67, no. 3, pp. 253–281, 1999.
- [3] Y. Hagihara, T. Ichikawa, H. Shinpo, and M. Suzuki, "Effects of chromium and cobalt compounds on burning rate of ammonium nitrate/hydroxyl-terminated polybutadiene composite propellants," *Science and Technology of Energetic Materials*, vol. 52, no. 6, pp. 390–395, 1991.
- [4] H. Nakamura, M. Akiyoshi, K. Sakata, and Y. Hara, "Effect of metal complex catalysis of tetraaza-(14)-anurene on the thermal decomposition of ammonium nitrate and ammonium perchlorate," *Science and Technology of Energetic Materials*, vol. 61, no. 3, pp. 101–107, 2000.
- [5] G. Singh and S. P. Felix, "Studies on energetic compounds: Part 36: Evaluation of transition metal salts of NTO as burning rate modifiers for HTPB-AN composite solid propellants," *Combustion and Flame*, vol. 135, no. 1-2, pp. 145–150, 2003.
- [6] M. Quinn Brewster, T. A. Sheridan, and A. Ishihara, "Ammonium nitrate-magnesium propellant combustion and heat transfer mechanisms," *Journal of Propulsion and Power*, vol. 8, no. 4, pp. 760–769, 1992.
- [7] V. P. Sinditskii, V. Y. Egorshv, A. I. Levshenkov, and V. V. Serushkin, "Ammonium nitrate: combustion mechanism and the role of additives," *Propellants, Explosives, Pyrotechnics*, vol. 30, no. 4, pp. 269–280, 2005.
- [8] F. Nihal Tüzün and B. Zühtü Uysal, "The effect of ammonium nitrate, coarse/fine ammonium nitrate ratio, plasticizer, bonding agent, and Fe_2O_3 content on ballistic and mechanical properties of hydroxyl terminated polybutadiene based composite propellants containing 20% AP," *Journal of ASTM International*, vol. 2, no. 6, pp. 233–245, 2005.
- [9] M. Kohga and S. Nishino, "Burning characteristics of ammonium nitrate-based composite propellants supplemented with ammonium dichromate," *Propellants, Explosives, Pyrotechnics*, vol. 34, no. 4, pp. 340–346, 2009.
- [10] T. Kuwahara and N. Shinozaki, "Burning mechanism of ammonium nitrate/aluminum composite propellants," *Science and Technology of Energetic Materials*, vol. 53, no. 3, pp. 131–136, 1992.
- [11] B. N. Kondrikov, V. E. Annikov, V. Y. Egorshv, L. DeLuca, and C. Bronzi, "Combustion of ammonium nitrate-based compositions, metal-containing and water-impregnated compounds," *Journal of Propulsion and Power*, vol. 15, no. 6, pp. 763–771, 1999.
- [12] H. Murata, Y. Azuma, T. Tohara et al., "The effect of magnalium(Mg-Al alloy) on combustion characteristics of ammonium nitrate-based solid propellant," *Science and Technology of Energetic Materials*, vol. 61, no. 2, pp. 58–66, 2000.
- [13] B. E. Greiner, R. A. Frederick, and M. D. Moser, "Combustion effects of C60 soot in ammonium nitrate propellants," *Journal of Propulsion and Power*, vol. 19, no. 4, pp. 713–715, 2003.
- [14] T. Kazita, T. Saito, T. Yamaya, M. Shimoda, and A. Iwama, "Ignition characteristics of GAP/AN/AP-based solid propellants for low pollution at sub-atmospheric pressures," *Science and Technology of Energetic Materials*, vol. 57, no. 1, pp. 1–8, 1996.
- [15] K. Kato and G. Nakasita, "Burning rate characteristics of GAP/AN propellant," *Science and Technology of Energetic Materials*, vol. 56, no. 3, pp. 130–134, 1995.
- [16] Y. Oyumi and E. Kimura, "IM characteristics of GAP/AN composite propellants," *Science and Technology of Energetic Materials*, vol. 57, no. 1, pp. 9–13, 1996.
- [17] M. Takizuka, "Combustion characteristics of GAP based composite propellants (I)—theoretical combustion performance and burning rate," *Science and Technology of Energetic Materials*, vol. 59, no. 4, pp. 181–191, 1998.
- [18] C. Nakajima, T. Saito, T. Yamaya, and M. Shimoda, "The effects of chromium compounds on PVA-coated AN and GAP binder pyrolysis, and PVA-coated AN/GAP propellant combustion," *Fuel*, vol. 77, no. 4, pp. 321–326, 1998.
- [19] P. Simões, L. Pedroso, A. Portugal, I. Plaksin, and J. Campos, "New propellant component, part II. Study of a PSAN/DNAM/HTPB based formulation," *Propellants, Explosives, Pyrotechnics*, vol. 26, no. 6, pp. 278–283, 2001.

- [20] M. D. Judge and P. Lessard, "An advanced GAP/AN/TAGN propellant. Part I: ballistic properties," *Propellants, Explosives, Pyrotechnics*, vol. 32, no. 2, pp. 175–181, 2007.
- [21] J. R. Goleniewski and J. A. Roberts, U.S. Patent 5783769-Solid Propellant with Non-crystalline Polyether/Energetic Plasticizer Binder, issued on July 21, 1998.
- [22] M. Kohga, W. Miyano, and T. Kojima, "Burning characteristics of polytetrahydrofuran-based composite propellant," *Journal of Propulsion and Power*, vol. 22, no. 6, pp. 1418–1421, 2006.
- [23] M. Kohga and K. Okamoto, "Thermal decomposition behaviors and burning characteristics of ammonium nitrate/polytetrahydrofuran/glycerin composite propellant," *Combustion and Flame*, vol. 158, no. 3, pp. 578–582, 2011.
- [24] M. Kohga, "Application of polytetrahydrofuran as a plasticizer of HTPB binder," *Science and Technology of Energetic Materials*, vol. 71, no. 3, pp. 77–82, 2010.
- [25] M. Kohga, "Mechanical properties and burning characteristics of AP / HTPB composite propellant using polytetrahydrofuran as a plasticizer," *Science and Technology of Energetic Materials*, vol. 71, no. 5-6, pp. 145–150, 2010.
- [26] K. Okamoto, M. Kohga, and K. Hasue, "Thermal behavior and tensile property of PTHF/HTPB blend," *Science and Technology of Energetic Materials*, vol. 70, no. 4, pp. 87–93, 2009.
- [27] M. Kohga and K. Okamoto, "Thermal decomposition behavior of AN-based composite propellant with hydroxyl-terminated polybutadiene/polytetrahydrofuran blend as a binder," *Science and Technology of Energetic Materials*, vol. 72, no. 6, pp. 161–168, 2011.
- [28] NASA Glenn's computer code Chemical Equilibrium with Applications, <http://www.grc.nasa.gov/WWW/CEAWeb/>.

Research Article

Multisized Inert Particle Loading for Solid Rocket Axial Combustion Instability Suppression

David R. Greatrix

Department of Aerospace Engineering, Ryerson University, 350 Victoria Street, Toronto, ON, Canada M5B 2K3

Correspondence should be addressed to David R. Greatrix, greatrix@ryerson.ca

Received 27 September 2011; Accepted 8 December 2011

Academic Editor: Valsalayam Sanal Kumar

Copyright © 2012 David R. Greatrix. This is an open access article distributed under the Creative Commons Attribution License, which permits unrestricted use, distribution, and reproduction in any medium, provided the original work is properly cited.

In the present investigation, various factors and trends, related to the usage of two or more sets of inert particles comprised of the same material (nominally aluminum) but at different diameters for the suppression of axial shock wave development, are numerically predicted for a composite-propellant cylindrical-grain solid rocket motor. The limit pressure wave magnitudes at a later reference time in a given pulsed firing simulation run are collected for a series of runs at different particle sizes and loading distributions and mapped onto corresponding attenuation trend charts. The inert particles' presence in the central core flow is demonstrated to be an effective means of instability symptom suppression, in correlating with past experimental successes in the usage of particles. However, the predicted results of this study suggest that one needs to be careful when selecting more than one size of particle for a given motor application.

1. Introduction

Over the last number of decades, a multitude of research efforts have been directed towards understanding the physical mechanisms, or at least the surrounding factors, behind the appearance of symptoms typically associated with nonlinear axial combustion instability in solid-propellant rocket motors (SRMs). The principal symptoms are the presence within the motor chamber of stronger finite-amplitude traveling axial pressure waves that may be shock fronted, commonly (although not always) accompanied by some degree of base chamber pressure rise (dc shift). Note that low-magnitude pressure waves due to vortex shedding from segmented/gapped components in the motor chamber are not included (here) in this more traditional category of nonlinear axial instability. Studies of nonlinear axial combustion instability have ranged from numerous experimental test firing series on the one hand [1–3], and linear/nonlinear acoustic theory modeling on the other (largely, the analysis producing frequency-based standing wave solutions for a given chamber geometry, but without some useful quantitative information) [4–7]. On occasion, researchers have employed a numerical modeling approach, to work towards a more comprehensive quantitative understanding of the physics involved (the nu-

merical model producing a traveling wave solution to a limit wave amplitude and corresponding small or larger dc shift, typically a time-based result evolving from an initial pulse disturbance introduced into the chamber flow) [8, 9]. Available computational power and associated result turnaround times commonly forced some simplifications in the given numerical model.

The motivation for the experimental, analytical, and numerical studies noted above was and is of course to bring this better understanding to bear in more precisely suppressing, if not eliminating, these axial instability symptoms. For example, it has been long known that inert (nonreactive) or reactive particles in the internal core flow can help to suppress axial combustion instability symptoms [10–12]. As pointed out by Blomshield [13], in his wide-ranging review of a number of cases of different motors experiencing combustion instability over the years, it is not always clear as to the quantity of particle loading (and corresponding particle size) that is needed to adequately suppress the given symptoms, if that is the suppression technique being exploited. An additional potential complication, pointed out by Waesche [14], is that it is not always clear that the effectiveness of particle or additive loading is due entirely to particle/drag effects within the central core flow, or in fact in part or in whole due

to altered combustion response of the propellant, as a result of the presence of the particle/additive at the burning surface before entering the core flow region. Waesche suggests that this effect may be more readily observed for reactive particles, rather than inert ones, considering the heat transfer effects in the solid phase [14]. Given this background from past experimental observations, it would be advantageous to have a predictive numerical simulation model that would help establish the particle loading/sizing requirement for a given SRM, in this case for using inert particles of differing sizes.

An effective numerical model combines the effects of the unsteady one- or two-phase flow, the transient combustion process, and the structural dynamics of the surrounding propellant/casing structure. A case study reported by Blomshield [13], where the changing of a heavyweight static-test motor casing to a lightweight casing structure led to the appearance of combustion instability symptoms, provides one motivation for inclusion of structural effects in the numerical model. Experimental observations by Dotson and Sako [15] on in-flight fluid-structure interaction effects lend further weight in this regard.

In the present investigation, an updated numerical model incorporating the above attributes is used in the prediction of the unsteady instability-related behavior in a cylindrical-grain motor and allows for an evaluation of the corresponding effectiveness of using two or more sets of inert spherical particles (same material (nominally aluminum), differing diameters) in suppressing instability symptoms. While aluminum as a common solid propellant fuel addition is reactive (noninert) in practice (and its burning and other behavior at and away from the propellant surface in the central flow may have a significant influence on the given SRM's combustion stability), the properties of aluminum are assumed for the inert particles in this study so as to allow for comparison to the results of future studies where the aluminum particles are modelled as reactive. In practice, one can note that inert particles composed of such materials as aluminum oxide (which forms from the combustion of aluminum and oxygen) or zirconium carbide do see usage for combustion stabilization purposes. The present study is a followon to the study reported in [16] (where the use of a single set of inert spherical particles is examined). In practice, one might see the use of two or more particle sizes in a given motor. This is sometimes done to target two or more different pressure wave frequencies that have been identified as problematic (e.g., one longitudinal and two transverse if using three particle sets). The Dobbins-Temkin correlation [17] indicates that the best particle diameter d_{opt} for suppression is a function of the inverse square root of the target frequency; that is, likely a smaller diameter particle is more effective at a higher transverse frequency, versus a lower axial frequency, everything else being equal

$$d_{\text{opt}} = \sqrt{\frac{9\mu}{\pi f \rho_m}}. \quad (1)$$

In the present paper, the focus for presented results will largely be on those cases where the transient burning response of the propellant is the primary mechanism for

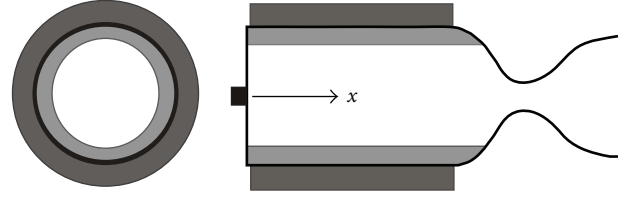


FIGURE 1: Schematic diagram of sleeved cylindrical-grain SRM, showing reference x -direction.

sustaining appreciable traveling pressure waves in the combustion chamber. A few additional results will illustrate the effect of normal acceleration (through radial vibration) as a complementary mechanism acting on the transient combustion process.

2. Numerical Model

A simplified schematic diagram of the physical system of an SRM, that is placed on a static test stand, is provided in Figure 1. In this case, the cylindrical-grain motor is free to vibrate radially without any external constraint (i.e., only constrained as indicated by the thick steel static-test sleeve surrounding the aluminum lightweight motor casing), while axial motion is constrained to a large degree by a thrust-measuring load cell at the lefthand boundary. Under normal (nominal) quasiequilibrium operating conditions, the internal gas flow (or gas-particle flow, if two-phase) moves smoothly from the burning propellant surface into the central core flow, heading downstream to eventually pass through and beyond the exhaust nozzle.

2.1. Equations Relevant to Two-Phase Flow in SRM. One defines b as the nonequilibrium sound speed of a 2-phase mixture, which for a single set of monodisperse particles within the gas can be estimated via [18]

$$b = a \left[\frac{1 + \beta_g (C_m/C_p) (T_p/T)}{\mathfrak{C} + \alpha_g \beta_g (\gamma - 1) (u_p/u) (1 - (u_p/u))} \right]^{1/2}, \quad (2)$$

where \mathfrak{C} denotes $\alpha_g^2 (1 + \beta_g (u_p/u)) (1 + \gamma \beta_g (C_m/C_p) (T_p/T))$. The gas phase void fraction α_g is defined by

$$\alpha_g = \frac{\mathcal{V} - \mathcal{V}_p}{\mathcal{V}} = 1 - \frac{\mathcal{V}_p}{\mathcal{V}}. \quad (3)$$

For a lower particle loading, one can assume that α_g is close to unity in value (\mathcal{V}_p is the volume occupied by the particles in an elemental total volume of \mathcal{V}). The particle-gas mass flux ratio β_g is stipulated as

$$\beta_g = \frac{\rho_p u_p}{\rho \alpha_g}. \quad (4)$$

One can define an average two-phase density in a given volume as

$$\rho_{2\text{ph}} = \frac{m}{\mathcal{V}} \approx \frac{N \cdot m_p + \rho \mathcal{V}}{\mathcal{V}} = \frac{\rho_p \mathcal{V} + \rho \mathcal{V}}{\mathcal{V}} = \alpha_p \rho_{2\text{ph}} + \rho, \quad (5)$$

where α_p is the particle-loading fraction in the flow, and N is the number of particles of average mass m_p in the elemental volume above, then one can show the correlation between particle density ρ_p and gas density ρ

$$\rho_p = \frac{N \cdot m_p}{\mathcal{V}} = \alpha_p \rho_{2ph} = \frac{\alpha_p}{1 - \alpha_p} \cdot \rho. \quad (6)$$

When one has two or more sets of particles of differing sizes (comprised of the same material; thus, the same solid specific heat C_m), one can use the following correlations:

$$\begin{aligned} \rho_p &= \frac{\sum_{i=1}^{N_{set}} N_i m_{p,i}}{\mathcal{V}} = \sum_{i=1}^{N_{set}} \rho_{p,i}, \\ \alpha_p &= \sum_{i=1}^{N_{set}} \alpha_{p,i}, \\ \beta_g &= \frac{\dot{m}_p}{\dot{m}_g} = \frac{\sum_{i=1}^{N_{set}} \rho_{p,i} u_{p,i}}{\rho u \alpha_g}, \\ \beta_g \frac{C_m T_p}{C_p T} &= \frac{C_m}{C_p T} \cdot \frac{\sum_{i=1}^{N_{set}} \rho_{p,i} u_{p,i} T_{p,i}}{\rho u \alpha_g} = \Sigma_1, \\ \beta_g \frac{u_p}{u} &= \frac{\sum_{i=1}^{N_{set}} \rho_{p,i} u_{p,i}^2}{\rho u^2 \alpha_g} = \Sigma_2, \\ \beta_g \frac{u_p^2}{u^2} &= \frac{\sum_{i=1}^{N_{set}} \rho_{p,i} u_{p,i}^3}{\rho u^3 \alpha_g} = \Sigma_3, \end{aligned} \quad (7)$$

so that the nonequilibrium sound speed can be estimated via

$$b = a \left[\frac{1 + \Sigma_1}{\alpha_g^2 (1 + \Sigma_2) (1 + \gamma \Sigma_1) + \alpha_g (\gamma - 1) (\Sigma_2 - \Sigma_3)} \right]^{1/2}. \quad (8)$$

Under nominal flow conditions, u/b would be unity at the nozzle throat.

The effect of particle mass loading ΔM_p into a solid propellant, that originally was of solid density $\rho_{s,o}$, on the loading mass fraction into a solid volume \mathcal{V} is given by

$$\begin{aligned} \alpha_{p,s} &= \frac{\Delta M_p}{\Delta M_{s,o} + \Delta M_p} \\ &= \frac{\rho_m \mathcal{V}_m}{\rho_{s,o} (\mathcal{V} - \mathcal{V}_m) + \rho_m \mathcal{V}_m} \\ &= \frac{1}{(\rho_{s,o}/\rho_m) (\mathcal{V}/\mathcal{V}_m - 1) + 1}. \end{aligned} \quad (9)$$

The new effective solid propellant overall density becomes

$$\begin{aligned} \rho_{s,new} &= \frac{\Delta M_p + \Delta M_{s,o}}{\mathcal{V}} \\ &= \frac{\rho_{s,o} (\mathcal{V} - \mathcal{V}_m) + \rho_m \mathcal{V}_m}{\mathcal{V}} \\ &= \rho_{s,o} \left(1 - \frac{\mathcal{V}_m}{\mathcal{V}} \right) + \rho_m \frac{\mathcal{V}_m}{\mathcal{V}}. \end{aligned} \quad (10)$$

By substitution, one can show that

$$\rho_{s,new} = \frac{\rho_{s,o}}{1 - \alpha_{p,s} + \alpha_{p,s} (\rho_{s,o}/\rho_m)}. \quad (11)$$

2.2. Equations of Motion-Governing Two-Phase Flow. The equations of motion describing the nonsteady core flow within the SRM must be solved in conjunction with the local pyrolysis rate r_b of the solid propellant, and the surrounding structure's instantaneous geometric deformation. As pertains to the present study of a small motor having a larger length-to-diameter ratio, the quasi-one-dimensional hydrodynamic conservation equations for the axial gas flow are given below

$$\begin{aligned} \frac{\partial \rho}{\partial t} + \frac{\partial(\rho u)}{\partial x} &= -\frac{1}{A} \frac{\partial A}{\partial x} \rho u + (1 - \alpha_p) \rho_s \frac{4r_b}{d} - \left(\frac{4r_b}{d} + \kappa \right) \rho, \\ \frac{\partial(\rho u)}{\partial t} + \frac{\partial}{\partial x} (\rho u^2 + p) &= -\frac{1}{A} \frac{\partial A}{\partial x} \rho u^2 - \left(\frac{4r_b}{d} + \kappa \right) \rho u - \rho a_e - \sum_{i=1}^{N_{set}} \frac{\rho_{pi}}{m_{pi}} D_i, \\ \frac{\partial(\rho E)}{\partial t} + \frac{\partial}{\partial x} (\rho u E + u p) &= -\frac{1}{A} \frac{\partial A}{\partial x} (\rho u E + u p) - \left(\frac{4r_b}{d} + \kappa \right) \rho E \\ &\quad + (1 - \alpha_p) \rho_s \frac{4r_b}{d} \left(C_p T_f + \frac{v_f^2}{2} \right) - \rho u a_e \\ &\quad - \sum_{i=1}^{N_{set}} \frac{\rho_{pi}}{m_{pi}} (u_{pi} D_i + Q_i). \end{aligned} \quad (12)$$

Here, the total specific energy of the gas is defined for an ideal gas as $E = p/[(\gamma - 1)\rho] + u^2/2$. The corresponding equations of motion for an i th inert (nonburning) particle set within the axial flow may be found from

$$\begin{aligned} \frac{\partial \rho_{pi}}{\partial t} + \frac{\partial(\rho_{pi} u_{pi})}{\partial x} &= -\frac{1}{A} \frac{\partial A}{\partial x} \rho_{pi} u_{pi} + \alpha_{pi} \rho_s \frac{4r_b}{d} - \left(\frac{4r_b}{d} + \kappa \right) \rho_{pi}, \\ \frac{\partial(\rho_{pi} u_{pi})}{\partial t} + \frac{\partial(\rho_{pi} u_{pi}^2)}{\partial x} &= -\frac{1}{A} \frac{\partial A}{\partial x} \rho_{pi} u_{pi}^2 - \left(\frac{4r_b}{d} + \kappa \right) \rho_{pi} u_{pi} - \rho_{pi} a_e + \frac{\rho_{pi}}{m_{pi}} D_i, \\ \frac{\partial(\rho_{pi} E_{pi})}{\partial t} + \frac{\partial(\rho_{pi} u_{pi} E_{pi})}{\partial x} &= -\frac{1}{A} \frac{\partial A}{\partial x} (\rho_{pi} u_{pi} E_{pi}) - \left(\frac{4r_b}{d} + \kappa \right) \rho_{pi} E_{pi} \\ &\quad + \alpha_{pi} \rho_s \frac{4r_b}{d} \left(C_p T_f + \frac{v_f^2}{2} \right) - \rho_{pi} u_{pi} a_e \\ &\quad + \frac{\rho_{pi}}{m_{pi}} \times (u_{pi} D_i + Q_i). \end{aligned} \quad (13)$$

Here, the total specific energy of a local grouping of particles from an i th set is given by $E_{pi} = C_m T_{pi} + u_{pi}^2/2$, where T_{pi} is the mean temperature of that group. As outlined in [19], the viscous interaction between the gas and a particle from the i th particle set is represented by the drag force D_i , and the heat transfer from the core flow to a particle from the i th set is defined by Q_i . In the case of drag between the gas and a representative spherical particle at a given axial location, one notes that

$$D_i = \frac{\pi d_{mi}^2}{8} C_d \rho (u - u_{pi}) |u - u_{pi}|, \quad (14)$$

where C_d is the drag coefficient for a sphere in a steady flow with low-flow turbulence (determined as function of relative Reynolds number, relative flow Mach number, and temperature difference between the particle and the gas). In the case of heat transfer from the core flow to a representative particle at a given axial location, the following applies:

$$Q_i = \pi d_{mi} k \cdot \text{Nu} \cdot (T - T_{pi}), \quad (15)$$

where the Nusselt number Nu can be found as a function of Prandtl and relative Reynolds number for a sphere of mean diameter d_{mi} . One will need to solve (13) for each of N_{set} particle sets as part of the calculation process, where for dual or triple particle set loading, N_{set} has a value of 2 or 3 in the present study.

Longitudinal acceleration a_l appears in the gas and particle momentum and energy equations as a body force contribution within a fixed Eulerian reference (fixing of $x = 0$ to motor head end, x positive moving right on structure as per Figure 1; acceleration of local surrounding structure rightward is designated positive a_l) and may vary both spatially along the length of the motor and with time. The effects of such factors as turbulence can be included through one or more additional equations that employ the information from the bulk flow properties arising from the solution of the above-one-dimensional equations of motion. The principal differential equations themselves can be solved via a higher-order, explicit, and finite-volume random-choice method (RCM) approach [19, 20]. The RCM solver employs a Riemann-solution technique noted for low artificial dispersion with time of wave activity in tubes, and so forth. The equations of motion of the gas and particles will be solved over a given time step Δt (on the order of 1×10^{-7} s for the present study, given the motor solution node allocation in the axial direction from head end to nozzle exit plane), in sequence with additional equations for structural motion and propellant burning rate as described below.

2.3. Equations for Structural Motion. Structural vibration can play a significant role in nonsteady SRM internal ballistic behavior, as evidenced by observed changes in combustion instability symptoms as allied to changes in the structure surrounding the internal flow (e.g., propellant grain configuration, wall thickness, and material properties) [13, 15, 21]. The level of sophistication required for modeling the motor structure (propellant, casing, static-test sleeve, and nozzle)

and applicable boundary conditions (load cell on static test stand) can vary, depending on the particular application and motor design. Loncaric et al. [22] and Montesano et al. [23] employed a finite-element approach towards the structural modeling of the given motor configuration. In the present study, a cylindrical-grain configuration allows for a simpler finite-difference approach via thick-wall theory, as reported in [20, 24]. The radial deformation dynamics of the propellant/casing/sleeve are modeled by a series of independent ring elements along the length of the motor. Axial motion along the length of the structure is modeled via beam theory, and bounded by the spring/damper load cell at the motor's head end. Viscous damping is applied in the radial and axial directions. Reference structural properties are assumed for an ammonium-perchlorate/hydroxyl-terminated polybutadiene (AP/HTPB) composite propellant surrounded by an aluminum casing and steel sleeve. For greater accuracy, some properties like the propellant/casing/sleeve assembly's natural radial frequency may be predetermined via a finite-element numerical solution, rather than via theoretical approximations [24].

2.4. Equations for Propellant Burning Rate. With respect to transient, frequency-dependent burning rate modeling, the Z-N (Zeldovich-Novozhilov) solid-phase energy conservation approach used in the present simulation program may be represented by the following time-dependent temperature-based relationship [25]:

$$r_b^* = r_{b,qs} - \frac{1}{(T_s - T_i - \Delta H_s/C_s)} \frac{\partial}{\partial t} \int_{-\infty}^0 \Delta T dy, \quad (16)$$

where $r_{b,qs}$ is the quasisteady burning rate (value for burning rate as estimated from steady-state information for a given set of local flow conditions), T_i is the initial propellant temperature, and in this context, $\Delta T = T(y, t) - T_i$ is the temperature distribution in moving from the burning propellant surface at $y = 0$ (and $T = T_s$) to that spatial location in the propellant where the temperature reaches T_i . One may note at this juncture the inclusion of a net surface heat release term, ΔH_s , in the calculations. The transient heat conduction in the solid phase can be solved by an appropriate finite-difference scheme. One needs to take care in setting the solid-phase spatial increment Δy , to be in accordance with the Fourier stability limit, $\Delta y_{Fo} = (2\alpha_s \Delta t)^{1/2}$, which is a function of the chosen time increment Δt [25]. The time increment itself must be coordinated between the flow and structural model solution systems [23].

In (16), r_b^* is the nominal (unconstrained) instantaneous burning rate, and its value at a given propellant grain location is solved at each time increment via numerical integration of the temperature distribution through the heat penetration zone of the solid phase. The actual instantaneous burning rate r_b may be found as a function of r_b^* through the empirical rate-limiting equation [25]

$$\frac{dr_b}{dt} = K_b (r_b^* - r_b). \quad (17)$$

The rate-limiting coefficient K_b effectively damps the unconstrained burning rate r_b^* when for a finite time increment Δt

$$K_b < \frac{1}{\Delta t}. \quad (18)$$

In the present approach, the surface-thermal gradient is free to find its own value at a given instant. One can argue that the use of (17) or some comparable damping function, while empirical, parallels the approach taken by past researchers in using a stipulated surface-thermal gradient; both approaches act to constrain the exchange of energy through the burning surface interface, allow for some variability in better comparing to a given set of experimental data, and prevent so-called burning-rate “runaway” (unstable divergence of r_b with time) [26]. As discussed in [25], the use of K_b at a set value does allow for a converged solution that is independent of the increment size for Δt and Δy , as long as one respects the Fourier stability requirement noted earlier.

The quasisteady burning rate $r_{b,qs}$ may be ascertained as a function of various parameters; in this study, as a function of local static pressure p , core flow velocity u (erosive burning component), and normal/lateral/longitudinal acceleration, such that:

$$r_{b,qs} = r_p + r_u + r_a. \quad (19)$$

The pressure-based burning component may be found through de St. Robert’s law

$$r_p = C p^n. \quad (20)$$

The flow-based erosive burning component (negative and positive) is established through the following expression [27]:

$$r_b = \left. \frac{r_b}{r_o} \right|_{\delta_r} \cdot r_o + r_e, \quad (21)$$

where at lower flow speeds, the negative component resulting from a stretched combustion zone thickness ($\sigma_r > \sigma_o$) may cause an appreciable drop in the base burn rate r_o , while at higher flow speeds, the positive erosive burning component r_e , established from a convective heat feedback premise [27], should dominate:

$$r_e = \frac{h(T_f - T_s)}{\rho_s [C_s(T_s - T_i) - \Delta H_s]}. \quad (22)$$

For the above case, where the base burning rate r_o is a function of the other mechanisms (pressure and acceleration), one finds the velocity-based component of burn rate from (21) via $r_u = r_b - r_o$. At higher flow speeds, r_u becomes equivalent to r_e . The effect of normal acceleration a_n resulting from radial propellant/casing/sleeve vibration may be determined via [28]

$$r_b = \left[\frac{C_p(T_f - T_s)}{C_s(T_s - T_i) - \Delta H_s} \right] \frac{(r_b + G_a/\rho_s)}{\exp[C_p \delta_o (\rho_s r_b + G_a)/k] - 1}, \quad (23)$$

where the compressive effect of normal acceleration and the dissipative effect of steady or oscillatory longitudinal (or lateral, if say for a star grain configuration) acceleration a_l are stipulated through the accelerative mass flux G_a

$$G_a = \left\{ \frac{a_n p}{r_b} \frac{\delta_o}{RT_f} \frac{r_o}{r_b} \right\}_{\phi=0} \cos^2 \phi_d. \quad (24)$$

Note that the longitudinal/lateral-acceleration-based displacement orientation angle ϕ_d is greater than the nominal acceleration vector orientation angle (ϕ ; zero when only normal acceleration a_n relative to the burning propellant surface is present) [28]. One should also note that a_n is negative when acting to compress the combustion zone, and treated as zero when directed away from the zone. For the above case, where the base burning rate r_o is a function of the other flow mechanisms (pressure and core flow), one finds the acceleration-based component of burning rate from (23) via $r_a = r_b - r_o$.

With respect to the burning surface temperature T_s , one has the option of treating it as constant, or allowing for its variation, depending on the phenomenological approach being taken for estimating the burning rate [25]. While in the past a number of estimation models might have used a constant value for T_s , more recently the usage of a variable T_s has become prevalent. However, based on good comparisons in general to experimental data as reported in [25], a constant T_s was employed in the present Z-N-based phenomenological numerical combustion model, for the present investigation.

3. Results and Discussion

The characteristics of the reference motor for this study are listed in Table 1. The motor, based in large measure on a similar experimental motor [20] is a smaller cylindrical-grain design with an aluminum casing and static-test steel sleeve, with a relatively large length-to-diameter ratio. The motor at the time of pulsing has a moderate port-to-throat area ratio, with a considerable propellant web thickness remaining. The predicted frequency response for the AP/HTPB propellant at three different settings for the net surface heat release value may be viewed in Figure 2 (positive value, exothermic heat release). The general response is given in terms of the nondimensional limit magnitude M_ℓ , defined by

$$M_\ell = \frac{r_{b,peak} - r_{b,o}}{r_{b,qs,peak} - r_{b,o}}, \quad (25)$$

where the reference burning rate $r_{b,o}$ in this case is the motor’s approximate mean burn rate at the point of pulsing (1.27 cm/s). The propellant’s resonant frequency f_r is set via the value of K_b (20000 s⁻¹) to be on the order of 1 kHz (a value within the range of what might be expected for this type of composite propellant at that base burning rate). This

TABLE 1: Reference motor characteristics.

Parameter	Value
Propellant grain length, L_p	52 cm
Initial port diameter, d_i	3.6 cm
Nozzle throat diameter, d_t	1.6 cm
Grain/nozzle-conv. length ratio, L_p/L_c	16 : 1
Propellant specific heat, C_s	1500 J/kg-K
Propellant density, ρ_s	1730 kg/m ³
Propellant thermal conductivity, k_s	0.4 W/m-K
Propellant thermal diffusivity, α_s	1.54×10^{-7} m ² /s
Propellant flame temperature, T_f	3000 K
Propellant surface temperature, T_s	1000 K
Propellant initial temperature, T_i	294 K
Gas specific heat, C_p	1920 J/kg-K
Specific gas constant, R	320 J/kg-K
Gas thermal conductivity, k	0.2 W/m-K
Gas absolute viscosity, μ	8.07×10^{-5} kg/m-s
Gas specific heat ratio, γ	1.2
De St. Robert exponent, n	0.35
De St. Robert coefficient, C	0.05 cm/s-(kPa) ⁿ
Particle solid density, ρ_m	2700 kg/m ³
Particle specific heat, J/kg-K	900 J/kg-K
Particle mass fraction, α_p	0%
Propellant elastic modulus, E_A	45 MPa
Propellant Poisson's ratio, ν_A	0.497
Casing inner wall radius, r_m	3.24 cm
Casing wall thickness, h_B	0.127 cm
Casing material density, ρ_B	2700 kg/m ³
Casing elastic modulus, E_B	80 GPa
Casing material Poisson's ratio, ν_B	0.33
Sleeve wall thickness, h_C	0.47 cm
Sleeve material density, ρ_C	7850 kg/m ³
Sleeve elastic modulus, E_C	200 GPa
Sleeve material Poisson's ratio, ν_C	0.30
Casing/prop. rad. damping ratio, ξ_R	0.35
Casing/prop. long. damping ratio, ξ_L	0.10

value for f_r is in fact relatively close to the fundamental longitudinal acoustic frequency f_{1L} of the combustion chamber, in providing examples later in this paper that are close to the worst-case scenario for susceptibility to axial combustion instability symptoms.

An initial pulsed-firing simulation run was completed as a starting reference for this study, in which no particles are present or any other suppression technique being applied. In Figure 3 for head-end pressure p_c as a function of time, one can see that, at some point, the principal compression wave reaches its quasiequilibrium strength from an initial disturbance pressure Δp_d of 2 atm, the sustained compression wave front arriving about every 1 ms, oscillating at the fundamental frequency f_{1L} of 1 kHz. The base pressure is not appreciably elevated over the nominal operating chamber pressure. The effect of normal acceleration on the burning process (related to the radial vibration of the motor

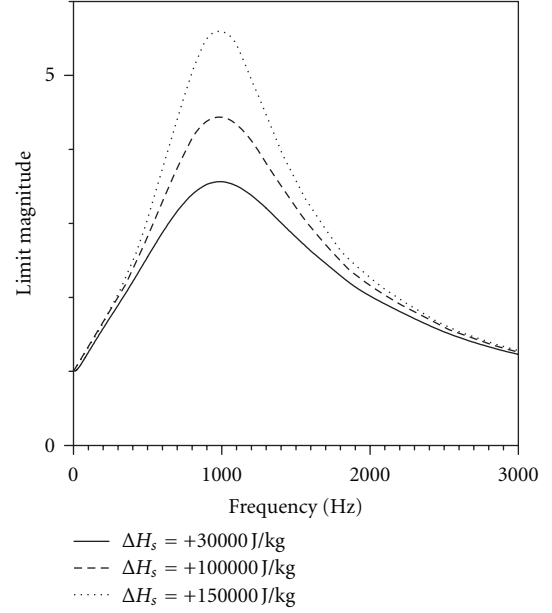


FIGURE 2: Frequency response of reference propellant ($r_{b,o} = 1.27$ cm/s, $K_b = 20000$ s⁻¹, differing ΔH_s) in terms of nondimensional limit magnitude.

propellant/casing; see [16, 20, 23]) has been nullified for this simulation (in order to isolate frequency-dependent Z-N combustion response as the predominant instability symptom driver), a factor in reducing the development of a dc shift. One can note that the limit pressure wave magnitude (Δp_w , peak to trough) is decreasing gradually with time after first reaching its quasiequilibrium level, as the cylindrical grain burns back and the base pressure rises.

One can refer to Figure 4 for the pressure-time profile for the same motor, but now with 5% particle loading (by mass) of inert spherical aluminum particles having a mean 10- μ m diameter. Of course, in practice, the aluminum particles would in fact be reactive (burning, if sufficient reactants like oxygen or chlorine are present in the surrounding gas), and as a result, in general continually decreasing in diameter with particle surface regression as they move aft towards the nozzle. There is also the possibility of particle agglomeration, or the coming together of two or more particles. Given the scope of the present investigation, calculations for particle regression or agglomeration were not to be done; one can consider the mean inert aluminum particle diameter for a given set as a reference size, providing results which may prove useful as a guideline when one does move to inclusion of particle burning in the computational model. Observing the results of Figure 4, suppression of axial wave development after an initial 2-atm pulse is near-complete (limit magnitude of the sustained pressure wave, at 0.26 s, is about 0.045 MPa [Δp_w], as compared to 1.42 MPa for the 0% loading case noted earlier [$\Delta p_{w,peak}$], giving a nondimensional attenuation M_a , defined by

$$M_a = \frac{\Delta p_{w,peak} - \Delta p_w}{\Delta p_{w,peak}}, \quad (26)$$

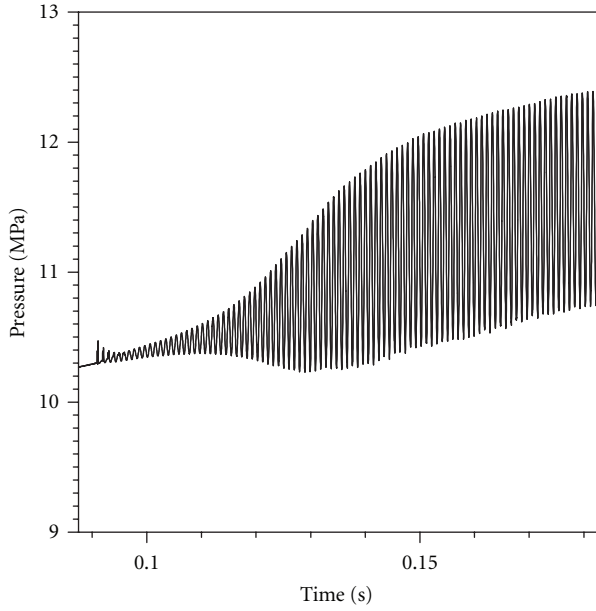


FIGURE 3: Predicted head-end pressure-time profile, reference motor ($K_b = 20000 \text{ s}^{-1}$, $\Delta H_s = 150000 \text{ J/kg}$, $\Delta p_d = 2 \text{ atm}$, $\alpha_p = 0\%$), acceleration nullified, no particles.

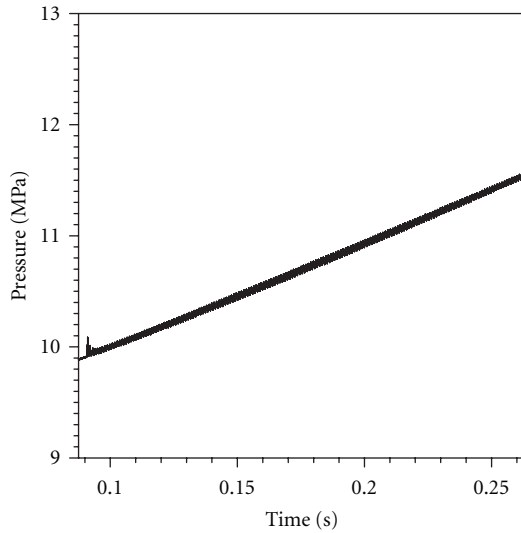


FIGURE 4: Predicted head-end pressure wave profile, reference motor ($K_b = 20000 \text{ s}^{-1}$, $\Delta H_s = 150000 \text{ J/kg}$, $\Delta p_d = 2 \text{ atm}$), acceleration nullified, 5% 10- μm Al particle loading by mass, single particle set.

a value of 0.97, noting that a value of unity is complete suppression). Historically, suppression of high-frequency tangential and radial pressure waves in SRMs by the use of particles in the range of 1 to 3% loading by mass has been in general largely successful. In the case of axial pressure waves, the effectiveness of particles from 1% to over 20% loading in suppressing wave development has been less consistent, relative to the previously mentioned transverse cases. In the case of Figure 4, remembering that acceleration as a factor has been nullified in the combustion process, a loading of

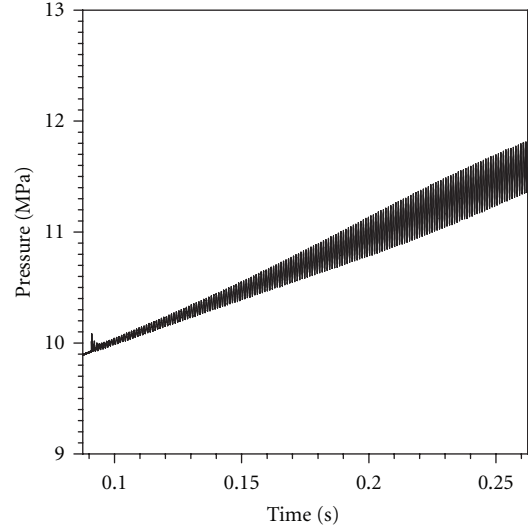


FIGURE 5: Predicted head-end pressure wave profile, reference motor ($K_b = 20000 \text{ s}^{-1}$, $\Delta H_s = 150000 \text{ J/kg}$, $\Delta p_d = 2 \text{ atm}$, $\alpha_p = 5\%$, $d_{m1} = 10 \mu\text{m}$, $d_{m2} = 5 \mu\text{m}$, $\alpha_{p1} = 2.5\%$, $\alpha_{p2} = 2.5\%$), two particle sets, acceleration nullified.

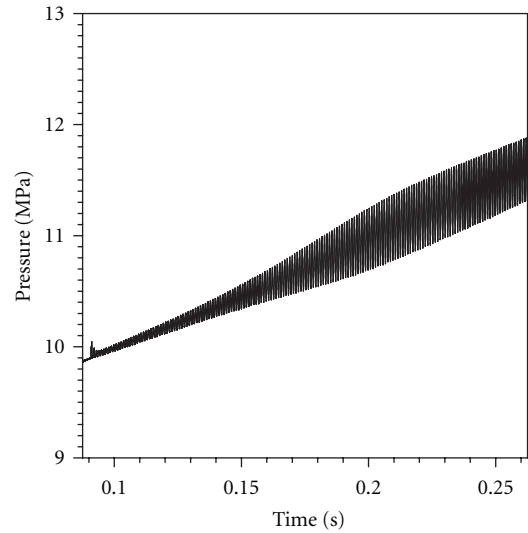


FIGURE 6: Predicted head-end pressure wave profile, reference motor ($K_b = 20000 \text{ s}^{-1}$, $\Delta H_s = 150000 \text{ J/kg}$, $\Delta p_d = 2 \text{ atm}$, $\alpha_p = 5\%$, $d_{m1} = 10 \mu\text{m}$, $d_{m2} = 5 \mu\text{m}$, $d_{m3} = 40 \mu\text{m}$, $\alpha_{p1} = 1.67\%$, $\alpha_{p2} = 1.67\%$, $\alpha_{p3} = 1.66\%$), three particle sets, acceleration nullified.

5% at 10 μm does appear to effectively suppress axial wave development in this particular motor, at this point in its firing.

In considering an example of two particle sets being used (5 and 10 μm diameters for particles of the same material), in Figure 5 one sees the result of an evenly split 1 : 1 distribution of the two sets at an overall loading of 5%. The limit = magnitude of the sustained pressure wave, at 0.26 s, is about 0.47 MPa, as compared to about ten times less for the uniform 10- μm -loading case noted for Figure 4, giving a nondimensional attenuation M_a value of 0.67 as compared to

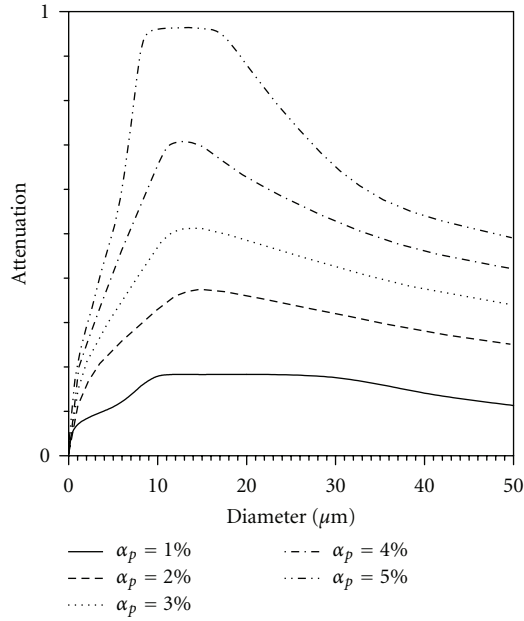


FIGURE 7: Nondimensional attenuation as function of particle diameter and loading of a single particle set, reference motor, acceleration nullified.

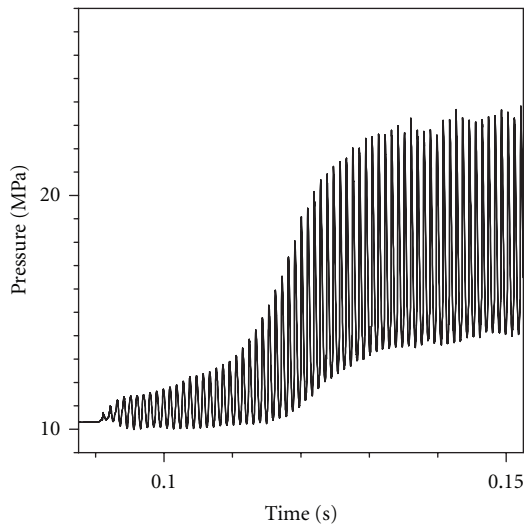


FIGURE 8: Predicted head-end pressure-time profile, reference motor ($K_b = 20000 \text{ s}^{-1}$, $\Delta H_s = 150000 \text{ J/kg}$, $\Delta p_d = 2 \text{ atm}$, $\alpha_p = 0\%$), acceleration active, no particles.

0.97. In considering an example of three particle sets being used (5, 10, and $40 \mu\text{m}$ diameters for particles of the same material), in Figure 6 one can observe the result of an evenly split 1 : 1 : 1 distribution of the three sets at an overall loading of 5%. The limit magnitude of the sustained pressure wave, at 0.26 s, is about 0.57 MPa, giving an M_a value of 0.6, or a bit less than the previous two-particle example (0.67). Referring to Figure 7 [16], one can observe that, in the limit of just using $5 \mu\text{m}$ particles at a 5% overall loading, the value for M_a

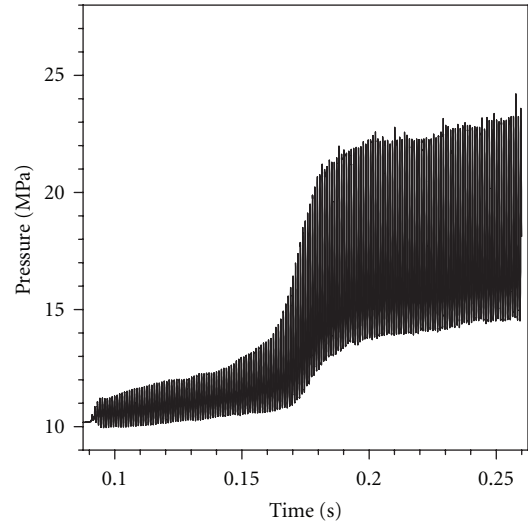


FIGURE 9: Predicted head-end pressure wave profile, reference motor ($K_b = 20000 \text{ s}^{-1}$, $\Delta H_s = 150000 \text{ J/kg}$, $\Delta p_d = 2 \text{ atm}$, $\alpha_p = 1.5\%$, $d_{m1} = 10 \mu\text{m}$, $d_{m2} = 5 \mu\text{m}$, $d_{m3} = 60 \mu\text{m}$, $\alpha_{p1} = 0.5\%$, $\alpha_{p2} = 0.5\%$, $\alpha_{p3} = 0.5\%$), three particle sets, acceleration active.

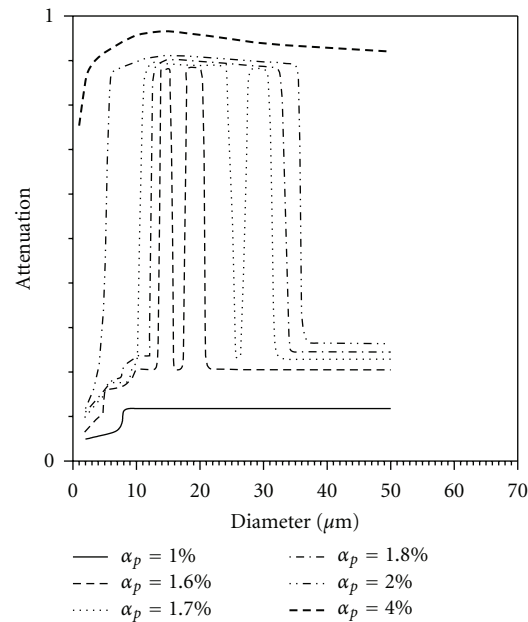


FIGURE 10: Nondimensional attenuation as function of particle diameter and loading of a single particle set, reference motor, acceleration active.

is around 0.52, while, for $40 \mu\text{m}$ particles at a 5% overall loading, the value for M_a is around 0.55.

Let's consider the case when vibration-induced acceleration is active as a mechanism working in conjunction with the transient response of the burning solid propellant. Referring to Figure 8, allowing for the effect of vibration-induced acceleration on combustion, one has a much more active motor in the absence of particles in the flow, with a substantially bigger limit magnitude (around 10.2 MPa at

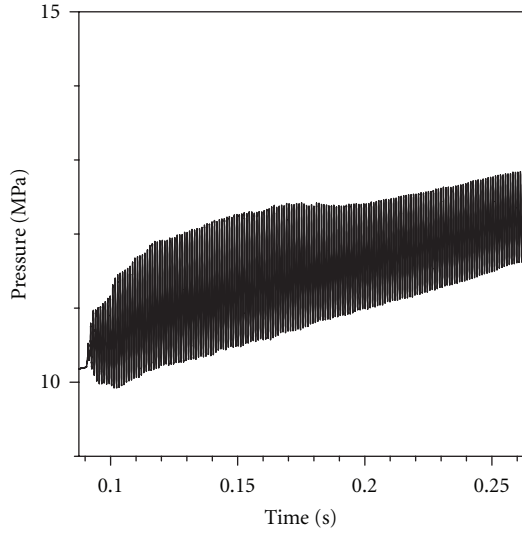


FIGURE 11: Predicted head-end pressure wave profile, reference motor ($K_b = 20000 \text{ s}^{-1}$, $\Delta H_s = 150000 \text{ J/kg}$, $\Delta p_d = 2 \text{ atm}$, $\alpha_p = 1.5\%$, $d_{m1} = 10 \mu\text{m}$, $d_{m2} = 5 \mu\text{m}$, $d_{m3} = 40 \mu\text{m}$, $\alpha_{p1} = 0.5\%$, $\alpha_{p2} = 0.5\%$, $\alpha_{p3} = 0.5\%$), three particle sets, acceleration active.

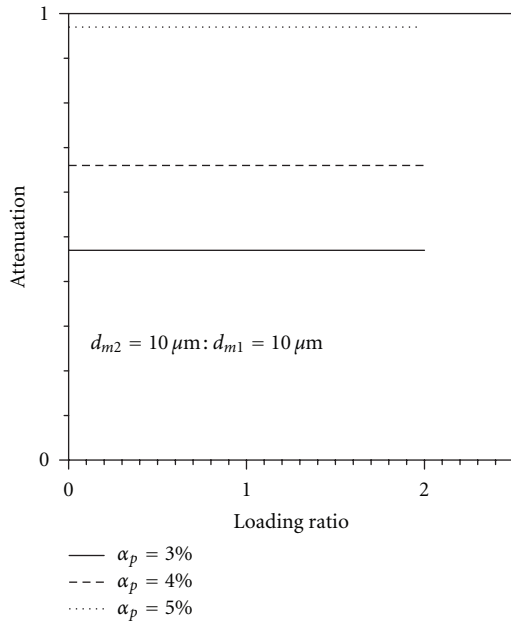


FIGURE 12: Nondimensional attenuation as function of particle diameter and loading distribution [$\alpha_{p2} : \alpha_{p1}$] for two sets of particles ($10 \mu\text{m}$ [d_{m1}] and $10 \mu\text{m}$ [d_{m2}] particles), reference motor, acceleration nullified.

0.26 s) for the now shock-fronted axial pressure wave moving back and forth within the chamber than that seen in Figure 3, and a much more visible dc shift is present. In considering an example of three particle sets being used (5, 10, and $60 \mu\text{m}$ diameters for particles of the same material), in Figure 9 one can observe the result of an evenly split 1 : 1 : 1 distribution of the three sets at an overall loading of 1.5%. The limit magnitude of the sustained pressure wave, at 0.26 s, is about

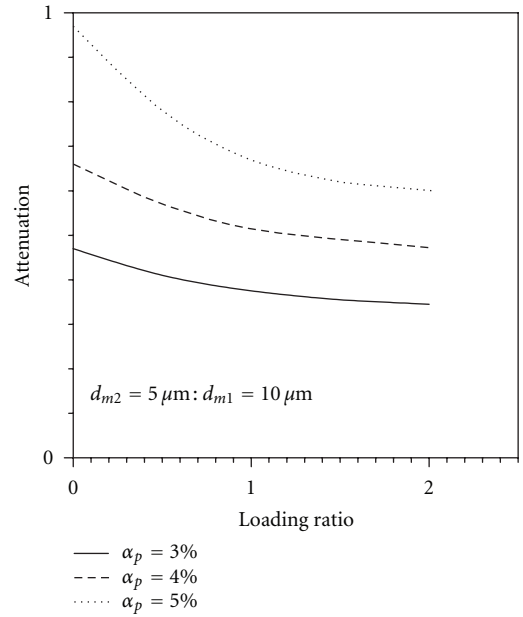


FIGURE 13: Nondimensional attenuation as function of particle diameter and loading distribution [$\alpha_{p2} : \alpha_{p1}$] for two sets of particles ($10 \mu\text{m}$ [d_{m1}] and $5 \mu\text{m}$ [d_{m2}] particles), reference motor, acceleration nullified.

8.97 MPa, giving an M_a value of 0.121. Referring to the single-set chart of Figure 10 [16], one can observe that in the limit of just using $5 \mu\text{m}$ particles at a 1.5% overall loading, the value for M_a is less than 0.15, using $10 \mu\text{m}$ particles at a 1.5% overall loading produces a value for M_a is less than 0.2, and for $60 \mu\text{m}$ particles at a 1.5% overall loading, the value for M_a is less than 0.2. In qualitative terms, one can state that the low-suppression attenuation observed in Figure 9 is reasonably consistent with what one would expect from the aggregate of the three individual diameter results of Figure 10 although, quantitatively, at least in this case, the 3-set attenuation seen in Figure 9 is a bit worse (lower) than any of the three in isolation.

One adjustment in particle size produces a significant change in the result of Figure 9, as evidenced by Figure 11. Using $40 \mu\text{m}$ particles in place of the $60 \mu\text{m}$ particles at a 0.5% loading as part of the overall 1.5% loading, the limit pressure wave magnitude is significantly decreased, down to 1.22 MPa from the earlier value of 8.97, or producing an M_a of around 0.88. Referring to the single-set trend chart of Figure 10, this indicates that the system has decided to shift to the high-suppression domain by this one adjustment, moving from the low-suppression domain that the system preferred in Figure 9.

Along the lines of Figures 7 and 10, one can produce charts showing trends as relates to using two sets of particles of the same material, but differing diameters. As the baseline case, Figure 12 shows an attenuation chart at three different overall particle mass loadings (α_p) for various loading distributions ($\alpha_{p2} : \alpha_{p1}$) of $10 \mu\text{m}$ particles. Acceleration effects on combustion are nullified for these examples. The

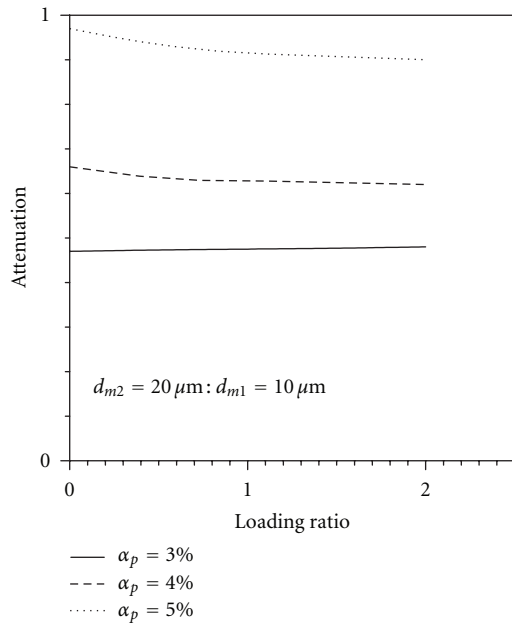


FIGURE 14: Nondimensional attenuation as function of particle diameter and loading distribution $[\alpha_{p2} : \alpha_{p1}]$ for two sets of particles ($10 \mu\text{m}$ [d_{m1}] and $20 \mu\text{m}$ [d_{m2}] particles), reference motor, acceleration nullified.

loading ratio in these examples is referenced to the $10 \mu\text{m}$ size (d_{m1}), since as illustrated in Figure 7, it is nominally around the best size for attenuation of pressure-wave development in the single-size case. Because the particles of the two sets are the same size, there would not be any change in attenuation, as reflected by the resulting curves being horizontal lines from left to right. Figure 13 by contrast shows downward sloping lines when using a distribution of 5 and $10 \mu\text{m}$ particles at different overall loadings. Each of the 3 curves would continue rightward to their respective asymptotic limit, whereby only $5 \mu\text{m}$ particles are ultimately present (see Figure 7 for limit values of attenuation at the three loadings of the $5\text{-}\mu\text{m}$ size). A chart such as that shown by Figure 13 would also be instructive towards the case of using reactive particles that would reduce in size (due to burnback) during their lifetime in the motor chamber. The level of attenuation may not be as effective as one might expect from the baseline nominal starting value for the particle diameter. Figure 14 shows downward sloping lines when using a distribution of 20 and $10 \mu\text{m}$ particles at different overall loadings, but of a less severe nature (relative to that seen in Figure 13), given the similar effectiveness of the two particle sizes below an overall loading of 5% as per Figure 7.

An alternative format for illustrating trends associated with using two sets of particles is provided in Figures 15, 16, and 17, for overall particle mass loading percentages of 3, 4, and 5%. Here, the three graphs are restricted to evaluating an even 1 : 1 split in the distribution of the two sets, but with the particle diameters varied relative to each other. A more dramatic change in attenuation effectiveness as a function of varying the particle diameters is seen in the curves of Figure 17, for the 5% loading case, which again (referring to

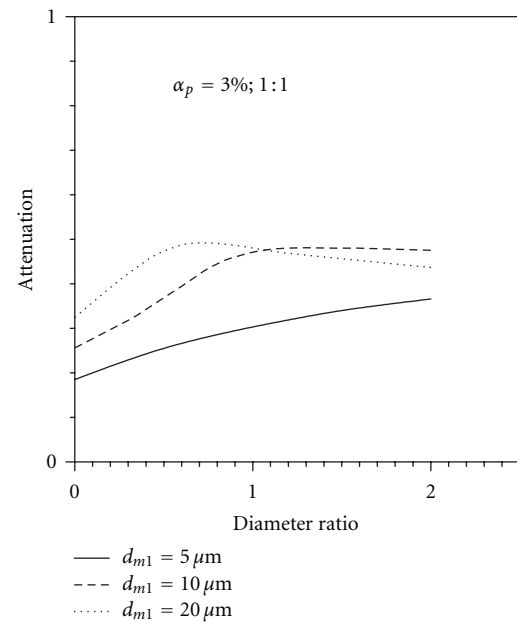


FIGURE 15: Nondimensional attenuation as function of particle diameter ($d_{m2} : d_{m1}$), for a 1 : 1 loading distribution for two sets of particles at total loading of 3%, reference motor, acceleration nullified.

the previous paragraph), tends to correlate with the trends associated with Figure 7.

4. Concluding Remarks

A numerical evaluation of the use of two or three sets of different-sized nonburning particles within the flow as a means for suppressing axial pressure wave development has been completed for a reference cylindrical-grain composite-propellant motor, in cases where the transient burning response of the propellant is the primary mechanism for driving the instability symptoms, and in cases where both the transient burning response in conjunction with vibration-induced acceleration is playing a role. The ability of the particles to suppress axial wave development is evident, at relatively low loading percentages, results that are consistent with experimental experience. This is clearly reflected by the respective attenuation maps. If this or a comparable numerical model proves to be suitably accurate, such maps could prove a useful tool for motor designers evaluating their own motor configurations for instability behavior.

The adverse effect of loading a second (or a third) particle set that has a size that is less effective in suppressing pressure wave motion is also made evident in the present results. This study also gives some indication of what might be expected with reactive particles, where due to particle size reduction with time (under burning) the suppression effectiveness may not be quite what one would have ideally expected. In a similar vein, the present results are an indicator of the potential adverse effects of the agglomeration of particles in producing particle sizes bigger than what one would ideally find desirable for suppressing wave activity. These and other

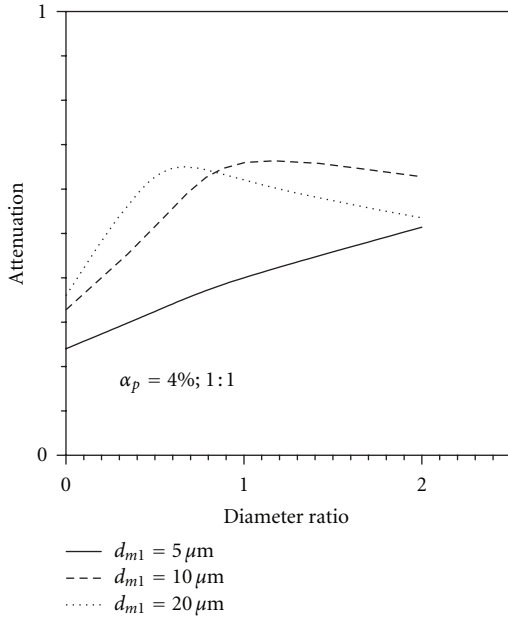


FIGURE 16: Nondimensional attenuation as function of particle diameter ($d_{m2} : d_{m1}$), for a 1:1 loading distribution for two sets of particles at total loading of 4%, reference motor, acceleration nullified.

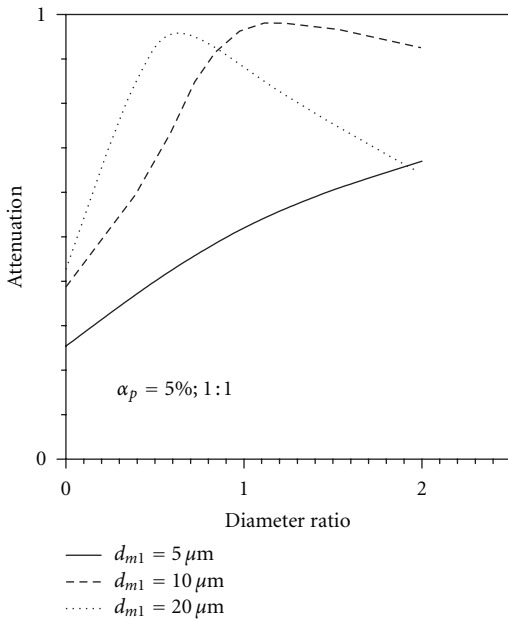


FIGURE 17: Nondimensional attenuation as function of particle diameter ($d_{m2} : d_{m1}$), for a 1:1 loading distribution for two sets of particles at total loading of 5%, reference motor, acceleration nullified.

issues, some of them potentially quite complex, remain to be explored in regards to the use and modelling of reactive particles for suppression of combustion instability in SRMs.

Nomenclature

- A : local core cross-sectional area, m^2
 a : gas sound speed, m/s
 a_l : longitudinal (or lateral) acceleration, m/s^2
 a_n : normal acceleration, m/s^2
 b : nonequilibrium sound speed of two-phase mixture
 C : de St. Robert coefficient, $m/s-Pa^n$
 C_m : particle specific heat, $J/kg-K$
 C_p : gas specific heat, $J/kg-K$
 C_s : specific heat, solid phase, $J/kg-K$
 D_i : drag of gas on a particle from i th particle set, N
 d : local core hydraulic diameter, m
 d_{mi} : mean particle diameter for i th particle set, m
 E : local total specific energy of gas in core flow, J/kg
 E_{pi} : local total specific energy, i th particle set in flow, J/kg
 f : frequency, Hz , or Darcy-Weisbach friction factor
 G_a : accelerative mass flux, kg/m^2-s
 h : convective heat transfer coefficient, W/m^2-K
 ΔH_s : net surface heat of reaction, J/kg
 K_b : burn rate limiting coefficient, s^{-1}
 k : gas thermal conductivity, $W/m-K$
 k_s : thermal conductivity, solid phase, $W/m-K$
 M_a : magnitude of attenuation
 M_ℓ : limit magnitude, cyclic input
 m_{pi} : mean mass of a particle from i th particle set, kg
 N_i : number of particles from the i th set in a given volume
 N_{set} : total number of particle sets
 n : exponent, de St. Robert's law
 p : local gas static pressure, Pa
 Δp_d : initial pulse disturbance step pressure, Pa
 Q_i : heat transfer from gas to a particle from i th particle set, W
 R : specific gas constant, $J/kg-K$
 r_b : instantaneous burning rate, m/s
 $r_{b,o}$: reference burning rate, m/s
 $r_{b,qs}$: quasisteady burning rate, m/s
 r_b^* : unconstrained burning rate, m/s
 r_o : base burning rate, m/s
 T_f : flame temperature, gas phase, K
 T_i : initial temperature, solid phase, K
 T_{pi} : temperature of particle from i th set, K
 T_s : burning surface temperature, K
 Δt : time increment, s
 u : core axial gas velocity, m/s
 u_{pi} : core axial particle velocity for particle from i th set, m/s
 v_f : nominal flamefront velocity, m/s
 Ψ : elemental volume, m^3
 x : distance from head end, m
 Δx : spatial increment in axial direction, m
 y : radial distance from burning surface, m
 Δy : spatial increment in radial direction, solid phase, m
 Δy_{Fo} : Fourier limit spatial increment, m
 α_g : gas phase void fraction

- α_p : total particle mass fraction of overall core flow
- α_{pi} : particle mass fraction of i th particle set in overall core flow
- α_g : thermal diffusivity, solid phase, m^2/s
- β_g : particle-gas mass flux ratio
- γ : gas ratio of specific heats
- δ_o : reference combustion zone thickness, m
- δ_r : resultant combustion zone thickness, m
- k : vibration-based wall dilatation term ($1/A \cdot \delta A/\delta t$), s^{-1}
- μ : absolute gas viscosity, $kg/m\cdot s$
- ρ : gas density, kg/m^3
- ρ_p : total density of particles in core flow, kg/m^3
- ρ_{pi} : density, i th particle set in core flow, kg/m^3
- ρ_m : solid density of particle, kg/m^3
- ρ_s : solid density of propellant, kg/m^3
- ρ_{so} : reference solid density of propellant (no particle loading), kg/m^3
- ϕ : acceleration orientation angle, rad
- ϕ_d : longitudinal/lateral-acceleration-based displacement orientation angle, rad.

References

- [1] W. G. Brownlee, "Nonlinear axial combustion instability in solid propellant motors," *AIAA Journal*, vol. 2, no. 2, pp. 275–284, 1964.
- [2] F. S. Blomshield, J. E. Crump, H. B. Mathes, R. A. Stalnaker, and M. W. Beckstead, "Stability testing of full-scale tactical motors," *Journal of Propulsion and Power*, vol. 13, no. 3, pp. 349–355, 1997.
- [3] F. S. Blomshield, H. B. Mathes, J. E. Crump, C. A. Beiter, and M. W. Beckstead, "Nonlinear stability testing of full-scale tactical motors," *Journal of Propulsion and Power*, vol. 13, no. 3, pp. 356–366, 1997.
- [4] E. W. Price, "Solid rocket combustion instability—an American historical account," in *Nonsteady Burning and Combustion Stability of Solid Propellants*, L. De Luca, E. W. Price, and M. Summerfield, Eds., vol. 143 of *Progress in Astronautics & Aeronautics Series*, pp. 1–16, AIAA Publications, Washington, DC, USA, 1992.
- [5] M. Barrère, "Introduction to nonsteady burning and combustion instability," in *Nonsteady Burning and Combustion Stability of Solid Propellants*, L. De Luca, E. W. Price, and M. Summerfield, Eds., vol. 143 of *Progress in Astronautics & Aeronautics Series*, pp. 17–58, AIAA Publications, Washington, DC, USA, 1992.
- [6] F. E. C. Culick, "Prediction of the stability of unsteady motions in solid-propellant rocket motors," in *Nonsteady Burning and Combustion Stability of Solid Propellants*, L. De Luca, E. W. Price, and M. Summerfield, Eds., vol. 143 of *Progress in Astronautics & Aeronautics Series*, pp. 719–780, AIAA Publications, Washington, DC, USA, 1992.
- [7] S. R. Fischbach, J. Majdalani, and G. A. Flandro, "Acoustic instability of the slab rocket motor," *Journal of Propulsion and Power*, vol. 23, no. 1, pp. 146–157, 2007.
- [8] D. E. Kooker and B. T. Zinn, "Triggering axial instabilities in solid rockets: numerical predictions," in *Proceedings of the 9th AIAA/SAE Joint Propulsion Conference*, Las Vegas, Nev, USA, November 1973, AIAA Paper No. 73-1298.
- [9] J. D. Baum and J. N. Levine, "Modeling of nonlinear longitudinal instability in solid rocket motors," *Acta Astronautica*, vol. 13, no. 6-7, pp. 339–348, 1986.
- [10] K. Ramohalli, "Technologies and techniques for instability suppression in motors," in *Nonsteady Burning and Combustion Stability of Solid Propellants*, L. De Luca, E. W. Price, and M. Summerfield, Eds., vol. 143 of *Progress in Astronautics & Aeronautics Series*, pp. 805–848, AIAA Publications, Washington, DC, USA, 1992.
- [11] E. W. Price, "Experimental observations of combustion instability," in *Fundamentals of Solid-Propellant Combustion*, K. K. Kuo and M. Summerfield, Eds., vol. 90 of *Progress in Astronautics & Aeronautics Series*, pp. 733–790, AIAA Publications, Washington, DC, USA, 1984.
- [12] F. S. Blomshield, K. J. Kraeutle, R. A. Stalnaker, M. W. Beckstead, and B. Stokes, "Aluminum combustion effects on combustion instability of high burn rate propellants," in *the 28th JANNAF Combustion Meeting*, vol. 3, pp. 419–438, October 1991.
- [13] F. S. Blomshield, "Historical perspective of combustion instability in motors: case studies," in *Proceedings of the 37th AIAA/ASME/SAE/ASEE Joint Propulsion Conference*, Salt Lake City, Utah, USA, July 2001, AIAA Paper No. 2001-3875.
- [14] R. H. W. Waesche, "Mechanisms and methods of suppression of combustion instability by metallic additives," *Journal of Propulsion and Power*, vol. 15, no. 6, pp. 919–922, 1999.
- [15] K. W. Dotson and B. H. Sako, "Interaction between solid rocket motor internal flow and structure during flight," *Journal of Propulsion and Power*, vol. 23, no. 1, pp. 140–145, 2007.
- [16] D. R. Greatrix, "Inert particles for axial-combustion-instability suppression in a solid rocket motor," *Journal of Propulsion and Power*, vol. 24, no. 6, pp. 1347–1354, 2008.
- [17] R. A. Dobbins and S. Temkin, "Measurements of particulate acoustic attenuation," *AIAA Journal*, vol. 2, no. 6, pp. 1106–1111, 1964.
- [18] M. Forde, "Quasi-one-dimensional gas/particle nozzle flows with shock," *AIAA Journal*, vol. 24, no. 7, pp. 1196–1199, 1986.
- [19] J. J. Gottlieb and D. R. Greatrix, "Numerical study of the effects of longitudinal acceleration on solid rocket motor internal ballistics," *Journal of Fluids Engineering*, vol. 114, no. 3, pp. 404–410, 1992.
- [20] D. R. Greatrix and P. G. Harris, "Structural vibration considerations for solid rocket internal ballistics modeling," in *Proceedings of the 36th AIAA/ASME/SAE/ASEE Joint Propulsion Conference*, Huntsville, Ala, USA, July 2000, AIAA Paper No. 2000-3804.
- [21] H. Krier, S. T. Surzhikov, and R. L. Glick, "Prediction of the effects of acceleration on the burning of AP/HTPB solid propellants," in *Proceedings of the 39th AIAA Aerospace Sciences Meeting*, Reno, Nev, USA, January 2001, AIAA Paper No. 2001-0343.
- [22] S. Loncaric, D. R. Greatrix, and Z. Fawaz, "Star-grain rocket motor—nonsteady internal ballistics," *Aerospace Science and Technology*, vol. 8, no. 1, pp. 47–55, 2004.
- [23] J. Montesano, K. Behdinin, D. R. Greatrix, and Z. Fawaz, "Internal chamber modeling of a solid rocket motor: effects of coupled structural and acoustic oscillations on combustion," *Journal of Sound and Vibration*, vol. 311, no. 1-2, pp. 20–38, 2008.
- [24] C. Baczynski and D. R. Greatrix, "Steepness of grain geometry transitions on instability symptom suppression in solid rocket motor," in *Proceedings of the 45th AIAA/ASME/SAE/ASEE Joint*

Propulsion Conference, Denver, Colo, USA, August 2009, AIAA Paper No. 2009-5177.

- [25] D. R. Greatrix, "Transient burning rate model for solid rocket motor internal ballistic simulations," *International Journal of Aerospace Engineering*, vol. 2008, Article ID 826070, 10 pages, 2008.
- [26] D. E. Kooker and C. W. Nelson, "Numerical solution of solid propellant transient combustion," *Journal of Heat Transfer*, vol. 101, no. 2, pp. 359–364, 1979.
- [27] D. R. Greatrix, "Model for prediction of negative and positive erosive burning," *Canadian Aeronautics and Space Journal*, vol. 53, no. 1, pp. 13–21, 2007.
- [28] D. R. Greatrix, "Parametric analysis of combined acceleration effects on solid-propellant combustion," *Canadian Aeronautics and Space Journal*, vol. 40, no. 2, pp. 68–73, 1994.

Research Article

Boron Particle Ignition in Secondary Chamber of Ducted Rocket

J. X. Hu, Z. X. Xia, W. H. Zhang, Z. B. Fang, D. Q. Wang, and L. Y. Huang

College of Aerospace and Materials Engineering, National University of Defense Technology, Changsha 410073, China

Correspondence should be addressed to Z. X. Xia, xiazhixun@nudt.edu.cn

Received 6 October 2011; Accepted 15 December 2011

Academic Editor: Valsalayam Sanal Kumar

Copyright © 2012 J. X. Hu et al. This is an open access article distributed under the Creative Commons Attribution License, which permits unrestricted use, distribution, and reproduction in any medium, provided the original work is properly cited.

In the secondary chamber of ducted rocket, there exists a relative speed between boron particles and air stream. Hence, the ignition laws under static conditions cannot be simply applied to represent the actual ignition process of boron particles, and it is required to study the effect of forced convective on the ignition of boron particles. Preheating of boron particles in gas generator makes it possible to utilize the velocity difference between gas and particles in secondary chamber for removal of the liquid oxide layer with the aid of Stoke's forces. An ignition model of boron particles is formulated for the oxide layer removal by considering that it results from a boundary layer stripping mechanism. The shearing action exerted by the high-speed flow causes a boundary layer to be formed in the surface of the liquid oxide layer, and the stripping away of this layer accounts for the accelerated ignition of boron particles. Compared with the King model, as the ignition model of boron particles is formulated for the oxide layer removal by considering that it results from a boundary layer stripping mechanism, the oxide layer thickness thins at all times during the particle ignition and lower the ignition time.

1. Introduction

Systematic advances in missile propulsion systems technology have provided large increases in missile performance capabilities. Replacement of much of solid propellant rocket oxidizer with free stream air, as in the ducted rocket concept, offers over 5 to 1 increase in missile range capability [1]. Boron has been considered for many years as a prime candidate used for increasing the ducted rocket capabilities based on its high potential energy release on both a volumetric and gravimetric basis coupled with a high energy of combustion, high combustion temperature, and low-molecular-weight products [2]. These properties make boron an attractive material for use in ducted rocket propellants [3]. In order for these advantages to be realized, however, the boron particles must ignite and burn completely within a very limited residence time. Since boron particles are generally initially coated with an oxide layer with inhibits combustion and since boron has an extremely high boiling point, which necessitates surface burning subsequent to oxide removal, this can become difficult, particularly under adverse operating conditions [4].

In previous work, two scenarios for boron ignition and combustion have been identified, which differ in the

controlling element in the overall process mechanism [5]. Two controversial theories remain to be resolved for describing boron ignition (removal of oxide coating) in terms of the rate limiting steps [4, 6, 7]. Previous experiments of Macek and semple [8] and Li and Williams [7] have demonstrated that when the boron particle temperature is high (e.g., 1800 K), the rate of boron diffusion exceeds the rate of oxygen diffusion across the oxide layer. Recent experimental observations indicating significant agglomeration and liquefaction of boron at 1213 K in both O₂ and Ar environments have also been interpreted as evidence supporting the diffusion of boron instead of oxygen within the oxide coating as the limiting process [3, 9].

Because ignition and combustion of boron particles involve the release of heat, layer evolution assumes the form of a thermo-hydrodynamic process, coupled with the solid boron substrate underneath and with the ambient oxidizing atmosphere, which is assumed to be stagnant [5]. It is important to note that most the current models of boron particles ignition constrain the symmetry to be conserved. That is to say that the oxidizing atmosphere is assumed to be stagnant and uniform if the particle and its initial oxide layer are given to be spherically symmetric. In the secondary

combustion chamber of ducted rocket, there always exists a relative speed between the boron particle and air stream [10]. Hence, the ignition laws under static conditions cannot be simply applied to represent the actual ignition process of boron particles, and it is required to study the effect of forced convective on the ignition of the boron particle. Much research has been conducted to study the ignition of the boron particle, both experimentally and theoretically, in pure oxygen and other atmospheres, with relatively little work available on ignition of the boron particle under forced convection conditions [11, 12]. Dirk Meinkohn developed a thin model to allow the oxide flow field to be derived in the creeping-flow approximation and demonstrated that boron particle ignition may then be caused by the Marangoni effect, which is shown to entail the spreading of punctures and ruptures in the oxide layer, leading to layer thinning or even complete layer removal [13, 14]. Preheating of the boron particles in gas generator makes it possible to utilize the velocity difference between gas and particles in secondary chamber for removal of the liquid oxide layer with the aid of Stokes' forces. Povitsky and Goldman demonstrated there is indication of regime of fast ignition enhanced by Stokes' forces by experimentally and numerical simulation [15].

The object of this study is to investigate the oxide layer movement and to characterize its influence on ignition of boron particles in the case of high initial relative particle velocity. An ignition model of boron particles is formulated for the oxide layer removal by considering that it results from a boundary layer stripping mechanism.

2. Formulation

2.1. Boundary Layer Stripping Analysis

2.1.1. Assumptions. The movement of the oxide layer on the front half-surface of the boron particle is shown schematically in Figure 1, using a spherical coordinate system with the particle center as origin. x is the curvilinear coordinate along the interface separating the two fluids and y is the coordinate perpendicular to it. $y = 0$ represents the interface between the gas layer and liquid oxide one. $y = +\infty$ represents the value of gas boundary layer. $y = -\infty$ represents the value of liquid boundary layer. u_g, u_l represent fluid velocity in gas or liquid boundary layer. R is the radius of the boron particle. X is the thickness of liquid oxide layer. U_∞ represents gas freestream velocity. $U(x)$ represents gas fluid velocity around the boron particle.

In order to solve the problem of liquid oxide layer movement, the following assumptions are adopted.

- (1) The temperature inside and around the boron particle is uniformity.
- (2) The flow is steady and incompressible.
- (3) There is no flow separation at the interface between solid particle and liquid oxide layer.
- (4) The value of liquid oxide boundary layer is less than the thickness of liquid oxide layer.

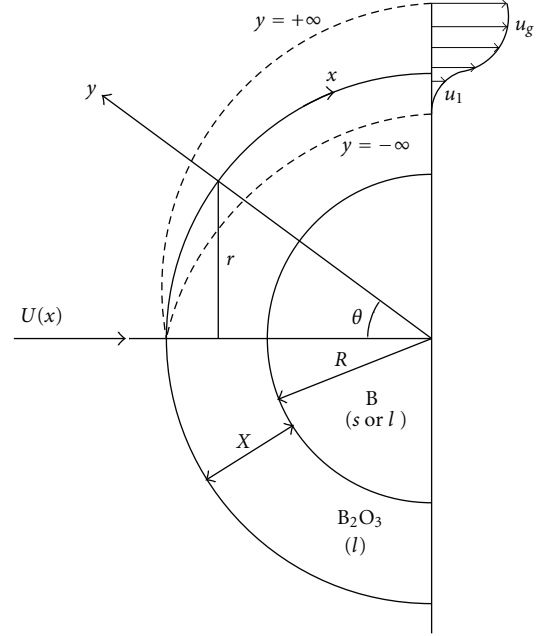


FIGURE 1: Scheme of oxide layer movement relative to surface of flowing boron particles.

- (5) The boron particle shape can be approximated by a sphere for the simplified analysis here, the oxide layer thickness is much smaller than particle radius, and hence the gas fluid velocity around the boron particle can be represented in the following expression:

$$U(x) = 1.5 U_\infty \sin \frac{x}{R}. \quad (1)$$

- (6) Equating the shear stress in the gas layer to that in the liquid layer at the interface yields the following equation:

$$\left(\mu_g \frac{\partial u_g}{\partial y} \right)_{y=0} = \left(\mu_l \frac{\partial u_l}{\partial y} \right)_{y=0}. \quad (2)$$

- (7) The pressure gradient in the gas layer and the liquid layer is equal:

$$\left(\frac{\partial P}{\partial x} \right)_l = \left(\frac{\partial P}{\partial x} \right)_g. \quad (3)$$

2.1.2. Equations and Solution. An approximate solution to the two-boundary-layer problem can be obtained by assuming arbitrary simple velocity distributions containing a few parameters and the using the momentum differential relations to determine three parameters [16]. If we assume that the flow is steady and incompressible, then it yields the boundary-layer differential equations for the gas and for the liquid.

The basic equations for the gas is given by

$$\begin{aligned} \frac{\partial(u_g r)}{\partial x} + \frac{\partial(v_g r)}{\partial y} &= 0, \\ u_g \frac{\partial u_g}{\partial x} + v_g \frac{\partial u_g}{\partial y} &= -\frac{1}{\rho_g} \frac{\partial P}{\partial x} + \frac{\mu_g}{\rho_g} \frac{\partial^2 u_g}{\partial y^2}. \end{aligned} \quad (4)$$

The boundary conditions for equations above is given by

$$\begin{aligned} y = 0 : v_g &= 0, \quad u_g = u_g(x), \quad \mu_g \frac{\partial u_g}{\partial y} = \mu_l \frac{\partial u_l}{\partial y}, \\ y = \infty : u_g &= U(x), \end{aligned} \quad (5)$$

where the pressure gradient in the gas boundary layer is given by

$$-\frac{1}{\rho_g} \frac{\partial P}{\partial x} = U \frac{\partial U}{\partial x}. \quad (6)$$

Then (4) can be given by

$$u_g \frac{\partial u_g}{\partial x} + v_g \frac{\partial u_g}{\partial y} = U \frac{\partial U}{\partial x} + \frac{\mu_g}{\rho_g} \frac{\partial^2 u_g}{\partial y^2}. \quad (7)$$

The basic equations for the liquid are given by

$$\frac{\partial(u_l r)}{\partial x} + \frac{\partial(v_l r)}{\partial y} = 0, \quad (8)$$

$$u_l \frac{\partial u_l}{\partial x} + v_l \frac{\partial u_l}{\partial y} = \frac{\rho_g}{\rho_l} U \frac{\partial U}{\partial x} + \frac{\mu_l}{\rho_l} \frac{\partial^2 u_l}{\partial y^2}. \quad (9)$$

The boundary conditions for equations above are given by

$$\begin{aligned} y = 0 : v_l &= 0, \quad u_l = u_g(x), \quad \mu_l \frac{\partial u_l}{\partial y} = \mu_g \frac{\partial u_g}{\partial y}, \\ y = -\infty : \mu_l \frac{\partial u_l}{\partial y} &= 0. \end{aligned} \quad (10)$$

In order for equations solution, the stream function, ψ , is defined by

$$u = \frac{L}{r} \frac{\partial \psi}{\partial y}, \quad v = -\frac{L}{r} \frac{\partial \psi}{\partial x}, \quad (11)$$

where L denotes the latent length.

Some normalized variable parameters are defined by

$$\begin{aligned} \xi &= \int_0^x \frac{r^2(x)U(x)}{L^2 U_\infty} dx, \quad \eta = \frac{yU(x)r(x)}{L\sqrt{2\mu_g U_\infty \xi/\rho_g}}, \\ \psi &= G(\eta) \sqrt{\frac{2\mu_g U_\infty \xi}{\rho_g}}. \end{aligned} \quad (12)$$

Then the equations for the gas can be simplified as

$$G''' + GG'' + \beta(\xi)(1 - G^2) = 0, \quad (13)$$

where $\beta(\xi) = 2\xi U_\infty ((L^2/r^2)dU/dx(1/U^2))$.

The boundary conditions for equations above can be simplified as

$$\begin{aligned} \eta = 0 : G &= 0, \quad G' = \bar{u}(x), \\ \eta = \infty : G' &= 1. \end{aligned} \quad (14)$$

Then the equations for the liquid can be simplified as

$$L''' + LL'' + \beta(\xi) \left(\frac{\rho_g}{\rho_l} - L^2 \right) = 0. \quad (15)$$

The boundary conditions for equations above can be simplified as

$$\begin{aligned} \eta = 0 : L &= 0, \quad L' = G', \quad L'' = G''\Gamma, \\ \eta = -\infty : L'' &= 0, \end{aligned} \quad (16)$$

where $\Gamma = \sqrt{\rho_g \mu_g / (\rho_l \mu_l)}$, gas viscosity $\mu_g = 6.2 \times 10^{-5} \text{ Pa} \cdot \text{s}$, liquid viscosity $\mu_l = 3.2 \times 10^{-4} \text{ Pa} \cdot \text{s}$.

After what may seem like an interminable manipulation of the governing equations, we have finally set up that particular form of the equations that will be most appropriate as well as convenient for the gas and liquid boundary layer flow. In order to solve (13) and (15), $G'(0)$ and $G''(0)$ should be first got. According to literature [17], $G'(0) = \bar{u}(x) = (\rho_g \mu_g / \rho_l \mu_l)^{1/3}$. Firstly, $G''(0)$ is given or estimated, the classical four-order Runge-Kutta method is used to solve these ordinary differential equations. If the obtained boundary values satisfy the actual boundary conditions at the outer edge; namely, $G'(+\infty) = 1$ and $L''(-\infty) = 0$, the calculation can be stopped, and the solutions have been found. Otherwise, we have to revise the estimated value of $G''(0)$ and repeat the numerical integrating procedure until all the boundary conditions at the outer edge are satisfied.

2.1.3. The Conditions of Aerodynamic Shattering. During aerodynamic shattering, the tangential friction stress is propitious to sweep the liquid oxide layer from solid particle, and the surface tension is unpropitious to sweep the liquid oxide layer.

The tangential friction stress can be expressed by

$$\tau = \left(\mu_g \frac{\partial u_g}{\partial y} \right)_{y=0} = \mu_g \frac{U^2 r G''(0)}{L \sqrt{2\mu_g U_\infty \xi}}. \quad (17)$$

For a spherical particle, the surface tension can be expressed by

$$F = \frac{C_1 \sigma}{R}. \quad (18)$$

According to literature [15], the constant $C_1 = 2.0$ and the coefficient of surface tension $\sigma = 0.01$.

We and Re can be expressed by

$$\text{We} = \frac{\rho_g u_r^2 d_p}{\sigma}, \quad \text{Re} = \frac{\rho_g u_r d_p}{\mu_g}, \quad (19)$$

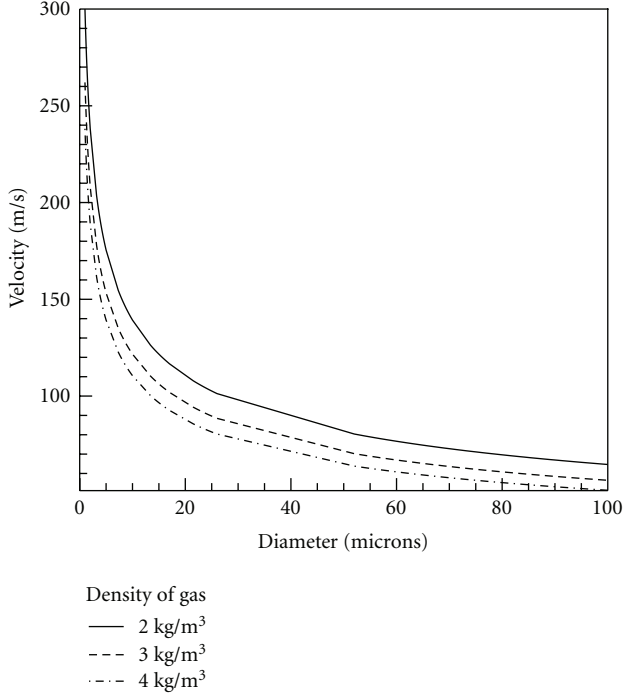


FIGURE 2: Critical velocity versus particle diameter for various gas densities.

where $u_r = U_\infty - W$ represents the relative velocity between gas flow and boron particles. W represents the velocity of boron particles. d_p represents the diameter of boron particles.

While the surface tension is less than the tangential friction stress, aerodynamic shattering may happen. That is to say, part of liquid oxide layer is detached from the particle if the following equation comes into existence:

$$\frac{We}{\sqrt{Re}} \geq \frac{8}{9} \frac{C_1}{G''(0)}. \quad (20)$$

The critical velocity $u_{r \min}$ can be reduced by the relation

$$u_{r \min} = \left(\frac{64C_1^2\sigma^2}{81G''(0)\rho_g\mu_g d_p} \right)^{1/3}. \quad (21)$$

Beyond $u_{r \min}$, part of liquid oxide layer is detached from the particle and it is shifted to the rear. The formula above permits determination of the range of critical velocities for boron particle coated by a thin liquid oxide layer. The critical velocity versus particle diameter for various gas densities is shown in Figure 2. It may be seen that it is difficult for aerodynamic shattering to happen when the particle diameter is less than 15 microns.

The mass of fluid in the circumferential liquid oxide layer being swept along by the gas steam at a distance $x = \pi(R + X)/2$ from the stagnation point is

$$\frac{dm}{dt} = \pi d_p \rho_l \int_{-\infty}^0 u_l dy = \pi d_p \rho_l \sqrt{\frac{d_p u_r \mu_l}{\rho_l}} \int_{-\infty}^0 L'(\eta) d\eta. \quad (22)$$

We can assume that the thickness of liquid oxide layer of boron particle is still uniformity along the uniformity after aerodynamic shattering. The following formula can be reduced

$$\frac{dm}{dt} = \rho_l \pi d_p^2 \frac{dX}{dt}. \quad (23)$$

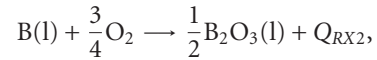
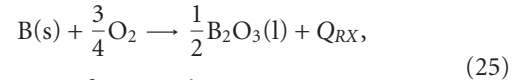
The change in the liquid oxide layer of boron particles due to aerodynamic shattering can be reduced:

$$\frac{dX}{dt} = \sqrt{\frac{u_r \mu_l}{(d_p \rho_l)}} \int_{-\infty}^0 L'(\eta) d\eta. \quad (24)$$

2.2. Ignition Model of Boron Particle in High-Speed Flow. The results obtained above are used for developing an ignition model of boron particles, adopting a spherical form for the particles. For nonspherical particles, the aerodynamic shattering of liquid oxide layer is the same in principle, but the relevant expressions are more complicated.

In the analysis below we resort to King's model, based on the assumption that the exothermic reaction between boron and oxygen takes place at the boron-boron oxide interface as a result of oxygen diffusion across the melting oxide layer [4, 15]. As the oxygen converts the boron into boric oxide, thickens the oxide layer, and releases heat, the oxide simultaneously vaporizes at the outer surface, this second process is endothermic and reduces the heating rate. Heat is added to or removed from the particle by convection and radiation, while inside the particle it is transferred by conduction from the surface to the center. Ignition occurs when the liquid oxide layer at the leading point of the particle is completely removed by the tangential friction stress effects [4, 15].

Step 1.

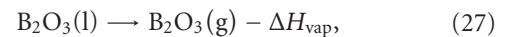


where $Q_{RX} = 6.132 \times 10^5$ J/mole, $Q_{RX2} = 6.342 \times 10^5$ J/mole.

$$w_B = \frac{64.8 \times 10^{-8}(R+X)^2 T_p P_{O_2} e^{-22600/T_p}}{X} \text{ (mole/s)}, \quad (26)$$

where w_B is the molar consumption rate of boron.

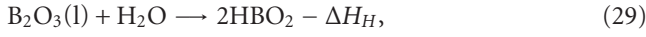
Step 2.



$$w_E = \frac{1.005 \times 10^{10}(R+X)^2 \alpha e^{-44000/T_p}}{T_p^{0.5} (1 + 4.5 \times 10^7 \alpha P(R+X)/(T_p Nu))} \text{ (mole/s)}, \quad (28)$$

where w_E is the molar rate of vaporization of boron, $\Delta H_{vap} = 3.78 \times 10^5$ J/mole.

Step 3.



$$E_{w_H} = 9.15 \times 10^{-7} \frac{\text{Nu}}{P} (R+X) T_p^{1/2} \exp \left[18.1 \left(1 - \frac{2100}{T_p} \right) \right] \\ \times \left\{ -0.15 \right. \\ \left. + \left[0.0225 + P_{\text{H}_2\text{O}} \right. \right. \\ \left. \left. \times \exp \left(-18.1 \left(1 - \frac{2100}{T_p} \right) \right) \right]^{0.5} \right\} \text{ (mole/s)}, \quad (30)$$

where w_H is the molar rate of removal of boric oxide, $\Delta H_H = 3.15 \times 10^5$ J/mole. The equation for particle radius and oxide layer thickness dynamic can be written as

$$\frac{dR}{dt} = -\frac{w_B M_B}{4\pi R^2 \rho_B}, \quad (31)$$

$$\frac{dX}{dt} = \frac{(w_B/2 - w_E - w_H) M_{\text{B}_2\text{O}_3}}{4\pi R^2 \rho_{\text{B}_2\text{O}_3}} \\ - \sqrt{\frac{u_r \mu_l}{(d_p \rho_l)}} \int_{-\infty}^0 L'(\eta) d\eta. \quad (32)$$

The first term on the right-hand side of formula (33) is due to King's model, and the second refers to our model of liquid oxide layer movement. For u_r less than $u_{r,\text{min}}$, the second term vanishes. The heat balance of liquid oxide layer is described by the equations (note that three different enthalpy balances must be employed depending on whether the particle temperature is less than, equal to, or greater than the melting point of boron, 2450 K):

$$\frac{dT_p}{dt} = \frac{Q_1}{(4\pi R^3 \rho_{\text{B}_2\text{O}_3} / 3) + 4\pi R^2 X \rho_{\text{B}_2\text{O}_3} c_{p\text{B}_2\text{O}_3}} \\ (T_p < 2450 \text{ K}, f = 0), \\ \frac{df}{dt} = \frac{Q_1}{4\pi R^3 \rho_B \Delta H_M / 3} \\ (T_p = 2450 \text{ K}, 0 < f < 1), \quad (33)$$

$$\frac{dT_p}{dt} = \frac{Q_2}{(4\pi R^3 \rho_{\text{B}_2\text{O}_3} / 3) + 4\pi R^2 X \rho_{\text{B}_2\text{O}_3} c_{p\text{B}_2\text{O}_3}} \\ (T_p > 2450 \text{ K}, f = 1),$$

where f is fraction of boron in the liquid phase, T_0 is free stream gas temperature, T_p is particle temperature, T_{RAD} is surrounding radiation temperature, Q_1, Q_2 are

heat transfer between particle and the surroundings, $Q_1 = w_B Q_{RX} - w_E \Delta H_{\text{vap}} - w_H \Delta H_H + 4\pi(R+X)^2 [h(T_\infty - T_p) + \sigma \epsilon \alpha_R (T_{\text{RAD}}^4 - T_p^4)]$, $Q_2 = w_B Q_{RX2} - w_E \Delta H_{\text{vap}} - w_H \Delta H_H + 4\pi(R+X)^2 [h(T_\infty - T_p) + \sigma \epsilon \alpha_R (T_{\text{RAD}}^4 - T_p^4)]$. The following values were used for other parameters appearing in equations above: $M_B = 10.82$, $\rho_B = 2.33 \times 10^3$ kg/m³, $M_{\text{B}_2\text{O}_3} = 69.64$, $\rho_{\text{B}_2\text{O}_3} = 1.85 \times 10^3$ kg/m³, $\text{Pr} = 0.72$, $\epsilon = 0.8$, $\alpha_R = 1$, $\Delta H_M = 2.1 \times 10^3$ J/mole, $h = 1.46 \times 10^{-2} \times \text{Nu} \times T_\infty^{0.8} / (R+X)$ J/(m² · s · K), $\text{Nu} = 2 + 0.6 \text{Re}^{1/2} \text{Pr}^{1/3}$, $c_{p\text{B}_2\text{O}_3} = 0.294 T_p$ J/(kg · K), $c_{p\text{B}_2\text{O}_3} = 2.84 \times 10^3$ J/(kg · K), $c_{p\text{B}_2\text{O}_3} = 1.84 \times 10^3$ J/(kg · K).

3. Results and Discussion

The model of boron ignition developed in this study involves nine independent parameters, value of which must be input to the resulting numerical computer program for prediction of particle ignition time and minimum gas temperature required for particle ignition [18]. There variables are relative velocity between gas flow and boron particles, initial oxide thickness, initial particle temperature, initial particle size, ambient temperature (surroundings gas temperature), effective surroundings radiation temperature, ambient pressure, water vapor mole fraction, and oxygen mole fraction. As part of this study, each of the above independent variables has been systematical varied to determine its effect on whether the particle will ignite and, if so, what the ignition time will be.

3.1. Effect of Ambient Temperature. In Figure 3 plots of oxide layer thickness, particle temperature, particle radius, and fraction boron melted versus time presented for a typical case in which the numerical analysis predicts particle ignition. The particle treated is 10 microns in radius with an initial oxide layer thickness of 0.1 micron and initial temperature of 1800 K. The pressure is 0.5 MPa, the oxygen mole fraction is 0.2, the water vapor mole fraction is zero, and the relative velocity between gas flow and boron particles is 100 m/s. The ambient temperature and effective surroundings radiation temperature are both 2100 K.

As may be shown in Figure 3, once the particle temperature exceeds approximately 2000 K, the oxide evaporation and the change due to aerodynamic shattering rise above the oxide generation rate, resulting in thinning of the oxide layer. The boron particle temperature continue to increase as the oxide layer thins while the boron melting point is reached. At this point the oxide thickness and particle temperature remain constant until the boron melts. After the boron particle has melted, the particle temperature resumes its rise and the oxide layer continues to thin until the particle ignite. Compared with King's model, as the ignition model of boron particles is formulated for the oxide layer removal by considering that it results from a boundary layer stripping mechanism, the oxide layer thickness thins at all times during the particle ignition and lower the ignition time.

In Figure 4, similar results are presented for a case identical except for reduction of the ambient temperature and effective surroundings radiation temperature by 200 K to

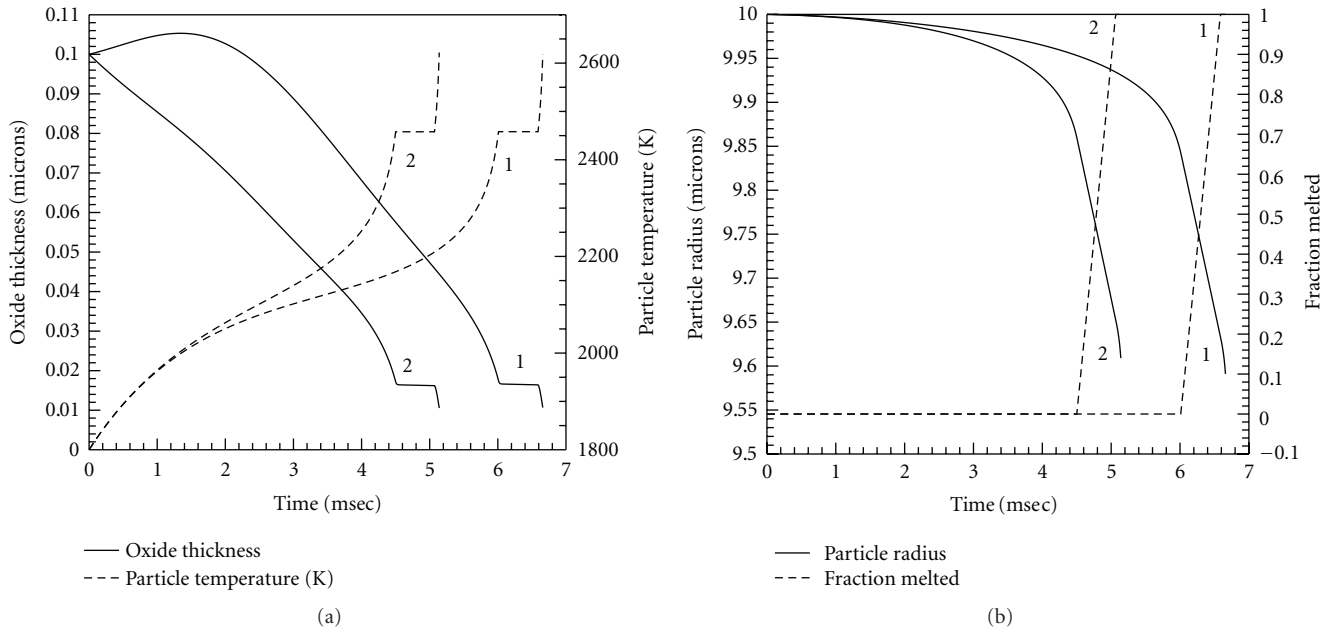


FIGURE 3: Predicted time dependence of important variables for particle which ignites at ambient temperature of 2100 K ((a) King's model (b) our model with film moving).

1900 K. The initial stages of the ignition process are quite similar. However, heat losses to the surroundings when the particle temperature rises above the 1900 K ambient temperature are sufficient to retard the evaporation rate sufficiently that it drops back to the generation rate with the result that the oxide layer ceases thinning. In this case, a stable quasi-steady-state is reached. The boron particle temperature remains a steady value, and the ignition does not occur.

3.2. Effect of Total Pressure and Oxygen Mole Fraction. The effects of total pressure and oxygen mole fraction in the gas-free stream on minimum gas temperature required for particle ignition and ignition time are shown in Figures 5 and 6. These calculations were all performed for particles of 10 microns radius with an initial temperature of 1800 K and initial oxide thicknesses of 0.1 microns. The calculations were carried out for a 100 m/s gas stream in the surroundings with water vapor mole fraction of zero at the conditions that ambient temperature and effective surroundings radiation temperature are both 2100 K. Similar trends were noted with other particle sizes and initial oxide thicknesses.

As shown in Figure 5, decreased total pressure lowers the gas temperature required for ignition at low oxygen mole fractions but raises the required gas temperature at high oxygen mole fractions. These fairly complex dependencies result from interaction of the effect of oxygen mole fraction on the oxide generation rate and the effect of total pressure on the oxide removal rate. Increase of the total pressure intensified oxygen diffusion through the oxide layer but reduced the oxide vaporizing rate. It also leads to increased gas density, with the attendance opposite influence on tangential friction stress [15]. Similar effects on the ignition time at a fixed gas temperature and velocity as functions of total pressure and

oxygen mole fraction are shown in Figure 6. At high oxidizer mole fractions, ignition time reduces with reducing total pressure while at low oxidizer mole fractions the pressure dependency is reversed.

3.3. Effect of Particle Radius. The effect of particle radius on ignition time was also studied. In Figure 7, predictions of ignition time versus particle radius for particle which are predicated to ignite are presented for several gas temperatures ranging from 2050 K to 2200 K, and the radiation surroundings temperature is set equal to ambient gas temperature. The particles (radius size range from 5 to 20 microns with an initial oxide layer thickness of 0.1 micron) were assumed to be preheated to 1800 K prior to ejection gas stream. The pressure is 0.5 MPa, the oxygen mole fraction is 0.2, the water vapor mole fraction is zero, and the relative velocity between gas flow and boron particles is 100 m/s. As shown in Figure 7, the ignition time decreases monotonically with decreasing particle radius due to the decrease in particle mass-to-surface area ratio with decreasing radius. For the higher ambient gas temperature, ignition time is shorter.

3.4. Effect of Water Vapor Mole Fraction. The effect of water vapor mole fraction in the gas-free stream on ignition time is shown in Figure 8. These calculations were all performed for particles of 10 microns radius with an initial temperature of 1800 K and initial oxide thicknesses of 0.1 microns. The pressure is 0.5 MPa, the oxygen mole fraction is 0.2, and the relative velocity between gas flow and boron particles is 100 m/s. The ambient temperature and effective surroundings radiation temperature are both 2100 K. As shown in Figure 8, the ignition time decreases monotonically with increasing water vapor mole fraction due to treating water

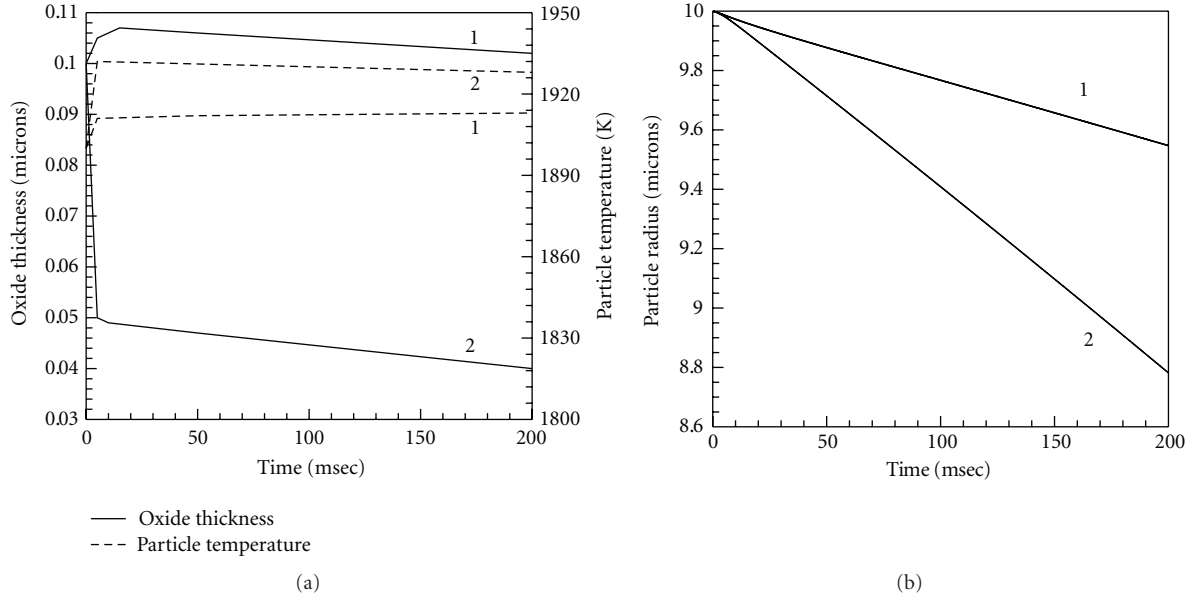


FIGURE 4: Predicted time dependence of important variables for particle which ignites at ambient temperature of 1900 K (a) King's Model (b) our model with film moving).

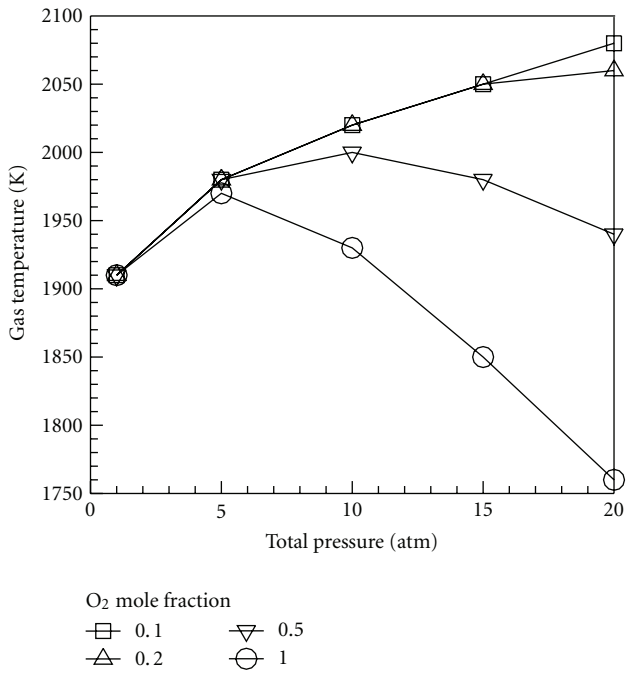


FIGURE 5: Minimum gas temperature required for ignition versus total pressure for various oxygen mole fractions.

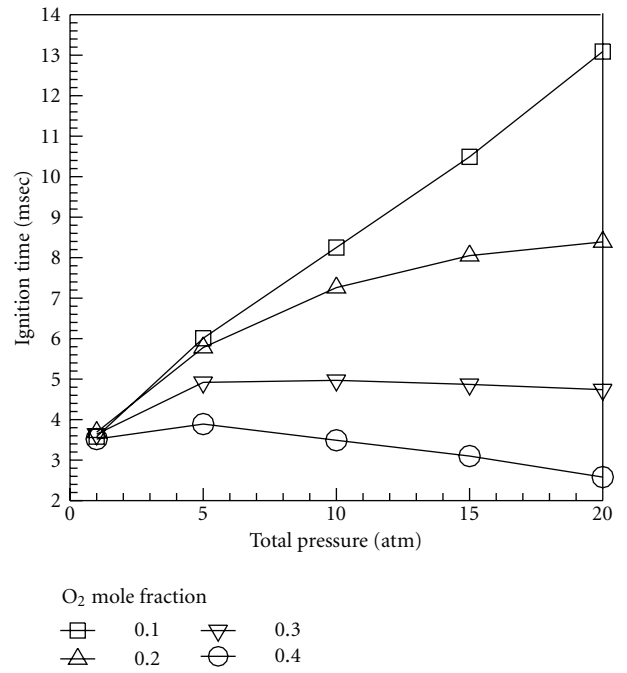


FIGURE 6: Ignition time versus total pressure for various oxygen mole fractions.

vapor as reacting by a diffusion-limited reaction with the boric oxide to aid in removal of the oxide layer.

4. Conclusions

The shearing action exerted by the high-speed flow causes a boundary layer to be formed in the surface of the liquid

oxide layer, and the stripping away of this layer accounts for the accelerated ignition of the boron particle. It is shown that migration of the liquid oxide layer on the front half-surface of the particle can be derived. The rate of disintegration is founded by integrating over the thickness of the liquid boundary layer to determine the mass flux leaving the boron particle surface at its equator. An ignition model of

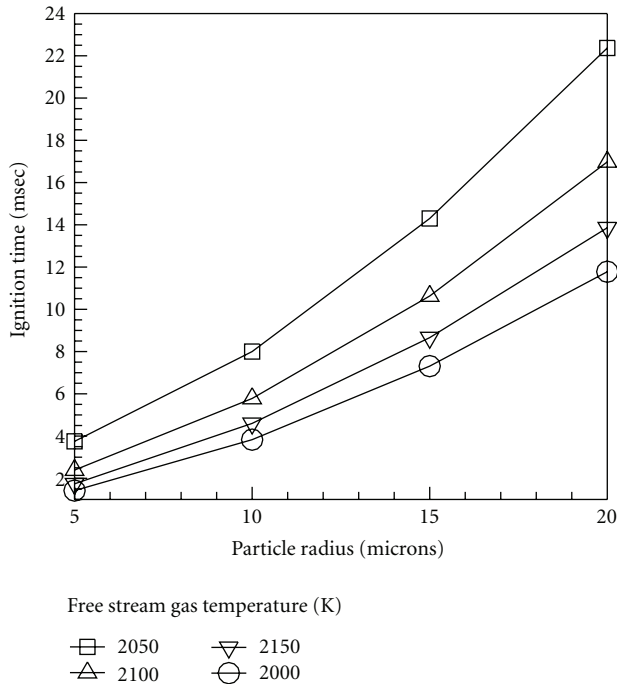


FIGURE 7: Ignition time versus particle radius for various ambient gas temperatures.

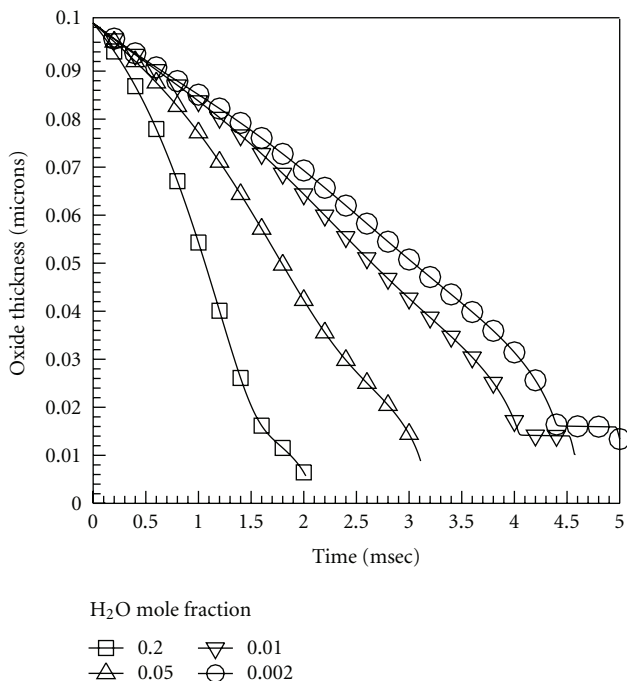


FIGURE 8: Oxide layer thickness versus time for various water vapor mole fractions.

boron particles is formulated for the oxide layer removal by considering that it results from a boundary layer stripping mechanism. Effects of various parameters on boron particle ignition were studied with this model. Compared with King's model, as the ignition model of boron particles is formulated for the oxide layer removal by considering that it

results from a boundary layer stripping mechanism, the oxide layer thickness thins at all times during the particle ignition and lower the ignition time. The present results support a physical mechanism through which preheated boron particles in gas generator of ducted rockets can be ignited in the secondary chamber by ejection into a high-speed stream.

Acknowledgments

The support of the China Sponsorship Council (CSC) (Grant no. 51006118) is gratefully acknowledged. J. X. Hu thanks Benveniste Natan of Technion-Israel Institute of Technology for the help and encouragement.

References

- [1] R. S. Fry, "A century of ramjet propulsion technology evolution," *Journal of Propulsion and Power*, vol. 20, no. 1, pp. 27–58, 2004.
- [2] B. Natan and A. Gany, "Ignition and combustion boron particles in the flow field of a solid fuel ramjet," *Journal of Propulsion and Power*, vol. 7, no. 1, pp. 37–43, 1991.
- [3] C. L. Yeh and K. K. Kuo, "Ignition and combustion of boron particles," *Progress in Energy and Combustion Science*, vol. 22, no. 6, pp. 511–541, 1996.
- [4] M. K. King, "Ignition and combustion of boron particles and clouds," *Journal of Spacecraft and Rockets*, vol. 19, no. 4, pp. 294–306, 1982.
- [5] D. Meinköhn, "Boron particle ignition and the marangoni effect," *Combustion Science and Technology*, vol. 176, no. 9, pp. 1493–1536, 2004.
- [6] G. Mohan and F. A. Williams, "Ignition and combustion of boron in O₂/inert atmospheres," *AIAA Journal*, vol. 10, no. 6, pp. 776–783, 1972.
- [7] S. C. Li and F. A. Williams, "Ignition and combustion of boron particles," *International Journal of Energetic Materials and Chemical Propulsion*, vol. 2, no. 1–6, pp. 248–271, 1991.
- [8] A. Macek and J. M. Semple, "Combustion of boron particles at atmospheric pressure," *Combustion Science and Technology*, vol. 1, no. 3, pp. 181–191, 1969.
- [9] W. Zhou, R. A. Yetter, F. L. Dryer, H. Rabitz, R. C. Brown, and C. E. Kolb, "Multi-phase model for ignition and combustion of boron particles," *Combustion and Flame*, vol. 117, no. 1–2, pp. 227–243, 1999.
- [10] J. X. Hu, Z. X. Xia, and D. Q. Wang, "Study on burning rate of boron particles in secondary chamber of ducted rocket under forced convection conditions," *Journal of Solid Rocket Technology*, vol. 30, no. 1, pp. 21–25, 2007.
- [11] R. O. Foelsche, R. L. Burton, and H. Krier, "Ignition and combustion of boron particles in hydrogen/oxygen explosion products," *AIAA 97-0127*, 1997.
- [12] M. A. Gurevich, I. M. Kir'yanov, and E. S. Ozerov, "Combustion of individual boron particles," *Combustion, Explosion, and Shock Waves*, vol. 5, no. 2, pp. 150–153, 1969.
- [13] D. Meinköhn, "Liquid oxide surface layers in metal combustion," *Combustion Theory and Modelling*, vol. 8, no. 2, pp. 315–338, 2004.
- [14] D. Meinköhn, "The effect of particle size and ambient oxidizer concentration on metal particle ignition," *Combustion Science and Technology*, vol. 181, no. 8, pp. 1007–1037, 2009.
- [15] A. Povitsky and Y. Goldman, "Boron particle ignition in high-speed flow," in *Proceedings of the 29th AIAA Joint Propulsion Conference*, vol. 2202, AIAA paper 93, 1993.

- [16] A. A. Ranger and J. A. Nicholis, "Aerodynamic shattering of liquid drops," *AIAA Journal*, vol. 7, no. 2, pp. 285–290, 1969.
- [17] M. Zhou and F. C. Zhuang, "Aerodynamic shattering of liquid drops using a boundary layer stripping mechanism," *Journal of National University of Defense Technology*, vol. 13, no. 3, pp. 29–33, 1991.
- [18] M. K. King, "Boron particle ignition in hot gas stream," *Combustion Science and Technology*, vol. 8, no. 5-6, pp. 254–273, 1974.